AFIT/GE/ENG/93D-07

A PHYSICS-BASED HETEROJUNCTION BIPOLAR TRANSISTOR MODEL FOR INTEGRATED CIRCUIT SIMULATION

THESIS

James A. Fellows
Captain, USAF

AFIT/GE/ENG/93D-07

Approved for public release; distribution unlimited

AFIT/GE/ENG/93D-07

A PHYSICS-BASED HETEROJUNCTION BIPOLAR TRANSISTOR MODEL FOR INTEGRATED CIRCUIT SIMULATION

THESIS

Presented to the Faculty of the Graduate School of Engineering

of the Air Force Institute of Technology

Air University

In Partial Fulfillment of the

Requirements for the degree of

Master of Science in Electrical Engineering

James A. Fellows, B.S.E.E

Captain, USAF

December 1993

Acknowledgements

I would like to thank my loving and selfless wife for her support and patience during this thesis effort. Her helpfulness at home and with our daughter Elise is deeply appreciated. This has been a challenging time for both of us, and she deserves far more credit than she has received.

I would like to thank my thesis advisor, Dr. Victor M. Bright, for his guidance, instruction, and encouragement. The many hours we spent at his whiteboard were invaluable in helping me to understand semiconductors. I would like to thank Dr. Burhan Bayraktaroglu and Dr. Chern Huang of WL/ELR. I am thankful for the measured data and geometry information provided by Bayraktaroglu. I appreciate the time and wisdom that they both shared with me through several insightful discussions on HBTs. I would also like to thank Captain Thomas Jenkins for the time he spent instructing me on operating the HP4145B, semiconductor parameter analyzer, as well as for the discussions on semiconductor device physics.

Table of Contents

List of Figures

List of Tables

List of Symbols

a_1	Radius of the emitter dot (cm).
a_2	Inner radius of the base contact (cm).
a_3	Approximate outer radius of the base contact (cm).
A	Any generic area (cm^2).
A_{be}	Area of the base-emitter junction (cm^2).
A_{bc}	Area of the base-collector junction (cm^2).
A_p	Auger recombination coefficient ($cm^6 \cdot s^{-1}$).
α	Caughey-Thomas mobility curve fit parameter.
α_F	Forward common-base current gain.
α_R	Reverse common-base current gain.
$\angle$	Angle of an S-parameter in polar form.
B_n	Radiative recombination coefficient ($cm^3 \cdot s^{-1}$).
BF	Ideal maximum forward common-emitter current gain.
BR	Ideal maximum reverse common-emitter current gain.
β_F	Forward common-emitter current gain.
β_R	Reverse common-emitter current gain.
β^*	Base transport factor.
C_{BE}	Total base-emitter capacitance (F).
C_{BC}	Total base-collector capacitance (F).
CJE	Base-emitter zero-bias depletion capacitance (F).
CJC	Base-collector zero-bias depletion capacitance (F).
C_j	Generic depletion capacitance (F).
C_{je}	Base-emitter depletion capacitance (F).
C_{jc}	Base-collector depletion capacitance (F).

C_d	Generic diffusion capacitance (F).
C_{de}	Base–emitter diffusion capacitance (F).
C_{dc}	Base–collector diffusion capacitance (F).
C_π	Total small–signal base–emitter capacitance (F).
C_μ	Total small–signal base–collector capacitance (F).
C_{bep}	Base–emitter parasitic capacitance (F).
C_{bcp}	Base–collector parasitic capacitance (F).
C_{cep}	Collector–emitter parasitic capacitance (F).
cbcdep	Internal base–collector depletion capacitance (F).
cbcx	External base–collector depletion capacitance (F).
$C_{\mu int}$	Total internal base–collector small–signal capacitance (F).
$C_{\mu ext}$	Total external base–collector small–signal capacitance (F).
d	Generic thickness of dielectric between two conductors (cm).
D_p, D_n	Minority hole and electron diffusivities ($cm^2 \cdot s^{-1}$).
D_{pE}, D_{pC}	Minority hole diffusivities in the emitter and collector ($cm^2 \cdot s^{-1}$).
D_{nB}	Minority electron diffusivity in the base ($cm^2 \cdot s^{-1}$).
E_{gGaAs}	Bandgap energy of intrinsic GaAs (eV).
ΔE_{gB}	Bandgap narrowing in the GaAs base due to high doping (eV).
E_{gE}	Bandgap energy of the AlGaAs emitter (eV).
E_{gB}	Bandgap energy of the GaAs base (eV).
ΔE	Bandgap difference between the emitter and base (eV).
ϵ_o	Permittivity in vacuum ($F \cdot cm^{-1}$).
ϵ_s	Generic semiconductor permittivity ($F \cdot cm^{-1}$).
ϵ_{GaAs}	Relative permittivity of GaAs.
ϵ_{AlGaAs}	Relative permittivity of the AlGaAs emitter.
ϵ_E	Permittivity of the emitter ($F \cdot cm^{-1}$).

ϵ_B	Permittivity of the base ($F \cdot cm^{-1}$).
ϵ_p	Permittivity of polyimide ($F \cdot cm^{-1}$).
F_{EN}	Thermionic electron flux across an abrupt base-emitter heterojunction ($cm^{-2} \cdot s^{-1}$).
f	Frequency (Hz).
f_T	Unity current-gain cutoff frequency (Hz).
f_{max}	Maximum frequency of oscillation (Hz).
g_π	Small-signal base-emitter junction conductance (S).
g_μ	Small-signal base-collector junction conductance (S).
g_o	Small-signal transistor common-emitter output conductance (S).
g_m	Small-signal transconductance (S).
Γ	Reflection coefficient of a transmission line.
γ	Emitter injection efficiency.
IKF	Corner for high current β_F degradation (A).
IKR	Corner for high current β_R degradation (A).
I_E	Total current through emitter terminal (A).
I_B	Total current through base terminal (A).
I_C	Total current through collector terminal (A).
I_{ES}	Base-emitter junction saturation current (A).
I_{CS}	Base-collector junction saturation current (A).
I_{CC}	Current through the base-collector junction due to the base-emitter voltage (A).
I_{EC}	Current through the base-emitter junction due to the base-collector voltage (A).
I_{CT}	Total current through the transistor from collector to emitter (A).
IS	Transport saturation current (A).
ISE	Base-emitter recombination saturation current (A).
ISC	Base-collector recombination saturation current (A).

I_{Cn}	Electron current from the base into the collector (A).
I_p	Hole current injected from the base into the emitter (A).
I_n	Electron current injected from the emitter into the base (A).
I_s	Electron current lost to SCR recombination (A).
I_r	Electron current lost to bulk base recombination (A).
I_1	Ideal base-collector drift-diffusion current (A).
I_2	Ideal base-emitter drift-diffusion current (A).
I_3	Total base-collector recombination current (A).
I_4	Total base-emitter recombination current (A).
I_{rec}	Generic recombination current (A).
k	Boltzmann's constant ($eV \cdot K^{-1}$).
l_{ee}	Diameter of an emitter dot (cm).
L	Any generic length (cm).
L_p, L_n	Minority hole and electron diffusion lengths (cm).
L_{pE}, L_{pC}	Minority hole diffusion lengths in the emitter and collector (cm).
L_{nB}	Minority electron diffusion length in the base (cm).
L_E	Length of a rectangular emitter finger (cm).
L_B	Length of a rectangular base finger (cm).
L_{int}	Internal inductance (H).
L_{ext}	External inductance (H).
L_{bp}	Base parasitic series inductance (H).
L_{ep}	Emitter parasitic series inductance (H).
L_{cp}	Collector parasitic series inductance (H).
L_T	Semiconductor/metal contact characteristic length (cm).
m	Number of base or collector fingers in parallel.
m_o	Electron rest mass (Kg).

m_n	Effective mass of an electron in GaAs (Kg).
MJE	Base-emitter junction grading factor.
MJC	Base-collector junction grading factor.
|M|	Magnitude of an S-parameter in polar form.
μ_o	Permeability in vacuum ($H \cdot cm^{-1}$).
μ_n, μ_p	Generic electron and hole mobilities ($cm^2 \cdot K \cdot eV^{-1} \cdot s^{-1}$).
μ_{max}	Maximum mobility for a particular carrier ($cm^2 \cdot K \cdot eV^{-1} \cdot s^{-1}$).
μ_{min}	Minimum mobility for a particular carrier ($cm^2 \cdot K \cdot eV^{-1} \cdot s^{-1}$).
n_i	Generic semiconductor intrinsic carrier concentration (cm^{-3}).
n_{iGaAs}	Intrinsic carrier concentration of GaAs (cm^{-3}).
n_{iE}, n_{iC}	Intrinsic carrier concentration in the emitter and collector (cm^{-3}).
n_{iB}	Intrinsic carrier concentration in the base (cm^{-3}).
n_{po}	Equilibrium concentration of minority electrons (cm^{-3}).
$n_{pB}'(W_B)$	Concentration of excess minority electrons at the collector edge of the neutral base region (cm^{-3}).
N	Generic doping concentration (cm^{-3}).
N_{ref}	Caughey-Thomas mobility curve fit parameter.
N_A	Acceptor dopant concentration in p-material (cm^{-3}).
N_D	Donor dopant concentration in n-material (cm^{-3}).
N_E, N_B, N_C	Emitter, base, and collector dopant concentrations (cm^{-3}).
N_t	Concentration of recombination centers in the base (cm^{-3}).
N_{CE}, N_{CB}	Conduction band density of states in the emitter and base (cm^{-3}).
N_{VE}, N_{VB}	Valence band density of states in the emitter and base (cm^{-3}).
NF	Forward current emission coefficient.
NR	Reverse current emission coefficient.
NE	Base-emitter leakage emission coefficient.

NC	Base-collector leakage emission coefficient.
η	Generic non-ideal emission coefficient.
N_{dot}	Number of emitter dots per finger.
N_{fin}	Number of base fingers.
p_{no}	Equilibrium concentration of minority holes (cm^{-3}).
q	Electron charge (C).
q_B	Normalized base charge.
Q_B	Total base charge (C).
Q_{Bo}	Zero-bias base charge (C).
Q_{VE}	Base-emitter junction depletion charge (C).
Q_{VC}	Base-collector junction depletion charge (C).
Q_F	Forward injected base charge (C).
Q_R	Reverse injected base charge (C).
R_B	Base series resistance (Ω).
R_C	Collector series resistance (Ω).
R_E	Emitter series resistance (Ω).
RE	SPICE BJT emitter resistance (Ω).
RB	SPICE BJT internal base resistance (Ω).
RC	SPICE BJT collector resistance (Ω).
R_{Bint}	Internal base series resistance (Ω).
R_{Bext}	External base series resistance (Ω).
R_{Bsh}	Base layer sheet resistance (Ω/□).
$R_{contact}$	Metal/semiconductor contact resistance (Ω).
R_{bulk}	Bulk semiconductor resistance (Ω).
R_{sp}	Spreading resistance (Ω).
R_{lc}	Lateral contact resistance (Ω).
R_{leak}	Semi-insulating GaAs leakage resistance (Ω).

ρ_s	Sheet resistance of a generic semiconductor layer ($\Omega/\square$).
ρ_n, ρ_p	n-type and p-type semiconductor resistivities ($\Omega \cdot cm$).
ρ_{Au}	Resistivity of gold metallization at 10 GHz ($\Omega \cdot cm$).
ρ_c	Generic specific contact resistance ($\Omega \cdot cm^2$).
ρ_{cp}	Specific contact resistance for a contact on p-type material ($\Omega \cdot cm^2$).
ρ_{cn}	Specific contact resistance for a contact on n-type material ($\Omega \cdot cm^2$).
S_{EN}	Effective base-emitter electron interface velocity ($cm \cdot s^{-1}$).
S_{CN}	Effective base-collector electron interface velocity ($cm \cdot s^{-1}$).
S_{11}	Input reflection coefficient with the output matched to Z_o.
S_{12}	Reverse transmission or isolation coefficient.
S_{21}	Forward transmission (gain or loss) coefficient.
S_{22}	Output reflection coefficient with the input matched to Z_o.
S_E	Rectangular emitter contact metallization width (cm).
S_B	Rectangular base contact metallization width (cm).
σ_n	Electron capture cross section (cm^2).
t	Generic thickness of a semiconductor or metal (cm).
T	Absolute temperature (K).
TF	Base forward transit time (s).
TR	Base reverse transit time (s).
τ_p, τ_n	Lifetimes of excess minority holes and electrons (s).
τ_{SRH}	Shockley-Read-Hall recombination lifetime (s).
τ_{Aug}	Auger recombination lifetime (s).
τ_{rad}	Radiative recombination lifetime (s).
τ_{ec}	Emitter-to-collector majority carrier transit time (s).
τ_{no}	Excess minority electron recombination lifetime (s).
τ_{po}	Excess minority hole recombination lifetime (s).

U	Generic recombination rate ($cm^{-3} \cdot s^{-1}$).
V_{bi}	Junction built-in voltage (V).
VJE	Base-emitter built-in potential (V).
VJC	Base-collector built-in potential (V).
V_T	Thermal voltage given by kT/q (V).
V_j^+	An ac voltage waveform incident to port j (V).
V_i^-	An ac voltage waveform reflected from port i due to the driving signal at port j (V).
V_{BE}	Externally applied base-emitter voltage (V).
V_{BC}	Externally applied base-collector voltage (V).
$V_{B'E'}$	Internal voltage across the base-emitter junction (V).
$V_{B'C'}$	Internal voltage across the base-collector junction (V).
$v_{B'E'}$	Small-signal base-emitter junction voltage (V).
$v_{B'C'}$	Small-signal base-collector junction voltage (V).
V	Generic externally applied voltage (V).
vbcx	Distributed base-collector voltage (V).
v_{th}	Average thermal velocity for an electron ($cm \cdot s^{-1}$).
v_{sat}	Electron saturation velocity in GaAs at 300 K ($cm \cdot s^{-1}$).
v_{nB}, v_{pE}	Minority electron and hole diffusion velocities ($cm \cdot s^{-1}$).
W_B	Zero-bias neutral base width (cm).
W	Any generic width (cm).
ω	Radian frequency.
ψ	The potential function of Poisson's equation (V).
x	Mole fraction of Aluminum in $Al_xGa_{1-x}As$.
X	Generic depletion region thickness (cm).
X_{pE}	Thickness of base-emitter SCR in the p-type base (cm).
X_{pC}	Thickness of base-collector SCR in the p-type base (cm).

x	Generic distance variable (cm).
X_c	Capacitive reactance (Ω).
XCJC	Fraction of base-collector depletion capacitance internal to the base.
Z_o	The characteristic impedance of a transmission line (Ω).
Z_L	The load impedance connected to a transmission line (Ω).

A PHYSICS-BASED HETEROJUNCTION BIPOLAR TRANSISTOR MODEL FOR INTEGRATED CIRCUIT SIMULATION

1. Introduction

The purpose of this research effort was to derive a physics-based dc model for a Heterojunction Bipolar Transistor (HBT). The dc model was then linearized to arrive at a small-signal model that accurately predicts the device's electrical behavior at microwave frequencies. This new model offers features not found in previous analytical or physics-based HBT models such as consideration of a cylindrical emitter-base geometry and is direct implemention into SPICE (Simulation Program with Integrated Circuit Emphasis). The device model parameters were determined from a knowledge of the device material, geometry, and fabrication process. The model was then developed by using semiconductor physics to calculate modified parameters for the existing SPICE bipolar junction transistor (BJT) model.

1.1 Background

The design and fabrication of HBTs have received increased attention in recent years. This attention is due primarily to the significantly greater performance potential that can be obtained from HBTs compared to the performance of traditional BJTs [1,2,3]. The most technologically mature HBTs are fabricated with $Al_xGa_{1-x}As/GaAs$ [4,5,6,7], although many other III-V compounds have been used [8,9,10,11]. Devices based on these III-V compounds as well as $Si/Si_{1-x}/Ge_x$ devices [12], are distinguished from homojunction devices by a wide energy bandgap emitter relative to the base. Both BJTs and HBTs are junction transistors typically fabricated with an n-type emitter and collector, and a p-type base. A representative

layer structure, doping concentration and energy bandgap diagram for an npn BJT are shown in Figs. 1.1 - 1.3. The corresponding diagrams for an Npn HBT are shown in Figs. 1.4 - 1.6. The capital "N" denotes a wide-gap material.

BJTs are typically lateral or planar in structure, while HBTs are vertical devices, as seen in Figs. 1.1 and 1.4, respectively. Fig. 1.6 shows the energy band diagram for an $Al_xGa_{1-x}As$ emitter / GaAs base Np heterojunction. The most important feature of the heterojunction is that it provides a larger barrier for holes attempting to move from the base to the emitter than for electrons moving from the emitter to the base. Consequently, the base of an HBT may be doped more heavily than the emitter without sacrificing transistor efficiency. This new design freedom is a direct result of the band gap difference and allows for previously unobtainable device figure of merit improvements [17,18]. Most notably, HBTs can be operated at higher speeds and with greater efficiency. However, the trend toward optimizing device performance requires a pattern for predicting device behavior.

The HBT is a relatively new device. Although HBTs were conceptualized by W. Shockley in 1948 [19], the first HBT was not fabricated until 1972 [20]. However, practical HBTs did not evolve until the advent of Molecular Beam Epitaxy (MBE). MBE provided high crystalline purity semiconductors, and the strict control over epitaxial layer thickness and doping necessary for realizing the HBT's theoretical performance potential.

Simulation is critical to furthering device technology, because it provides device and integrated circuit design feedback. The purpose of simulation is to accurately predict the electrical performance of either

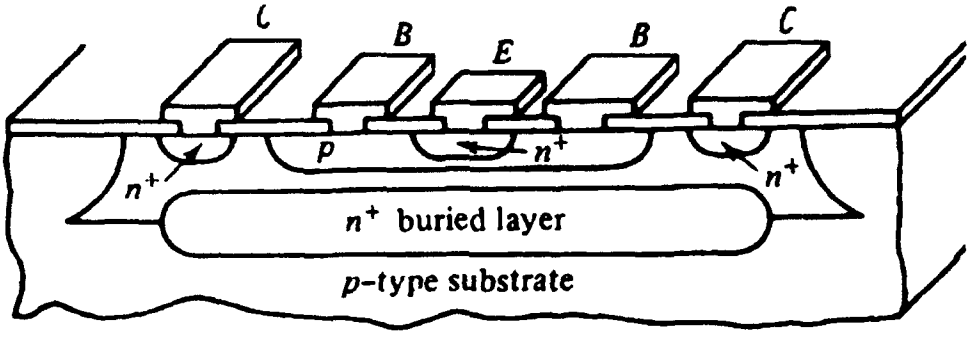

Figure 1.1 Representative layer structure of an npn BJT [13:171].

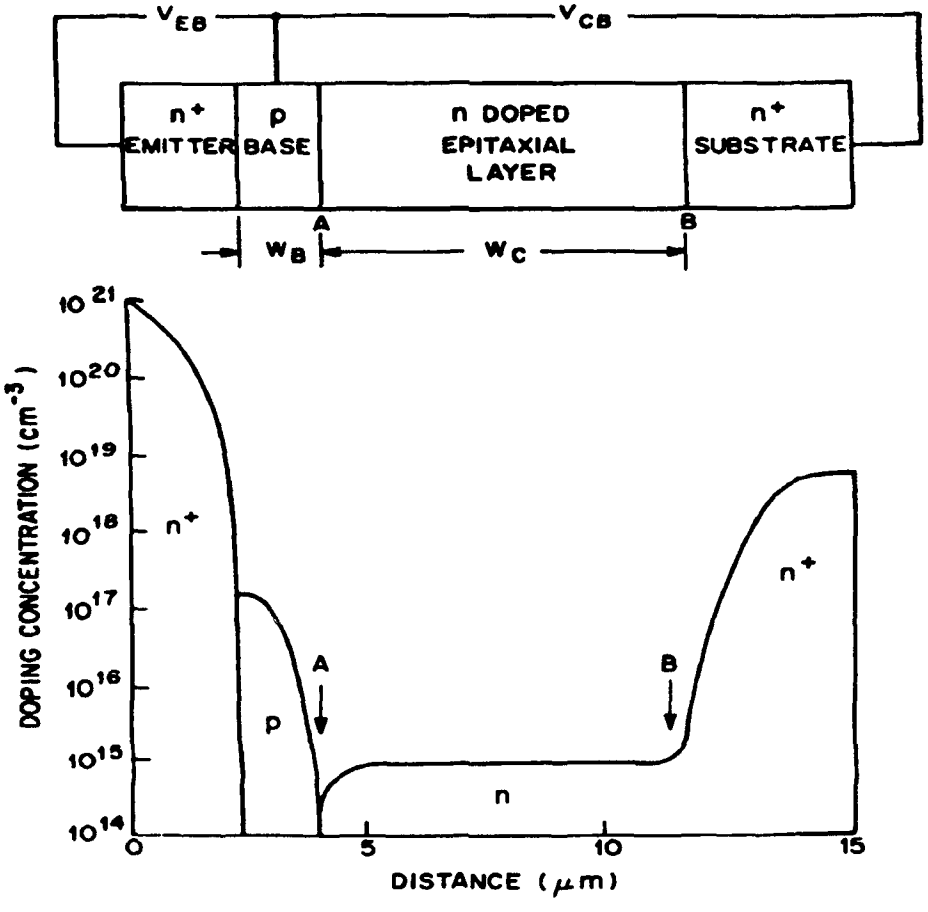

Figure 1.2 Typical doping profile of an npn BJT [14:146].

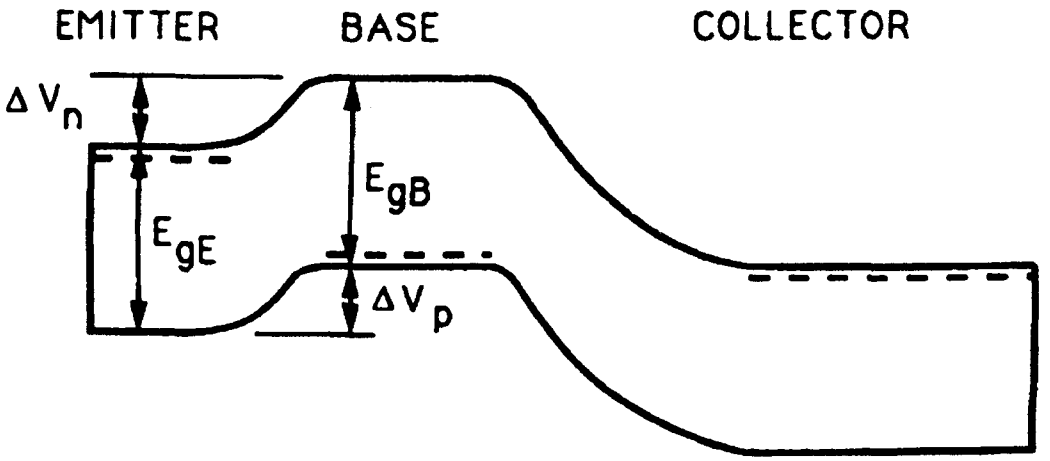

Figure 1.3 Energy bandgap diagram of a forward-biased npn BJT [15:336].

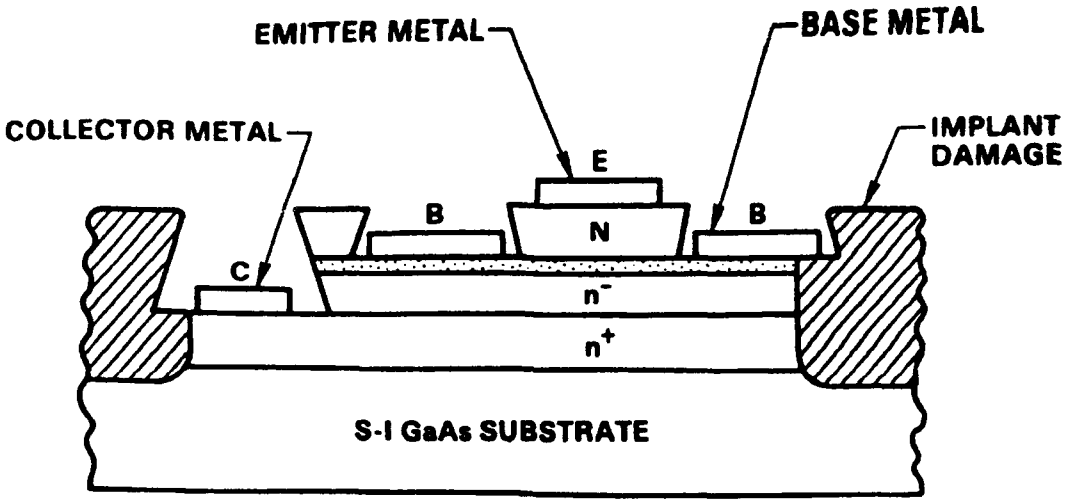

Figure 1.4 Representative layer structure for an npn AlGaAs/GaAs HBT [15:373].

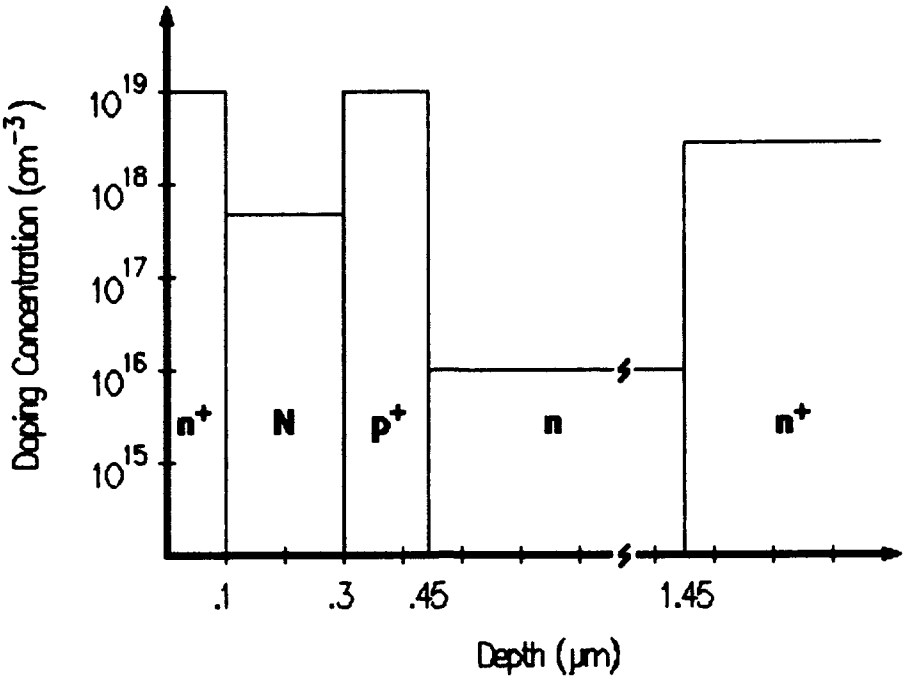

Figure 1.5 Typical doping profile of an Npn AlGaAs/GaAs HBT.

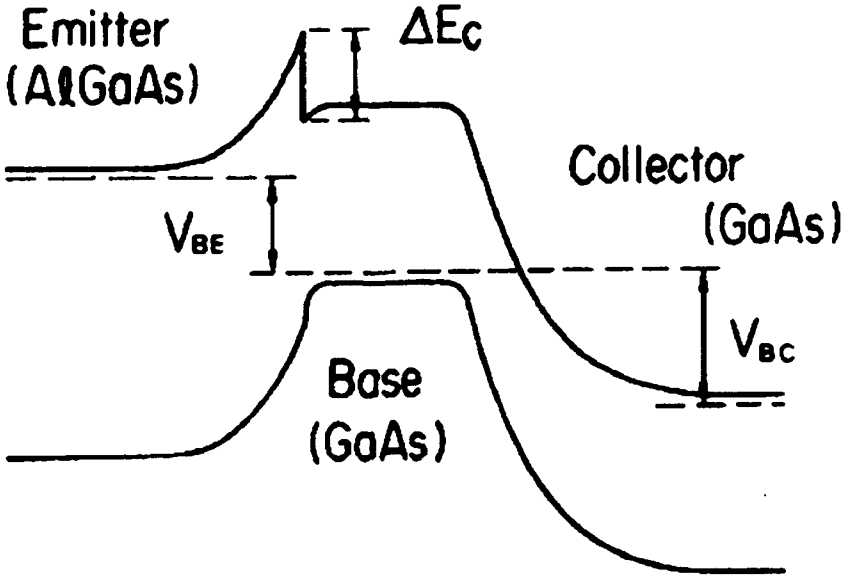

Figure 1.6 Energy bandgap diagram of an abrupt-emitter forward-biased Npn AlGaAs/GaAs HBT [16:198].

an individual device design or a collection of devices connected to accomplish a specific function. The ability to simulate actual device performance requires a model. The bipolar transistor model can be represented as either a large (dc) or small-signal (microwave) equivalent circuit, as shown in Figs. 1.7 and 1.8. Figure 1.7 represents the SPICE large-signal equivalent circuit where:

C_{BE} is the total base-emitter capacitance;

C_{BC} is the total base-collector capacitance;

R_B, R_C, and R_E are the base, collector and emitter series resistances respectively;

I_B and I_C are the current sources representing the current into the base and collector terminals respectively;

$V_{B'E'}$ and $V_{B'C'}$ are the internal junction voltages.

Figure 1.8 represents the small-signal hybrid-π equivalent circuit where:

C_π is the total base-emitter capacitance;

C_μ is the total base-collector capacitance;

g_π is the dynamic base-emitter junction conductance;

g_μ is the dynamic base-collector junction conductance;

g_o is the transistor common-emitter output conductance;

g_m is the transconductance;

$v_{B'E'}$ and $v_{B'C'}$ are the internal small-signal junction voltages.

The model topologies, like those shown in Figs. 1.7 and 1.8, along with their equivalent circuit element values, fully describe actual device electrical behavior.

The goal of any physics-based model is to be as accurate and as simple as possible while relating device material and geometry parameters to equivalent circuit element values. Typically, the first step in

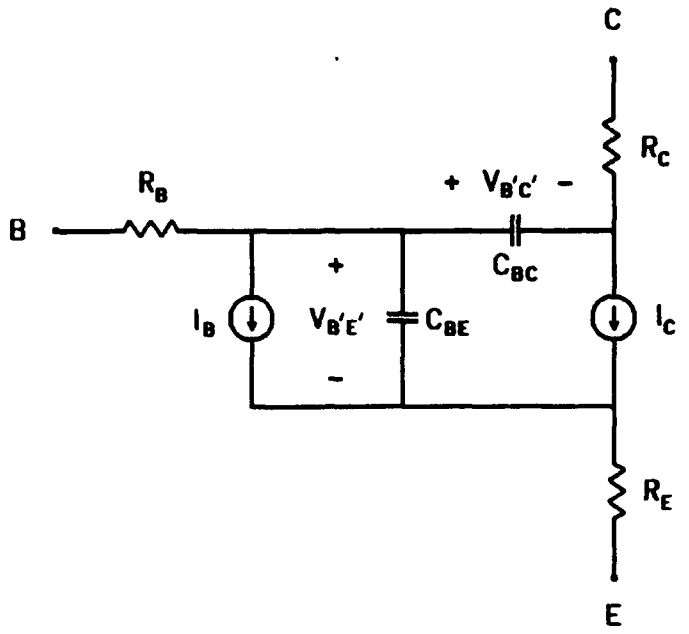

Figure 1.7 Large-signal junction transistor equivalent circuit [21:61].

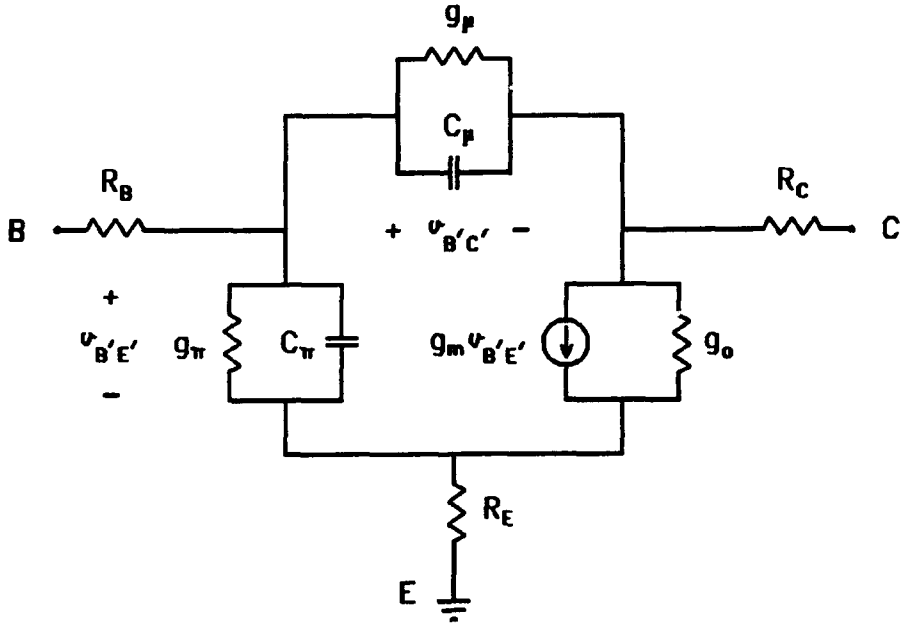

Figure 1.8 Hybrid-π small-signal junction transistor equivalent circuit [21:68].

generating a model is to perform on-wafer device measurements. The measurements for large-signal characterization are dc I-V curves and Gummel plots (log I_C and log I_B versus V_{BE}). The measurements for ac small-signal characterization are high frequency scattering (S)-parameters. S-parameters are ideally suited for microwave analysis because the impedance matching technique used in S-parameter measurements is accurate over a wide frequency range. Measuring current or voltage waveforms at gigahertz frequencies is difficult because signal amplitudes vary with position along the test line, and because open and short circuits are frequency dependent.

Once the measurements have been made, they must be related to the particular equivalent circuit chosen as the model, or the corresponding equations, through a parameter extraction process. There are basically three forms of parameter extraction: graphical, analytical, and numerical [22]. Often, portions of all three methods must be used to arrive at physically real parameters. The unknown parameters for which one must solve are the equivalent circuit element values or variables in the equations that define the equivalent circuit elements. There are many parameter extraction techniques with varying degrees of complexity. In and of itself, model generated data that are in good agreement with measured data are not a sufficient criteria for successful physical parameter extraction. Numerical optimization can easily produce a set of equivalent circuit element values to fit the measured data accurately; however, the optimization routine is merely curve fitting and may generate non-physical parameters or non-unique solutions. Therefore, constraining certain parameters within a specified value or implementing an independent extraction technique is necessary.

1.2 Problem Statement

Many large and small-signal HBT models are empirically derived following the previous procedure. Devices are fabricated, data are measured, and model parameters are extracted by curve fitting to a known circuit topology. Curve-fit or empirical model parameters do not have any physical meaning and would require each new design to be fabricated at considerable time and expense prior to simulation. Fabricating a device as a prerequisite to modeling is essentially reverse engineering and defeats the purpose of a physical model: to predict the electrical performance before the device is fabricated. A physics-based dc/microwave model is needed.

A physical model's parameters are directly related to the device material, geometry, and fabrication process. The solutions to semiconductor physics equations provide both the large and small-signal equivalent circuit parameters. In this thesis, a methodology to determine HBT model parameter values for the existing HSPICE BJT topology is developed. The result is simple physics-based dc and small-signal HBT models that accurately predict dc through microwave device performance. The physical nature of the model provides insight into optimization of new device designs, because simulation is possible as soon as new designs are envisioned.

Wright Laboratory, Solid State Electronics Directorate, Research Division (WL/ELR), is conducting a program to develop GaAs-based HBTs for microwave applications. This program has made several advances in developing and maturing HBT technology. The devices fabricated by WL/ELR are unique because of their cylindrical emitter-base geometry. Currently,

WL/ELR does not have a model that accurately describes the devices they have fabricated.

1.3 Summary of Current Knowledge

Several authors have proposed HBT models within the past few years. These models represent a variety of techniques for both large and small-signal equivalent circuits.

1.3.1 Large-Signal Modeling. B. Ryum and I. Abdel-Motaleb [23] derived a physics-based analytical HBT model. Using semiconductor physics, expressions for each of the terminal currents (I_E, I_B, and I_C) are analytically determined. Included in the equation for I_B are the neutral base, the emitter-base space charge region (SCR), the emitter-base heterointerface, and surface recombination currents. Each current component can be calculated from the device material, geometry, and process parameters. Implementing the model is not simple and would require modification of the SPICE source code. However, the article is an excellent reference for HBT device physics.

C. Parikh and F. Lindholm [24] also derived a physics-based analytical HBT model. Equations for the neutral base, SCR, and surface recombination currents as well as collector hole current are determined. These components are included in expressions for the I_C and I_B terminal currents where most parameters can be found from knowledge of the device material, fabrication process, and geometry. This model is similar to Ryum and Abdel-Motaleb's, and would also require modification of the SPICE source code.

A detailed physics-based large-signal HBT model was presented by P. Grossman and J. Choma [25]. The authors remark that the central

problem with HBT simulation is accounting for SCR and surface recombination. The model topology presented by Grossman and Choma is the most comprehensive physics-based model reviewed in this thesis. Empirical and analytical relations are used to determine element values. The authors present a simplification of their model that may be implemented in SPICE along with the SPICE parameters calculated from their specific process and geometry.

M. Hafizi, C. Crowell, and M. Grupen [26] also provided a list of SPICE model parameters. However, each of their model parameters was calculated with an iterative least square curve fit of measured data. Once extracted, the parameters were entered in SPICE and excellent agreement was obtained between SPICE calculations and measured data. This work is a good example of numerical parameter extraction from measured I-V characteristics, once a model topology is assumed.

J. Liou and J. Yuan [27] derived a physics-based analytical HBT model stressing that only device material, geometry, and process parameters were required to characterize their model. Their approach is slightly less analytically intensive than that of Ryum and Abdel-Motaleb [23], or Parikh and Lindholm [24]. The equations they include for series resistances are oversimplified for most HBT structures. No SPICE parameters are provided, though the authors state their model can be readily implemented in SPICE.

1.3.2 Small-Signal Modeling. Due to their linear operation, small-signal equivalent circuits are generally simpler than their large-signal counterparts. However, their analysis is often more complex, because at higher frequencies one must contend with extrinsic device

parasitic capacitances and inductances. One simple approach, reported by D. Pehlke and D. Pavlidis [28], measures device S-parameters and analytically calculates the equivalent circuit element values. Equivalent circuit parameters are extracted by converting the S-parameters to H-parameters and solving for resistor, capacitor, and inductor element values with impedance equations.

Another approach, by S. Maas and D. Tait [29], measured S-parameters, and analytically calculated emitter, base and collector resistances. The remaining element values were determined by S-parameter optimization. R. Trew *et al.* [30] have attempted to minimize the non-unique and non-physical element values that may be obtained from S-parameter fitting. Their method uses a constraining equation based upon the emitter-to-collector delay time, τ_{ec}, such that optimization of the S-parameters *provides pseudo-physical* equivalent circuit element values. The technique used by D. Costa *et al.* [31] does not require any numerical optimization. The complexity of their equivalent circuit demands measurement of test structures, and the use of matrix manipulation to determine various device parasitics.

1.4 Assumptions and Scope

This thesis effort assumes $Al_xGa_{1-x}As/GaAs$ HBTs and the corresponding material parameters and expressions that are unique to $Al_xGa_{1-x}As/GaAs$ semiconductors. Most HBTs are fabricated from these materials; however, the proposed methodology is applicable to other materials if the material constants are known. The approach further assumes the following:

i) the dc model can be represented by the dc SPICE equivalent circuit topology of Fig. 1.7;

ii) the microwave model can be represented by the hybrid-π equivalent circuit topology of Fig. 1.8;

iii) carrier transport across the emitter-base heterojunction is characterized by the drift-diffusion model and not by thermionic emission;

iv) standard, non-degenerate Boltzmann statistics apply. (Despite the fact that the GaAs base of a typical HBT may be degenerately doped, this assumption is made as a starting point. If the Boltzmann approximation is suspected to hinder model accuracy, then this assumption can be reconsidered);

v) there is uniform doping in the wide-gap emitter, base, collector, and subcollector regions (i.e., no built-in drift fields).

vi) carrier mobility in AlGaAs can be sufficiently approximated by using the empirical mobility expressions for GaAs;

vii) the base-emitter junction and contacts have a cylindrical geometry (i.e., emitter dots as compared to the typical emitter stripes).

The proposed model will not include the effects of temperature. Some researchers have presented electrical-thermal models [32-37]; however, the proposed model will assume device temperature is constant at 300 K. This assumption is generally valid for low collector current density. At high collector current densities, a departure of the model data from the measured data due to device self-heating is expected, and will be readily identifiable. Accurate thermal modeling would have greatly increased the difficulty of the model derivation and led to exceeding the allowed time for thesis completion.

For simplicity, the model will be one-dimensional. Numerical simulators often provide two and three-dimensional results. However, in a junction transistor, all significant effects are one-dimensional; the

remaining effects are negligible. Both the dc and microwave models will be complete once model generated data are within ± 5% of measured data. The ± 5% criterion is a reasonable objective for a physics-based model. This metric is comparable to the performance of published physics-based models. Model simplicity may be traded-off for model accuracy to satisfy this criterion.

1.5 Approach

The initial objective is a simple physics-based dc HBT model. The model's simplicity is demonstrated through direct implementation in SPICE, a CAD tool whose use is widespread among device and circuit engineers.

The model will be physics-based because all equivalent circuit model parameters will be calculated using semiconductor physics and a knowledge of:

i) material parameters and related expressions such as carrier mobility, lifetime, intrinsic carrier concentration, bandgap, and permittivity,

ii) device geometry such as junction area, configuration of contacts and number of base fingers, and

iii) process parameters such as doping profile, Al mole fraction, and layer thicknesses.

Solutions to the semiconductor physics equations depend on all three types of parameters. Mathcad 3.1 [38] was used to solve the equations determining the SPICE model parameters for the topology shown in Fig. 1.7. These model parameters were directly included in the SPICE model statement for the particular HBT modeled.

WL/ELR has provided the process parameters and device geometry for one particular HBT device on each of three wafers designated as 4490, 4491, and 4457. Obtaining complete and accurate physical information is critical to successful model generation. Reliable material constants and related expressions have been researched and consolidated from various published sources. WL/ELR has also performed much of the data measurements. A full set of data consists of both high-frequency measurements and dc measurements as well as information regarding the doping profile and device geometry. The high frequency measurements are the device S-parameters at several dc bias points. These S-parameters were measured from 1 to 50 GHz using a Hewlett-Packard (HP) 8510C Network Analyzer. The dc measurements encompass forward I-V characteristics and Gummel plots. Successful modeling of other HBT designs assists in validating that the proposed modeling technique is valid for various device geometry and process parameters.

The version of SPICE used to simulate the developed model to generate model data is Meta-Software's HSPICE version H92 [39,40]. This software is licensed to AFIT, and is available on the VLSI laboratory computer network. HSPICE calculated the model's terminal voltages and currents, which were then saved on a disk with the measured data. Both the measured and modeled data were then imported to a TriMetrix's technical graphics and data analysis package, Axum 3.0 [41]. Several devices from wafers 4490 and 4491 were provided by WL/ELR. An HP 4145B Semiconductor Parameter Analyzer was used to obtain additional dc measurements as necessary for comparison with the model. Axum was used to plot the measured and modeled data on the same axes for visual comparison. DC current versus voltage was plotted on linear-linear or log-linear scale

and an analysis of each data point was performed. If the average absolute value of the percent difference among each modeled and measured data point over the entire range of transistor operation is within ± 5%, then the model is considered useful for device simulation, and the simple physics-based HBT dc model problem is solved.

The dc model was then linearized to obtain the small-signal model that is valid at microwave frequencies. Any non-linear equivalent circuit element may be approximated with a linear element if its performance is considered over a sufficiently small region of operation. The specific region of operation in this case is around the dc bias point. HSPICE ac analysis essentially linearizes the dc model, which results in the small-signal hybrid-π equivalent circuit of Fig. 1.8.

When given the operating point, HSPICE can output the S-parameters of the HBT model at any given frequency. S-parameters are dependent on frequency, the intrinsic device (that is, the linearized dc model), and the extrinsic parameters. These extrinsic parameters are parasitic inductances and capacitances which must be calculated and incorporated into the microwave model. Operating at dc or low frequency, the parasitics are negligible. At microwave frequencies their effect becomes significant and must be modeled. An attempt was made to characterize the extrinsic elements using semiconductor physics and a knowledge of device material, geometry, and fabrication process.

In addition to HSPICE, an HP 85150B Microwave and RF Design Systems software package [42] was also used to simulate the modeled device's dc and microwave performance. The intrinsic device parameters used in HSPICE were imported to the HP software along with the extrinsic element values. The modeled data were then saved to a file and plotted with the measured

data for a visual and mathematical comparison. The parasitics were analytically modified until the average absolute value of the percent difference over the entire range of operation was within ± 5% for both the magnitude and angle of the complex S-parameters. As with the dc analysis, model accuracy may be traded-off for model simplicity.

1.6 Thesis Overview

Chapter 2 discusses published HBT models in more detail stating how each effort relates to this thesis. Chapter 3 covers the theory of large and small-signal junction transistors relative to SPICE BJT model parameters. In Chapter 4, the methodology of determining HBT model parameters from a knowledge of the device material, geometry and fabrication process is discussed. This methodology is specific to HBTs fabricated by WL/ELRD with a cylindrical emitter-base geometry and emitter bridge. dc and microwave modeled data are compared to measured data in Chapter 5. Conclusions and recommendations for future work are presented in Chapter 6.

2. Literature Review

Understanding and appreciating the evolution of HBT device modeling is important. A brief review of the pioneering efforts of J. Ebers and J. Moll [43], as well as H. Gummel and H. Poon [44], which resulted in the well known Ebers-Moll and Gummel-Poon BJT models is an excellent place to start. Because of the simplicity and versatility of these two models, it is not surprising to find that all of the reviewed HBT large-signal models are derivatives.

The Ebers-Moll (EM) model [43] is essentially two terminal current equations for I_E and I_C which describe the large-signal behavior of the junction transistor across all modes of operation:

$$I_E = I_{ES}\left[\exp\left(\frac{qV_{BE}}{kT}\right) - 1\right] - \alpha_R I_{CS}\left[\exp\left(\frac{qV_{BC}}{kT}\right) - 1\right] \qquad (2.1)$$

$$I_C = \alpha_F I_{ES}\left[\exp\left(\frac{qV_{BE}}{kT}\right) - 1\right] - I_{CS}\left[\exp\left(\frac{qV_{BC}}{kT}\right) - 1\right] \qquad (2.2)$$

The four unknowns I_{ES}, I_{CS}, α_F, and α_R (only three of which are independent) represent the emitter and collector saturation current, and the common-base forward and reverse current gain, respectively. An equivalent circuit topology for the basic EM model is shown in Fig. 2.1. The reciprocity theorem relates all four parameters to *IS*, the saturation current common to both I_{ES} and I_{CS}: $\alpha_F I_{ES} = \alpha_R I_{CS} = IS$. The model's current sources are given by

$$I_{CC} = IS\left[\exp\left(\frac{qV_{BE}}{kT}\right) - 1\right] \qquad (2.3)$$

$$I_{BC} = IS\left[\exp\left(\frac{qV_{BC}}{kT}\right) - 1\right] \qquad (2.4)$$

The EM model is a physical model because it is derived from the *pn* diode equation and the four unknowns which are calculated from device material and fabrication process parameters.

The Gummel-Poon (GP) model [44] improves upon the EM model by accounting for base width modulation (the Early effect), space charge region (SCR) recombination, emitter crowding, high-level injection and base push-out effects. The EM equation for I_{CC} is modified to include the factor Q_{Bo}/Q_B:

$$I_{CC} = -IS \cdot Q_{Bo} \frac{\exp(qV_{BE}/kT) - \exp(qV_{BC}/kT)}{Q_B} \qquad (2.5)$$

where Q_{Bo} is the zero-bias base charge and Q_B is the total base charge comprised of Q_{Bo}, emitter and collector capacitive contributions (Q_{VE} and Q_{VC}), as well as forward and reverse current-controlled contributions (Q_F and Q_R). This "integral charge control" relationship is the major feature of the GP model. The GP equivalent circuit model is shown in Fig. 2.2, where τ_F and τ_R are the mean forward and reverse transit times of the minority carriers in the neutral base. Twenty-one parameters are required to fully describe the model. A minimum of five variables must be specified, with *a priori* default values, to compute the full set of parameters. All of the currents, voltages, and charges are normalized including Q_B, which becomes $q_B = Q_B/Q_{Bo}$. When q_B and the ideality factors are approximately unity, the GP model reduces to the EM model.

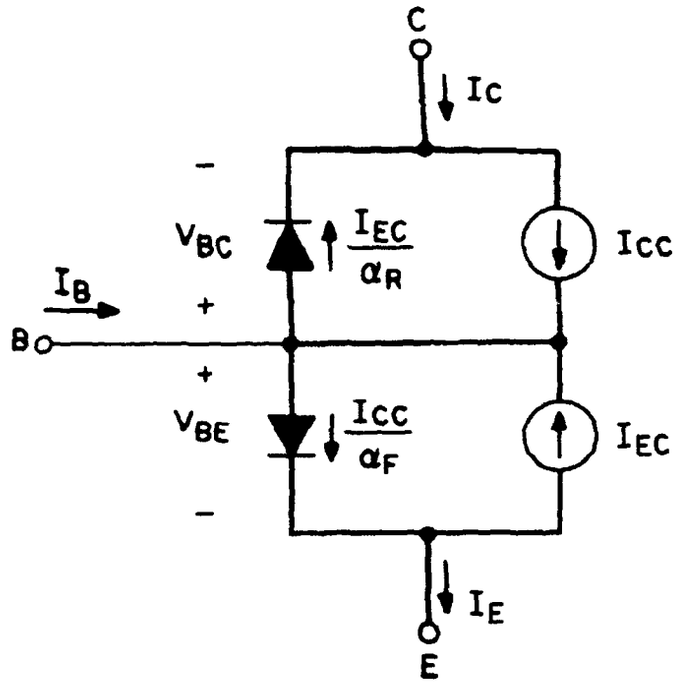

Figure 2.1 The basic npn bipolar transistor Ebers-Moll equivalent circuit [21:41].

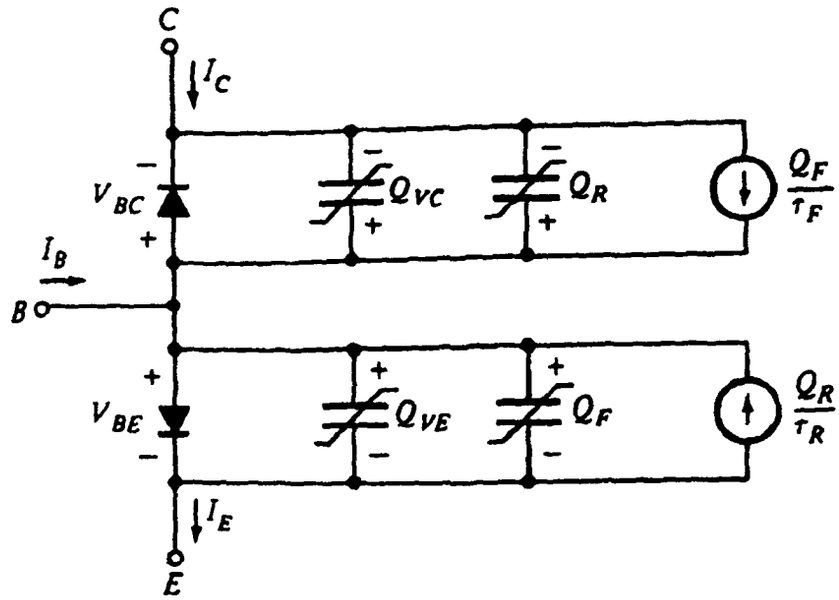

Figure 2.2 An npn bipolar transistor Gummel-Poon equivalent circuit [44:207].

2.1 Large-Signal Modeling

2.1.1 Ryum and Abdel-Motaleb. B. Ryum and I. Abdel-Motaleb [23] derived a physically-based analytical HBT model. Noticing that EM models neglect surface and interface recombination, the authors developed a GP model considering Early voltage, mobile carriers in the SCR, base-widening effect at high current, and SCR and base recombination. Thermionic emission is assumed to be the dominant transport mechanism of carriers over the conduction energy band spike at the base-emitter heterointerface. The authors' methodology assumes the non-degenerate Boltzmann statistics, a uniform base, and constant quasi-fermi levels in the SCR. After calculating the minority carrier boundary conditions, an expression is obtained for I_{CC}, the current injected from the emitter to the collector, in the form of Gummel and Poon's expression for I_{CC} Similar to the GP I_{CC} equation, the denominator of the resultant equation is Q_B. However, the minority carrier velocity factors are included in the numerator. Q_B is comprised of the same five components as in the GP model and each is analytically determined. All the parameters of the resulting equation for I_{CC} can be calculated from the device material, fabrication process, and geometry parameters.

The authors covered recombination current in detail expressing four components, though the derivations may be found in one of their later publications [46]. Considered and included in the device terminal current equations are the neutral base, the emitter-base SCR, the emitter-base heterointerface, and the surface recombination currents. It is shown that even for heavily doped bases, the neutral base recombination current I_{br} is negligible if the effective base width, W_B, is much less than the minority electron diffusion length in the base, L_{nb}.

The model is compared to experimental data from abrupt and graded HBTs and deviates less than 5% on the common-emitter I-V characteristics and only 4% on the current gain. Also, comparison with a published numerical model [47] for the common-emitter current gain, β, and the unity current gain, f_T, yields 6.5% and 17% differences, respectively. Furthermore, it appears the authors have used their model to gain insight into HBT device physics because empirical device phenomena have been modeled and their causes confirmed. Examples of such device phenomena are increased interface recombination, lowered turn-on voltage, emitter-size effect, and base-widening. Device design parameters and trade-offs may be realized more easily with such a model because changes in electrical performance due to physical changes may be plotted as quickly as the parameter changes are entered in the software.

Ryum and Abdel-Moteleb have developed a very good physics-based model. Many of their semiconductor physics equations were used to develop the models in this thesis. However, their model is not directly implemented in SPICE because they do not calculate all of the necessary SPICE parameters. Also, their model is meant to be used only for dc simulations.

2.1.2 Parikh and Lindholm. C. Parikh and F. Lindholm [24] point out that Ryum and Abdel-Motaleb's model is valid only for low injection and constant base doping. They discovered that the GP model is not valid when the transistor is in saturation, and that Parikh's and Lindholm's model also is not valid in saturation due to intrinsic assumptions of charge-control models which require determination of Q_F and Q_R. The model derived by Parikh and Lindholm is valid for arbitrary doping profiles, all levels of injection, abrupt and graded junctions, as well as

single and double-HBTs (that is, when both the base-emitter and base-collector are heterojunctions). Their methodology was to rederive Gummel and Poon's charge-control relation given the new minority carrier boundary conditions which are the result of the thermionic emission and tunneling current mechanisms. The *pn* product they obtained for heterojunctions is clearly derived and is stated in Eq. (2.6) for comparison with the conventional homojunction *pn* product:

$$p(X_{pE})\,n(X_{pE}) = -(F_{EN}/S_{EN})\,p(X_{pE}) + n_{iB}^2 \exp(qV_{BE}/kT)\,. \tag{2.6}$$

The first term on the right hand side is due to the presence of a conduction band spike, whereas the second term is the homojunction product. The first term is negligible for sufficiently graded heterojunctions which results in drift-diffusion as the dominant carrier transport mechanism.

Equation (2.7) is the major result of Parikh's and Lindholm's work. This expression for I_{CC} is different from Ryum's and Abdel-Motaleb's expression. The thermionic emission contribution is not included as factors in the numerator but as additional Q_B terms in the denominator as given by [24]

$$I_{CC} = -q^2 D_n n_{iB}^2 A \frac{[\exp(qV_{BE}/kT) - \exp(qV_{BC}/kT)]}{q\int_{X_{pE}}^{X_{pC}} p\,dx + \frac{qD_n}{S_{EN}} p(X_{pE}) + \frac{qD_n}{S_{CN}} p(X_{pC})}\,. \tag{2.7}$$

This technique allows for a more physical interpretation of the effect of the heterojunction energy band spike, because a large spike will impede the injection of electrons into the base. This effect is readily seen from Eq. (2.7) as an increase in the denominator, thus decreasing I_{CC}. The

base charge given by $q\int p \cdot dx$ is comprised of the five components identified by Gummel and Poon [44].

Equations for the neutral base, SCR, and surface recombination currents as well as collector hole current were determined. These currents were used to provide expressions for the I_C and I_B terminal currents where most parameters can be found from a knowledge of the device material, geometry, and fabrication. The expressions derived by Parikh and Lindholm for I_B and I_C account for thermionic emission at the base-emitter heterojunction. These expressions are different from the SPICE equations for I_B and I_C which will be derived in the next chapter. Consequently, Parikh's and Lindholm's model (like Ryum's and Abdel-Motaleb's) is not directly implemented into SPICE, nor does it consider an HBT's microwave performance.

2.1.3 Grossman and Oki. An alternate method was taken by P. Grossman and A. Oki [49] to obtain a large-signal HBT model. All of the models discussed thus far have been analytical models in which equations describing device physics have been calculated for terminal currents and applied to a particular model topology. Grossman and Oki have developed an empirical model based on the GP model.

Their analysis begins with a discussion of the base current of an HBT which they claim is dominated by either surface or SCR recombination current as opposed to the neutral base recombination dominance seen in homojunction transistors. The recombination currents directly affect the current gain β of an HBT depending on which current is dominant. Because the various components of recombination current have different kT-like dependencies on the junction voltages, HBTs do not typically demonstrate

a region of constant β as do BJTs. That is, the bias dependent recombination currents result in a bias dependent β.

The two main equations governing Grossman's and Oki's model are for I_C and I_B which are functions of the forward and reverse Early voltages, six different saturation current parameters, and six different ideality factors (three each for forward and reverse bias). This dependence is a deviation from the traditional GP charge-control relation; however, the parameters can be related to the familiar forward and reverse Gummel plots.

The experimental nature of this model becomes evident when the authors determine empirical relations describing the temperature dependence of the saturation currents and the ideality factors (such as $\ln(IS) = -T_s/T + \ln(I_{so})$, where T_s and I_{so} are constants). The saturation currents and ideality factors are then extracted from measured Gummel plots. The authors state that fitting constant slopes to measured data which are plotted on log-log scale to extract model parameters will produce less than 10% error. However, a numerical fit of the equations would provide much better agreement.

This model is a good example of graphical parameter extraction combined with detailed temperature dependence. Temperature simulation was accomplished by electrically modeling a thermal equivalent circuit; however, no details were provided. The results are a measured I-V characteristic clearly showing the negative slope indicative of self heating effects that is matched well by model data. However, the empirical nature of the model limits its ability to be used in device design.

2.1.4 Grossman and Choma. A detailed physics-based large-signal HBT model is presented by P. Grossman and J. Choma [25]. This work identifies shortcomings in the EM and GP models with respect to HBTs and attempts to account for the time dependence of the base, collector and emitter charging currents. The authors remark that the central problem with using a simple EM model for HBT simulation is not accounting for SCR and surface recombination. The topology consisted of: 1) diodes to model injection and recombination mechanisms, 2) resistors to model recombination limiting mechanisms, 3) capacitors to model non-transit related charge storage, and 4) current sources to model breakdown mechanisms and time dependent electron collection. This is the most comprehensive physics-based model reviewed in this thesis. The temperature dependence is modeled with empirical relationships as in Grossman's and Oki's model. Empirical and analytical relations are used to determine the model's element values.

Grossman and Choma also present a simplification of their model that may be implemented in SPICE along with the process parameters. The report states that this SPICE model accurately simulates HBT circuits operating below 3 GHz. The authors would like to increase the complexity of their physically-based model as well as incorporate their complete model into SPICE. As presented, their model does not provide details for calculating all of the required SPICE model parameters. Additionally, the model is only accurate up to 3 GHz and does not consider extrinsic device parasitics.

2.1.5 Hafizi et al. M. Hafizi, C. Crowell, and M. Grupen [26] also identified limitations in the EM and GP models to describe HBT performance. Their method stresses a non-constant β_F due to dominant

recombination in the emitter-base SCR, whereas the traditional EM and GP equations derived for BJTs assume a constant β_F. Therefore, the graphical technique of Fig. 2.3 for determining EM parameters from Gummel plots cannot be used. Existing extraction techniques rely upon a measurable departure from the ideal relationship (that is, $\exp(qV_{BC}/NR \cdot kT)$ where the reverse ideality factor *NR* is nearly 1). Note that when an exponential function is plotted on a $\log_{10}$ scale, a scaling factor of $(\log_{10}e)^{-1}$ is required. This 2.3 scaling factor is included in Fig. 2.3. Because the HBT ideality factors *NF*, *NE*, and *NC* are not equal to one (due to either a SCR or surface recombination current dominance), a numerical least square fit procedure is implemented involving iterative matrix factorization of measured I-V data.

These ideality factors can be seen in the extended EM model of Fig. 2.4. The two left-most diodes have been added to the topology of Fig. 2.1 to model the SCR recombination at low bias voltages. The capacitors are clearly seen as the depletion (C_{je} and C_{jc}) and diffusion (C_{de} and C_{dc}) capacitances. Equations for I_C and I_B are readily taken from a simple dc nodal analysis involving the currents flowing through the diodes and the current source.

At this point the twelve (excluding capacitances) model parameters of Fig. 2.4 are extracted numerically, which is generally mathematically intensive. The procedure involves fitting measured I-V data to a linearized equation for V_{BE} as a function of β_{Fmax} (*BF*), *ISE*, and *NE*. To be consistent with the SPICE BJT model parameters, all further reference to the maximum common-emitter current gains, β_{Fmax} and β_{Rmax}, will be denoted by *BF* and *BR*, respectively.

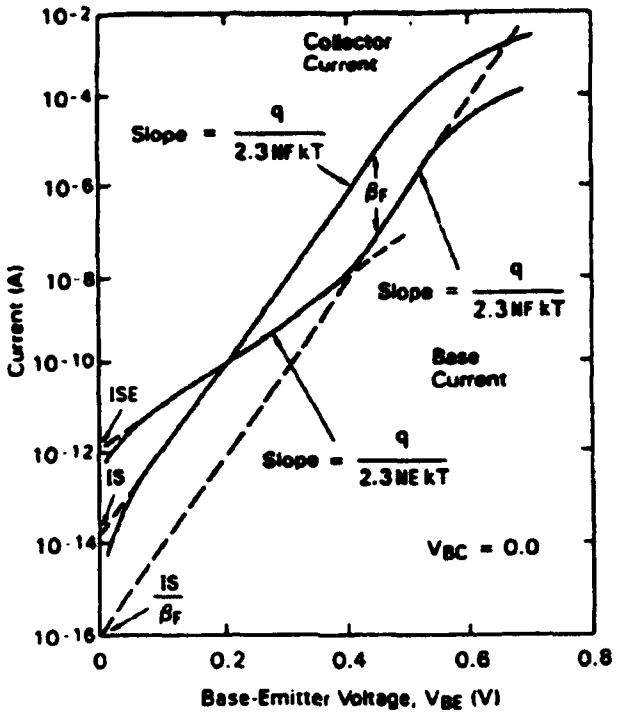

Figure 2.3 Gummel plot for a BJT showing model parameters [26:2123].

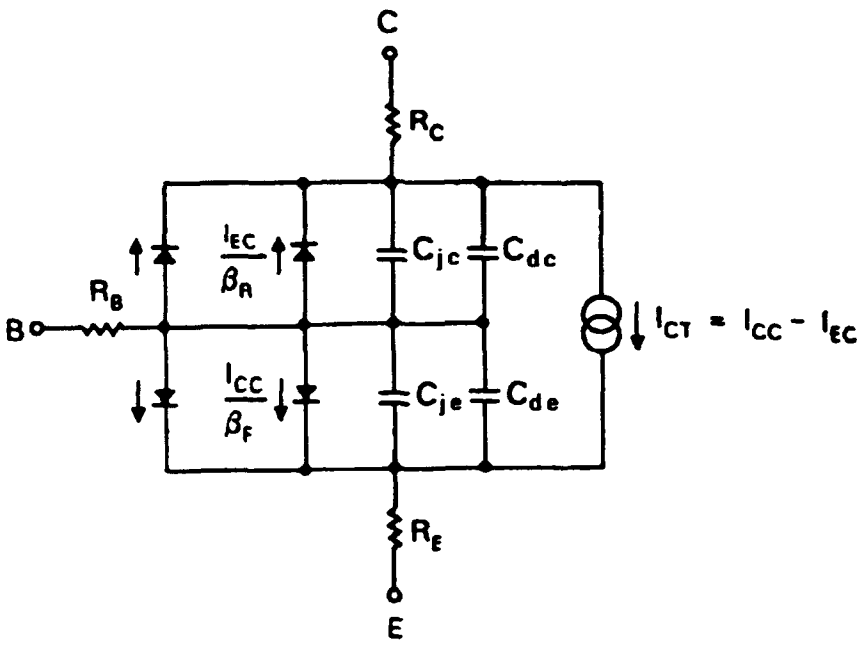

Figure 2.4 An extended EM large-signal equivalent circuit [26:2122].

The same technique is then used to extract *NF*, R_B and R_E. The remaining parameters are extracted from the reverse mode operation. Device temperature may be calculated from the ideal base-collector exponential relationship. Diffusion and depletion capacitances were calculated using SEDAN III as an alternative to S-parameter measurements. SEDAN is a one-dimensional program that, when given device material and process parameters, simultaneously solves Poisson's equation and the current transport and continuity equations. All device measurements were accomplished using an HP4145B semiconductor parameter analyzer and the extraction of model parameters was completed on a desktop computer.

Once extracted, the parameters were entered into the SPICE BJT model statement and excellent agreement was obtained between SPICE calculations and measured data. A good example of numerical parameter extraction directly from measured I-V characteristics is presented that is easily implemented in SPICE due to the simple EM and GP related topology. However, all the resulting SPICE BJT model parameters are curve fit parameters. The model cannot be used for device design since the model parameters are not physical and cannot be related to the device material, geometry, or fabrication process.

2.2 Small-Signal Modeling

Due to their linear operation, small-signal equivalent circuits are generally simpler than their large-signal counterparts. However, the analysis is often more complex because at higher frequencies one must contend with extrinsic device parasitic capacitances and inductances.

2.2.1 Pehlke and Pavlidis. One simple approach reported by D. Pehlke and D. Pavlidis [28] measures device S-parameters and analytically

calculates the equivalent circuit element values. S-parameters were measured from 0.5 GHz to 25 GHz. The authors' equivalent circuit, shown in Fig. 2.5 is the conventional small-signal T-model. Analytical parameter extraction was implemented by converting the S-parameters to H-parameters and solving for resistor, capacitor, and inductor element values with impedance equations. Unique values are extracted by exploiting the behavior of capacitors and inductors at low and high frequencies.

The attractiveness of this technique is its simplicity: rudimentary equivalent circuit and no test structure measurement. The authors are forced to perform some fitting to determine the four emitter element parameters described by Z_{BE} and z_E, because there are four unknowns and only two equations. Pehlke and Pavlidis have developed an efficient technique to analytically determine small-signal equivalent circuit element values from the measured S-parameters. However, they do not consider parasitic capacitances, which are known to signficantly affect the microwave performance of most HBTs. Additionally, the model they derive is never simulated to verify that it can produce modeled S-parameters that are in good agreement with the measured S-parameters.

2.2.2 Maas and Tait. Another approach by S. Maas and D. Tait [29] also advises against the use of on-wafer test patterns and unbiased or "cold" device measurements. This technique is simple and uses an equivalent circuit (Fig. 2.6) slightly different than Pehlke's and Pavlidis'. The focus here is to determine resistor values prior to any S-parameter fitting routine. S-parameters are measured and Z_{12} is calculated. Z_{12} is then used to determine emitter, base, and collector resistances. A conversion of the S-parameters to H_{21} aids in finding the

current gain factor. Finally, the remaining element values are determined by S-parameter optimization.

2.2.3 Trew et al. A problem with optimization or S-parameter fitting mentioned earlier is that, unless care is taken, non-unique and non-physical element values may be obtained. Knowing the desirability of extracting as many parameters as possible using measurements and calculations independent of S-parameters, R. Trew *et al.* [30] have found one solution to this problem. Their method uses a constraining equation based upon the emitter-to-collector delay time, τ_{ec}. τ_{ec} is a function of the model's resistive and capacitive elements. Measured H_{21} is used to extrapolate f_T and determine the device's τ_{ec}, from the relationship $\tau_{ec} = (2\pi f_T)^{-1}$. By placing an empirical constraint on τ_{ec}, optimization of the S-parameters will provide pseudo-physical equivalent circuit element values. The authors' state that to match empirical data, parasitics were added; however, no detail on parasitic calculation is provided. Like all the other small-signal modeling techniques found in the literatue, S-parameters must be measured *before* all equivalent circuit element parameters can be extracted.

2.2.4 Costa et al. The technique used by D. Costa *et al.* [31] does not require any numerical optimization. However, due to the complexity of their equivalent circuit, measurement of three test structures to determine various device parasitics is required. Through multiple conversions between S, Y and Z-parameters, the parasitic elements are subtracted, leaving the intrinsic device modeled as a hybrid-π network. The intrinsic element values, which are directly related to Y-parameters, are then uniquely de-embedded via more matrix manipulation. The authors state their method is limited by the necessity for accurate

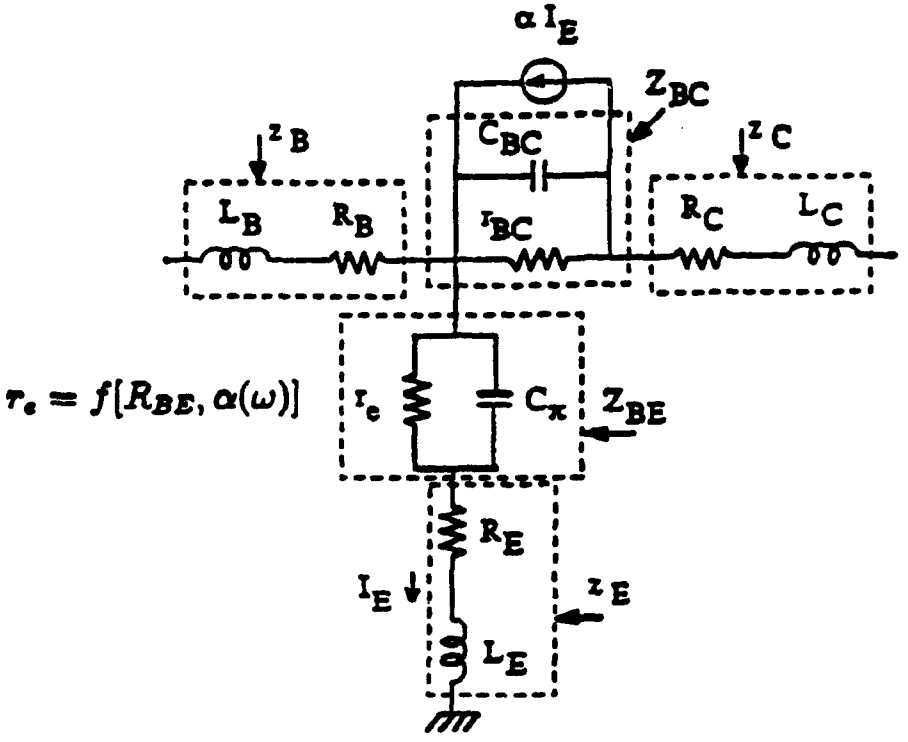

Figure 2.5 Pehlke's small-signal T-model equivalent circuit [28:2368].

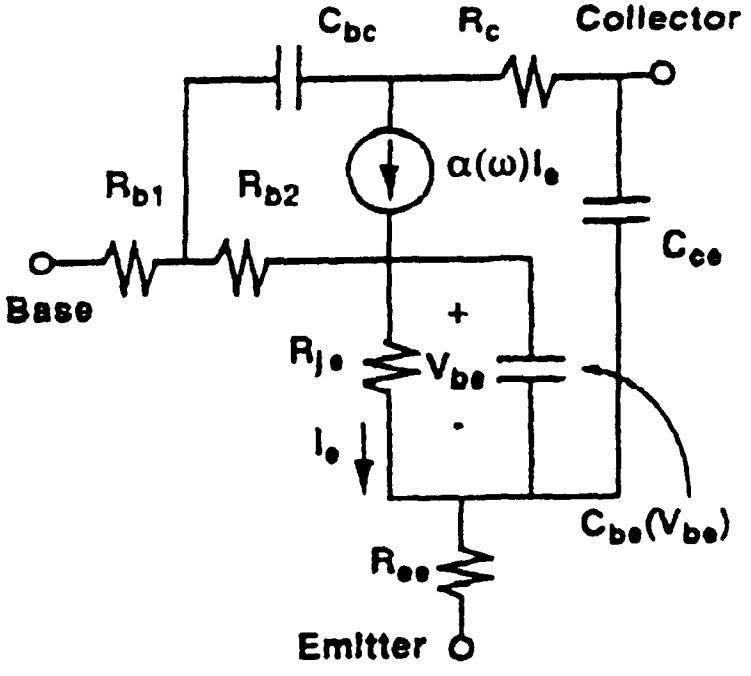

Figure 2.6 Maas' small-signal equivalent circuit [29:502].

geometrical and material parameters during parasitic extraction. The technique of Costa *et al.* is one of several published techniques to extract equivalent circuit element values from measured S-parameter data.

2.3 Summary of Literature

Several techniques for both large and small-signal modeling of HBTs were reviewed. Each of the large-signal models is derived from either the EM or GP model topology and equations. Expressions for I_C and I_B are prominent in most efforts because these terminal currents are the easiest to obtain from common-emitter I-V characteristics. The particular method of determining expressions for I_C and I_B varies among researchers. The basic approach is to find a relation describing the minority carrier concentration at the edge of the SCR from which an expression for current injected into the base may be obtained. Thermionic emission is well accepted to model the dominant current flow mechanism for abrupt heterojunctions. Drift-diffusion best models the carrier transport of graded heterojunctions where the conduction band spike is negligible. Although empirically curve fit HBT models have been directly implemented in SPICE, additional work is needed to develop a simple physics-based HBT model in SPICE. Any model that derives equations for I_B and I_C different from SPICE I_B and I_C equations must be modified to be consistent with the existing SPICE BJT model prior to SPICE implementation. The alternative is to create a unique HBT model in SPICE by modifying the source code. SPICE implementation is preferred due to its widespread use and versatility in simulating integrated circuits.

The small-signal models have either a hybrid-π or T-model equivalent circuit. These topologies are equivalent and each may be converted to the

other because they are simply linearized versions of the large-signal transistor topology. S-parameter measurements over a wide range of frequencies are key to small-signal modeling. To better suit the particular method used, measured S-parameters are often converted to H, Y and Z-parameters. Modeling the extrinsic device parasitics (and their subsequent mathematical subtraction from the model) is a primary concern. Costa *et al*. have completed the most comprehensive effort in this area but their circuit is bulky and their procedure involved. Therein lies the trade-off and challenge of small-signal modeling: to obtain the simplest model that accurately describes device performance. Additionally, care must be exercised when parameter extraction calls for fitting measured data. Otherwise, a non-unique or non-physical circuit will be obtained.

None of the microwave HBT models found in the literature are purely physics-based. Every technique uses some form of empirical curve fitting to the measured S-parameters. Whether element values are optimized (curve fit) or analytically extracted, the use of measured S-parameters classifies the model as empirical. The more empirical a model is, the less insight is obtained on how the device material, geometry, and fabrication process effect the device's electrical performance. An accurate physics-based microwave HBT model has not yet been developed.

3. Theory

All transistor modeling can be categorized as either large-signal or small-signal modeling. This chapter discusses the theory of both large and small-signal modeling with respect to modeling HBT electrical performance. Large-signal modeling is covered by examining the physics of junction transistors. The goal is to provide an understanding of the physical model and the basis for each large-signal equivalent circuit element value. The concept of linearization is discussed as the method by which the large-signal model is transformed into a small-signal model. The purpose of each element in the small-signal topology will be provided. The chapter concludes by discussing the theory and importance of S-parameters in characterizing transistors at microwave frequencies.

3.1 Physical Large-Signal Modeling

As a first step, a junction transistor can be thought of as nothing more than two back-to-back diodes. This is essentially the physical interpretation assumed in the classic Ebers-Moll model [43]. Each diode physically represents either the base-emitter or base-collector junction. Shockley's diode equation [50], with the addition of a potentially non-ideal emission coefficient, η, can analytically represent each diode [14]:

$$I = IS\left[\exp\left(\frac{qV}{\eta kT}\right) - 1\right] \tag{3.1}$$

$$IS = qA\left(\frac{D_p p_{no}}{L_p} + \frac{D_n n_{po}}{L_n}\right) \tag{3.2}$$

$$L_n = (D_n \tau_n)^{1/2} \tag{3.3}$$

$$L_p = (D_p \tau_p)^{1/2} \tag{3.4}$$

where V is the voltage across the junction which is identical to the external voltage applied to the terminals (V);

IS is the junction saturation current (A);

A is the area of the junction (cm^2);

D_p and D_n are the minority hole and electron diffusivities ($cm^2 \cdot s^{-1}$);

p_{no} and n_{po} are the equilibrium concentrations of minority holes and electrons (cm^{-3});

L_p and L_n are the minority hole and electron diffusion lengths (cm);

τ_p and τ_n are the lifetimes of excess minority carriers in n-material and p-material, respectively (s).

Associated with every p-n junction diode is a SCR or depletion region. The thickness or width of this depletion region, X, is dependent on the voltage across the junction, V, as given by [45]

$$X = \left[\frac{2 \epsilon_s}{q} \left(\frac{N_A + N_D}{N_A N_D} \right) (V_{bi} - V) \right]^{1/2} \tag{3.5}$$

$$V_{bi} = \frac{kT}{q} \ln \left(\frac{N_A N_D}{n_i^2} \right) \tag{3.6}$$

where ϵ_s is the permittivity of the semiconductor, $\epsilon_s = \epsilon_r \epsilon_o$, ($F \cdot cm^{-1}$);

N_A is the dopant concentration in the p-material (cm^{-3});

N_D is the dopant concentration in the n-material (cm^{-3});

n_i is the semiconductor's intrinsic carrier concentration (cm^{-3});

V_{bi} is the junction built-in voltage (V).

The exponent of ½ in Eq. (3.5) is unique to abrupt junctions in which the transition from n-type to p-type semiconductor occurs on the order of several angstroms. Mathematically, the exponent, also called the junction grading factor, results from the solution to Poisson's equation [51:76]

$$\frac{d^2\psi}{dx^2} = \frac{-qN_D}{\epsilon_s} \tag{3.7}$$

where ψ is the potential function (V);

x is the distance variable (cm).

Linear or exponential grading of the junction (i.e., the dopant concentrations are functions of x) will result in exponents as low as ½. The junction grading factors are process parameters which may be defined in SPICE. The precise growth controls available with MBE allow for very abrupt junctions. Junctions created by Metal Organic Chemical Vapor Deposition (MOCVD) are unintentionally graded over approximately 100 - 200 Å due to the less precise layer thickness control.

In the case of an HBT, Eqs. (3.5) and (3.6) would be valid only for the base-collector homojunction. Because all practical HBTs have an emitter-base heterojunction, the emitter and base have different permittivities, ϵ_E and ϵ_B. The E and B subscripts signify emitter and base respectively in the following expressions for heterojunction depletion widths on the emitter and base sides of the junction [23:873]:

$$X_E = \left[\frac{2\epsilon_E\epsilon_B}{q} \cdot \frac{N_B(V_{bi} - V_{BE} - 1.64V_T)}{N_E(\epsilon_E N_E + \epsilon_B N_B)}\right]^{1/2} \tag{3.8}$$

$$X_B = \frac{N_E}{N_B} X_E \tag{3.9}$$

where V_{BE} is the voltage applied to the base relative to the emitter (assuming an Npn transistor), N_B and N_E are the base and emitter dopant concentrations respectively, V_T is the thermal voltage given by kT/q and 1.64 is an empirically derived factor. The expression for determining the built-in voltage of a heterojunction is given by [52]:

$$V_{bi} = V_T \ln\left(\frac{N_E N_B}{n_{iE} n_{iB}}\right) + |\Delta E_C| - \frac{\Delta E}{2} + V_T \ln\left(\frac{N_{VE} N_{CB}}{N_{CE} N_{VB}}\right) \qquad (3.10)$$

where n_{iE} is the intrinsic carrier concentration of the wide-gap emitter;

n_{iB} is the intrinsic carrier concentration of the base;

ΔE_C is the conduction band energy difference between the emitter and the base;

ΔE is the bandgap difference between the emitter and the base;

N_{CE} and N_{CB} are the conduction band density of states in the emitter and the base, respectively;

N_{VE} and N_{VB} are the valence band density of states in the emitter and the base, respectively.

Equation (3.10) reduces to Eq. (3.6) when both the emitter and base have the same energy bandgap.

Figure 3.1 shows the band diagrams for a homojunction and a heterojunction at equilibrium. The homojunction is typical for the emitter-base junction of a Si BJT where the emitter is doped more heavily than the base; thus, there is more depletion region and band-bending in the base. The heterojunction diagram is drawn to scale for an abrupt $Al_{0.35}Ga_{0.65}As/GaAs$ emitter-base junction. In this case, most of the band-bending occurs in the emitter. In both diagrams, the vertical dashed line represents the metallurgical junction.

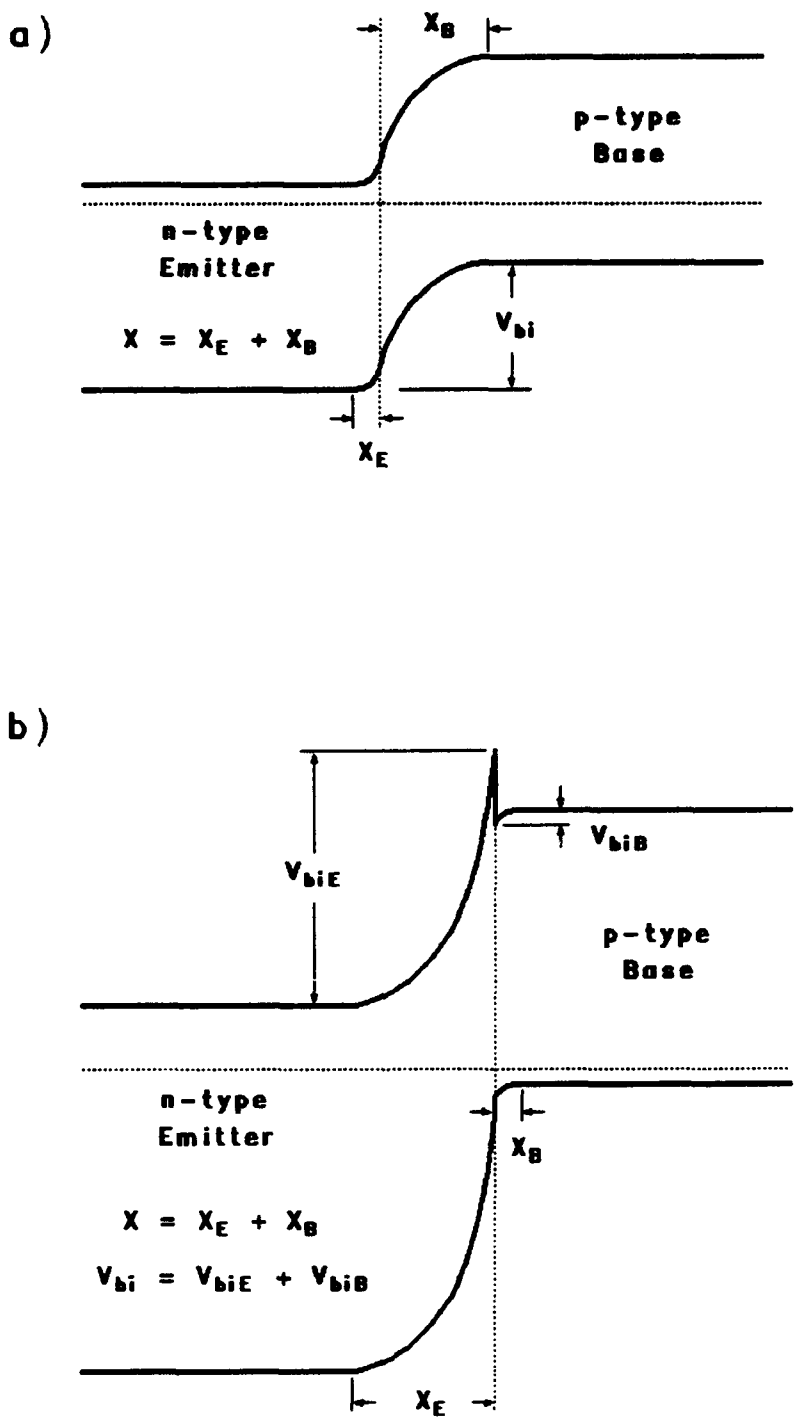

Figure 3.1 Homojunction (a) and heterojunction (b) band diagrams at equilibrium.

While the junction is reverse-biased, minority carrier drift current is the dominant transport mechanism across the depletion region. Therefore, under zero-bias and reverse-bias the region can then be considered a dielectric void of charge, which can be modeled by a capacitance. This depletion capacitance is described by the following expressions for a homojunction and a heterojunction, respectively,

$$C_j = \frac{\epsilon_s A}{X} \tag{3.11}$$

$$C_j = \frac{\epsilon_E \epsilon_B A}{\epsilon_E X_B + \epsilon_B X_E} \tag{3.12}$$

Notice that the heterojunction expression reduces to that of the homojunction when $\epsilon_E = \epsilon_B$.

While the junction is forward-biased, relatively large numbers of majority carriers diffuse across the junction and become excess minority carriers. The excess minority carriers are stored within the neutral regions before recombining, or in the case of the base, before diffusing across the thin base into the collector. This charge storage effect can be modeled by a diffusion capacitance as given by [14:96]:

$$C_d = \frac{A}{V_T}\left(\frac{qL_p p_{no}}{2} + \frac{qL_n n_{po}}{2}\right)\exp\left(\frac{V}{V_T}\right) \tag{3.13}$$

The simplicity of the basic Ebers-Moll model can be traded-off for more accuracy by including a depletion and diffusion capacitor for each junction. The resulting equivalent circuit is shown in Fig. 3.2. I_1 and I_2 have the form of Eq. (3.1) and represent the currents through the base-collector and base-emitter junctions. C_{je} and C_{de} are the base-emitter depletion and diffusion capacitances, whereas C_{jc} and C_{dc} are the base-collector depletion and diffusion capacitances. The model's current

source is defined by $I_{CT} = I_{CC} - I_{EC}$, where I_{CC} and I_{EC} were given in Eqs. (2.3) and (2.4) such that

$$I_{CT} = IS\left[\exp\left(\frac{V_{BE}}{NF \cdot V_T}\right) - \exp\left(\frac{V_{BC}}{NR \cdot V_T}\right)\right] \tag{3.14}$$

Physically, I_{CT} is the net current from collector to emitter through the transistor. Looking at Fig. 2.1, one can see that I_{CC} is the current across the base-emitter junction due to V_{BC} and I_{EC} is the current across the base-collector junction due to V_{BE}. In other words, each junction acts as a voltage controlled current source with respect to the other junction. I_{CT} is merely the composite current source from collector to emitter.

Another physical phenomena that is not yet considered by the model is the voltage drop across the neutral regions. The voltage applied to the terminals of a transistor is never the voltage seen by the respective junctions because of series resistances. The emitter, base, and collector resistances are dependent upon the device geometry, but can generally be described by four components: contact resistance, bulk resistance, spreading resistance, and lateral contact resistance. Fig. 3.3 shows the relationship between the geometry of a rectangular finger HBT, the emitter resistance, R_E, and the three components of base series resistance, R_B. The figure is purely for illustrative purposes and is not drawn to scale. Also, the following resistance equations are derived for a geometry with two base fingers and two collector contacts. Because such a design is symmetric about the emitter, only one base contact is shown.

Contact resistance occurs when a current moves normally through a metal-semiconductor interface without spreading or changing direction in the semiconductor. The expression for contact resistance is given by [53] where ρ_c is the specific contact resistance ($\Omega \cdot cm^2$);

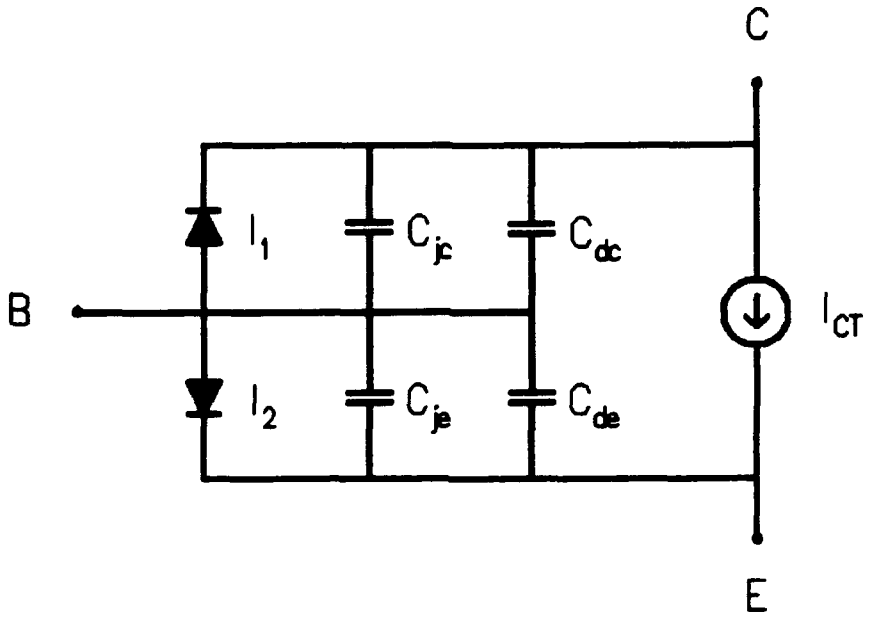

Figure 3.2 Ebers-Moll equivalent circuit modified to include junction capacitances.

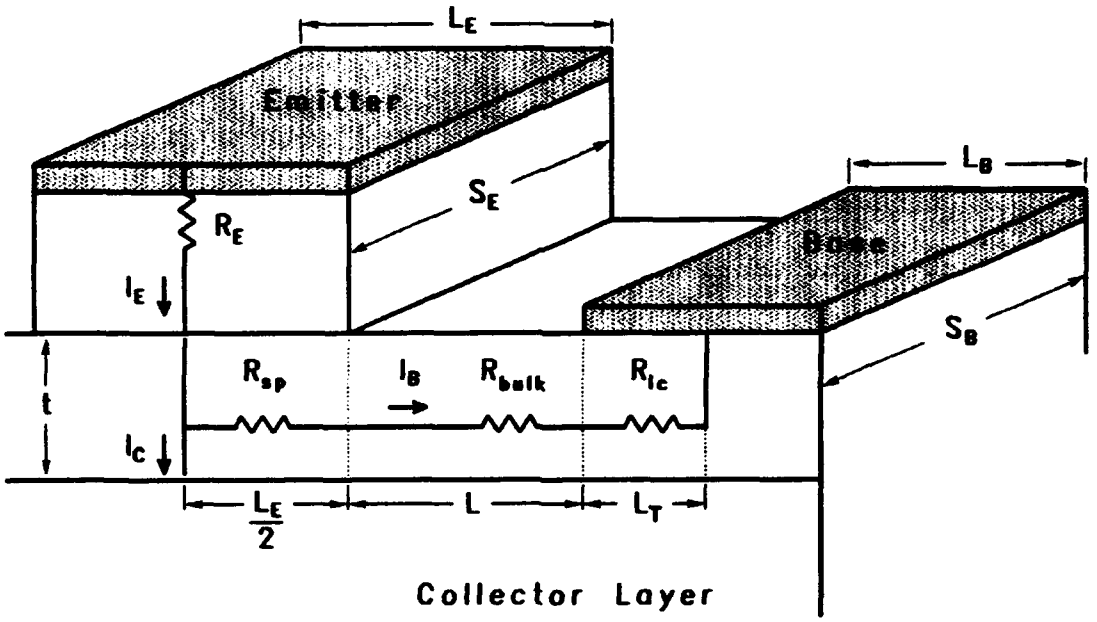

Figure 3.3 Lateral view of an HBT showing emitter resistance, R_E, and the three components of base resistance, R_B.

$$R_{contact} = \frac{\rho_c}{A} \tag{3.15}$$

A is the area of the contact, $A = S_E L_E$ (cm^2).

Bulk resistance occurs when current moves a length, L, normal to the cross-sectional area, A, of a semiconductor having resistivity, ρ, and is given by the classic resistance expression

$$R_{bulk} = \frac{\rho L}{A} \tag{3.16}$$

Spreading resistance occurs when current enters a sheet region normally and leaves in parallel. Equation (3.17) describes the base spreading resistance of a rectangular emitter finger having a base finger on either side [53:205]

$$R_{sp} = \frac{\rho}{t} \cdot \frac{L_E}{S_E} \cdot \frac{1}{3} \cdot \frac{1}{2} \tag{3.17}$$

where ρ is the resistivity of the semiconductor ($\Omega \cdot cm$);

t is the thickness of the region through which the current spreads (cm);

S_E is the width of the emitter finger (cm);

L_E is the length of the emitter finger (cm);

1/3 is the spreading factor;

1/2 is due to the current spreading through half of the emitter width to get to one base contact.

Lateral contact resistance occurs when a current enters a region beneath and parallel to the surface of the contact it flows through. Equations (3.18) and (3.19) describe the lateral contact resistance of a rectangular contact [53:206]

$$R_{1c} = \rho_s \cdot \frac{L_T}{S_B} \coth\left(\frac{L_B}{L_T}\right) \tag{3.18}$$

$$L_T = \left(\frac{\rho_c}{\rho_s}\right)^{1/2} \tag{3.19}$$

where ρ_s is the sheet resistance of the region beneath the contact ($\Omega/\square$);

L_B is the contact metallization length (cm);

S_B is the contact metallization width (cm);

L_T is the contact characteristic length (cm).

The total emitter series resistance, R_E, of Fig. 3.3 is the sum of the contact and bulk resistances calculated from Eqs. (3.15) and (3.16). The base current is split evenly in half between the two base contacts due to their symmetry about the emitter. Only one of these paths is shown in Fig. 3.3; thus, the total base series resistance, R_B, resulting from two identical paths in parallel, is given by

$$R_B = \frac{R_{sp} + R_{bulk} + R_{1c}}{2} \tag{3.20}$$

Recombination currents, which can be significant in HBTs, are not accounted for in the basic Ebers-Moll model. These recombination currents are components of I_B, and are primarily the surface, SCR, and neutral base recombination currents. A composite recombination current, which is dependent on the junction voltage, can be modeled with a non-ideal diode. A non-ideal diode is represented analytically by a non-unity emission coefficient. To accurately model the behavior of the transistor in all modes of operation, a recombination current diode is needed for each junction, I_3 and I_4. The complete large-signal equivalent circuit is shown in Fig. 3.4, where [21]

$$I_1 = \frac{IS}{BR}\left[\exp\left(\frac{V_{B'C'}}{NR \cdot V_T}\right) - 1\right] \tag{3.21}$$

$$I_2 = \frac{IS}{BF}\left[\exp\left(\frac{V_{B'E'}}{NF \cdot V_T}\right) - 1\right] \tag{3.22}$$

$$I_3 = ISC\left[\exp\left(\frac{V_{B'C'}}{NC \cdot V_T}\right) - 1\right] \tag{3.23}$$

$$I_4 = ISE\left[\exp\left(\frac{V_{B'E'}}{NE \cdot V_T}\right) - 1\right] \tag{3.24}$$

$V_{B'E'}$ and $V_{B'C'}$ are the intrinsic voltages seen by the two junctions. These intrinsic voltages must be differentiated from the applied voltages V_{BE} and V_{BC} due to the voltage drop across the series (also called parasitic) resistances. This circuit may be linearized to produce the small-signal hybrid-π equivalent circuit.

Through circuit analysis, it will be shown that the topology of Fig. 3.4 is equivalent to the SPICE circuit of Fig. 1.7. The first step in the transformation to Fig. 1.7 is to add each pair of parallel capacitors. The composite base-emitter capacitance, $C_{je}+C_{de}$, becomes C_{BE}. Similarly, the composite base-collector capacitance, $C_{jc}+C_{dc}$, becomes C_{BC}. The intermediate circuit, redrawn to facilitate topology comparison, is shown in Fig. 3.5.

As mentioned previously, each diode can be analytically represented with its respective I-V expression. Composite current sources can be obtained by combining the diode current equations. The result is the SPICE large-signal equivalent circuit of Fig. 3.6. Expressions for I_B and I_C are identical to the equations used by SPICE to calculate the terminal currents for any given junction voltages. Equations (3.25) and (3.26) fully characterize the dc large-signal model in SPICE [39].

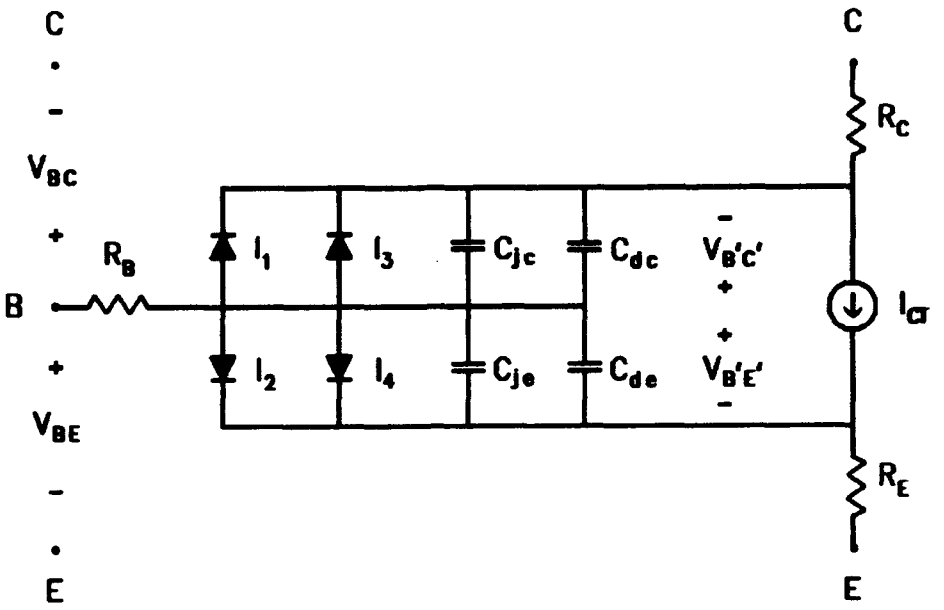

Figure 3.4 The complete large-signal equivalent circuit.

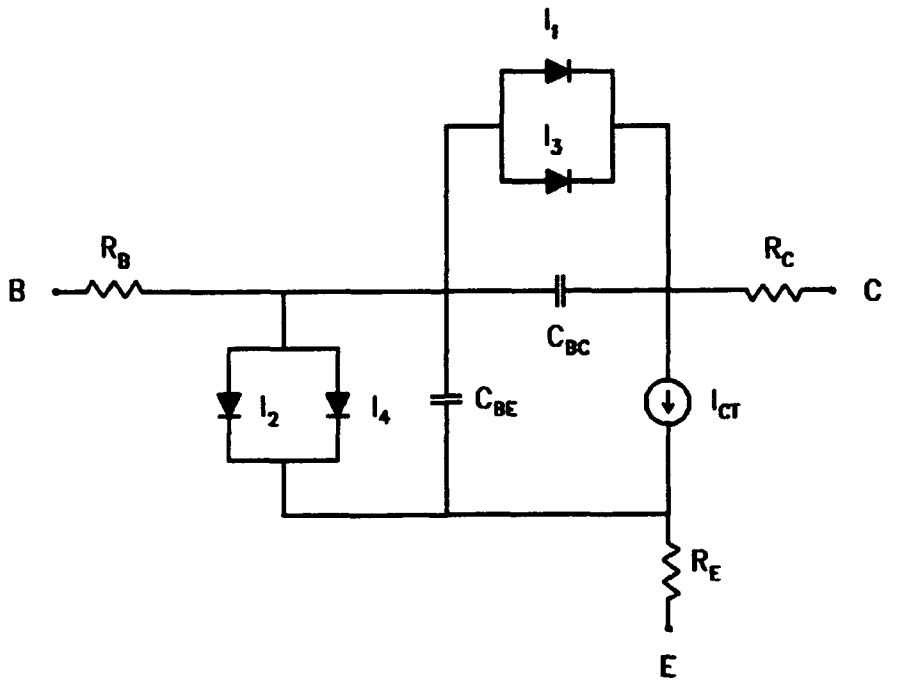

Figure 3.5 Intermediate circuit in the derivation of the SPICE large-signal equivalent circuit.

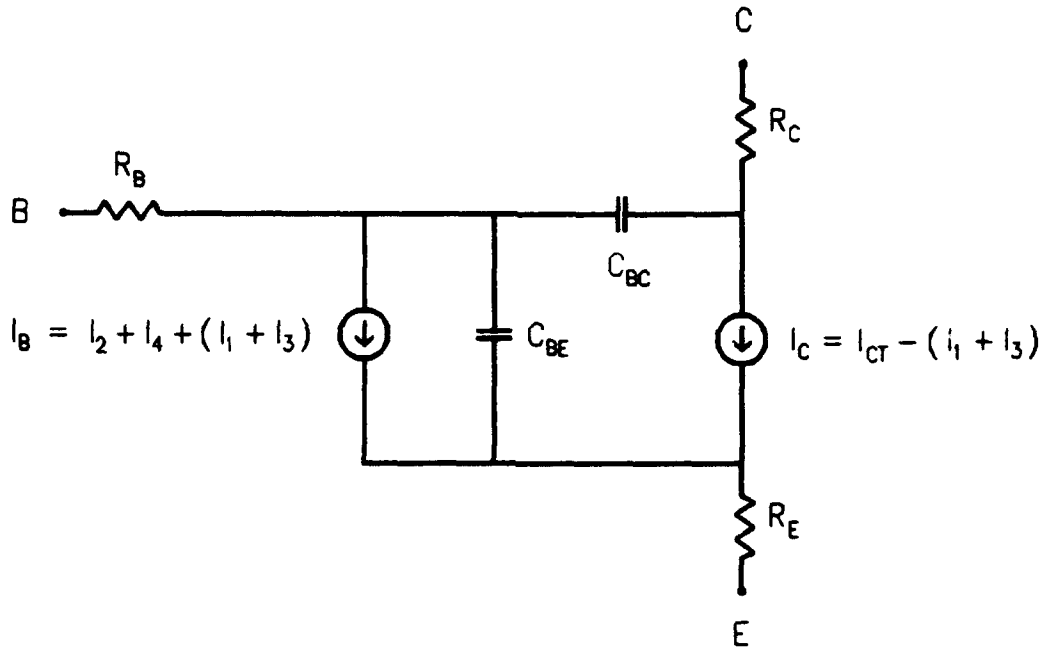

Figure 3.6 Complete SPICE large-signal equivalent circuit showing components of I_B and I_C.

$$I_C = IS\left[\exp\left(\frac{V_{B'E'}}{NF \cdot V_T}\right) - \exp\left(\frac{V_{B'C'}}{NR \cdot V_T}\right)\right] - \frac{IS}{BR}\left[\exp\left(\frac{V_{B'C'}}{NR \cdot V_T}\right) - 1\right]$$

$$- ISC\left[\exp\left(\frac{V_{B'C'}}{NC \cdot V_T}\right) - 1\right] \qquad (3.25)$$

$$I_B = \frac{IS}{BF}\left[\exp\left(\frac{V_{B'E'}}{NF \cdot V_T}\right) - 1\right] + \frac{IS}{BR}\left[\exp\left(\frac{V_{B'C'}}{NR \cdot V_T}\right) - 1\right] + ISE\left[\exp\left(\frac{V_{B'E'}}{NE \cdot V_T}\right) - 1\right]$$

$$+ ISC\left[\exp\left(\frac{V_{B'C'}}{NC \cdot V_T}\right) - 1\right] \qquad (3.26)$$

Having established the physical basis for the SPICE large-signal BJT circuit, the required model parameters will be examined. Table 3-1 lists the SPICE model parameters which must be modified to accurately characterize an HBT. Semiconductor device physics can be used to determine values for each parameter excluding the emission coefficients. Because of their complex dependence on the device material, geometry, and fabrication process, accurate values for the emission coefficients are

Table 3-1

SPICE BJT Model Parameters [39]

Parameter	Units	Description
BF	-	Ideal maximum forward current gain, β_{Fmax}
BR	-	Ideal maximum reverse current gain, β_{Rmax}
IS	A	Transport saturation current
ISE	A	Base-emitter leakage saturation current
ISC	A	Base-collector leakage saturation current
NF	-	Forward current emission coefficient
NR	-	Reverse current emission coefficient
NE	-	Base-emitter leakage emission coefficient
NC	-	Base-collector leakage emission coefficient
RE	Ω	Emitter resistance
RB	Ω	Base resistance
RC	Ω	Collector resistance
CJE	F	Base-emitter zero-bias depletion capacitance
CJC	F	Base-collector zero-bias depletion capacitance
MJE	-	Base-emitter junction grading factor
MJC	-	Base-collector junction grading factor
VJE	V	Base-emitter built-in potential
VJC	V	Base-collector built-in potential
TF	sec	Base forward transit time
TR	sec	Base reverse transit time
XCJC	-	Fraction of base-collector depletion capacitance internal to base

better determined through some form of parameter extraction or curve fitting.

3.2 Linearization

The large-signal equivalent circuit is designed to model a transistor in all four modes of operation: cutoff, active, saturation and inverted. The modes of operation are best described by the polarity of the voltage that appears across each junction as seen in Fig. 3.7. The transistor described by Fig. 3.7 is a pnp BJT where n_p (p_n) is the minority electron (hole) concentration in the p (n) regions. The large-signal model is often called a non-linear model and is primarily used for digital applications, where the transistor acts like a switch. The "on" and "off" states correspond to saturation and cutoff modes respectively as illustrated in Fig. 3.8. V_{EC} is the common-emitter configuration output voltage. The switching time corresponds to the time required for the transistor to traverse from one state to the other along the load line. Switching time is a figure of merit for digital devices and can be defined as either "turn-on" or "turn-off" time. Increasing excess minority carrier storage in the base occurs during turn-on, whereas those same carriers (as well as additional carriers stored while in saturation), are removed during turn-off as depicted Fig. 3.9. Figure 3.9 demonstrates an npn transistor operating in the common-base configuration where the base terminal is common to both the input voltage, V_{EB}, and the output voltage, V_{CB}. The input current pulse is I_E. The turn-on time, τ_0, is the time required for the collector current to reach 90% of its saturated value (V_{CC}/R_L). The storage time, τ_1, is the time required for the excess minority carrier concentration at the collector edge of the base to return

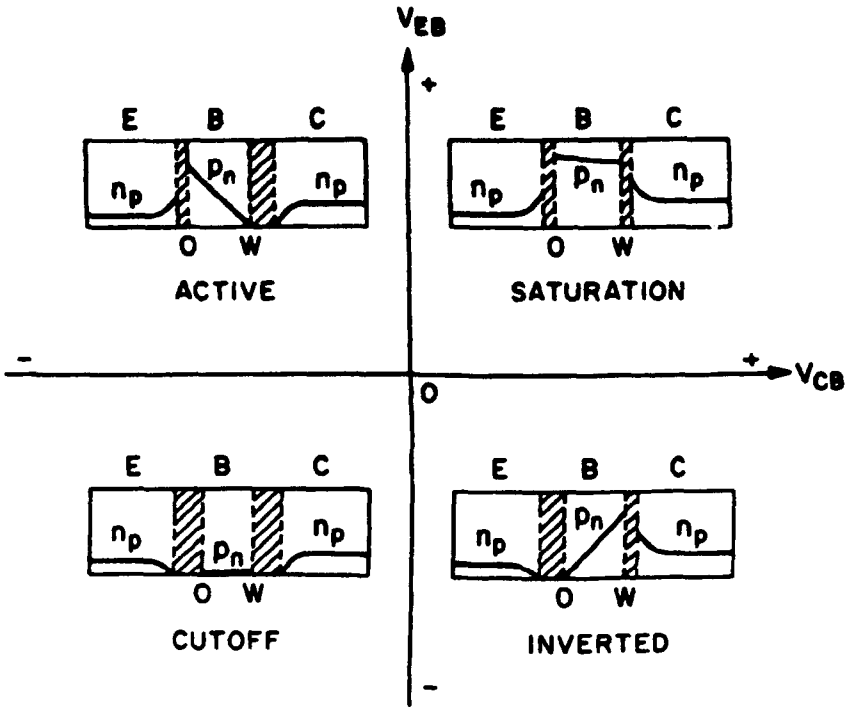

Figure 3.7 Pnp junction transistor modes of operation and associated minority carrier concentrations [51:122].

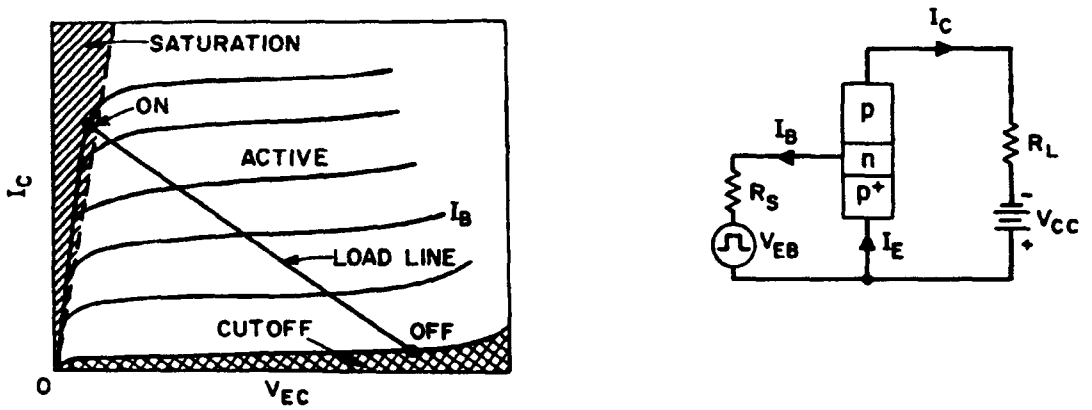

Figure 3.8 (a) Relationship between load line, bias point and modes of operation and (b) corresponding digital switching circuit [51:139].

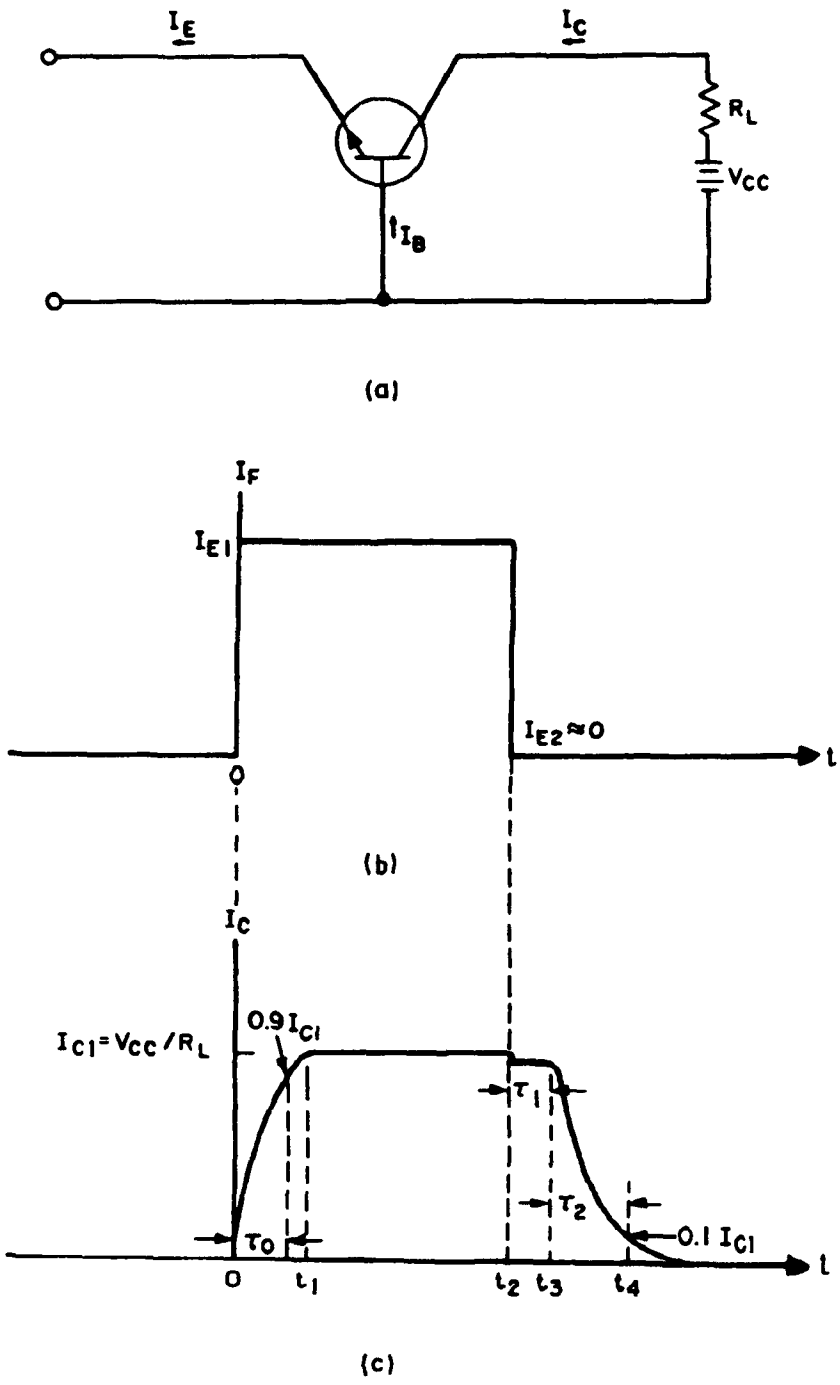

Figure 3.9 (a) Common-base circuit configuration, (b) emitter current pulse and (c) corresponding collector current response illustrating transistor switching times [14:179].

to zero. This is the time for the device to leave saturation and enter the active mode as the base discharges. Once the active mode is reached, the base continues to discharge until the device essentially enters cutoff after time τ_2, the decay time.

Amplifier applications are best modeled with a small-signal or linear equivalent circuit where the transistor is operated at a specific bias point in the active mode. The linear equivalent circuit elements are part of the non-linear equivalent circuit, because the linear model is operating at a point on the non-linear curve. Note that any point on the load line of Fig. 3.8 corresponds to a unique bias point defined by V_{EC}, I_C, and I_B.

3.3 Physical Small-Signal Modeling

During the derivation of the SPICE large-signal equivalent circuit, the diodes were replaced by non-linear current sources. The value of each current source is dependent on the junction voltage. Because the small-signal model characterizes the transistor operating at a specific dc bias point, each diode's current and voltage are approximately constant. Any device whose voltage and current are constant can be modeled with the corresponding resistance or inverse of resistance, conductance. This conductance is a small-signal or dynamic conductance which graphically is equivalent to the slope of the diode's I-V curve at the bias point. Mathematically, the conductance parameters are calculated via the partial derivatives of current with respect to junction voltages [39]:

Reverse Base Conductance:

$$g_\mu = \left.\frac{\partial I_B}{\partial V_{B'C'}}\right|_{V_{B'E'}=const.} \tag{3.27}$$

Forward Base Conductance:

$$g_\pi = \left.\frac{\partial I_B}{\partial V_{B'E'}}\right|_{V_{B'C'}=\text{const.}} \tag{3.28}$$

Output (Collector) Conductance:

$$g_o = \left.\frac{\partial I_C}{\partial V_{C'E'}}\right|_{V_{B'E'}=\text{const.}} \tag{3.29}$$

Transconductance:

$$g_m = \left.\frac{\partial I_C}{\partial V_{B'E'}}\right|_{V_{B'C'}=\text{const.}} \tag{3.30}$$

Both HSPICE and the HP 85150B Microwave and RF Design Systems [42] software perform the partial differentiation to obtain the four conductance parameters. An ac analysis in HSPICE provides g_m, $1/g_\pi$, and $1/g_o$ given the model parameters of Table 3-1, and the dc operating point. Most small-signal applications operate in the active region, where the base-collector junction is reverse-biased. Under reverse-bias the impedance of C_μ is much smaller than r_μ, therefore HSPICE considers r_μ negligible. Although the hybrid-π small-signal circuit is electrically valid for all modes of operation, the HSPICE assumption on r_μ limits simulations to the active mode. Recall from Fig. 1.8 that C_μ is the dc model's C_{BC} at a specific bias point, and that C_π is C_{BE} at a specific bias point. The hybrid-π small signal circuit is shown in Fig. 3.10.

Impedance can be thought of as a frequency dependent resistance. The impedance of a capacitor is $(\omega C)^{-1}$, where ω is radian frequency and C is the value of the voltage dependent capacitance. Similarly, the impedance of an inductor is ωL, where L is the value of the current dependent inductance. Obviously, operating at dc, capacitors are open circuits and inductors are short circuits. The impedance of an inductor

increases linearly with increasing frequency and the impedance of a capacitor decreases non-linearly with increasing frequency.

At low frequencies, ($f \leq 1$ MHz), small-valued capacitors (~10 fF) and inductors (~10 pH) may still be considered open and short circuits, respectively. However, at microwave frequencies, ($f \geq 1$ GHz), those same capacitors and inductors become parasitic and degrade transistor performance. Thus, the microwave small-signal circuit is not only a linearized version of the large-signal circuit, but must include parasitics as well. The linearized dc model is referred to as the intrinsic device. The transistor including the surrounding network of parasitic inductances and capacitances is referred to as the extrinsic device.

3.4 S-Parameters

The measurements used to characterize a microwave network are S-parameters. Each S-parameter is an element of an . x *i* matrix where *i* is the number of network ports. For a single transistor in a common-emitter configuration there are two ports, so the S-parameter matrix is given by [54:221]

$$\begin{bmatrix} V_1^- \\ V_2^- \end{bmatrix} = \begin{bmatrix} S_{11} & S_{12} \\ S_{21} & S_{22} \end{bmatrix} \begin{bmatrix} V_1^+ \\ V_2^+ \end{bmatrix} \tag{3.31}$$

$$S_{ij} = \left. \frac{V_i^-}{V_j^+} \right|_{V_k^+ = 0 \text{ for } k \neq j} \tag{3.32}$$

where V_j^+ is a voltage waveform incident to port j, and V_i^- is the voltage waveform reflected from port i due to the driving signal at port j. An S-parameter signal flow graph is shown in Fig. 3.11. The condition in Eq. (3.32) states that only one port may be driven at a time; all other

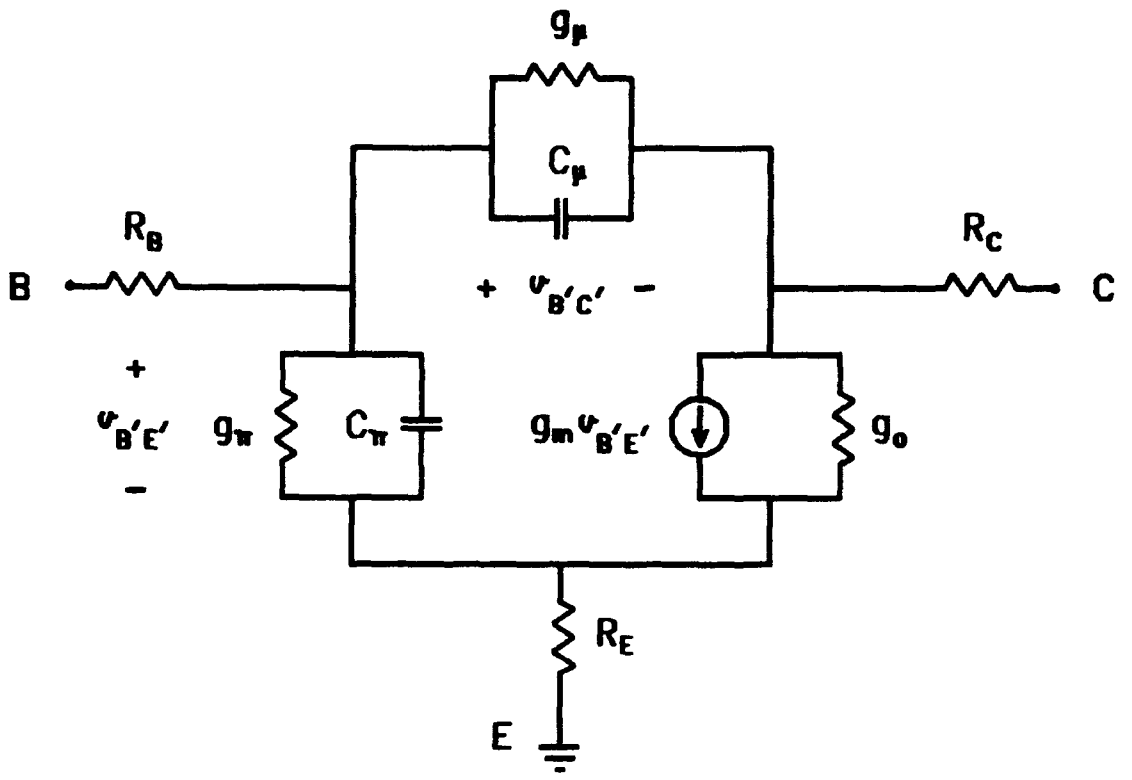

Figure 3.10 The hybrid-π small-signal equivalent circuit.

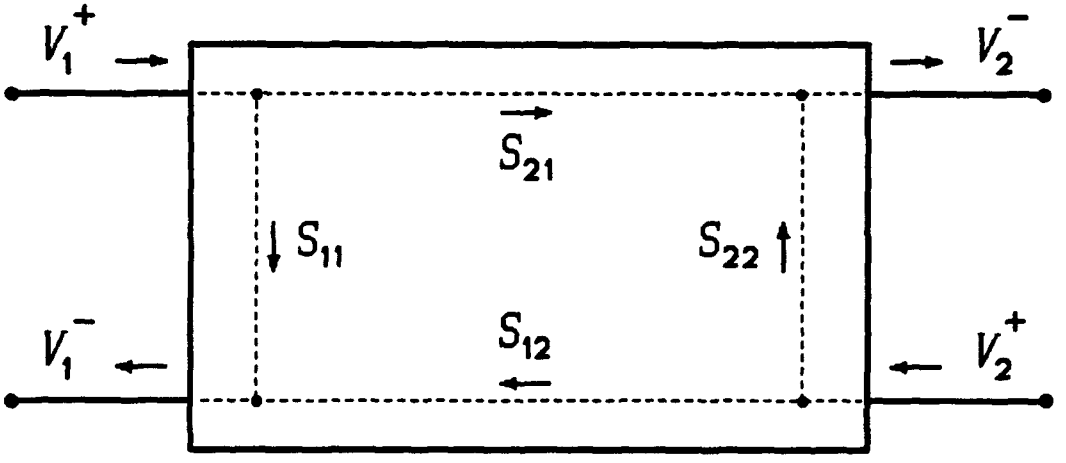

Figure 3.11 Two-port S-parameter flow graph [54:221]

incident signals are set to zero. This condition is satisfied simply by impedance matching. Matching a port to its characteristic impedance eliminates all reflections back on that port in the form of incident waves. Equation (3.33) defines the reflection coefficient of a transmission line in terms of its characteristic (Z_o) and load (Z_L) impedances.

$$\Gamma = \frac{Z_L - Z_o}{Z_L + Z_o} \tag{3.33}$$

When the load is matched ($Z_L = Z_o$), $\Gamma = 0$ independent of the length of the line and the frequency of operation. The accuracy and ease of impedance matching makes S-parameter measurements ideal for characterizing microwave devices over wide frequency ranges. The definitions of each of the four two-port S-parameters are given below [55:278]:

S_{11} = the input reflection coefficient with the output matched to Z_o,

S_{12} = the reverse transmission or feedback coefficient with the input matched to Z_o,

S_{21} = the forward transmission (gain or loss) coefficient with the output matched to Z_o,

S_{22} = the output reflection coefficient with the input matched to Z_o.

Because S-parameters are complex, they can be expressed in either rectangular ($a+jb$) or polar ($|M|\cdot\angle$) format. Typically, for graphical analysis, the reflection coefficients S_{11} and S_{22} are plotted on a Smith Chart, while the gains S_{12} and S_{21} are plotted on a polar graph.

As mentioned in the literature review, several authors have fit measured S-parameters to either the hybrid-π or T-model topology to determine the equivalent circuit element values. To perform such a fit, one needs to have an idea of what parasitics are physically significant.

Parameter extraction via curve-fitting, if the solution converges, will always determine element values which will produce the measured S-parameters. However, obtaining a physics-based small-signal model should be possible by estimating parasitic element values from the device materials, geometry, and fabrication process.

4. Methodology

The initial objective of this thesis effort was to develop a large-signal model of an HBT that would accurately predict the device's performance over its range of operation. As previously stated, this model is a physical model whose parameters are directly related to the device material, geometry, and fabrication process. Furthermore, this model was implemented in the readily available SPICE package. The obvious merits of such a model are its physical nature, its ease of use and straightforward derivation.

Given the large-signal equivalent circuit topology of Fig. 3.6, the first step was to calculate physics-based values for each of the corresponding model parameters of Table 3.1. Physical constants and equations that provided accurate values for each of the SPICE model parameters were researched. Knowledge of the device geometry was obtained from portions of the mask layout. Knowledge of the process was obtained from the wafer doping profile as well as through discussions with WL/ELRD. A detailed methodology on each area: material, geometry, and fabrication process follows.

4.1 Knowledge of Device Material

Throughout the model derivation several general constants were used which are shown in Table 4-1. Note again that the model does not consider thermal effects as T is constant at 300 K. The devices modeled were fabricated with an $Al_xGa_{1-x}As$ wide-gap emitter, a GaAs base and a GaAs collector. X is a variable which represents the mole fraction of aluminum within the ternary III-V compound, $Al_xGa_{1-x}As$. The compound is a direct-

Table 4-1

General Constants Used in Calculations

Parameter	Units	Description
$k = 8.61738 \times 10^{-5}$	$eV \cdot K^{-1}$	Boltzmann's constant
$q = 1.602 \times 10^{-19}$	C	Electron Charge
$\epsilon_o = 8.854 \times 10^{-14}$	$F \cdot cm^{-1}$	Permittivity in vacuum
$\mu_o = 4\pi \times 10^{-9}$	$H \cdot cm^{-1}$	Permeability in vacuum
$m_o = 9.1095 \times 10^{-31}$	Kg	Electron rest mass
$T = 300$	K	Absolute temperature

bandgap semiconductor in the range $0 \leq x \leq 0.45$. Consequently, HBTs are fabricated with $x \leq 0.45$ to avoid the phonon interaction associated with carrier generation-recombination in indirect-bandgap semiconductors. A typical value of x is 0.30; the value of x for each of the devices modeled is 0.35. The most significant effect of the Al is increasing the bandgap energy. Both the $Al_xGa_{1-x}As$ bandgap energy and permittivity are linear functions of x.

Because the GaAs base is so heavily doped, bandgap narrowing becomes significant. For example, at $N_A = 1 \times 10^{16}$ the narrowing is only 3.5 meV, while at $N_A = 5 \times 10^{19}$ the narrowing is 59 meV, which represents a 4.1% reduction in the GaAs intrinsic bandgap of 1.424 eV. As a result of this narrowing, the intrinsic carrier concentration in the base increases by a factor of three.

There are two other materials which play an important role in the model derivation: gold and polyimide. Gold is the metal used for the contacts and interconnects. Polyimide is the dielectric used to separate layers of metal on the wafer since GaAs does not have a stable native

oxide as does Si. Table 4.2 summarizes the material parameters and related expressions.

Another material parameter critical to model derivation is minority carrier mobility. Mobility is simply a proportionality constant relating carrier velocity to electric field. Physically, mobility is related to the mean time between collisions for a carrier, and is therefore affected by lattice and impurity scattering mechanisms [51]. Empirical expressions for electron and hole mobility in GaAs have been determined in the literature [53,56,57]. The fit for both carriers has the form of a Caughey-Thomas equation given by [58]:

$$\mu = \frac{\mu_{max} - \mu_{min}}{1 + \left(\frac{N}{N_{ref}}\right)^{\alpha}} + \mu_{min} \tag{4.1}$$

where μ_{max} and μ_{min} are maximum and minimum values of mobility for each type of carrier; N_{ref} and α are curve-fit constants. Table 4-3 lists mobility parameter values for both electrons and holes in GaAs. Given an impurity density of N, the mobility of electrons in p-type GaAs is assumed the same as the mobility of electrons in n-type GaAs [56].

Diffusivity is a material parameter that is a function of mobility and the Fermi-Dirac integrals [14:29]:

$$D_n = \mu_n\left(\frac{kT}{q}\right)\left[1 + 0.35355\left(\frac{n}{N_C}\right) - 9.9\times10^{-3}\left(\frac{n}{N_C}\right)^2 + 4.45\times10^{-4}\left(\frac{n}{N_C}\right)^3\right] \tag{4.2}$$

$$D_p = \mu_p\left(\frac{kT}{q}\right)\left[1 + 0.35355\left(\frac{p}{N_V}\right) - 9.9\times10^{-3}\left(\frac{p}{N_V}\right)^2 + 4.45\times10^{-4}\left(\frac{p}{N_V}\right)^3\right] \tag{4.3}$$

where n and p are the electron and hole concentrations (cm^{-3});

N_C is the effective density of states in the conduction band (cm^{-3});

Table 4-2(a)

Material Parameters and Expressions Used in Calculations

Expression	Units	Description
$E_{gGaAs} = 1.424$	eV	Bandgap energy of intrinsic GaAs
$N_{CB} = 4.7 \times 10^{17}$	cm^{-3}	Conduction band density of states in the GaAs base [14]
$N_{VB} = 7.0 \times 10^{18}$	cm^{-3}	Valence band density of states in the GaAs base [14]
$N_{CE} = 2.5 \times 10^{19} \cdot (0.067 + 0.083x)^{3/2}$	cm^{-3}	Conduction band density of states in the AlGaAs emitter for $0 \leq x \leq 0.45$ [48]
$N_{CE} = 2.5 \times 10^{19} \cdot (0.48 + 0.31x)^{3/2}$	cm^{-3}	Valence band density of states in the AlGaAs emitter for $0 \leq x \leq 0.45$ [48]
$n_{iGaAs} = 1.79 \times 10^{6}$	cm^{-3}	Intrinsic carrier concentration of GaAs
$\Delta E_{gB} = 1.6 \times 10^{-8}(N_B)^{1/3}$	eV	Bandgap narrowing in the GaAs base [56]
$n_{iB} = n_{iGaAs}\exp\left(\frac{\Delta E_{gB}}{kT}\right)^{1/2}$	cm^{-3}	Intrinsic carrier concentration in the GaAs base as a function of doping [56]
$E_{gE} = E_{gGaAs} + 1.247x$	eV	Bandgap energy of the AlGaAs emitter for $0 \leq x \leq 0.45$ [59]
$E_{gB} = E_{gGaAs} - \Delta E_{gB}$	eV	Bandgap energy of the GaAs base
$\Delta E = E_{gE} - E_{gB}$	eV	Bandgap difference between the emitter and base at the abrupt emitter-base heterojunction
$\Delta E_C = 0.797x$	eV	Difference in conduction band energy between emitter and base
$n_{iE} = n_{iB}\exp\left(\frac{\Delta E}{kT}\right)^{1/2}$	cm^{-3}	Intrinsic carrier concentration in the AlGaAs emitter [24]

Table 4-2(b)

Material Parameters and Expressions Used in Calculations

Expression	Units	Description
$\epsilon_{GaAs} = 13.18$	—	Relative permittivity of GaAs
$\epsilon_{AlGaAs} = \epsilon_{GaAs} - 3.12x$	—	Relative permittivity of the AlGaAs emitter for $0 \leq x \leq 0.45$ [59]
$\epsilon_E = \epsilon_{AlGaAs}\epsilon_o$	$F \cdot cm^{-1}$	Permittivity of the emitter
$\epsilon_B = \epsilon_{GaAs}\epsilon_o$	$F \cdot cm^{-1}$	Permittivity of the base
$\epsilon_p = 3.5\epsilon_o$	$F \cdot cm^{-1}$	Permittivity of polyimide
$v_{sat} = 1 \times 10^7$	$cm \cdot s^{-1}$	Electron saturation velocity in GaAs at 300 K
$\rho_{Au} = 2.44 \times 10^{-6}$	$\Omega \cdot cm$	Resistivity of gold metallization at 10 GHz [60]
$S_o = 1 \times 10^6$	$cm \cdot s^{-1}$	Surface recombination velocity for AlGaAs [32]
$L_s = 1 \times 10^{-5}$	cm	Surface diffusion length for AlGaAs

Table 4-3

Mobility Parameter Values for GaAs [53,56]

Parameter	Units	Electrons	Holes
μ_{max}	$cm^2 \cdot V^{-1} \cdot s^{-1}$	8000	400
μ_{min}	$cm^2 \cdot V^{-1} \cdot s^{-1}$	943	40
N_{ref}	cm^{-3}	2.84×10^{16}	2.5×10^{17}
α	—	0.753	0.417

N_V is the effective density of states in the valence band (cm^{-3}). The factor in brackets is the first four terms of the Fermi-Dirac integral expansion. For nondegenerate semiconductors, the carrier concentration is typically much less than the corresponding density of states. In this case, the term in the brackets is essentially unity and the resulting expression for diffusivity as a function of mobility is called the Einstein relationship. Note that diffusivity has the units of $cm^2 \cdot s^{-1}$, so q may be omitted if k has the units $eV \cdot K^{-1}$ as in Table 4-1. As seen in Eqs. (3.2)-(3.4), diffusivity is needed to calculate saturation currents and diffusion lengths.

Mobility can also be used to calculate the resistivity, ρ ($\Omega \cdot cm$), of a semiconductor [51:36]:

$$\rho_n = \frac{1}{qN_D\mu_n} \tag{4.4}$$

$$\rho_p = \frac{1}{qN_A\mu_p} \tag{4.5}$$

Currently, very little is known about mobility in $Al_xGa_{1-x}As$, which is a function of not only the impurity concentration but also of x. However, since no empirical curve-fit expressions could be found in the literature, carrier mobility in the emitter was estimated using the expressions for GaAs.

4.2 Knowledge of Device Geometry

The most common microwave transistor geometry is interdigitated where the emitter and base metallization fingers are interdigitated and the emitters are rectangular stripes. The HBTs modeled in this effort are unique because they have emitter dots rather than stripes. Consequently,

the expressions for calculating the three components of base resistance (Eqs. 3.16-3.19) had to be reconsidered for cylindrical geometry. Figure 4.1 shows the layout of one of the HBTs. In particular, the layout is a 3 micron emitter dot, 5 dot, 1 finger (3u5d1f) device. Actually, the emitter dots are approximately cylinders sitting on a base finger. This can be seen in Fig. 4.2 which is a side view cut along AB, where: w_{cl} is the width of the collector contact, d_{eb} is the vertical distance between the base and emitter metallizations, s_{bc} is the lateral spacing between the base and collector contacts, and d_{ec} is the vertical distance between the emitter bridge and the collector contact. The emitter-base dot dimensions for a general emitter diameter are shown in Fig. 4.3. This figure will be instrumental in calculating the base resistance.

Two geometry dependent parameters used to calculate several SPICE model parameter values are the base-emitter junction area, A_{be}, and the base-collector junction area, A_{bc}. The expressions for each area are clearly derived from Fig. 4.3 and given by:

$$A_{be} = N_{dot} N_{fin} \pi \left(\frac{l_{ee}}{2} - 0.1 \times 10^{-4} \right)^2 \tag{4.6}$$

$$A_{bc} = N_{dot} N_{fin} (l_{ee} + 2 \times 10^{-4})(2 l_{ee}) \tag{4.7}$$

where N_{dot} is the number of emitter dots per base finger;

N_{fin} is the number of base fingers;

l_{ee} is the diameter of each emitter dot, $l_{ee} = 2a_2$ (cm).

Notice that the radius of an emitter dot, a_2, (e.g. 3 microns) is not the radius of the base-emitter junction, a_1. Due to fabrication and lithography considerations, $a_2 - a_1$ is the contact spacing between the base and emitter contacts which is 0.1 microns for all the devices modeled.

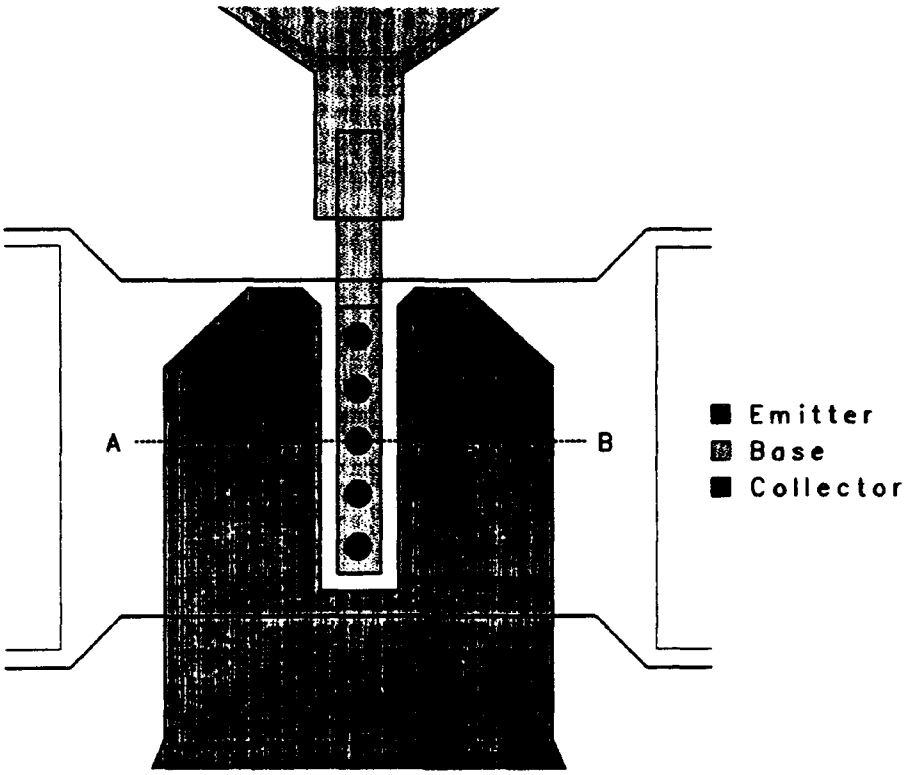

Figure 4.1 Mask layout of a 3u5d1f AlGaAs HBT [60].

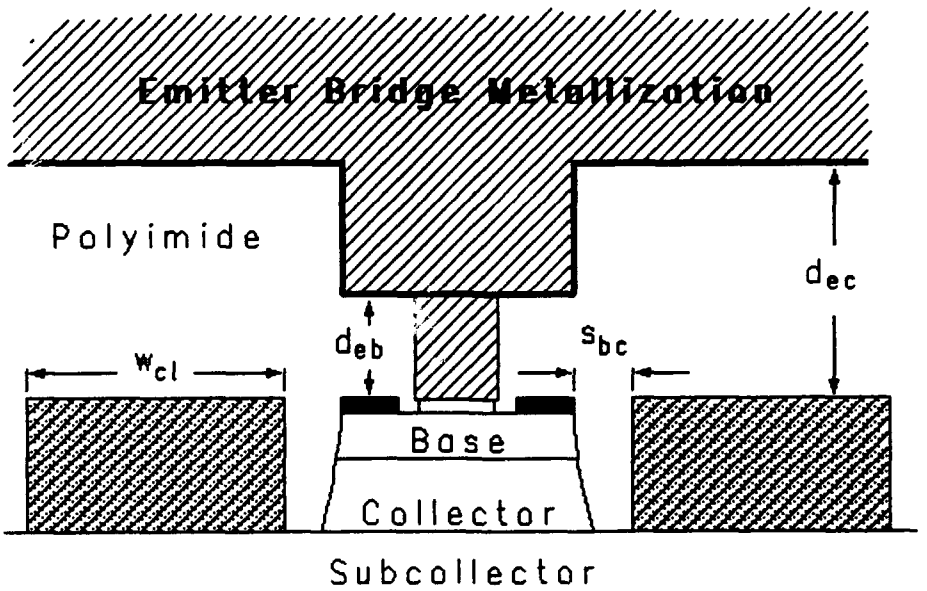

Figure 4.2 Lateral view of 3u5d1f HBT geometry.

4.3 Knowledge of the Fabrication Process

The first step in fabricating HBTs is to grow epitaxial layers onto a GaAs wafer. The layer doping profiles were designed by WL/ELR and grown by its supplier of epi-material, Epitronics. The doping profile in Table 4-4 shows the layer structure for one of the three devices modeled. The other two devices were fabricated to Table 4-4 with the following exceptions: the 3uldlf device has a collector doping concentration of 2×10^{16} cm^{-3}; the 2u6d2f device has a collector doping concentration of 1×10^{17} cm^{-3} and a collector thickness of 3.5×10^{-5} cm. The intrinsic AlGaAs buffer layer between the GaAs substrate and the GaAs subcollector serves primarily to minimize substrate leakage. The p-type base dopant is carbon.

Each of the devices modeled was fabricated via MOCVD so the base-emitter junction was unintentionally graded over approximately 150 Å or 1.5×10^{-6} cm. Assuming that this graded region is fully within the emitter, the conduction band spike of Fig. 3.1(b) is almost completely eliminated. The resulting metallurgical base-emitter junction can be treated as a homojunction where carrier flow is assumed to be by drift-diffusion. The presence of a spike causes thermionic emission of carriers and changes the standard *pn* products at the SCR boundaries [23,24,62]. Because the $Al_{0.35}Ga_{0.65}As$ emitter still exists beyond the grading, the effective bandgap difference, ΔE, calculated from Table 4-2 remains unchanged.

Another parameter that is dependent upon both the material and fabrication process is the specific contact resistance, ρ_c. For the devices fabricated by WL/ELR, there is a different ρ_c value for contacts to n-type and p-type semiconductors: $\rho_{cn} = 1 \times 10^{-6}$ $\Omega \cdot cm^2$ and

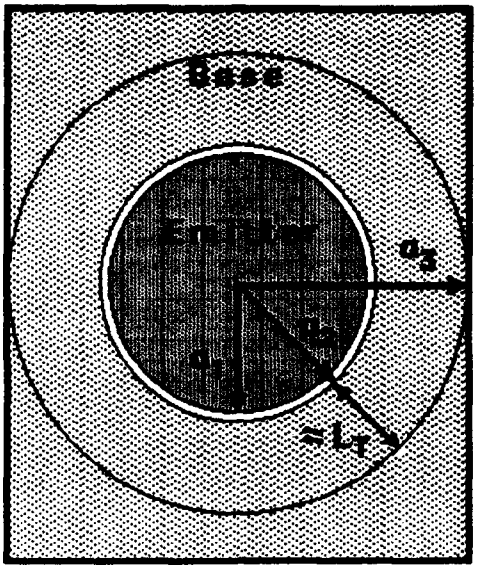

Figure 4.3 Top view of emitter and base contacts showing the dot geometry.

Table 4-4

Layer Doping Profile for 3u5dlf Device

Layer	x	Doping (cm^{-3})	Thickness (cm)
$In_xGa_{1-x}As$ cap	0.5	2×10^{19}	3×10^{-6}
$In_xGa_{1-x}As$ grading	0.5 → 0	1×10^{19}	2.5×10^{-6}
GaAs emitter	0	5×10^{18}	1×10^{-5}
$Al_xGa_{1-x}As$ grading	0 → 0.35	5×10^{17}	5×10^{-6}
$Al_xGa_{1-x}As$	0.35	5×10^{17}	5×10^{-6}
GaAs Base	0	5×10^{19}	7×10^{-6}
GaAs Collector	0	8×10^{15}	1×10^{-4}
GaAs Subcollector	0	3×10^{18}	1×10^{-4}
$Al_xGa_{1-x}As$ Buffer	0.3	—	3×10^{-5}
GaAs substrate	0	—	5×10^{-2}

$\rho_{cp} = 5 \times 10^{-6}\ \Omega \cdot cm^2$. Au was used to contact the emitter semiconductor, Au/Ge/Ni was used to contact the collector, and Ti/Pt/Au was used to contact the base semiconductor.

After determining the device's physical characteristics solely from its material, geometry and fabrication process, SPICE model parameters must be calculated to accurately predict the device's electrical characteristics. The following section describes the methods used to calculate each of the SPICE parameters of Table 3-1. These calculated parameters are not unique to SPICE and may be programmed in any device or circuit simulator that recognizes the Ebers-Moll or Gummel-Poon junction transistor equivalent circuit topology.

4.4 Determination of SPICE Model Parameters

A Mathcad 3.1 [38] program written to calculate all of the SPICE model parameters is included in Appendix A. This section will discuss more of the theory behind the various parameters as well as the methods of calculation.

4.4.1 Forward base transit time, TF. Physically, *TF* is the time required for minority carriers entering the neutral base from the emitter to diffuse across the base to the base-collector SCR. This parameter is derived in the literature [45,51,53,63]. However, there are three expressions for *TF* which have received widespread use.

The most elementary form assumes: 1) $I_E \approx I_C$, 2) $W_B/L_{nB} \leq 0.1$ [51:117], 3) the excess minority carrier concentration at the collector edge of the neutral base, $n_{pB}'(W_B) = 0$ [45:160], and 4) the base region is uniformly doped (no drift field). The first assumption states that whatever current diffuses into the base from the emitter must also drift

out of the base into the collector. The second and third assumptions state that the excess carrier concentration is linear with distance, and that the excess base charge, Q_B, has a triangular area under the concentration curve. The resulting expression for TF is given by:

$$TF = \frac{Q_B}{I_C} = \frac{W_B^2}{2D_{nB}} \tag{4.8}$$

where W_B is the effective base width, i.e., the value shown in Table 4-4 less the portions of depleted base at each junction.

Another derivation is similar to the previous with the exception that $n_{pB}'(W_B) \neq 0$ [53:208]. Instead, $n_{pB}'(W_B) = n_c$, the saturated velocity carrier concentration due to velocity overshoot across the base-collector SCR. This results in the expression for TF having an additional term as given by:

$$TF = \frac{W_B^2}{2D_{nB}} + \frac{W_B}{v_{sat}} \tag{4.9}$$

Clearly, the additional term becomes negligible for $W_B/v_{sat} \ll W_B^2/2D_{nB}$.

The final expression for TF is derived mainly in the context of microwave transistors. The difference is due to a phase shift forced upon the carriers as they diffuse across the base. The base transport factor, β^*, includes an imaginary term at microwave frequencies [63:1167]:

$$\beta^* = sech\left[\left(\frac{W_B}{L_{nB}}\right)^2 + j\omega TF\right]^{1/2} \tag{4.10}$$

Setting β^* equal to its -3 dB value one obtains:

$$TF = \frac{W_B^2}{2.43D_{nB}} \tag{4.11}$$

Note that the factor of 2.43 is for a transistor with no drift field in the base, that is, all current across the base is via diffusion [64,65]. One can readily see that the factor of 2.43 will increase as a base drift field is introduced since carriers will drift as well as diffuse across the base, thus reducing *TF*. Interestingly, Hooke also states that using a cosh to represent β^* will result in a factor of 2 instead of 2.43 for a uniformly doped base.

4.4.2 Maximum forward common-emitter current gain, BF.

β is defined mathematically by [51:127]:

$$\beta \equiv \frac{\Delta I_C}{\Delta I_B} = \frac{\alpha_F}{1 - \alpha_F} \tag{4.12}$$

$$\alpha_F \equiv \frac{I_{Cn}}{I_E} \tag{4.13}$$

where I_{Cn} is the current due to only electrons from the base into the collector. Therefore, α_F, the common-base current gain, is the percentage of total emitter current that makes it through the base after recombination.

Generally, transistors are designed with an emitter efficiency, γ, very close to unity. Assuming this to be the case for simplicity, the following expression for β results [51:128]:

$$\beta = \frac{2L_{nB}^2}{W_B^2} \tag{4.14}$$

If Eq. (4.8) is chosen as the correct expression for *TF*, then Eq. (4.14) may be restated in another widely accepted form:

$$\beta = \frac{\tau_{no}}{TF} \tag{4.15}$$

where τ_{no} is the minority electron lifetime in the base. Both of these expressions for β are approximations because they assume that the only significant source of base current is bulk base recombination [53:209]. In fact, Eqs. (4.14) and (4.15) overestimate β by as much as an order of magnitude. However, neither expression accounts for the increased emitter efficiency resulting from the base-emitter heterojunction bandgap difference.

In Si BJTs, the emitter is doped much more heavily than the base to improve efficiency (See Fig. 1.2). This ensures that a few orders of magnitude more electrons enter the base from the emitter than holes enter the emitter from the base. Device designers of HBTs are not constrained to dope the base less than the emitter to achieve this same objective. As can be shown from Kroemer's wide-gap emitter theory [17], the base of an HBT may be doped two or three orders of magnitude more heavily than the emitter. This has a tremendous impact on device performance, primarily in decreasing parasitic base resistance, RB, increasing the unity current gain cutoff frequency, f_T, and increasing the maximum frequency of oscillation, f_{max}.

Although W. Shockley first conceptualized the HBT [19], H. Kroemer can be considered the father of the HBT for his early theoretical papers [17,18]. An Npn HBT band diagram with associated currents is shown in Fig. 4.4 where:

I_r is the electron current lost to bulk recombination;

I_s is the electron current lost to SCR recombination;

I_p is the hole current injected from the base into the emitter;

I_n is the electron current injected from the emitter into the base.

The following derivation for β_{max} of an HBT is taken from Kroemer [17]:

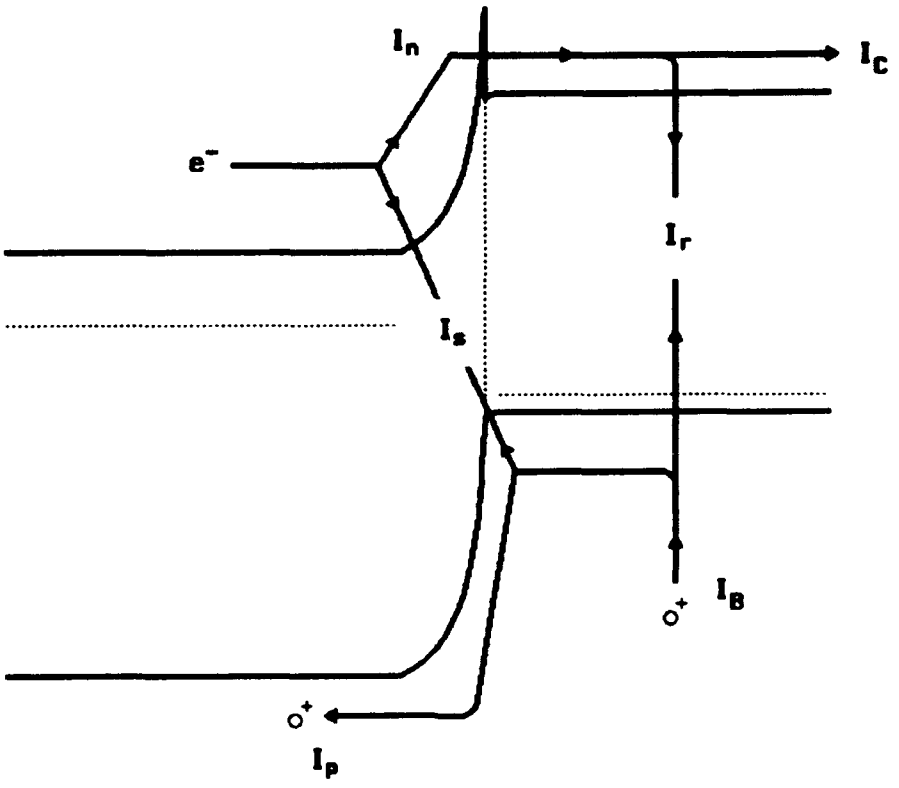

Figure 4.4 Energy bandgap diagram of a forward-biased Npn AlGaAs/GaAs HBT showing current components. [17:15].

$$\beta = \frac{I_C}{I_B} = \frac{I_n - I_r}{I_p + I_s + I_r} < \frac{I_n}{I_p} = \beta_{max} \tag{4.16}$$

where β_{max} is the current gain assuming all recombination currents go to zero. Equations (3.1) and (3.2) can be used to solve for β_{max}:

$$I_n = \frac{qA D_{nB} n_{oB}}{L_{nB}} \left[\exp\left(\frac{qV}{kT}\right) - 1\right] \tag{4.17}$$

$$I_p = \frac{qA D_{pE} p_{oE}}{L_{pE}} \left[\exp\left(\frac{qV}{kT}\right) - 1\right] \tag{4.18}$$

$$\beta_{max} = \frac{I_n}{I_p} = \frac{D_{nB}}{L_{nB}} \cdot \frac{D_{pE}}{L_{pE}} \cdot \frac{n_{oB}}{p_{oE}} \tag{4.19}$$

The mass action law definition, expressions for carrier average diffusion velocity definition, and expressions for intrinsic carrier concentrations in terms of the effective density of states [51:19] can be substituted into Eq. (4.19). Equation (4.26) is the resulting expression for β_{max}.

$$n_{oB} = \frac{n_{iB}^2}{N_B} \tag{4.20}$$

$$p_{oE} = \frac{n_{iE}^2}{N_E} \tag{4.21}$$

$$v_{nB} = \frac{D_{nB}}{L_{nB}} \tag{4.22}$$

$$v_{pE} = \frac{D_{pE}}{L_{pE}} \tag{4.23}$$

$$n_{iE}^2 = N_{CE} N_{VE} \exp\left(\frac{-E_{gE}}{kT}\right) \tag{4.24}$$

$$n_{iB}^2 = N_{CB} N_{VB} \exp\left(\frac{-E_{gB}}{kT}\right) \tag{4.25}$$

$$\beta_{max} = \frac{v_{nB}}{v_{pE}} \cdot \frac{N_E}{N_B} \cdot \frac{N_{CB} N_{VB}}{N_{CE} N_{VE}} \cdot \exp\left(\frac{E_{gE} - E_{gB}}{kT}\right) \tag{4.26}$$

Clearly, for a homojunction device, $E_{gE} = E_{gB}$ and the exponential factor is unity. This result shows that Si BJTs must have the emitter doped much more than the base to achieve a practical β. However, consider an HBT in which the bandgap difference between the emitter and base is a nominal 200 meV. The corresponding *BF* will be more than three orders of magnitude larger than *BF* for the Si BJT given the same base and emitter dopings. Because AlGaAs/GaAs HBTs suffer more from parasitic base recombination currents than do Si BJTs, practical current gains do not share the same

wide margin over BJTs. Nevertheless, the example shows the control that the bandgap difference has on the maximum common-emitter current gain.

4.4.3 Minority carrier lifetime in the base, τ_{no}. Although τ_{no} is not a SPICE model parameter, it is needed in the calculations of the model's saturation currents. τ_{no} is the average length of time an excess minority electron can exist in the p-type base before recombining.

The three main types of recombination in which a minority electron in p-type GaAs can participate are Shockley-Read-Hall (SRH), radiative and Auger recombination. An expression for τ_{no} at low-injection is given by [57:698]:

$$\tau_{no} = \left(\frac{1}{\tau_{SRH}} + \frac{1}{\tau_{Aug}} + \frac{1}{\tau_{rad}} \right)^{-1} \tag{4.27}$$

$$\frac{1}{\tau_{SRH}} = \sigma_n v_{th} N_t \tag{4.28}$$

$$\frac{1}{\tau_{Aug}} = A_p N_B^2 \tag{4.29}$$

$$\frac{1}{\tau_{rad}} = B_n N_B \tag{4.30}$$

$$v_{th} = \left(\frac{8kT}{\pi m_n} \right)^{1/2} \tag{4.31}$$

where σ_n is the electron capture cross section (cm^2);

v_{th} is the average thermal velocity for an electron, $v_{th} = 1.04 \times 10^7$ $cm \cdot s^{-1}$;

m_n is the effective mass of an electron in GaAs, $m_n = 0.067 m_o$;

N_t is the concentration of recombination centers in the base (cm^{-3});

A_p is the Auger recombination coefficient, $A_p \simeq 1 \times 10^{-30}$ $cm^6 \cdot s^{-1}$;

B_n is the radiative recombination coefficient, $B_n = 2 \times 10^{-10}$ $cm^3 \cdot s^{-1}$.

One problem associated with using Eq. (4.28) is the wide range of σ_n values reported in the literature [23,51,52]. The capture cross section of an electron should be dependent only on the material, yet differences up to three orders of magnitude are reported. Additionally, N_t is very process dependent and can easily change by up to two orders of magnitude. Despite the fact that further work needs to be done to characterize the lifetime of excess minority electrons in heavily doped p-type GaAs, the value provided by Eq. (4.27) is not without merit.

Using liberal values in Eq. (4.28), $\sigma_n = 1 \times 10^{-14}$ cm^2 and $N_t = 1 \times 10^{14}$ cm^{-3} [52], the individual recombination lifetimes for the devices modeled are listed in Table 4-5.

Table 4-5

Calculated Values for Minority Electron Bulk Base Recombination Lifetimes

Component	Lifetime (s)
Shockley-Read-Hall	9.623×10^{-8}
Auger	4×10^{-10}
Radiative	1×10^{-10}
Total	7.993×10^{-11}

Clearly, radiative recombination dominates at this base doping density. The SRH lifetime is nearly three orders of magnitude larger than the radiative lifetime. Even if the SRH lifetime was reduced by two orders of magnitude, in an attempt to account for worst case σ_n and N_t values, the total lifetime, τ_{no}, would still be dominated by radiative recombination at a value of 7.386×10^{-11} s. Thus, such a large change in non-dominating SRH lifetime reduces the total lifetime by only 7.6%.

Assuming that the value of τ_{no} listed in Table 4-5 is accurate, a physical value of *BF* may be estimated by substituting Eq. (3.3) into Eq. (4.14). As expected, the resulting *BF* was two to three times the value determined from measured I-V data. The explanation, given earlier, is that Eq. (4.14) only considers bulk base recombination. Empirical β_F clearly depends on surface, emitter-base SCR, and heterointerface recombination (in abrupt HBTs) currents as well. Each of these other parasitic components will serve to reduce the value of *BF* calculated by Eq. (4.14) closer to the empirical value. The value of *BF* used in the SPICE BJT model card is neither a theoretical maximum, nor an empirical value, but rather the β due only to bulk base recombination [25].

Having accepted Eq. (4.27) to calculate τ_{no}, the excess minority hole lifetime in the collector, τ_{po}, needs to be determined. Because the collector is doped much less than the base, τ_{po} is expected to be much longer than τ_{no}. The literature has minimal research on lifetimes of holes in n-type GaAs. Lundstrom *et al.* [57:700] show that $\tau_{po} \approx 20$ ns for $N_D \leq 1 \times 10^{18}$ cm^{-3}. Since the highest value of collector doping, N_C, in the devices modeled is 1×10^{17} cm^{-3}, $\tau_{po} = 20$ ns was used in the calculations.

The diffusivity values determined from Eqs. (4.2) and (4.3), along with the values of τ_{no} and τ_{po}, can be substituted into Eqs. (3.3) and (3.4) to obtain minority carrier diffusion lengths, L_{nB} and L_{pC}. The diffusion length is a characteristic length defining the distance minority carriers must diffuse into a semiconductor to have a density of e^{-1} or approximately 37% of their junction density. The exponential decay is obviously due to recombination. The diffusion length (cm) of minority holes in the AlGaAs emitter, L_{pE}, is calculated from the empirical expression [23:876]:

$$L_{pE} = \frac{42.46 - \log N_E}{9.21 \times 10^3}. \tag{4.32}$$

4.4.4 Leakage saturation currents, ISE and ISC. Because the two leakage saturation currents are really the recombination saturation currents associated with the recombination diodes I_3 and I_4, they cannot be calculated from Eq. (3.2). Equation (3.2) is a junction saturation current that characterizes the ideal drift-diffusion transport of carriers. Each component of recombination current in a junction transistor results from some type of trap or state that facilitates the capture or emission of carriers. An expression for each component invariably comes from the following integral [66]

$$I_{rec} = qA\int_{x_1}^{x_2} U dx \tag{4.33}$$

where U is the recombination rate ($cm^{-3} \cdot s^{-1}$);

x_1 and x_2 are the boundaries between which recombination is expected to occur (cm).

Recall from the literature review that Ryum and Abdel-Motaleb [23] and Parikh and Lindholm [24] derived expressions for HBT terminal currents including all pertinent recombination components. Although these models are not immediately implemented in any commercial circuit simulator such as SPICE, they can be adapted to fit the SPICE expressions for I_B and I_C seen in Eqs. (3.25) and (3.26).

SPICE combines the effects of all recombination currents into two diodes, one for each junction. *ISE* is the composite recombination saturation current for leakage dependent on $V_{B'E'}$ while *ISC* is the saturation current for leakage dependent on $V_{B'C'}$. Thus, *ISE* and *ISC* are

simply the sums of the individual recombination saturation currents. The components considered in the devices modeled were neutral base, both SCR, and base-emitter surface recombination currents. Heterointerface recombination was not considered, since with a graded emitter the metallurgical junction is GaAs/GaAs and the number of interface states is negligible. Expressions for each component may be found in the Mathcad 3.1 file in Appendix A.

4.4.5 Transport saturation current, IS and reverse parameters, BR and TR. The expression for *IS* is given by [67]

$$IS = \frac{qA_{be} n_{iB}^2 D_{nB}}{W_B N_B} \tag{4.34}$$

The base-collector junction saturation current, I_{CS}, is determined by

$$I_{CS} = qA_{bc}\left(\frac{D_{nB} n_{iB}^2}{L_{nB} N_B} + \frac{D_{pC} n_{iC}^2}{L_{pC} N_C}\right). \tag{4.35}$$

Next, α_R, the reverse common-base current gain was found using the reciprocity theorem [45]: $\alpha_R = IS/I_{CS}$. α_R was then used to calculate the reverse common-emitter current gain, *BR*, using the form of Eq. (4.12). One way to conceptualize *BR* is to swap the emitter and collector, then follow Kroemer's derivation. The result is a homojunction where the base is doped two to three orders of magnitude more than the emitter. As expected from Eq. (4.26), $BR < 1$. Assuming τ_{no} is the same regardless of whether the electrons are coming from the emitter or collector, Eq. (4.15) may now be used to estimate, the reverse base transit time, *TR*.

4.4.6 Junction grading factors, MJE and MJC. As mentioned in Section 4.3, each of the HBTs modeled were grown epitaxially via MOCVD. Despite the unintentional grading of each junction the modeled devices

were characterized with a junction grading factor of 0.5 since they may be considered only slightly graded.

4.4.7 Built-in junction voltages, VJE and VJC. The emitter-base built-in voltage, *VJE*, was calculated from Eq. (3.10). Similarly, the base-collector built-in voltage, *VJC*, was calculated from Eq. (3.6).

4.4.8 Zero-bias depletion capacitances, CJE and CJC. Substituting Eqs. (3.8) and (3.9) into Eq. (3.12) when $V_{BE} = 0$, results in the emitter-base heterojunction zero-bias depletion capacitance, *CJE*. Similarly, substituting Eq. (3.5) into Eq. (3.11) when $V = V_{BC} = 0$, results in *CJC*.

4.4.9 Internal capacitance ratio, XCJC. *XCJC* defines the portion of the bias-dependent base-collector depletion capacitance, C_{jc}, that is internal to the device (i.e., beneath the base-emitter junction). This model parameter allows C_{jc} to be distributed across the base series resistance, RB, for more accurate modeling. Obviously, for a dc simulation *XCJC* would be meaningless, since all capacitors are open circuits. However, for an ac small-signal or S-parameter analysis, the total base-collector depletion capacitance is split into two parts: one capacitance, *cbcdep*, from the internal collector to the internal base node and another, *cbcx*, distributed across the base resistance as shown in Fig. 4.5. The equations which SPICE solves internally for these small-signal equivalent circuit capacitors are [39]

$$cbcdep = XCJC \cdot CJC\left(1 - \frac{V_{B'C'}}{VJC}\right)^{-MJC} \qquad (4.36)$$

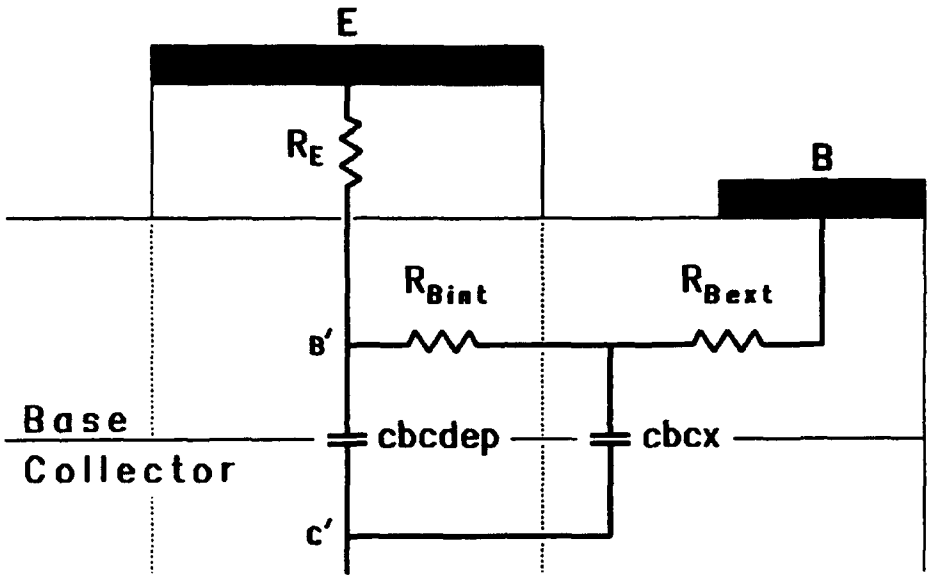

Figure 4.5 Lateral view of HBT showing the base–collector depletion capacitance distributed across the base series resistance.

$$cbcx = (1 - XCJC) \cdot CJC\left(1 - \frac{vbcx}{VJC}\right)^{-MJC} \tag{4.37}$$

$$XCJC = \frac{A_{be}}{A_{bc}} \tag{4.38}$$

where *vbcx* is the externally distributed base–collector junction voltage.

4.4.10 Emitter series resistance, RE. The emitter series resistance was estimated using Eqs. (3.15) and (3.16). Using the specific contact resistance for n–type contacts, $\rho_{cn} = 1 \times 10^{-6}\ \Omega \cdot cm^2$, and the value of A_{be} calculated from Eq. (4.6), the contact resistance component of RE was estimated. As seen in Fig. 3.3, a second component of RE is bulk resistance. However, recall from Table 4–4 that the emitter is actually five distinct n–type semiconductor layers. The resistivity of each layer was approximated using Eq. (4.4). This method ignores the effects of grading both In and Al into GaAs since the empirical mobility of electrons in GaAs from Eq. (4.1) was used in Eq. (4.4). This approximation is valid

primarily because each of the five layers is relatively thin. Also, a higher mobility will result in a lower resistivity. Since it is known that intrinsic $In_{0.53}Ga_{0.47}As$ has a mobility approximately 1.6 times intrinsic GaAs [15:384], one can reasonably assume this method of determining RE may slightly overestimate the resistivity of the layers containing In. However, since little to no empirical data exists on the mobility of AlGaAs, assuming the mobility of AlGaAs is less than the mobility of GaAs, one can reason that the resistivity of the layers containing Al is slightly underestimated. As calculated, RE is dominated by contact resistance, which for the 2u6d2f device was 96.5% of the total resistance.

4.4.11 Base series resistance, RB. The three components of RB for a rectangular geometry were shown in Fig. 3.3. and calculated from Eqs. (3.16) - (3.19). Taking the concepts from Fig. 3.3 and applying them to the cylindrical geometry of Fig. 4.3, one can see that RB has the same three components.

R_{sp} is contributed by the disk of base material beneath the emitter contact. This value is independent of the emitter dot radius and is given by [68:215]

$$R_{sp} = \frac{R_{Bsh}}{8\pi} \tag{4.39}$$

where R_{Bsh} is the base region sheet resistance, $R_{Bsh} = \rho/t$ $(\Omega/\square)$.

R_{bulk} is due to the thin white annular region in Fig. 4.3 and is easily shown to be described by

$$R_{bulk} = \frac{R_{Bsh}}{2\pi} \ln\left(\frac{a_2}{a_1}\right) \tag{4.40}$$

R_{1c} is the resistance due to the radial base current entering the region beneath the base contact and leaving normal to the contact. The base contact outer perimeter is rectangular; however, since most of the current will enter the contact within a radial distance L_T of its front edge [69:392], the base contact can be approximated by an annular region with inner radius a_2, and outer radius a_3. The expression for lateral contact resistance in which current enters the inner radius, a_2, of an annular contact with outer radius a_3, is given by [70]

$$R_{1c} = \frac{R_{Bsh} L_T}{2\pi a_2} \left[\frac{K_1\left(\frac{a_3}{L_T}\right) I_0\left(\frac{a_2}{L_T}\right) + I_1\left(\frac{a_3}{L_T}\right) K_0\left(\frac{a_2}{L_T}\right)}{I_1\left(\frac{a_3}{L_T}\right) K_1\left(\frac{a_2}{L_T}\right) + K_1\left(\frac{a_3}{L_T}\right) I_1\left(\frac{a_2}{L_T}\right)} \right] \tag{4.41}$$

$$L_T = \left(\frac{\rho_{cp}}{R_{Bsh}}\right)^{1/2} \tag{4.42}$$

where I_0 and K_0 are zero-order modified Bessel functions of the first and second kind; I_1 and K_1 are first-order modified Bessel functions of the first and second kind. Equations (4.39)-(4.42) are valid for a single emitter dot; therefore, since all dots are in parallel, the total base resistance is found by dividing the single dot value by the total number of dots in the device geometry.

4.4.12 Collector series resistance, RC. The collector current spreads and moves through the subcollector layer in the same way that the base current moves through the base layer. Consequently, RC has the same three components as RB including an additional bulk resistance in the collector layer, R_{Cbulk}. R_{Cbulk} is very bias dependent; when the transistor is operated in the active region, the collector is fully

depleted and does not contribute to the series resistance. However, when the transistor is saturated, almost the entire collector region is resistive.

Essentially, the only current in the collector region is due to the electrons that have diffused through the base directly beneath the emitter contact. Because the emitter dots are relatively small, the collector cross-sectional area can be approximated by a square with side length equal to the dot diameter, l_{ee}. This approximation allows RC to be calculated entirely with rectangular geometry.

4.4.13 Ideality factors, NF, NR, NE, and NC. Ideality factors or emission coefficients describe the kT-like dependence of current on junction voltage. Because of the base-collector homojunction, the reverse ideality factor, *NR* is assumed to be 1.0. *NF* describes the forward drift-diffusion of carriers across the base-emitter junction and is expected lie between 1.0 and 1.2. The strong influence of base-emitter SCR and surface recombination, which have a $2kT$-like dependence, cause *NE* to be close to 2.0. Similarly, *NC* is expected to lie between 1.5 and 2.0. The ideality factors are the only model parameters that have an exponential effect on model data. Even a third decimal place deviation in *NE* or *NF* can produce a noticeable change in the I-V characteristics so a good guess value is usually inadequate for good agreement. For this reason each of the three unknown ideality factors was curve fit to measured data using HSPICE optimization.

4.4.14 Corner for high current β_F degradation, IKF. This model parameter is used to characterize the degradation of β_F at high collector currents. An approximate expression for *IKF* is given by

$$IKF = qA_{be}N_C v_{sat} \tag{4.43}$$

This expression identifies the critical (collector) current obtained when the concentration of carriers crossing the reverse biased base-collector junction approaches the concentration of mobile charge carriers in the collector, N_C.

4.5 SPICE dc Simulation

While seeking to determine the most accurate values for the SPICE HBT model parameters, a SPICE testbench was written that would provide a set of I-V curves. Annotated HSPICE files for the three devices modeled are included in Appendix B. I-V curves for an npn junction transistor consist of I_C against V_{CE} for various discrete values of I_B. To obtain this data the SPICE testbench required a voltage source, Vce, a current source, Ib, a source resistance, Rsrc, and a BJT element, Q1. The $1 \times 10^{2\mu}$ Ω source resistance was placed in parallel with the current source to facilitate convergence and to ensure that all of Ib entered the base. The SPICE dc testbench circuit is shown in Fig. 4.6.

Next, using the SPICE *.dc* statement, a dc simulation was run using a nested sweep of both Vce and Ib. Vce was swept with enough resolution to generate a curve over the range of interest and Ib was incremented to match the measured data. During the simulation, data was printed to the screen using the *.print dc* statement. Columns of data for Vce, Vbe, Ib, and Ic were saved to an ASCII data file. The initial simulations used model parameter data consolidated from Rockwell [71:33] and TRW [26:2126] HBTs. These parameters were replaced as physics-based values of the parameters that described WL/ELR's HBTs were calculated. Throughout the model derivation process, interim model data was compared to measured

data. Differences between the two were noted and sensitivity analyses were run to determine which SPICE model parameters had the largest impact on minimizing the difference. Often, manual curve-fit values were obtained via trial-and-error. Once good agreement was obtained, the curve-fit parameters were examined to see if there was possibly a physical basis to substantiate the new value. Several iterations of the Mathcad program were required to develop physics-based parameter values that provided consistently good agreement for all three devices modeled.

4.6 SPICE ac Simulation

The first step in a SPICE ac analysis is to provide a dc bias to the HBT element. This is done by choosing specific values for Vce and Ib in the active region corresponding to the bias points of measured S-parameters. Network ports then need to be defined using the *.net* statement whose syntax is [40]

.net output input ROUT = val2 RIN = val1

where ***input*** is the ac input voltage or current source name;

output is the output port defined by a voltage between two nodes, an output current, or element current;

ROUT is the output or load resistance with value ***val2***;

RIN is the input or source resistance with value ***val1***.

In the common-emitter configuration, the input port may be defined by Ib, and the output port by i(Vce), the output collector current, as shown in Fig. 4.7. Given both ports defined by currents, HSPICE initially calculates the H matrix and converts the *h*-parameters to whatever metric is desired: *z*-, *y*-, *g*-, or *s*-parameters.

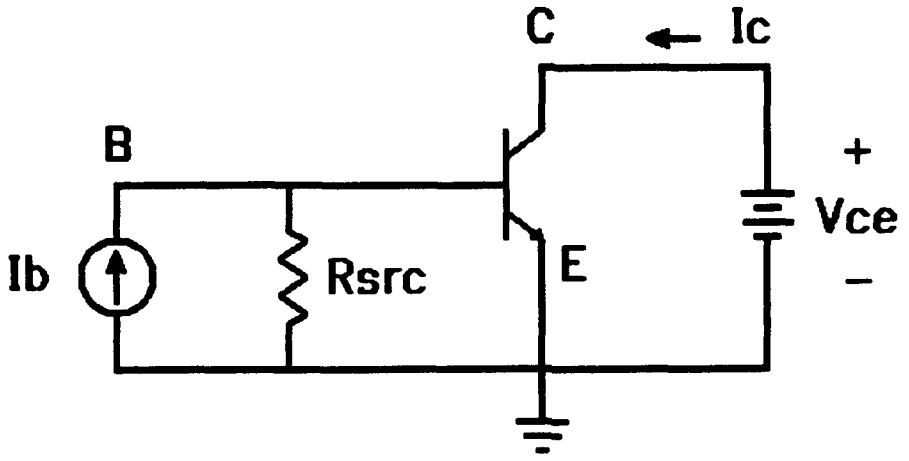

Figure 4.6 SPICE junction transistor dc testbench.

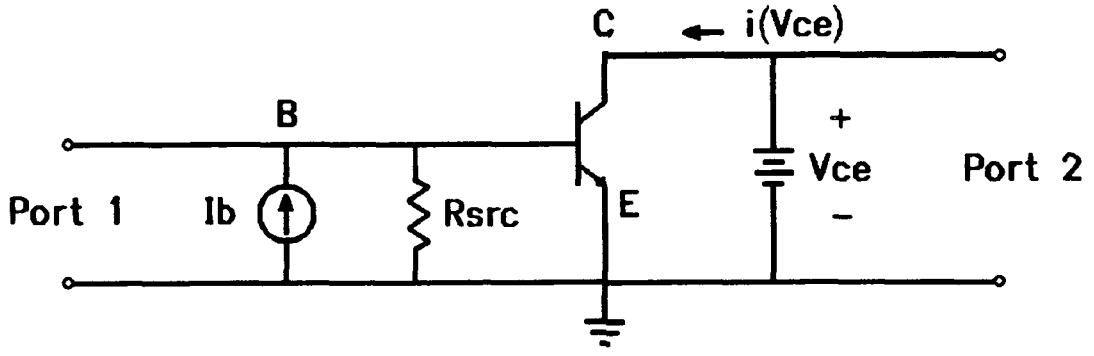

Figure 4.7 SPICE junction transistor ac testbench.

The *.ac* statement performs the ac analysis and has many options. For the purpose of this model, a 50 point linear sweep of frequency from 1 GHz to 50 GHz was conducted. HSPICE linearizes the dc circuit of Fig. 3.6 by solving Eqs. (3.27)-(3.30). The resulting hybrid-π equivalent circuit is shown in Fig. 4.8. A script of the ac simulation in which all small-signal element values are calculated may be found in Appendix B. HSPICE automatically isolates the dc and ac sources during an ac simulation by shorting all the dc voltage sources and opening all the dc current sources.

Similar to the dc analysis, using the *.print ac* statement, data was printed to the screen and saved to a file. The data saved were the four S-parameters in polar form ($|M|\cdot\angle$). Saving the data in polar form was necessary to avoid subsequent conversion because the analysis software, Axum, requires the data in polar form to accurately plot. Since the measured S-parameters provided by WL/ELR were in rectangular form ($a+jb$), they had to be converted to polar form in Axum.

4.7 Adding Parasitics to the Small-signal Equivalent Circuit

An incremental section of transmission line can be represented by a lumped-element equivalent circuit comprised of a series resistance and inductance and a shunt conductance and capacitance. Considering the microwave operation of the HBT, modeling the device with a lumped series inductor on each terminal is logical. Similarly, a capacitor shunting each pair of nodes is also common in the literature [31,72,73]. The resulting small-signal hybrid-π equivalent circuit having three parasitic capacitors and three parasitic inductors is shown in Fig. 4.9.

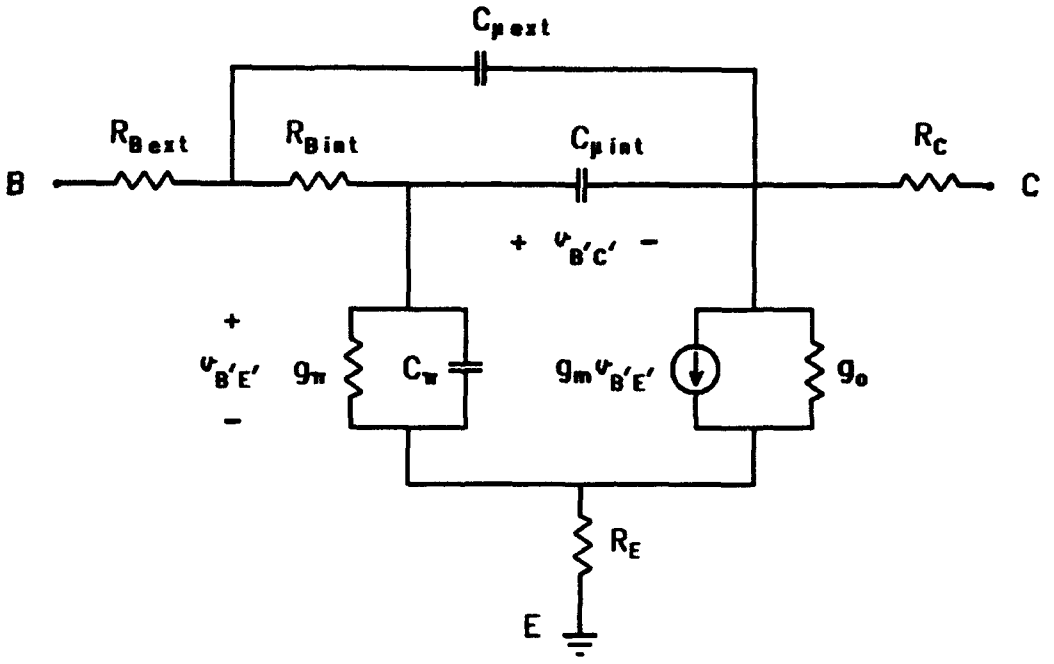

Figure 4.8 HSPICE hybrid-π small-signal equivalent circuit with base-collector depletion capacitance distributed across the base resistance.

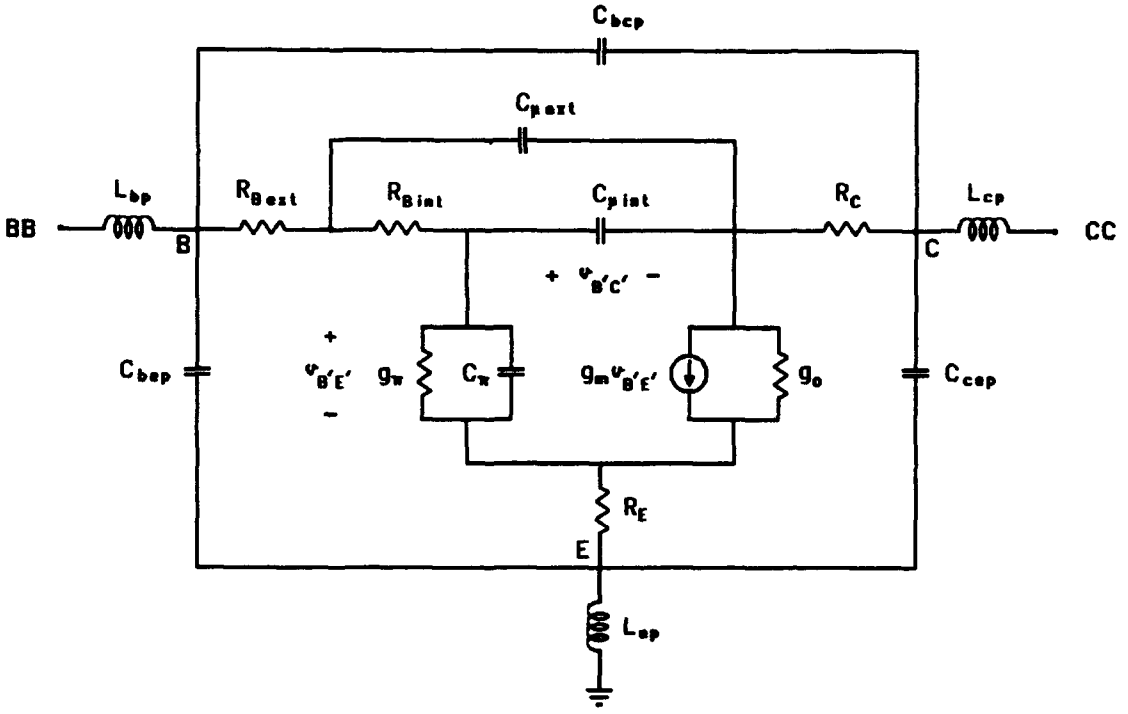

Figure 4.9 Small-signal hybrid-π equivalent circuit complete with parasitic elements.

Most of the geometry variables used in the parasitic calculations were obtained from a large layout of the device, similar to Fig. 4.1. For the devices modeled, the width of the base finger is always two microns wider than the diameter of the emitter dot. Consequently, the width of the base finger was a convenient metric from which to determine all other geometry parameters using a ruler appropriately scaled for maximum accuracy.

Determining where parasitics need to be considered is important when the device geometry consists of probe pads. The probe pads for each of the devices modeled are coplanar and were designed for an impedance of 50 Ω. Thus, the pads themselves do not contribute any parasitic reactance or susceptance; only the interconnects and contacts need to be considered.

The resistance typically in series with each inductance is the resistance of the metal interconnects due to the finite resistivity of Au. At microwave frequencies this resistance may be calculated as [60:146]

$$R = \frac{\rho_{Au} L}{3 m t W} \tag{4.44}$$

where ρ_{Au} has the value shown in Table 4-2;

L is the length of the metal strip in the direction of current (cm);

t is the thickness of the metal strip (cm);

W is the width of the metal strip (cm);

m is the number of identical strip fingers in parallel.

This resistance was found to be up to two orders of magnitude smaller than the terminal series resistances (RE, RB, and RC) and was therefore neglected.

The total inductance of any geometry is the sum of its internal and external inductances [74:246]. The internal inductance per unit length of

a wire is simply $L_{int} = \mu/8\pi$ (H) [74:247], where μ is the permeability of the wire, which for non-magnetic materials is essentially μ_o from Table 4-1. When two conductors are nearby each other, as in the case of a planar transmission line, external inductance typically dominates and may be approximated by [60:99]

$$L_{ext} = \frac{\mu_o d L}{m W} \tag{4.45}$$

where d is the separation between the two planar conductors (cm).

Recall the geometry of Figs. 4.1 and 4.2 and consider the parasitic collector inductance, L_{cp}. The collector metallization and the emitter bridge can be approximated as a section of planar transmission line in the region where they overlap (i.e., beneath the emitter bridge). Using Eq. (4.45), L_{cp} may be estimated by substituting d_{ec} for d and w_{c1} for W. For the 3u5d1f device, $m = 2$ since there are two collector fingers. L is the length of each finger beneath the emitter bridge (or approximately the width of the bridge).

The parasitic base inductance, L_{bp}, can be similarly estimated. One must remember that inductances add in series and look for ways to simplify the geometry such that Eq. (4.45) may be used. Figure 4.10 represents the base contact of a single dot. Notice that for each dot the base metal can be approximated by two strips of width w_{bb} and length $l_{ee}/2$ in series with the parallel combination of two strips of width l_{eb} and length l_{ee}. This configuration of base metal can be approximated as a section of planar transmission line separated from the emitter bridge by a distance d_{eb}. L_{bp} can now be easily estimated by calculating the inductance of a single dot, multiplying this amount by the number of dots per finger and dividing by the number of base fingers in the geometry.

The parasitic emitter inductance, L_{ep} can be estimated by the parallel combination of L_{cp} and L_{bp}. The reason for this is that emitter is common to both L_{cp} and L_{bp} (i.e., the emitter bridge is one of the planar conductors contributing to L_{cp} and L_{bp}). Therefore, both L_{cp} and L_{bp} are parallel components of L_{ep}.

The parasitic capacitance can be estimated using the classic expression for the static capacitance of a parallel plate geometry, $C = \epsilon A/d$. This formula holds since for $A = WL$, $W \geq L \geq d$ in all cases for the devices modeled. The same variables used to characterize the collector inductance can be used to estimate the collector–emitter parasitic capacitance, C_{cep}. A is the area of the collector metallization beneath the emitter bridge, d_{ec} is the distance between the two parallel plates, and ϵ is the permittivity of polyimide.

Estimating the base–emitter parasitic capacitance, C_{bep}, is simpler than estimating L_{bp}. A is the area of just the base metal which is approximately $A_{bc} - A_{be}$. Obviously, d is d_{eb} from Fig. 4.2. One can also notice from Fig. 4.2 that a cylinder of emitter metal connects the bridge to the emitter semiconductor. The capacitance contribution due to this emitter post has not been considered. This additional component of C_{bep} is expected to cause the actual base–emitter parasitic capacitance to be at least two times larger than the calculated parallel plate C_{bep}. Actually, same emitter trench and posts were not considered in the estimate of C_{cep}. Thus, one would expect C_{cep} to be similarly underestimated by at least a factor of two. The point is that there are more parasitic capacitance components than just the simple parallel plate approximations. Although such contributions are known to exist, physically calculating these additional contributions is non-trivial.

When considering C_{bcp}, the base-collector interelectrode capacitance, there is no interconnect or pad overlap. This results in a fringing capacitance. A key expression in calculating this fringing capacitance is given by [75]:

$$\kappa = \left[\frac{(L + L_{so} + L_o)L_{so}}{(L + L_{so})(L_o + L_{so})}\right] \tag{4.46}$$

where the variables are defined in Fig. 4.11. The complete expression and variables involved in this interelectrode fringing capacitance are included in the Mathcad file in Appendix A. The assumption is that both conductors lie in the same plane. The simplifications of the base metal shown in Fig. 4.10 are also key to estimating C_{bcp}. s_{bc} from Fig. 4.2 is equivalent to L_{so} for all components of fringing C_{bcp}. The base-collector capacitance of a single dot is calculated and multiplied by the total number of dots in the geometry since capacitors add in parallel.

Logically, one might also contemplate a parasitic resistance associated with the interconnects. This resistance, in parallel with the associated parasitic capacitance, would model any current leakage between the base and collector terminals to ground. Using the classic resistance formula

$$R_{leak} = \frac{\rho L}{tW} \tag{4.47}$$

where ρ is the resistivity of intrinsic GaAs, $\rho \simeq 1 \times 10^6\ \Omega\cdot$cm; L and W are the same order of magnitude; t is the depth of the leakage current into the substrate, $t \ll 1$ cm. Clearly then, $R_{leak} \gg 10^6\ \Omega$.

Model calculated S-parameters were collected at multiple bias points for each device via HSPICE ac simulations for two different equivalent circuit configurations: Fig. 4.8 (the bare model without the parasitic

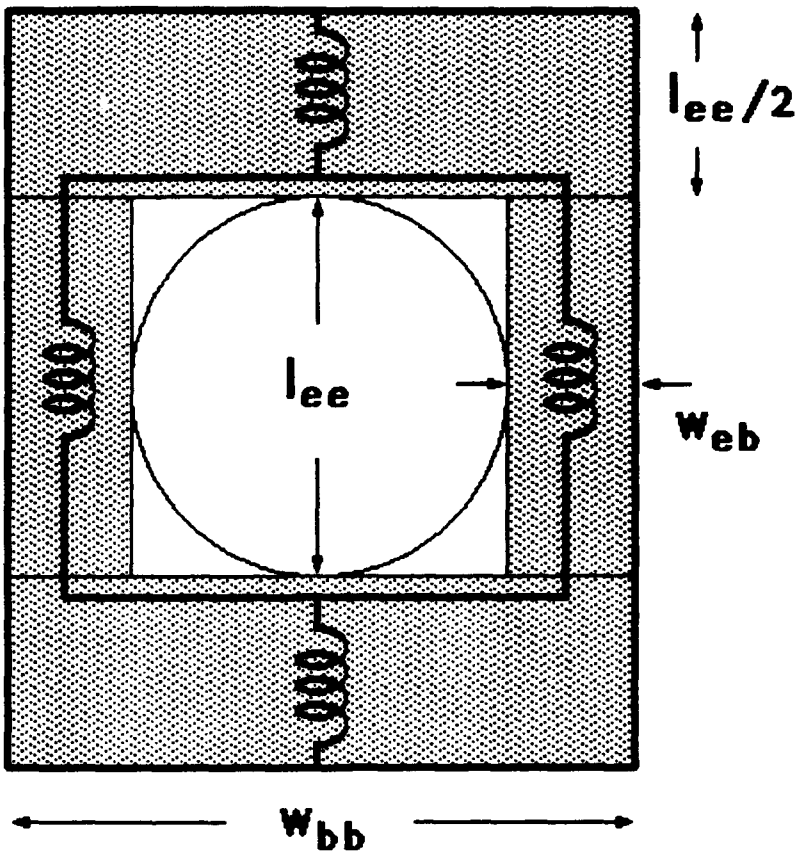

Figure 4.10 Top-view of the simplified base metallization geometry for a single emitter dot.

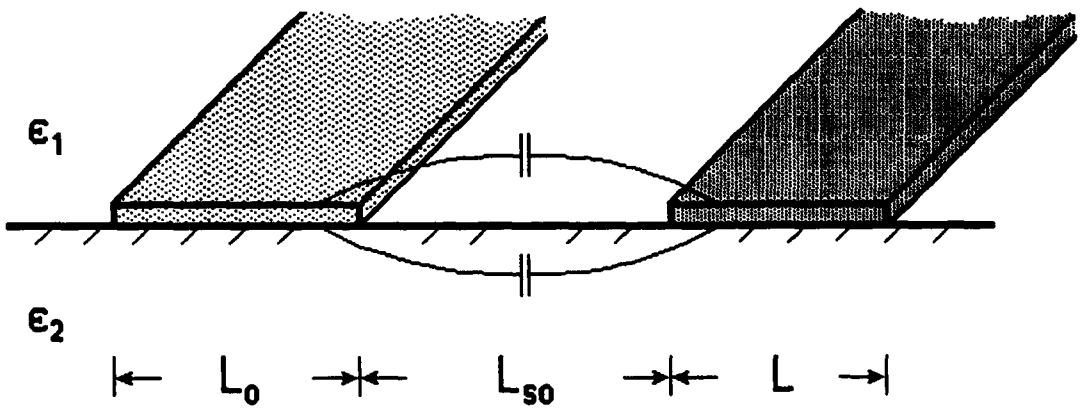

Figure 4.11 Annotated diagram of fringing capacitance between two conductors lying in the same plane.

elements) and Fig. 4.9 (the full model with all six parasitic elements). Each of these sets of model data were then plotted against the corresponding measured data.

5. Results and Discussion

In this chapter, modeled data from HSPICE simulations are compared to measured data provided by WL/ELRD. The dc and microwave results are presented in separate sections. In either case, a review of the physical significance of each model parameter is provided along with a sensitivity analysis. The sensitivity analysis shows how the model's electrical characteristics (I-V curves and S-parameters) are affected by the various HSPICE model parameters. This analysis is useful not only in providing insight into model physics but also for optimizing device designs. Model parameters can be modified to obtain a desired device characteristic. Information regarding the device material, geometry, and fabrication can then be determined from the resulting model parameters by working the model derivation process backward.

The data comparison is accomplished by plotting modeled and measured data on the same axes for each of the three devices. Additionally, the percent difference of representative sets of data points is presented. This information is used to quantify the model's accuracy as well as qualify areas where the model needs improvement. Each section closes with a discussion of the results. Table 5-1 lists the definitions used to qualitatively describe both the dc and microwave performance of the model. The percentages represent the average magnitude of the percent difference between modeled and measured data. These definitions are reasonable for a physics-based model and will be used consistently throughout this chapter.

Table 5-1

Definitions for Qualitative Model Performance

Average |Percent Difference|	Agreement Qualifier
$\|\Delta\%\| \leq 2.5\%$	Excellent
$2.5\% < \|\Delta\%\| \leq 5\%$	Very Good
$5\% < \|\Delta\%\| \leq 15\%$	Good
$15\% < \|\Delta\%\| \leq 25\%$	Fair
$25\% \leq \|\Delta\%\|$	Poor

5.1 DC Results

The DC steady-state model is fully characterized by Eqs. (3.25) and (3.26), which are the HSPICE expressions for the collector and base terminal currents, respectively. For convenience, these equations are restated here:

$$I_C = \frac{IS}{qb}\left[\exp\left(\frac{V_{B'E'}}{NF \cdot V_T}\right) - \exp\left(\frac{V_{B'C'}}{NR \cdot V_T}\right)\right] - \frac{IS}{BR}\left[\exp\left(\frac{V_{B'C'}}{NR \cdot V_T}\right) - 1\right]$$

$$- ISC\left[\exp\left(\frac{V_{B'C'}}{NC \cdot V_T}\right) - 1\right] \qquad (5.1)$$

$$I_B = \frac{IS}{BF}\left[\exp\left(\frac{V_{B'E'}}{NF \cdot V_T}\right) - 1\right] + \frac{IS}{BR}\left[\exp\left(\frac{V_{B'C'}}{NR \cdot V_T}\right) - 1\right] + ISE\left[\exp\left(\frac{V_{B'E'}}{NE \cdot V_T}\right) - 1\right]$$

$$+ ISC\left[\exp\left(\frac{V_{B'C'}}{NC \cdot V_T}\right) - 1\right] \qquad (5.2)$$

The model parameters that affect the dc characteristics are the saturation currents (*IS*, *ISE*, and *ISC*), the ideality factors (*NF*, *NR*, *NE*, and *NC*), the series resistances (RE, RB, and RC), and the common-emitter current gains (*BF* and *BR*). Notice that a factor of *qb* has been added to the denominator of the first term in Eq. (5.1). *qb* results from the Gummel-Poon model and has a default value of unity in the SPICE BJT model.

Although neglected in the dc model derivation of Chapter 3, *qb* can have a significant effect on the agreement with measured data. The HSPICE expressions for qb are

$$qb = \frac{q_1}{2}\left[1 + (1 + 4q_2)^{1/2}\right] \tag{5.3}$$

$$q_1 = \left(1 - \frac{V_{B'C'}}{VAF} - \frac{V_{B'E'}}{VAR}\right)^{-1} \tag{5.4}$$

$$q_2 = \frac{ISE}{IKF}\left[\exp\left(\frac{V_{B'E'}}{NF \cdot V_T}\right) - 1\right] + \frac{ISC}{IKR}\left[\exp\left(\frac{V_{B'C'}}{NR \cdot V_T}\right) - 1\right] \tag{5.5}$$

where *VAF* and *VAR* are the forward and reverse early voltages (V);

IKF and *IKR* are the forward and reverse high-level injection, β degradation currents (A).

The early voltages are metrics for base-width modulation where I_C increases with increasing V_{CE}. However, since the base of a typical HBT is doped much more heavily than either the emitter or collector, base-width modulation is negligible and q_1 becomes unity. *IKF* is a parameter that characterizes the high current degradation of β_F due to the high-level injection of carriers from the base into the emitter. Because of the high current densities obtainable with HBTs, base pushout (also called the Kirk effect), is a common phenomena. The Kirk effect causes the effective base width to increase, thereby decreasing β_F. The Kirk effect can be modeled with *IKF* or included in the four recombination parameters: *ISE*, *ISC*, *NE*, and *NC*. The Kirk effect was not significant in the one finger devices and was modeled with the recombination parameters in the two finger device.

Because common-emitter I-V characteristics were the only dc measurements obtained on the three devices modeled, only common-emitter

I-V characteristic sensitivities to HSPICE model parameters will be discussed. The additional usefulness of Gummel plot sensitivities will be addressed in the next chapter.

The series resistances, though not shown in Eqs (5.1) and (5.2), directly influence the junction voltages, $V_{B'E'}$ and $V_{B'C'}$. Both RE and RC affect the slope of the I-V curves in saturation. While in saturation, an increase in RC means a higher V_{CE} needs to be applied to maintain the same I_C. The transistor will remain in saturation at higher V_{CE} (a decreased slope) since more voltage is dropped across a larger resistor, decreasing the voltage seen by the internal collector node, $V_{C'}$. Finally, the active mode is reached when the base-collector junction becomes reverse biased ($V_{C'} > V_{B'}$).

A similar scenario occurs when RE is increased. Given a constant I_B for each curve, to maintain the same I_C, the potential at $V_{E'}$ must increase due to the increased voltage drop across RE. Consequently, the input voltage V_{BE} must increase to maintain the same $V_{B'E'}$. Kirchhoff's voltage law then demands that the output voltage V_{CE} also increase resulting in a lower slope through saturation. The slope is more sensitive to changes in RE and decreases linearly with increasing RC or RE.

RB had no effect on the I-V curves. Since I_B is a constant for each curve, any change in RB results in a corresponding change in V_{BE} necessary to maintain the proper $V_{B'E'}$ and $V_{B'C'}$ relationship. The only effect that a change in RB had on the terminal characteristics of the simulated model was a change in V_{BE}, the applied input voltage. As expected, V_{BE} changed proportionally with RB.

5.1.1 3u1d1f and 3u5d1f Device dc Results. The 3u1d1f and 3u5d1f devices have regions of nearly constant current gain as shown in

Figs. 5.1 and 5.2. For each device, a linear regression of the top six empirical data points shows that β_F is nearly constant at the value indicated by the regression line. Using this value of β_F in the model card for *BF* will produce I-V curves that agree well for all except the lowest I_B curves. This is because recombination currents, which degrade β_F, are the most noticeable at low bias. *ISE*, *ISC*, *NE*, and *NC* are necessary to model any bias dependence of β_F, including an HBT's offset voltage bias dependence. However, because the 3uldlf and 3u5dlf devices have a region where β_F is nearly constant, a more simple model that accounts for recombination using a constant empirical *BF* was developed.

The comparison between modeled and measured common-emitter I-V characteristics for the 3uldlf device is shown in Figs. 5.3 and 5.4. The model parameters were calculated with the Mathcad 3.1 program in Appendix A. The HSPICE dc testbench used to generate the modeled data is in Appendix B. The set of HSPICE BJT dc parameters used to generate the model data of Figs. 5.3 and 5.4 is shown in Table 5-2.

As mentioned in Chapter 4, *NR* was assumed to be unity. Although HSPICE was not used to optimize any model parameters, *BR* and *NF* were manually fit to best match the measured data. First, *BR* was chosen small enough to provide very good agreement in the reverse active region. Next, *NF* was chosen to best match the two sets of data in the saturation region and at the offset voltage. For models that account for recombination with an empirical *BF*, increasing *NF* shifts the set of I-V curves to the right, and decreasing shifts the curves to the left. *NR* and *BR* have the reverse effect on the set of I-V curves. Increasing each of these parameters will shift the curves to the left. Naturally, the curves are more sensitive to changes in *NF* and *NR* because of the exponential dependence.

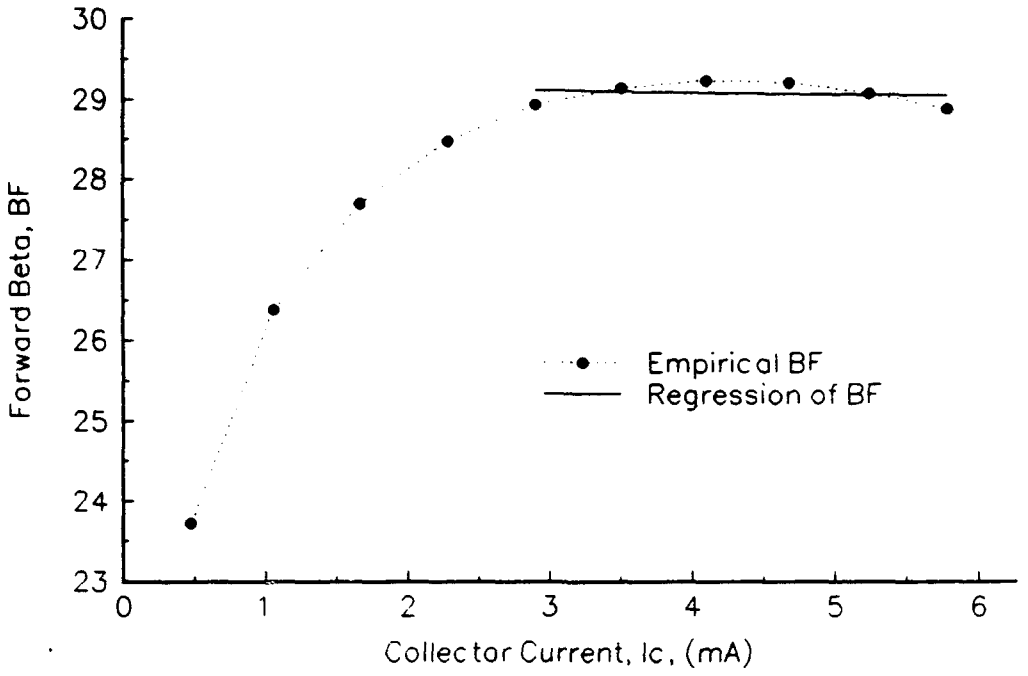

Figure 5.1 Plot of BF versus I_C with linear regression showing region of nearly constant BF for the 3u1d1f device.

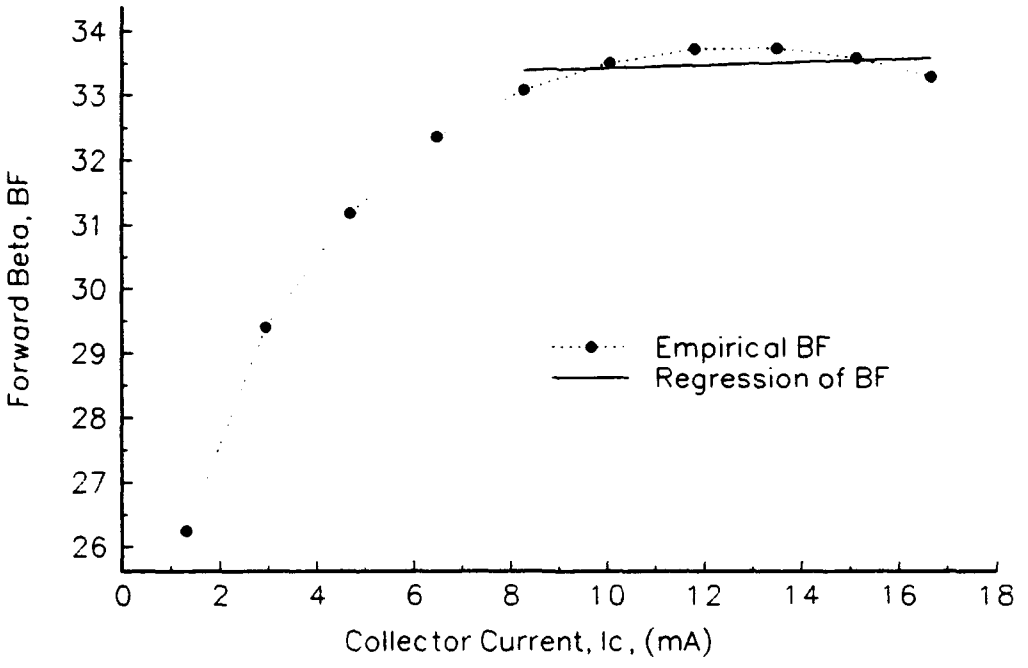

Figure 5.2 Plot of BF versus I_C with linear regression showing region of nearly constant BF for the 3u5d1f device.

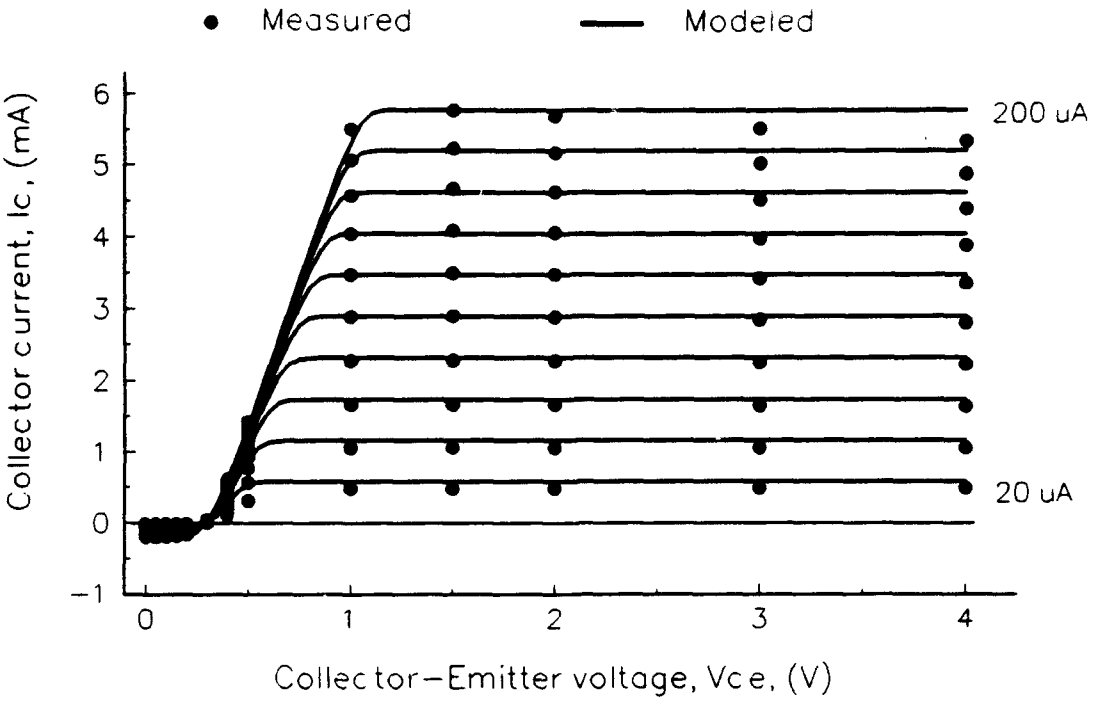

Figure 5.3 I-V characteristics for the 3uldlf device with I_B swept in 20 μA increments.

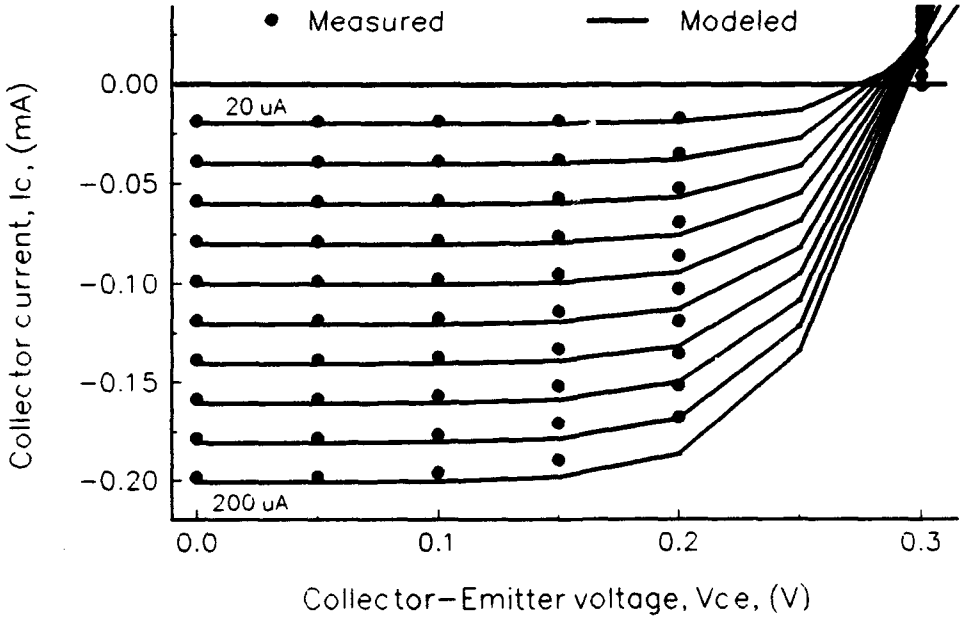

Figure 5.4 Reverse I-V characteristics for the 3uldlf device with I_B swept in 20 μA increments.

The specific contact resistance for n-type contacts, ρ_{cn}, was estimated at $1 \times 10^{-6}\ \Omega \cdot cm^2$. The actual value is dependent on process variations and could vary by a factor of two in either direction. The value used by Mathcad to calculate RE and RC for all three devices modeled was $2 \times 10^{-6}\ \Omega \cdot cm^2$, only because this value tended to provide better agreement on S_{21} at the lower frequencies.

The 3uldlf device has very good agreement in the forward and reverse active regions and good to poor agreement in saturation depending on the degree of saturation. In saturation, the modeled curves do not quite have the same variable slope as the measured curves do. This observation may be related to the bias dependence of RC. Increasing RC has been shown to decrease the slope of each I-V curve. However, HSPICE does not consider that the actual value of RC changes with $V_{B'C'}$. To do this, HSPICE would require information on the doping and thickness of the collector layer. Instead, HSPICE regards RC as a constant. Thus, the slopes of all the curves change by the same amount when RC is changed (i.e., independent of bias). Carrier recombination is another phenomenon that effects the slopes of the curves in saturation, but only at low bias. If a sufficient number of data points were recorded, the measured curves for the few lowest I_B values would show a distinctly lower slope than the corresponding modeled curves. This is due to recombination hindering a faster rise in I_C at the lower bias levels. This bias dependence is not modeled by the constant empirical *BF*; therefore, the modeled curves have steeper, bias insensitive slopes.

Another bias dependence not accounted for with the constant empirical *BF* is that of the offset voltage. The offset voltage of the modeled curves increases with increasing bias. The proper relationship

has offset voltage inversely proportional to bias [26]. The model's inability to accurately model the bias dependent offset voltage results in poor agreement at V_{CE} = 0.3 V for both the 3uldlf and 3u5dlf devices. This is because the interpolated measured offset voltages occur in the range of 0.285 to 0.3 V. The small collector current magnitudes at V_{CE} = 0.3 V intensify the percent differences.

The same modeling procedure was performed on the 3u5dlf device and the resulting model parameters are listed in Table 5-3. The ensuing I-V characteristics are shown in Figs. 5.5 and 5.6. Because the emitter dot diameter is the same for both the one dot and five dot devices, RE and RB for the 3u5dlf device are exactly one fifth of the respective 3uldlf values. This is because each of the dots are in parallel RC has a more complex geometry dependence, but is approximately one fifth of the 3uldlf value for the same reason. The 3u5dlf saturation current is larger than the value calculated for the 3uldlf device primarily due to the larger junction areas.

Once again, the effects of device self-heating are readily seen in the highest four curves at $V_{CE} \geq 3$ volts. In fact, the top curve (I_B = 500 μA) is effected almost immediately after entering the forward active region. Like the 3uldlf device, the 3u5dlf device model slightly overestimates the active region collector current for the lowest four curves (50 $\mu A \leq I_B \leq 200$ μA). This is due to the model having a constant β_F that was chosen to match the near constant empirical β_F of the highest six curves (250 $\mu A \leq I_B \leq 500$ μA).

Overall, the physics-based models for the 3uldlf and 3u5dlf devices provide very good agreement with the measured data. Plots of the average magnitude of the percent difference between modeled and measured data

Table 5-2

3u1d1f SPICE BJT dc Model Parameters

Parameter	Units	Value Used in HSPICE BJT Model Card
BF	-	83.541
BR	-	0.1512
NF	-	1.1121
NR	-	1.0000
ISE	A	default 0
ISC	A	default 0
IS	A	2.2345×10^{-26}
RE	Ω	33.6707
RB	Ω	43.2846
RC	Ω	68.713

Table 5-3

3u5d1f SPICE BJT dc Model Parameters

Parameter	Units	Value Used in HSPICE BJT Model Card
BF	-	83.429
BR	-	0.0569
NF	-	1.1393
NR	-	1.0000
ISE	A	default 0
ISC	A	default 0
IS	A	1.1169×10^{-25}
RE	Ω	6.7341
RB	Ω	8.6569
RC	Ω	16.785

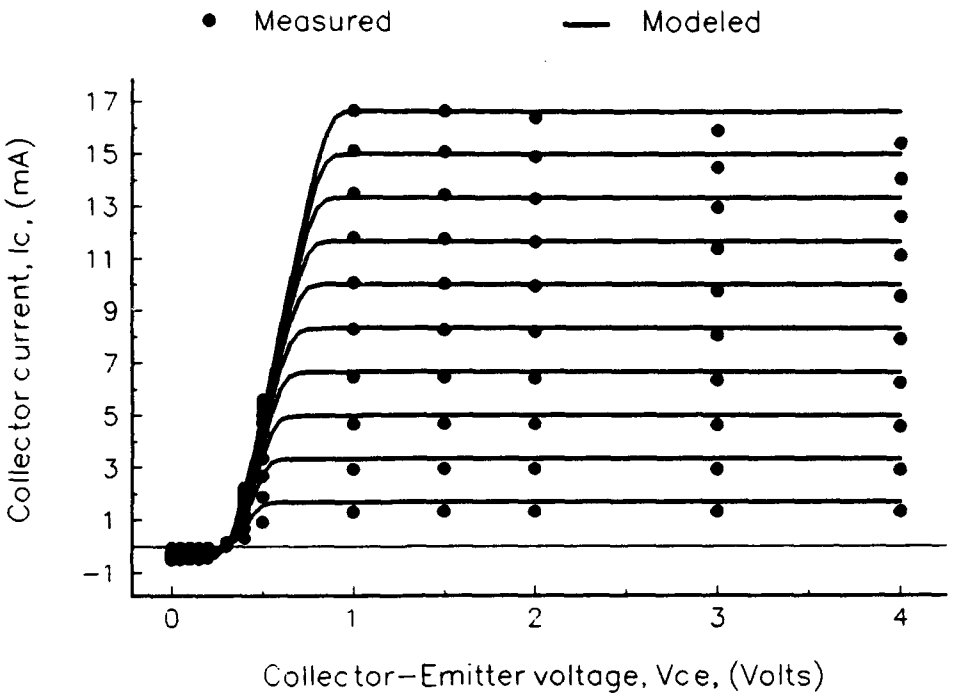

Figure 5.5 I–V characteristics for the 3u5d1f device with I_B swept in 50 μA increments.

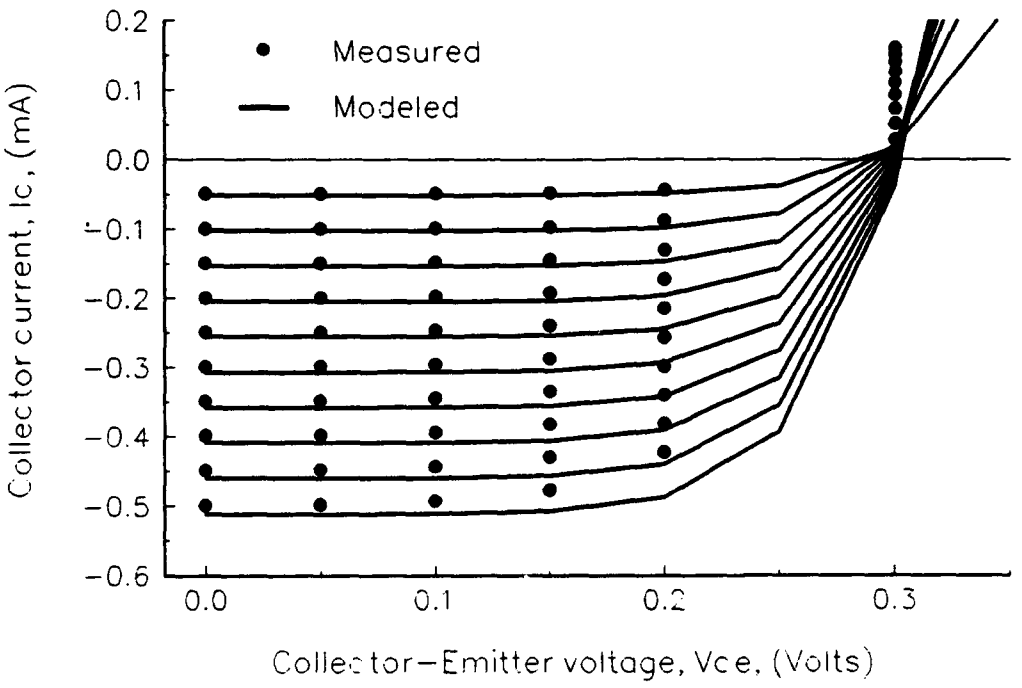

Figure 5.6 Reverse I–V characteristics for the 3u5d1f device with I_B swept in 50 μA increments.

points for each of the devices are shown in Figs. 5.7 and 5.8. Each bar indicates how far the modeled I_C value (theory) is from the measured value (actual) at each measured point averaged over all the constant I_B curves. The cluster of bars on both graphs represents data at V_{CE} = 0, 0.05, 0.1, 0.15, and 0.2 V. The data presented quantifies the performance of the model.

The 3uldlf model overestimates I_C by less than 4% in the reverse active region, (0, 0.05, and 0.1 V). Good agreement is maintained as the device leaves the reverse active region and begins to enter saturation (0.15 and 0.2 V). The approximate 60, 21, and 15% differences (occurring at 0.3, 0.4, and 0.5 V, respectively) are due to difficulties matching a variable slope in the saturation region. Thus, inaccuracies in modeling the bias dependence of RC and recombination result in fair to poor agreement in the saturation region. The largest difference of 60% at 0.3 V is due to the offset voltage increasing with bias rather than decreasing with bias as the measured curves do. Even though the offset voltages for the model and actual device are within the same range of V_{CE}, the actual and modeled offsets on average do not coincide within the range.

Very good agreement is obtained in the forward active region (1, 1.5, and 2 V) with a difference of less than 5%. The overestimation at the two highest V_{CE} values (3 and 4 V) is due to transistor self-heating which reduces the measured I_C values.

The 3u5dlf dc model performs just as well as the 3uldlf model. In the reverse active region (0, 0.05, and 0.1 V), the model overestimates I_C an average of less than 5%. When the device begins to enter saturation (0.15 and 0.2 V), the model maintains good agreement. Similar to the

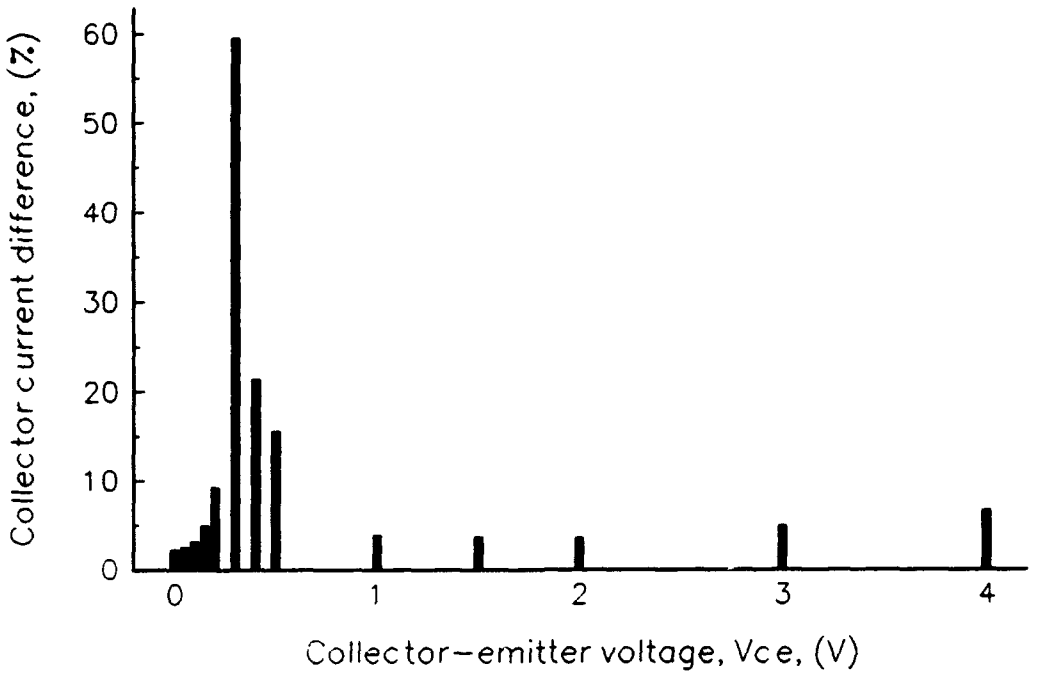

Figure 5.7 Magnitude of the percent difference between modeled and measured I_C averaged over all ten I_B curves.

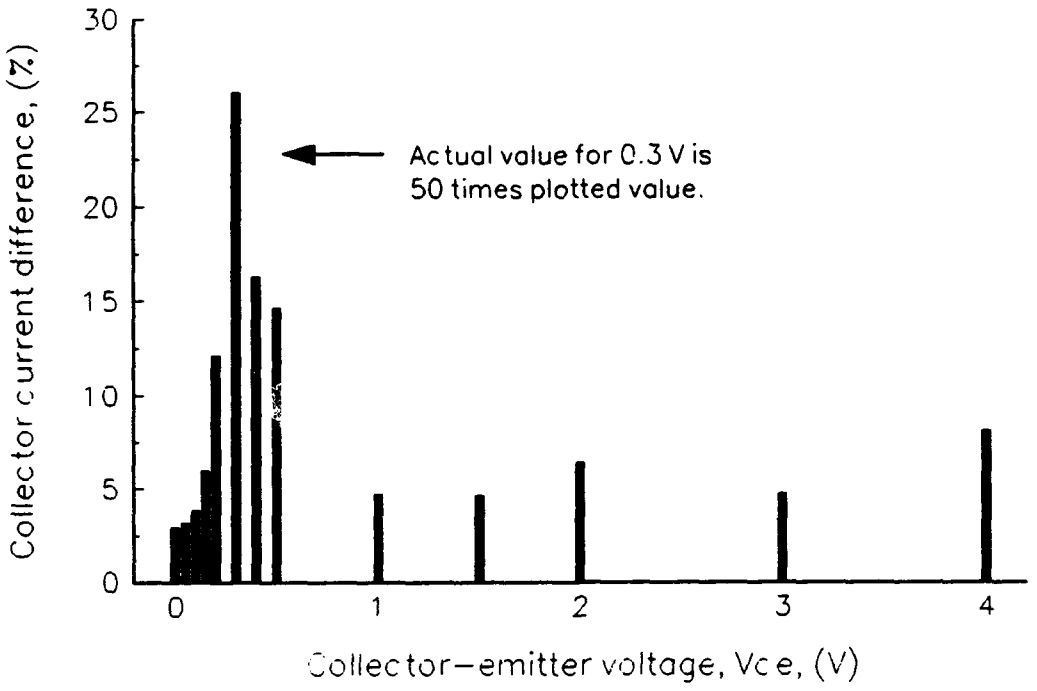

Figure 5.8 Magnitude of the percent difference between modeled and measured I_C averaged over all ten I_B curves.

3uldlf device, inaccuracies in modeling the bias dependence of RC and recombination result in fair to poor agreement in the saturation region. Again, the largest difference (an average of 1300%) occurs at 0.3 V.

As discussed earlier, this is due to the bias dependencies of RC and β_F. The bias dependence of RC could be corrected by modifying the SPICE code to handle a variable RC. The bias dependence of β_F can be accounted for by curve fitting values for *ISE*, *ISC*, *NE*, and *NC*. However, the same problem was encountered when fitting values for *ISE*, *ISC*, *NE*, and *NC* for the 3uldlf and 3u5dlf devices. The problem is that the HSPICE optimization routine is too sensitive to the initial values chosen for *ISE* and *ISC*. Several initial values were chosen within an order of magnitude from the physics-based value calculated by Mathcad. For each optimization attempt, the modeled data were as much as a factor of two different from the measured data in the forward active region. The conclusion is that process variations, which are difficult to account for physically, caused the actual recombination saturation currents to be significantly different than the physically calculated values. For this reason, the 3uldlf and 3u5dlf devices were modeled by accounting for recombination with an empirical β_F. Unless the bias dependence of the offset voltage is accounted for somehow, the average percent difference in I_C will always result in poor agreement within the range of the offset voltages.

Very good agreement is obtained in the forward active region (1, 1.5, and 2 V) with an average difference of about 5%. As with the 3uldlf device, the 7% average difference at 3 and 4 V can be attributed to self-heating.

5.1.2 2u6d2f Device dc Results. Figure 5.9 shows the excellent agreement that can be obtained by neglecting *ISE* and *ISC*, and

using an empirical β_F for *BF* with the 2u6d2f device. Since β_F is not constant, an expression for *BF* as a function of I_B was determined via Axum's curve fitting capabilities as shown in Fig. 5.10. When the model was simulated, I_B was not swept but rather defined as a constant for each I-V curve using the ***.param*** statement. The expression for *BF* was included in the ***.param*** statement so that for each value of I_B, HSPICE calculated the empirical *BF* value. The model card *BF* was set equal to the *BF* of the ***.param*** statement. To generate multiple I-V curves, new ***.param*** statements were added using the ***.alter*** statement. The ***.alter*** statement commands HSPICE to perform a new simulation based on the information in the new ***.param*** statements. Although this model appears to provide excellent agreement, it could never be used as a component in a larger circuit where I_B is variable since HSPICE requires a known constant I_B value from which it calculates *BF*. HSPICE cannot solve user functions of realtime variables.

Accurate physics-based modelling of a non-constant β transistor is a difficult task primarily because the I-V curves are highly sensitive to *NE* and *NC*. The default values of *ISE* and *ISC* in SPICE are zero. This means that unless values of *ISE* and *ISC* in the range of 10^{-14} to 10^{-20} A are put in the model card, no recombination current will be modeled and the value of *BF* will become the effective (actual device) β_F modeled. In fact, if one is attempting to model a junction transistor with a known constant β_F, *ISE* and *ISC* can be neglected, and the transistor can be modeled with *BF* as the empirical β_F rather than the maximum β_F as was done for the 3uldlf and 3u5dlf devices.

To develop a more robust dc model for the 2u6d2f device, the optimization function of HSPICE was used to curve-fit the measured data

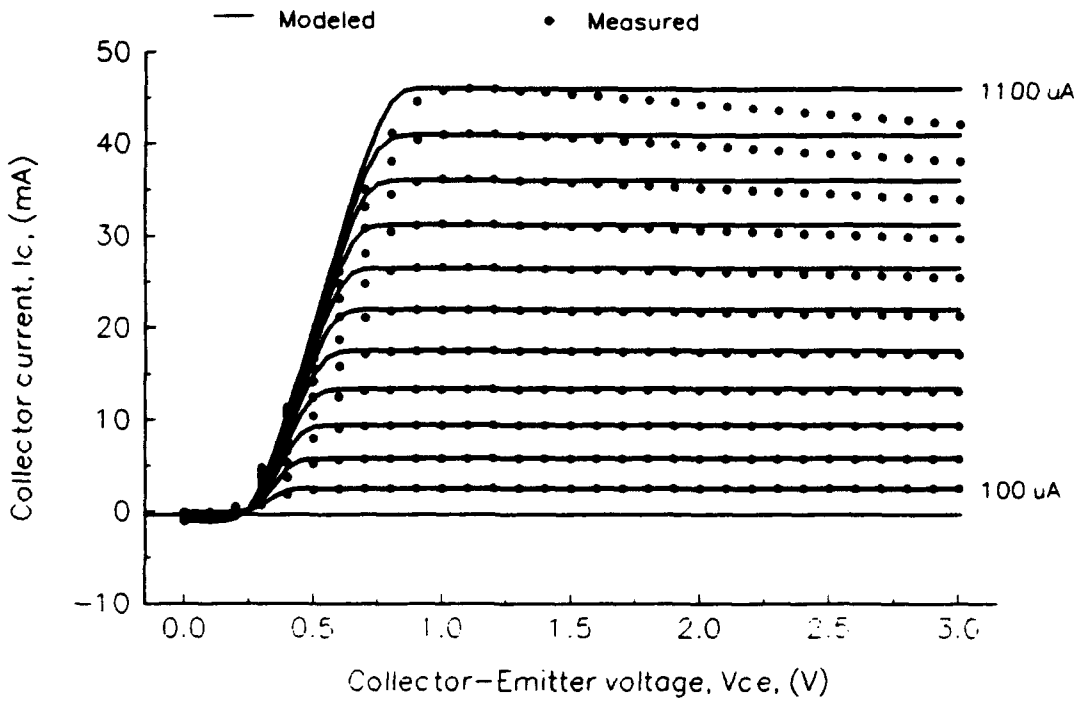

Figure 5.9 I–V characteristics for the 2u6d2f device with variable BF in SPICE and I_B swept in 100 μA increments.

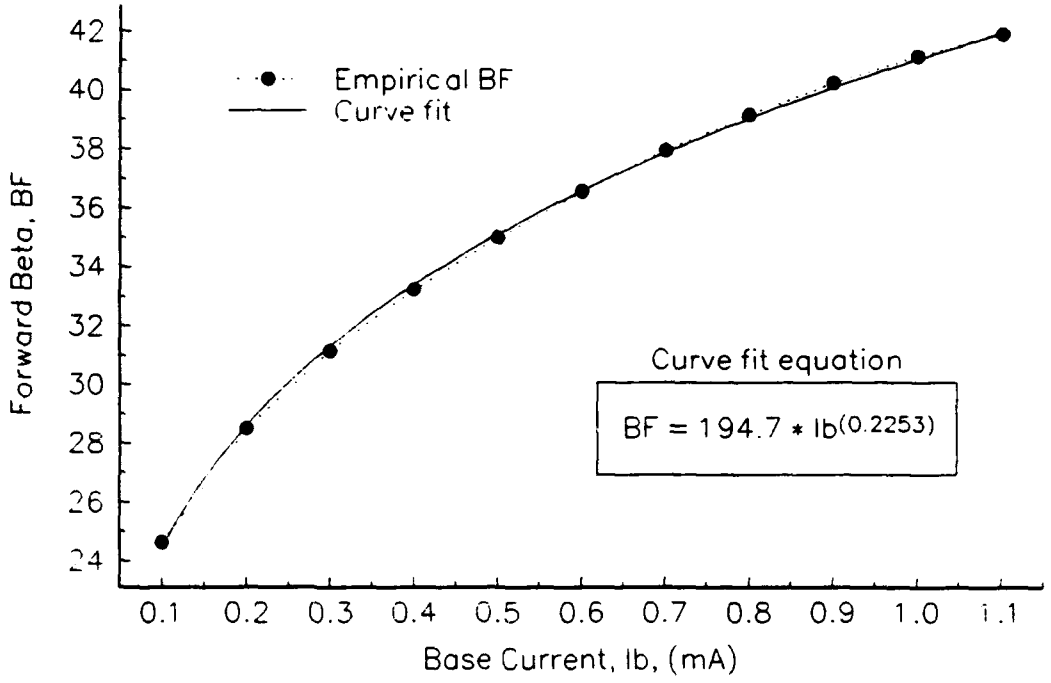

Figure 5.10 Curve fit expression for BF as a function of base current for the 2u6d2f device.

and simultaneously determine values for *NF*, *NE*, *NC*, *ISE*, and *ISC*. Measured data points that deviated noticeably from the constant I_C line due to device self-heating were not included in the optimization so as not to confuse HSPICE or corrupt the temperature independence of the model. Forcing a temperature independent model to match measured data points that are known to deviate from an expected ideal, as a result of temperature effects, is unwise.

When fitting parameters, HSPICE requires three data points. The syntax is [40]

.param Modparam = opt(initial, low, high)

where ***Modparam*** is the name of the model parameter requiring optimization;

initial is the best guess value of the parameter;

low and ***high*** define the range in which optimization occurs.

With the exception of the ideality factors, ***initial*** was the value calculated by Mathcad. The results of the HSPICE optimization for the 2u6d2f device are shown in Table 5-4. The HSPICE file written to perform the optimization and a script of the results can be found in Appendix B.

The I-V characteristics for the 2u6d2f device model that considers the bias dependence of recombination using *NE*, *NC*, *ISE*, and *ISC* are shown in Figs. 5.11 and 5.12. The corresponding model parameters are listed in Table 5-5. The value of *BF*, as calculated by Eq. (4.15), is due only to bulk base recombination. All four of the model's ideality factors are within the expected ranges discussed in Section 4.4.13. Notice also that *IS* is several orders of magnitude smaller than either *ISE* or *ISC*. As expected, *ISE* and *ISC* are larger because they are the recombination saturation currents which are significant in most HBTs. The terms involving *ISE* and *ISC* serve to reduce *BF* to the actual β_F depicted on the

Table 5-4

Optimized Parameters for the 2u6d2f Device

Parameter	Initial	Low	High	Optimized
NF	1.100	1.000	1.200	1.1049
NE	1.900	1.700	2.100	1.7000
NC	1.950	1.750	2.100	1.7595
ISE (A)	3.11e-18	1.00e-20	1.00e-16	2.432e-19
ISC (A)	5.00e-14	1.00e-16	1.00e-13	4.393e-16

Table 5-5

2u6d2f SPICE BJT dc Model Parameters

Parameter	Units	Value Used in HSPICE BJT Model Card
BF	-	83.926
BR	-	0.6338
NF	-	1.1049
NR	-	1.0000
NE	-	1.7000
NC	-	1.7595
ISE	A	2.432×10^{-19}
ISC	A	4.393×10^{-16}
IS	A	1.111×10^{-25}
RE	Ω	6.7896
RB	Ω	4.8379
RC	Ω	2.20

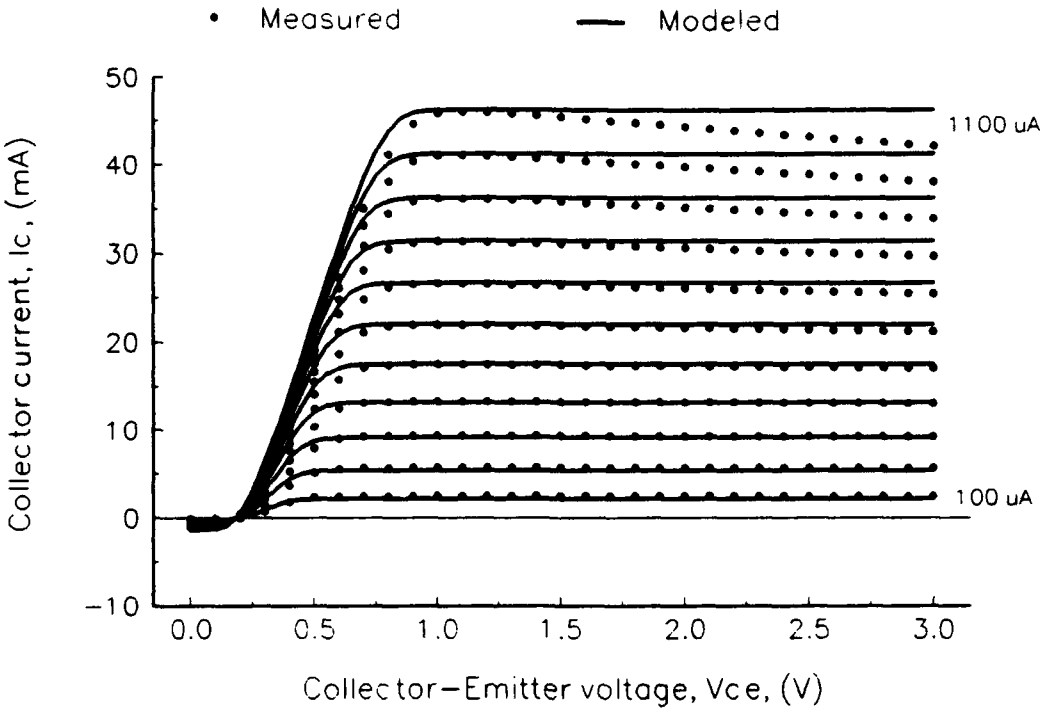

Figure 5.11 I-V characteristics for the 2u6d2f device with I_B swept in 100 μA increments.

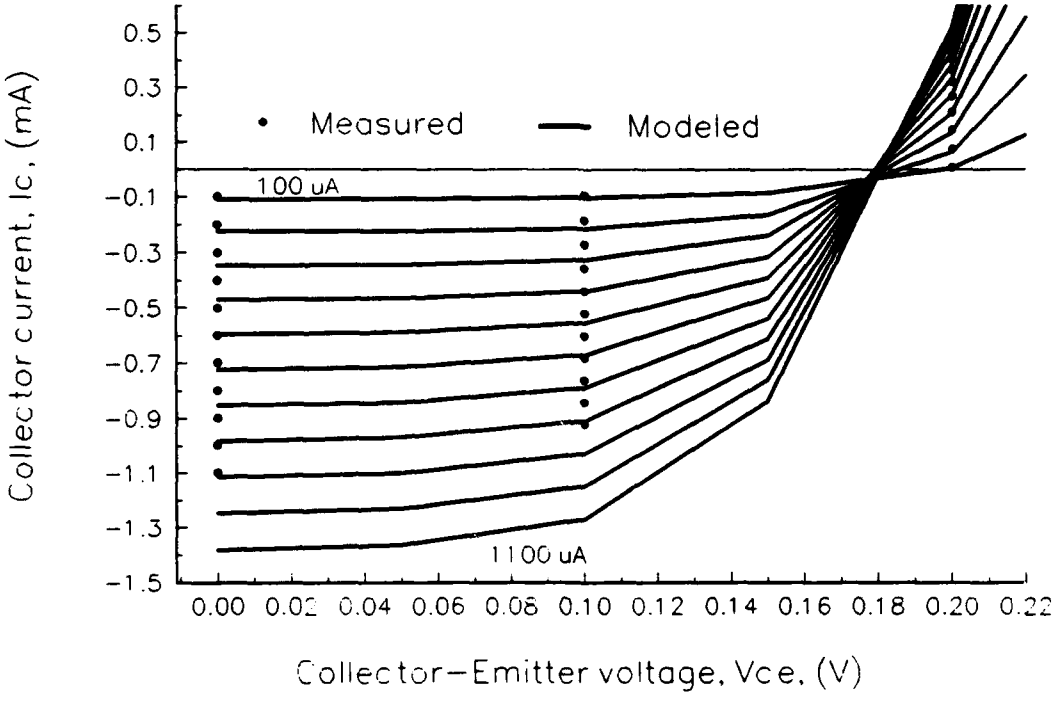

Figure 5.12 Reverse I-V characteristics for the 2u6d2f device with I_B swept in 100 μA increments.

modeled curves by I_C/I_B in the active region.

Notice in Fig. 5.12 that the modeled curves show a decreasing offset voltage with increasing I_B. Since the recombination currents have less impact with increasing bias, the base-emitter junction is able to turn-on more quickly, hence lower offset voltages. The modeled offset voltage has not only the proper bias dependence, but for each curve the modeled and measured offset voltages are nearly identical. This distinct improvement over the 3uld1f and 3u5d1f models is directly attributed to modeling the bias dependence of recombination with *NE*, *NC*, *ISE*, and *ISC*.

Figure 5.13 shows the magnitude of the percent difference between modeled and measured collector current averaged over 11 I_B curves. The agreement in the forward active region (1, 1.1, 1.2 V) is excellent due to the curve fitting of measured data to extract the three ideality factors and recombination saturation currents: *NF*, *NE*, *NC*, *ISE*, and *ISC*. The two data points at 0 and 0.1 V show the model overestimating I_C by an average of almost 20%. This is only fair agreement and is a direct result of overestimating the physics-based value of *BR*. The good to poor agreement of the model through saturation ($0.2 \leq V_{CE} \leq 0.7$ V) is indication of the model's difficulty in precisely matching the variable saturation slope due to the bias dependence of RC. Very good agreement is obtained as the model leaves the saturation region and begins to enter the active region (0.8 and 0.9 V). with an average difference in collector current of less than 5%. The steady and predictable rise in the bars beyond 1.2 V is due solely to device self-heating.

Unfortunately, there is no good way to physically calculate the HSPICE BJT model ideality factors: *NF*, *NE*, *NC*. These three values which are so crucial to the ultimate fit of the model can only be determined via

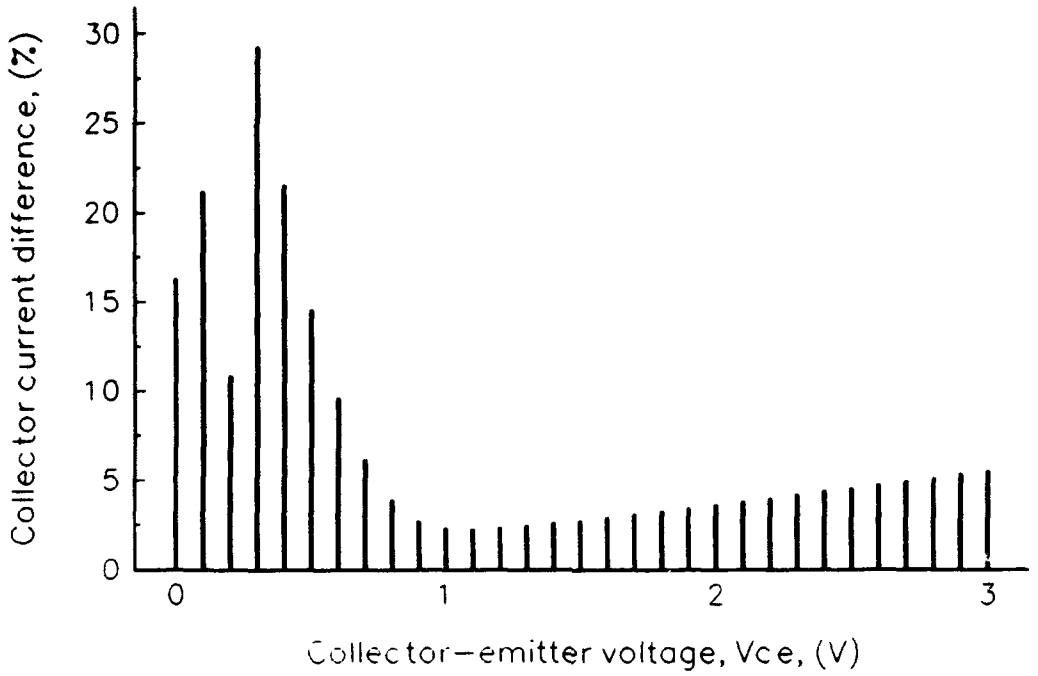

Figure 5.13 Percent difference between modeled and measured I_C for the 2u6d2f device at I_B = 800 μA.

parameter extraction. The dc models derived in this thesis are physics-based with the exception of *BF* and *NF* (for the one finger devices), and *NF*, *NE*, *NC*, *ISE*, and *ISC* (for the 2u6d2f device). The series resistances and transport saturation current are determined only from a knowledge of the device material, geometry, and fabrication process. Aside from the agreement in saturation (which can be imputed to the bias dependence of RC and recombination), the 3uldlf and 3u5dlf models fall within the ± 5% difference criterion for model success. This level of performance is at least as good as models found in current literature [23,24,26,27]. The 2u6d2f model has fair agreement in the reverse active region, good to poor agreement in the saturation region, and excellent agreement in the forward active region (neglecting differences due to self-heating). Additionally, the models have proven to support a cylindrical emitter-base geometry, and

are readily implemented in SPICE; all the user must do is provide physical information and the Mathcad file automatically calculates the entire set of model parameters.

5.2 Microwave Results

All microwave simulations were conducted using the HSPICE ac testbench described in Section 4.6. A bias point was chosen and the four common-emitter S-parameters from 1 to 50 GHz were obtained. The general contour of each S-parameter with respect to the Smith chart or polar graph will be discussed, followed by plots comparing the measured and modeled S-parameters at a selected bias point for each device. The section concludes with a sensitivity analysis of a few key model parameters which will show how agreement can be improved.

5.2.1 General S-parameter contours. S_{11} is defined as the input reflection coefficient with the output port matched to the transmission line characteristic impedance, Z_o. S_{11}, like all the S-parameters, sweeps clockwise around the Smith chart as frequency is increased. This path can be related to the decreasing capacitive reactance of the device which is given by $X_c = 1/j\omega C$ as well as the increasing inductive reactance given by $X_l = j\omega L$. Because impedances plotted on a Smith chart are normalized to Z_o, the magnitude of S_{11} lies on a constant resistance circle, which is directly related to RB. S_{22} is defined as the output reflection coefficient and follows a path similar to S_{11}. Within the modeled frequency range (1 to 50 GHz), both reflection coefficients are almost entirely due to a capacitive reactance.

S_{21} is defined as the forward transmission gain and generally has a magnitude greater than unity which decreases with frequency. S_{12} is

defined as the isolation or feedback of the device. The magnitude of S_{12} is small at low microwave frequencies and increases with frequency.

5.2.2 Comparison of modeled and measured S-parameters. The additional model parameters that characterize the device's ac performance deal with the transport, removal, and storage of charge. These parameters are the zero-bias depletion capacitances (*CJE* and *CJC*), the junction grading factors (*MJE* and *MJC*), the built-in junction voltages (*VJE* and *VJC*), the forward and reverse base transit times (*TF* and *TR*), and the internal capacitance ratio (*XCJC*). All of these SPICE model parameters, along with the dc bias, are used to calculate the three hybrid-π equivalent circuit (see Fig. 4.8) capacitors: C_{π}, $C_{\mu int}$, and $C_{\mu ext}$. The six additional parasitic elements (see Fig. 4.9) were calculated by Mathcad and added to the microwave HBT model. The leakage resistors described by Eq. (4.45) were calculated to be in excess of $10^6\ \Omega$. Placing a resistor of this magnitude in parallel with each of the three parasitic capacitors C_{bep}, C_{bcp}, and C_{cep} barely had a fourth decimal place effect on the modeled S-parameters because the impedance of the capacitors was so much smaller. Therefore, pad leakage resistors are not included in the model.

Table 5-6 summarizes the complete list of SPICE model parameters for the 3uld1f device, including all parasitics. As before, all parameters with the exception of *NF*, *NE*, and *NC* are physically calculated. Figures 5.14 - 5.17 compare the modeled and measured S-parameters for the 3uld1f device at a moderate bias of V_{CE} = 2 V and I_B = 100 μA. The I-V characteristics of Fig. 5.3 clearly show that the device is operating in the forward active region which is typical for small-signal applications.

Table 5-6

3uldlf SPICE BJT Full Model Parameters

BF = 28.90	*TF* = 0.95681 ps
BR = 0.005	*TR* = 0.52870 ns
NF = 1.116	*CJE* = 9.8515 fF
NR = 1.0000	*CJC* = 11.190 fF
RE = 33.6707 Ω	*MJE* = 0.50
RB = 9.3857 Ω	*MJC* = 0.50
Rbext = 33.8989 Ω	*VJE* = 1.7018 V
RC = 67.800 Ω	*VJC* = 1.3691 V
IS = 1.0363×10^{-26} A	*XCJC* = 0.2053
L_{ep} = 1.6965 pH	C_{cep} = 0.100 fF
L_{bp} = 1.6965 pH	C_{bep} = 0.739 fF
L_{cp} = 3.3090 pH	C_{bcp} = 15.00 fF

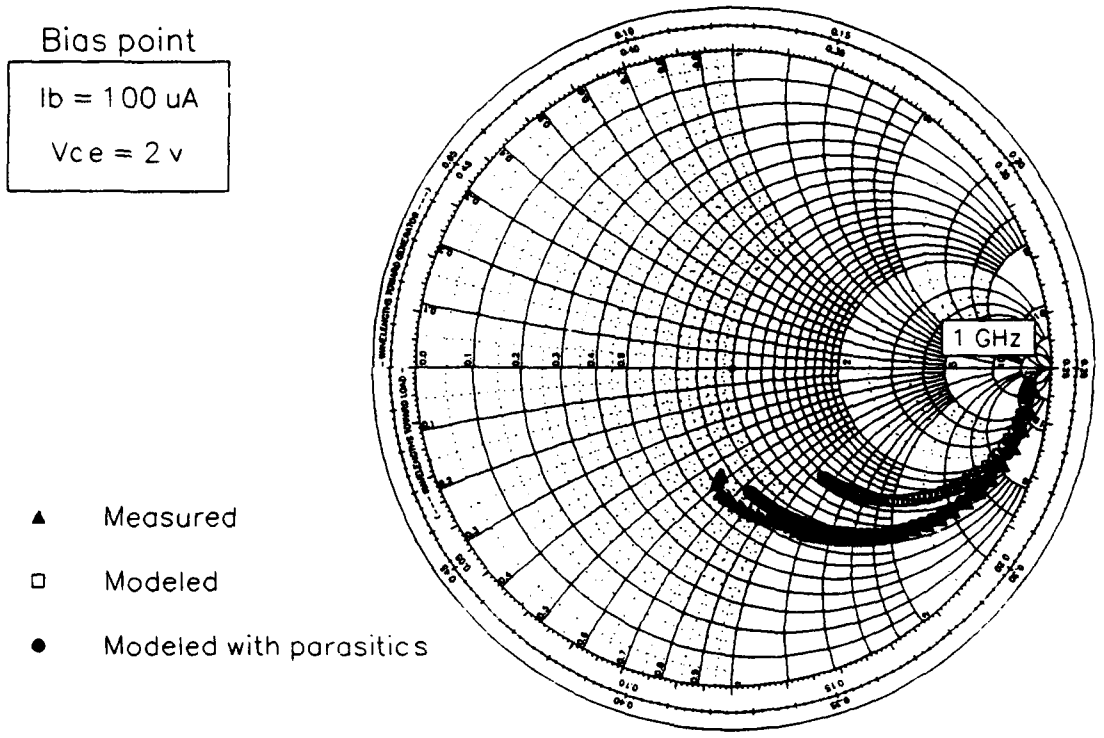

Figure 5.14 Comparison of S_{11} for the 3uldlf device from 1 to 50 GHz.

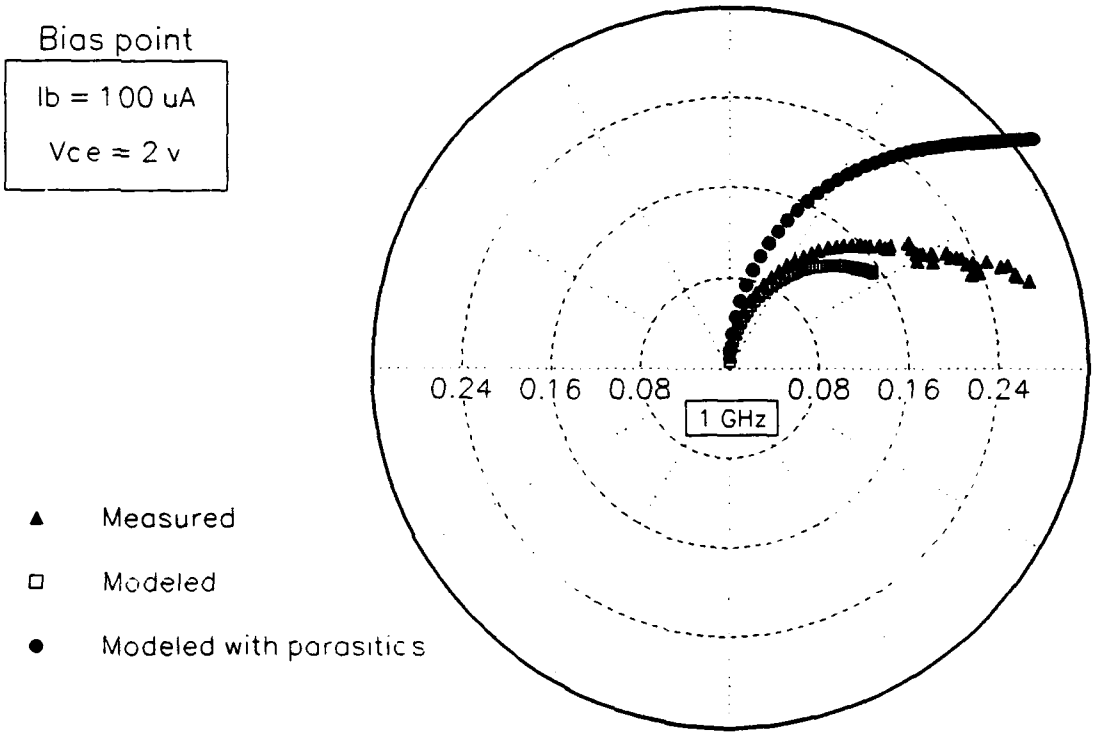

Figure 5.15 Comparison of S_{12} for the 3uldlf device from 1 to 50 GHz.

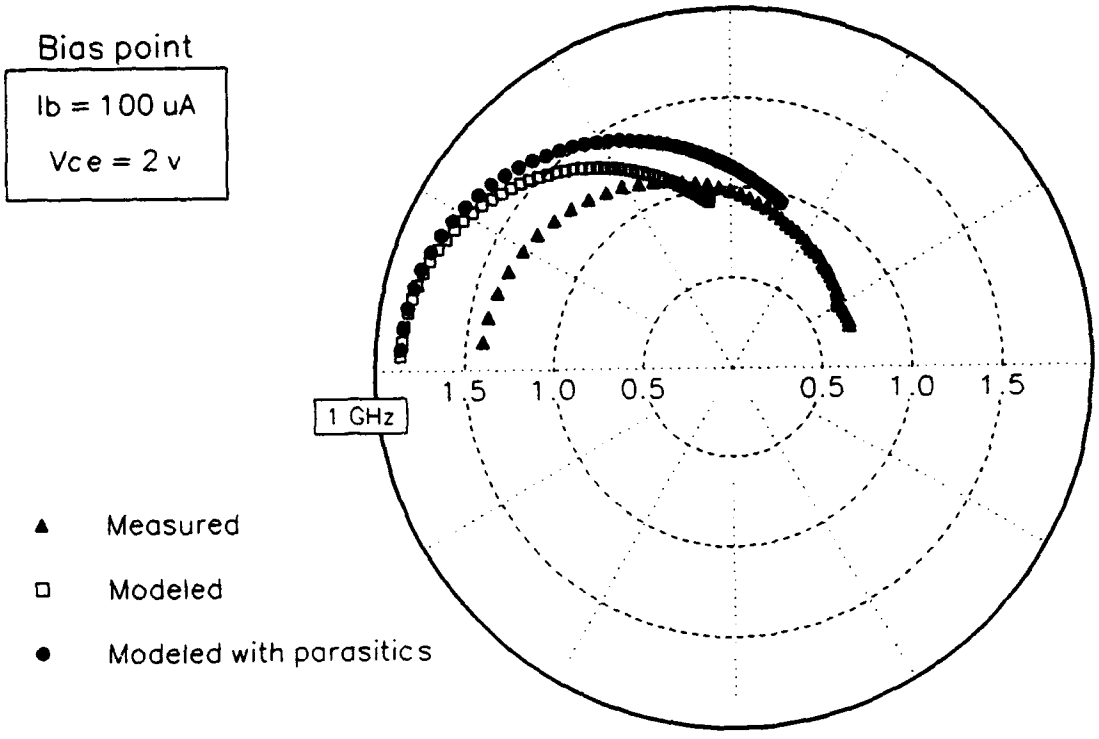

Figure 5.16 Comparison of S_{21} for the 3uldlf device from 1 to 50 GHz.

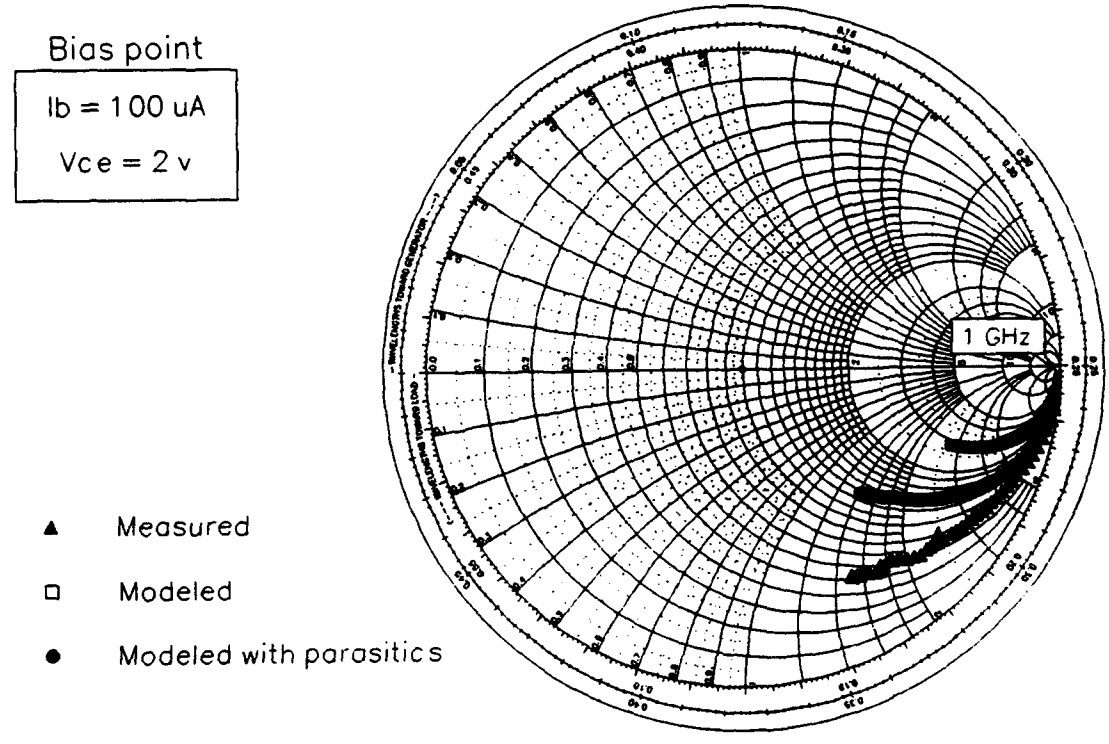

Figure 5.17 Comparison of S_{22} for the 3uldlf device from 1 to 50 GHz.

The comparison of S_{11} in Fig. 5.14 shows excellent agreement between the modeled and measured data. Notice that two sets of modeled data are plotted. One set is merely the linearized version of the dc model, or the hybrid-π circuit of Fig. 4.8. The other set was produced by the full model with physics-based values for all six parasitics. The importance of accurate parasitic modeling is seen by how much closer the full model comes to the measured data. The full model curve follows practically the same constant resistance circle as the measured curve. This is a result of the accurate calculation of RB. In fact, the value of RB can be estimated from S_{11}. Notice that the measured curve follows the r = 0.8 circle which, being normalized to 50 Ω, correlates to an RB of 40 Ω. The Mathcad file calculated the sum of the intrinsic and extrinsic base resistances at 43.28 Ω.

The 3uld1f comparison of S_{12} is shown in Fig. 5.15. The full model curve starts off well but as frequency increases the angle does not decrease rapidly enough. Because the measured curve lies within the two sets of modeled data, one or more parasitics may have been overestimated. C_{bcp} is a suspect since a smaller value will increase the impedance between the base and collector. This should minimize coupling and reduce S_{12}.

S_{21} for the 3uld1f device is shown in Fig. 5.16. The modeled curves have the same general shape but the gain is too large, especially at the lower frequencies, and the angle at higher frequencies does not drop enough. A small increase in RE will pull the gain down at low frequencies but will not effect the angle at the high frequencies. Figure 5.17 shows the comparison for S_{22}. Adding parasitics clearly took a step in the right direction, but fell short since the full model curve lies in between the bare model (without parasitics) curve and the measured curve.

Similar plots are shown in Figs. 5.18 - 5.21 for the 3u5d1f device at a moderate bias of V_{CE} = 2 V and I_B = 300 μA. The complete list of SPICE model parameters for the 3u5d1f device is shown in Table 5-7. The full model for S_{11} (Fig. 5.18) improves the angle so that the modeled and measured curves are no longer askew. Notice that the full model's magnitude is initially less than that of the measured points. The modeled and measured points converge at 3 GHz, and then the measured magnitudes are less for frequencies above 4 GHz. Although the reason is not obvious, this occurrence could be attributed to $C_{\mu ext}$ being split across the base resistance.

The full model curve for S_{12} shown in Fig. 5.19 matches the measured data better than the model without parasitics, though both need to extend below the zero angle line at higher frequencies. This same problem will be discussed in more detail with the 2u6d2f device. The 3u5d1f S_{21} full model data has better agreement than the 3uld1f S_{21}, however; both models suffer from too large a magnitude in the low frequencies. The measured 3u5d1f S_{22} has a unique curve that follows a constant resistance circle up through 6 GHz then runs straight across the Smith chart, almost as if some capacitive and inductive reactances are competing to decide the path. Both of the modeled curves follow constant resistance circles for nearly the entire 50 GHz range. The model without parasitics follows the r = 1.1 circle and the full model follows the r = 0.6 circle. The full model begins to bend downward but only at the uppermost frequencies.

The bare model data of both of the one finger devices are relatively far apart from the measured data. This could indicate that the one finger devices have parasitics that are comparable to the intrinsic device impedances. The intrinsic device can be thought of as being surrounded by

Table 5–7

3u5d1f SPICE BJT Full Model Parameters

BF = 33.30	*TF* = 0.95811 ps
BR = 0.0231	*TR* = 1.40460 ns
NF = 1.1557	*CJE* = 49.257 fF
NR = 1.0000	*CJC* = 35.706 fF
RE = 6.7341 Ω	*MJE* = 0.50
RB = 1.8771 Ω	*MJC* = 0.50
Rbext = 6.7798 Ω	*VJE* = 1.7018 V
RC = 16.79 Ω	*VJC* = 1.3454 V
IS = 5.2047×10^{-26} A	*XCJC* = 0.2053
L_{ep} = 1.4224 pH	C_{cep} = 13.650 fF
L_{bp} = 8.4823 pH	C_{bep} = 3.6943 fF
L_{cp} = 1.7090 pH	C_{bcp} = 31.566 fF

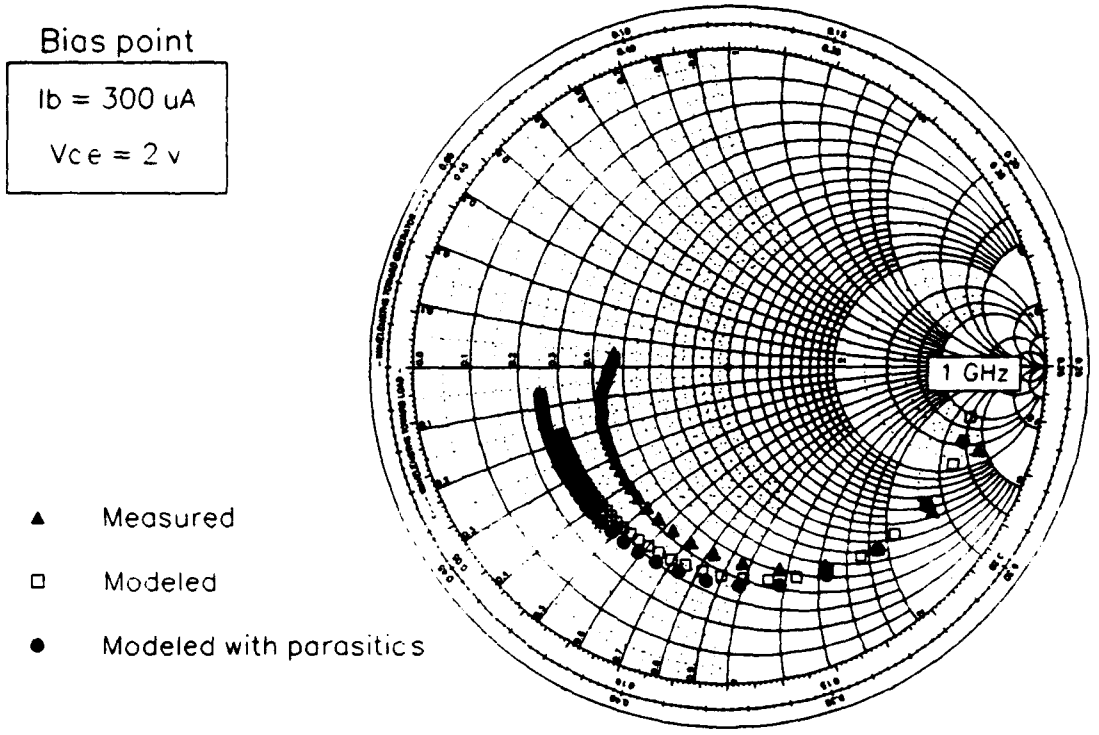

Figure 5.18 Comparison of S_{11} for the 3u5d1f device from 1 to 50 GHz.

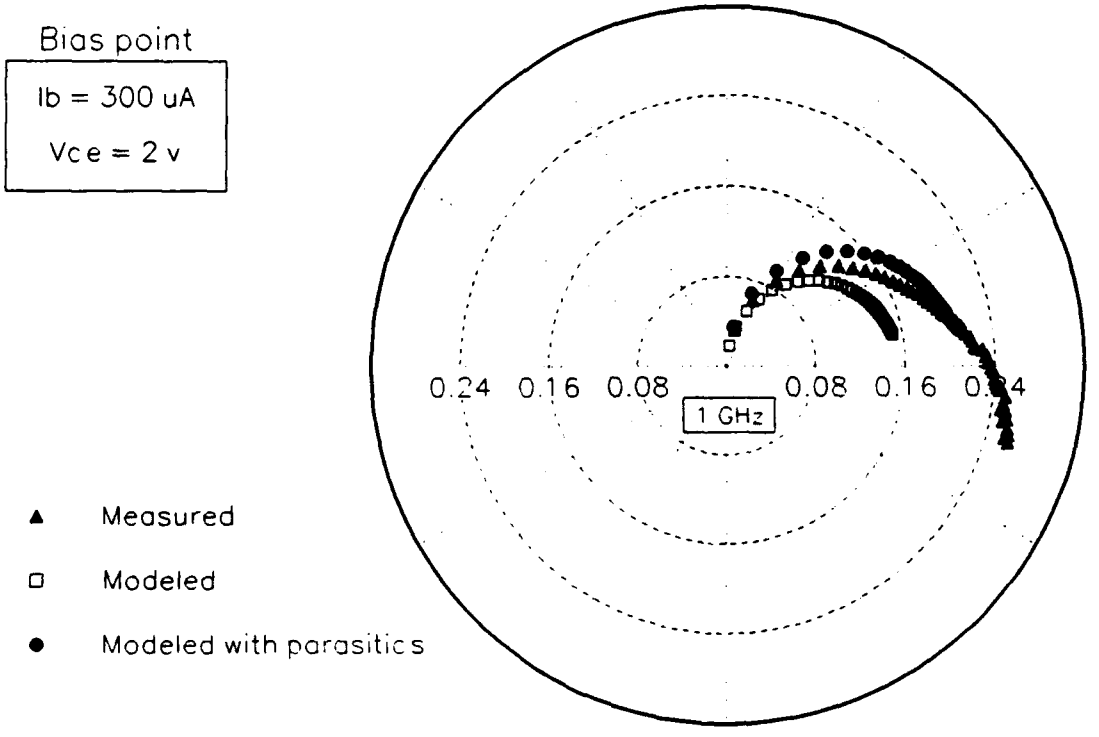

Figure 5.19 Comparison of S_{12} for the 3u5d1f device from 1 to 50 GHz.

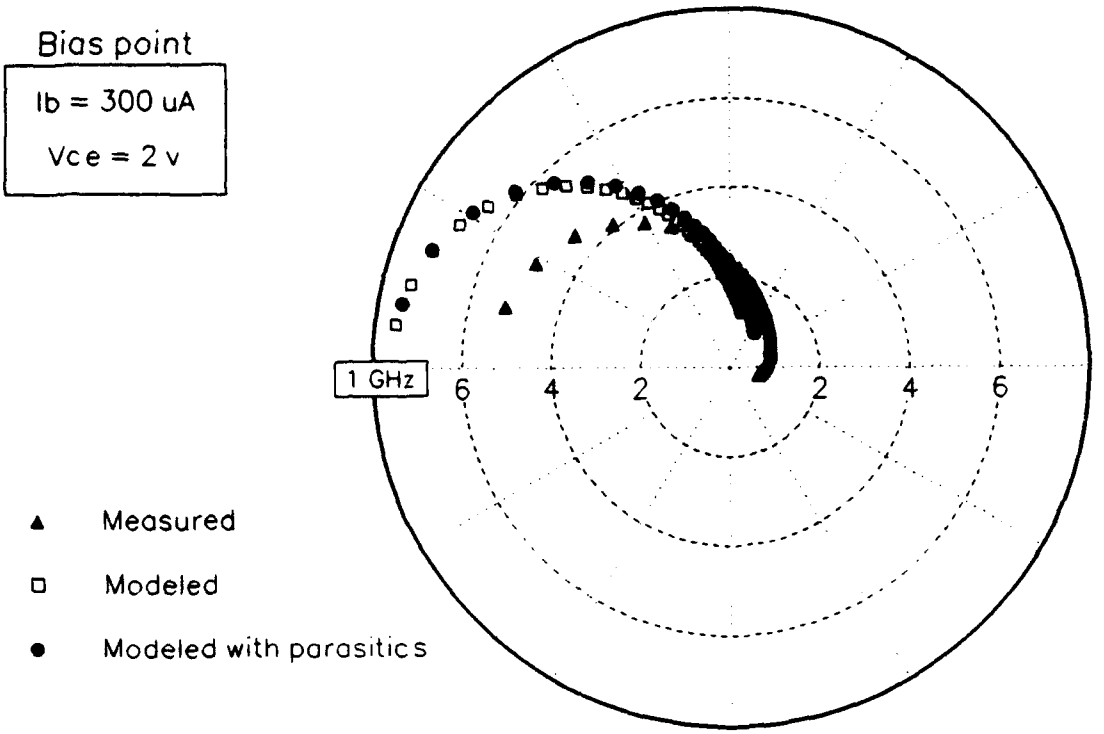

Figure 5.20 Comparison of S_{21} for the 3u5d1f device from 1 to 50 GHz.

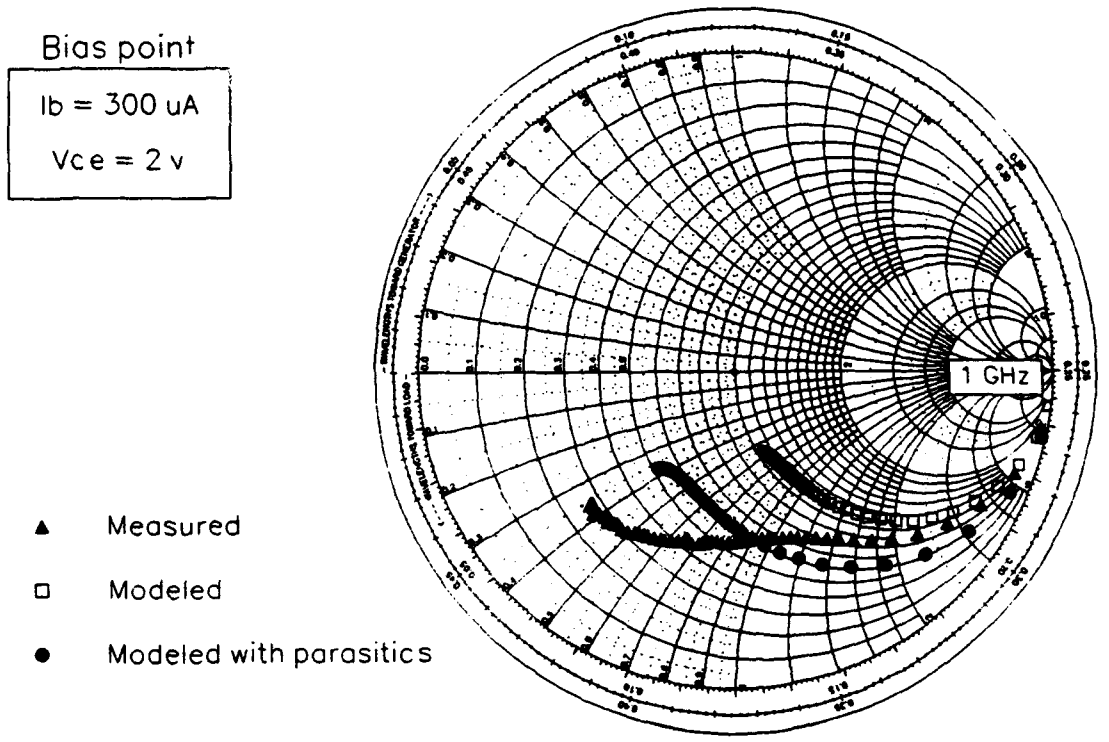

Figure 5.21 Comparison of S_{22} for the 3u5d1f device from 1 to 50 GHz.

a shell of series inductances and a shell of shunt capacitances [31]. If the S-parameters of these shells are large with respect to those of the intrinsic device, then their effect is pronounced and accurate modeling is even more important.

The bare model S-parameters of the 2u6d2f device are close to the measured S-parameters. Analogous to the one finger devices, this could be attributed to the relatively small contribution of the parasitic shells. Very good to excellent agreement was obtained on all of the 2u6d2f S-parameters as shown in Figs. 5.22 - 5.25. The full set of 2u6d2f model parameters is listed in Table 5-8. The S-parameters were measured in the active mode with a bias of V_{CE} = 1 V and I_B = 800 μA. Although their equivalent circuits are related by linearization, dc model agreement is not the strongest factor influencing microwave agreement. At the bias point chosen for S-parameter simulations, the 3u1d1f and 3u5d1f devices have about a 1 and 0.3% difference, respectively. The 2u6d2f device has about a 3% difference, yet the S-parameters for the 2u6d2f device have better agreement than the other two devices.

The bare model S_{11} follows nearly the same constant resistance circle (r = 0.2) as the measured S_{11} shown in Fig. 5.22. The effect of the parasitics on the model was to shift S_{11} clockwise around the Smith chart (increasing inductive reactance), especially in the 1 to 7 GHz frequency range. The combination of the parasitic and intrinsic device reactances resulted in S_{11} having less capacitive reactance at the lower frequencies. Additionally, the magnitude increased slightly at the higher frequencies. To complete the agreement, the modeled data points need to be spread out more at the higher frequencies to enter the inductive reactance region of the Smith chart. The model parameter changes required to obtain better

Table 5-8

2u6d2f SPICE BJT Full Model Parameters

BF = 83.926	*TF* = 0.95243 ps
BR = 0.6338	*TR* = 0.12611 ns
NF = 1.1049	*CJE* = 48.855 fF
NR = 1.0000	*CJC* = 157.58 fF
NE = 1.7000	*MJE* = 0.50
NC = 1.7595	*MJC* = 0.50
ISE = 2.432×10^{-18} A	*VJE* = 1.7018 V
ISC = 4.393×10^{-17} A	*VJC* = 1.4107 V
IS = 1.111×10^{-25} A	*XCJC* = 0.1590
RE = 6.7896 Ω	RC = 2.200 Ω
RB = 0.7821 Ω	Rbext = 4.0557 Ω
L_{ep} = 0.4841 pH	C_{cep} = 18.488 fF
L_{bp} = 2.3562 pH	C_{bep} = 7.3255 fF
L_{cp} = 0.6093 pH	C_{bcp} = 106.13 fF

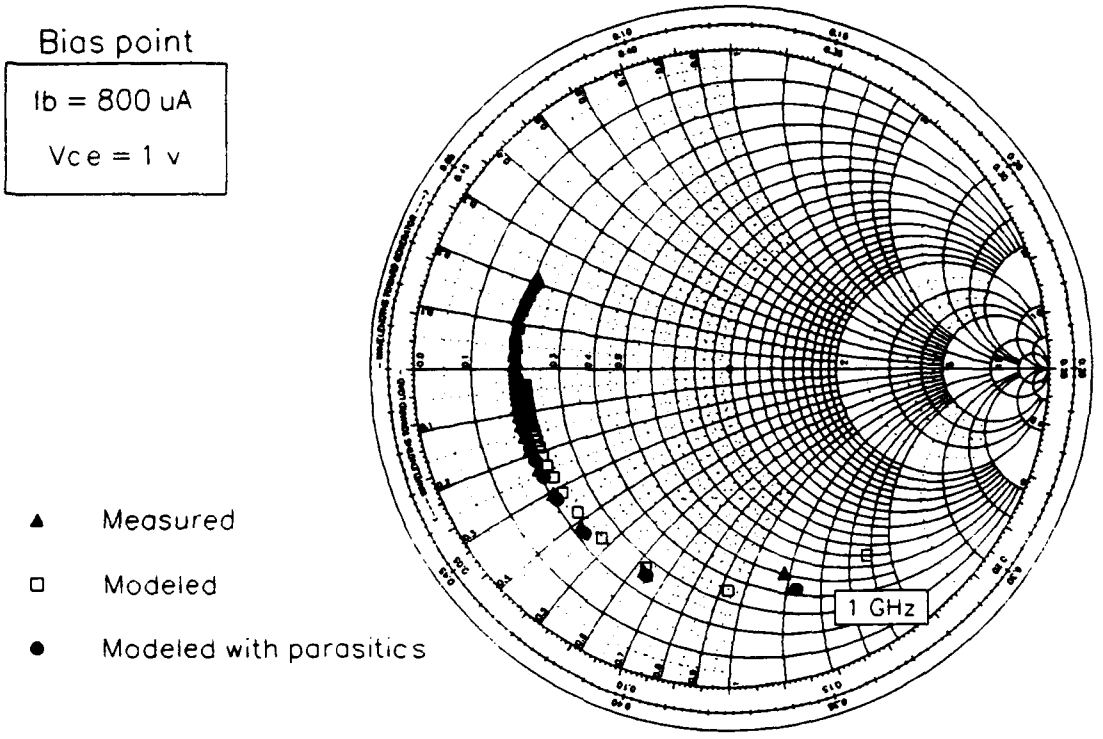

Figure 5.22 Comparison of S_{11} for the 2u6d2f device from 1 to 50 GHz.

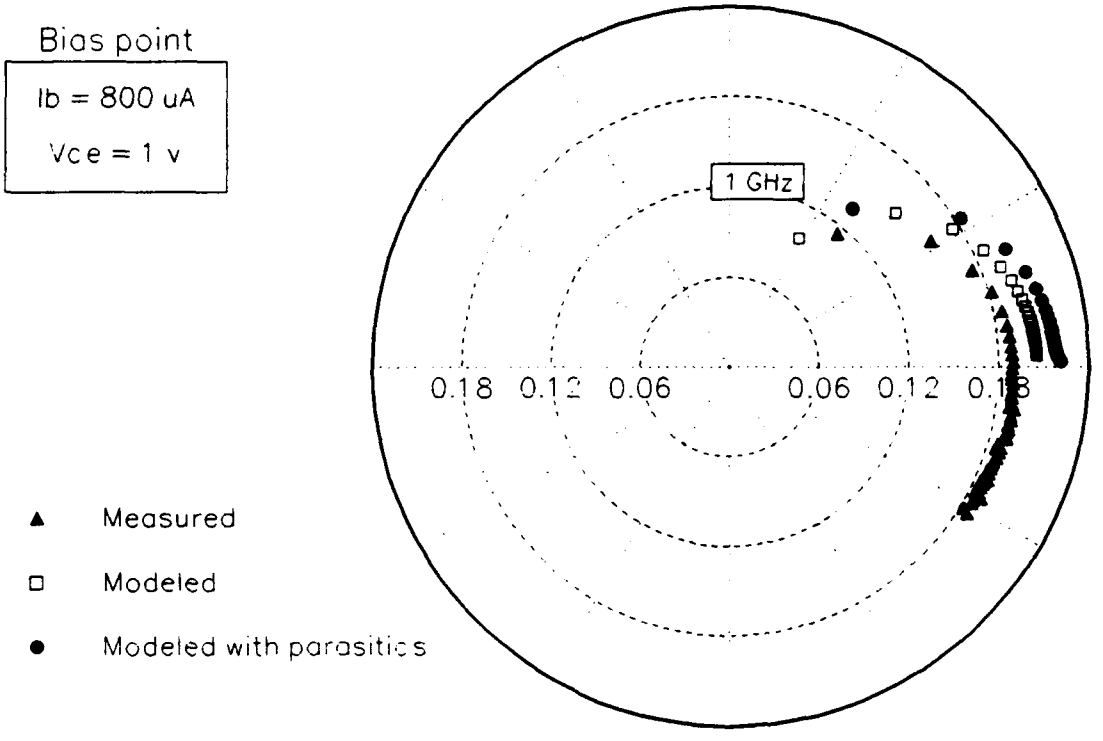

Figure 5.23 Comparison of S_{12} for the 2u6d2f device from 1 to 50 GHz.

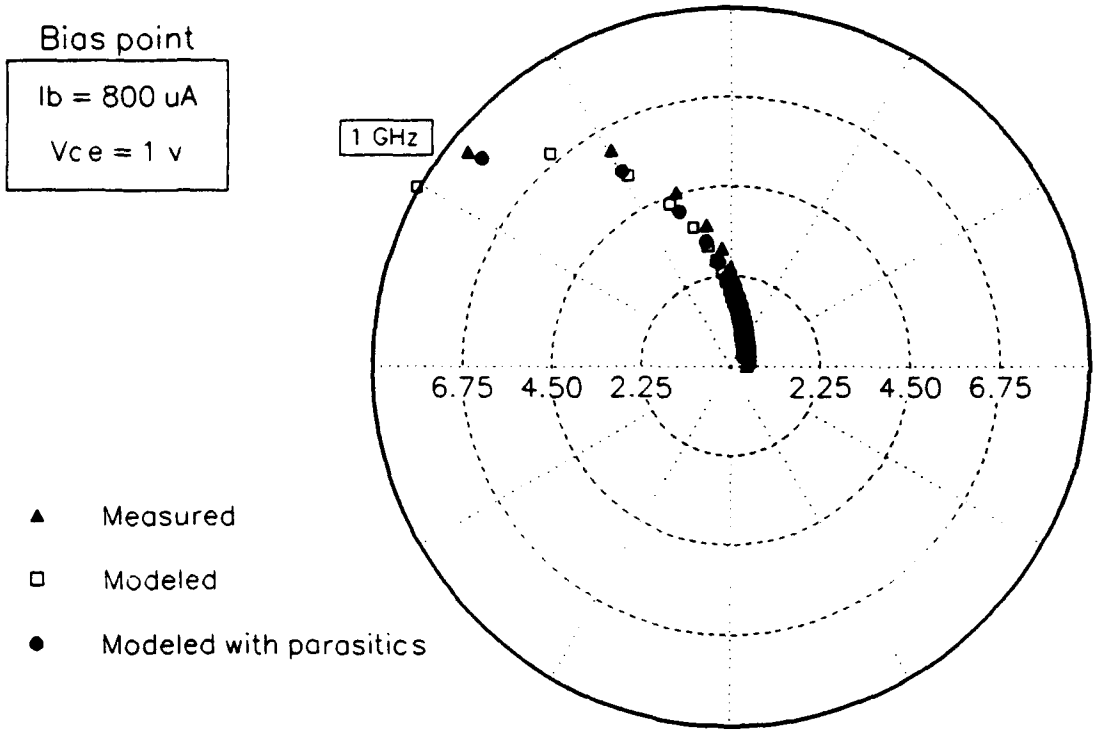

Figure 5.24 Comparison of S_{21} for the 2u6d2f device from 1 to 50 GHz.

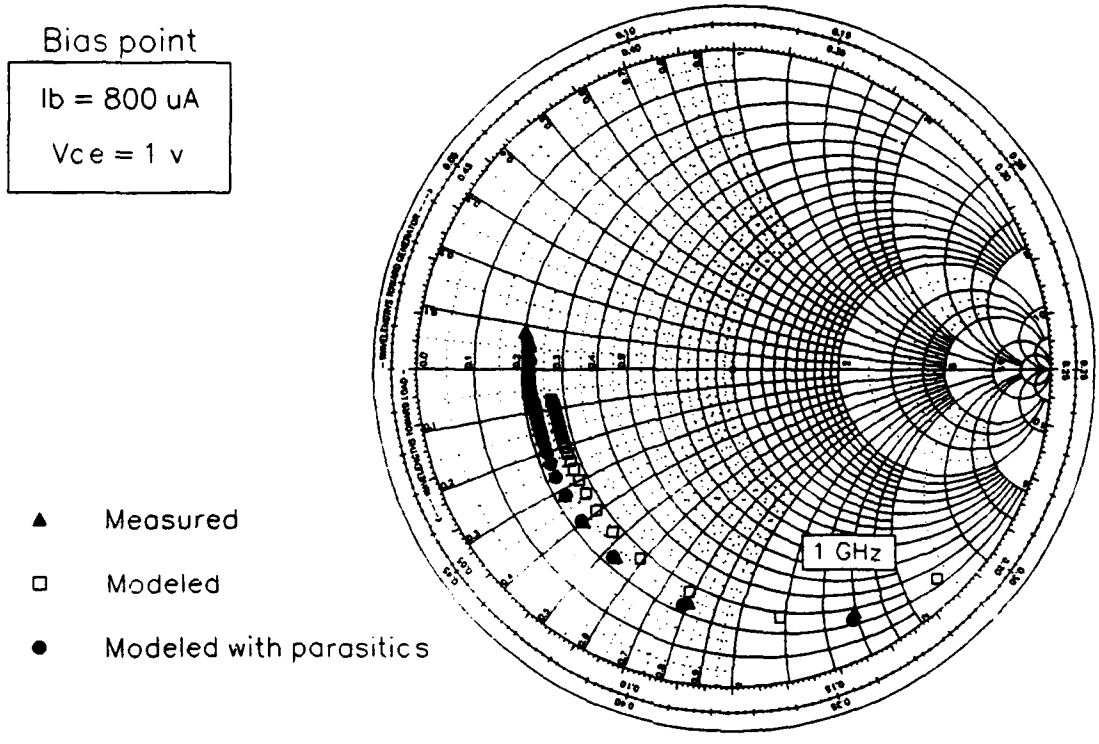

Figure 5.25 Comparison of S_{22} for the 2u6d2f device from 1 to 50 GHz.

agreement will be discussed in a detailed sensitivity analysis of the next section.

Adding parasitics improved the angle agreement for S_{12} but pushed the magnitude out too far at higher frequencies. The same concern with S_{12} arises here as with the 3u5d1f device: the model is not as frequency dependent above 20 or 30 GHz as it needs to be. The impedance of the shunt capacitors decreases non-linearly with increasing frequency, therefore their effect should become less noticeable at higher frequencies. The impedance of the series inductors increases linearly with increasing frequency. The expected result is that the capacitors will influence the S-parameters more in the lower frequency range (1 to 10 GHz), while the inductors will dominate in the higher frequency range (30 to 50 GHz).

The effect of adding parasitics shifted the lower frequency data points for S_{21} closer to the measured data points. Notice that the model needs to become more inductive to better match at the higher frequencies. This is also the case with the full model for S_{22}. In fact, all the 2u6d2f S-parameters could be improved above 20 GHz. This common phenomenon could be directly linked to an underestimation of the series inductances calculated by Mathcad. Nevertheless, similar to S_{11}, very good agreement is obtained for S_{22} up through about 20 GHz.

The next set of plots (Figs. 5.26 - 5.31) will quantitatively assess the performance of the model by showing how well the 2u6d2f full model met the ± 5% agreement success criterion. Data concerning S_{11} is shown in Fig. 5.26. Aside from the data point at 1 GHz, the magnitude of S_{11} is less than 1% different from the measured magnitude for the entire range up to 50 GHz. As expected, the percent difference in angle is below 5% up to

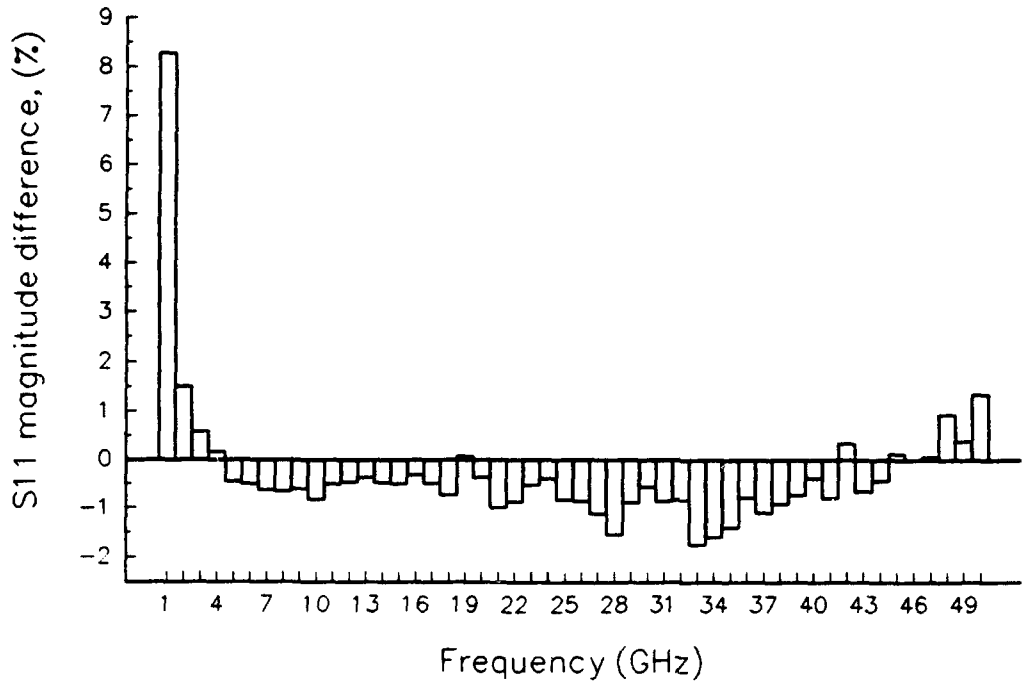

Figure 5.26 Percent difference between the modeled and measured magnitude of S_{11} for the 2u6d2f device at a 1 V, 800 μA bias.

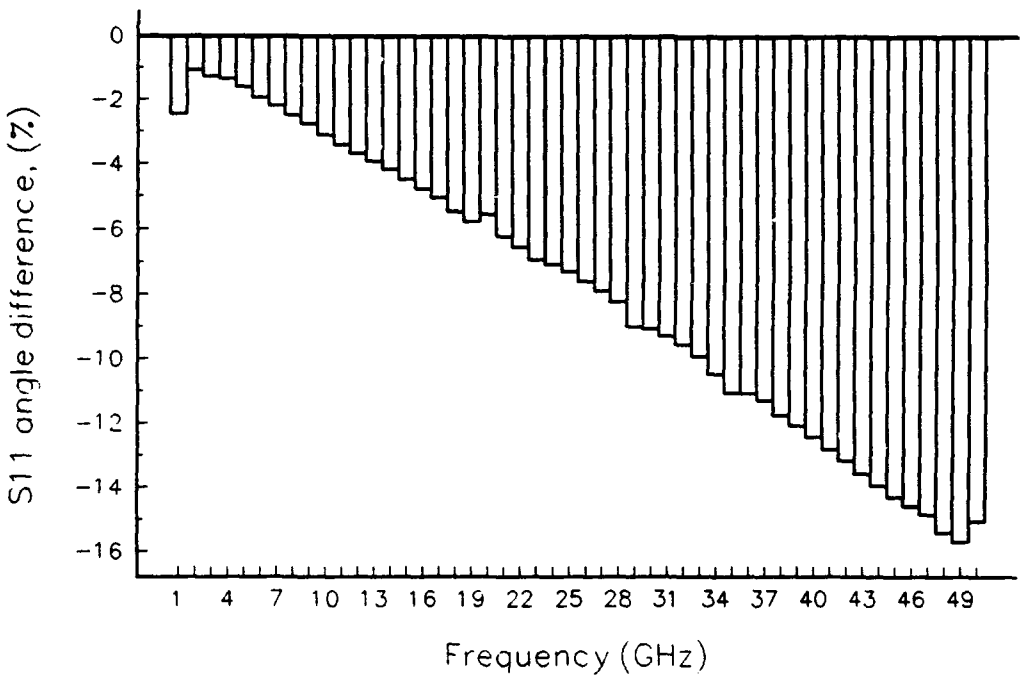

Figure 5.27 Percent difference between the modeled and measured angle of S_{11} for the 2u6d2f device at a 1 V, 800 μA bias.

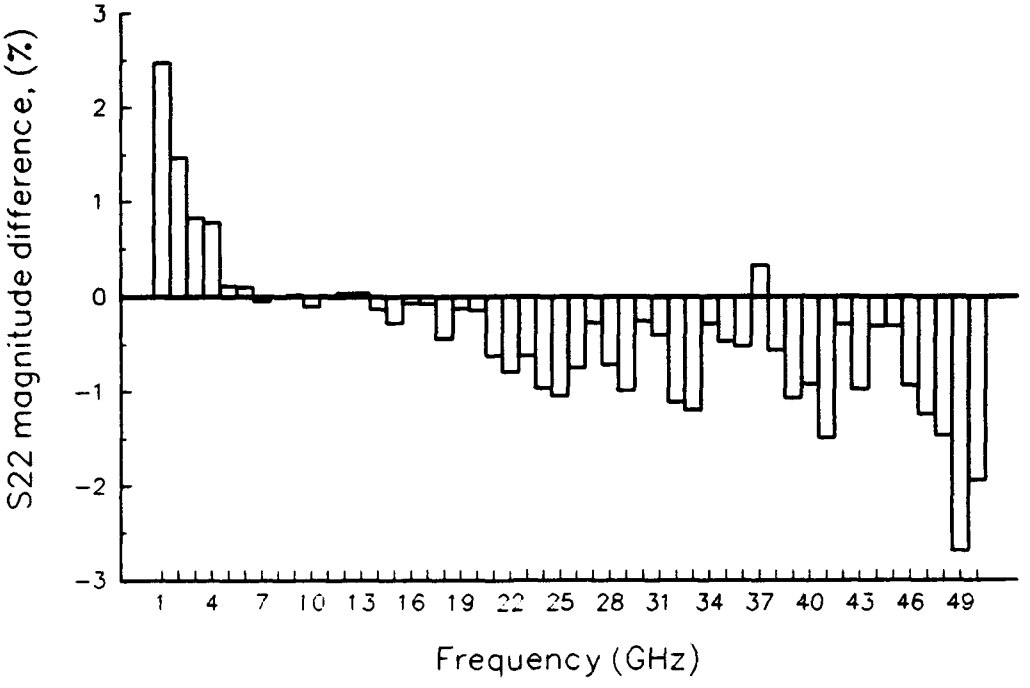

Figure 5.28 Percent difference between the modeled and measured magnitude of S_{22} for the 2u6d2f device at a 1 V, 800 μA bias.

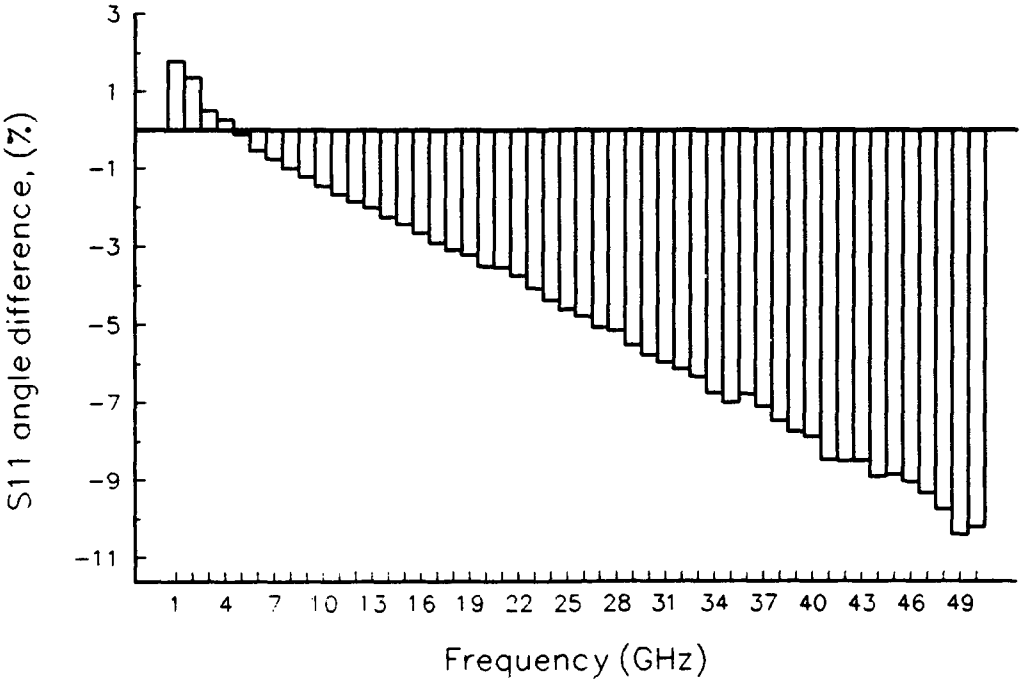

Figure 5.29 Percent difference between the modeled and measured angle of S_{22} for the 2u6d2f device at a 1 V, 800 μA bias.

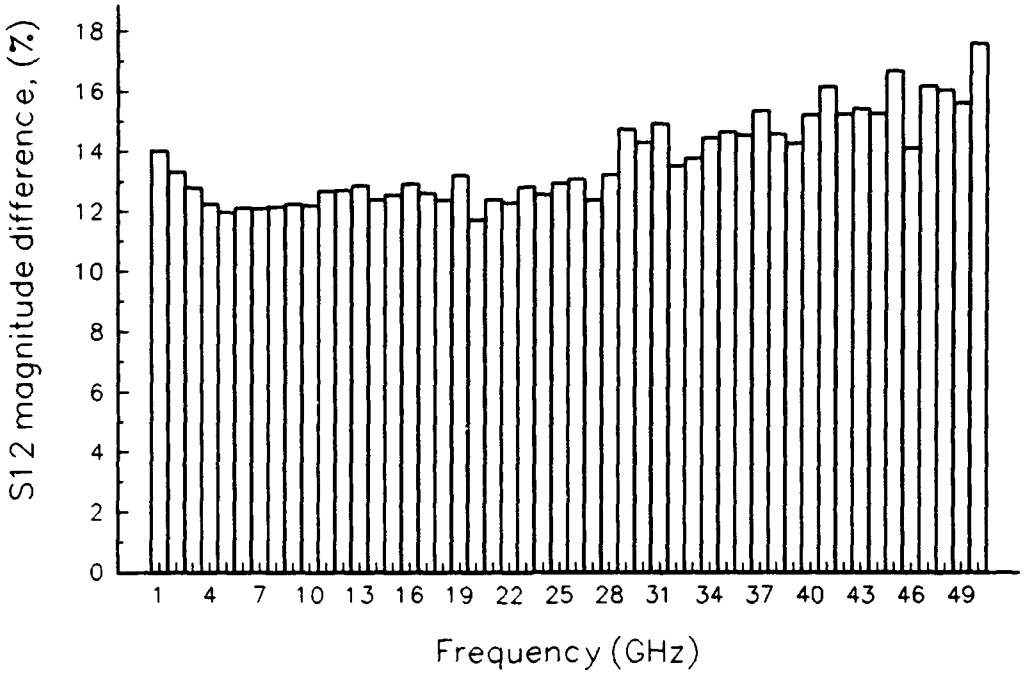

Figure 5.30 Percent difference between the modeled and measured magnitude of S_{12} for the 2u6d2f device at a 1 V, 800 μA bias.

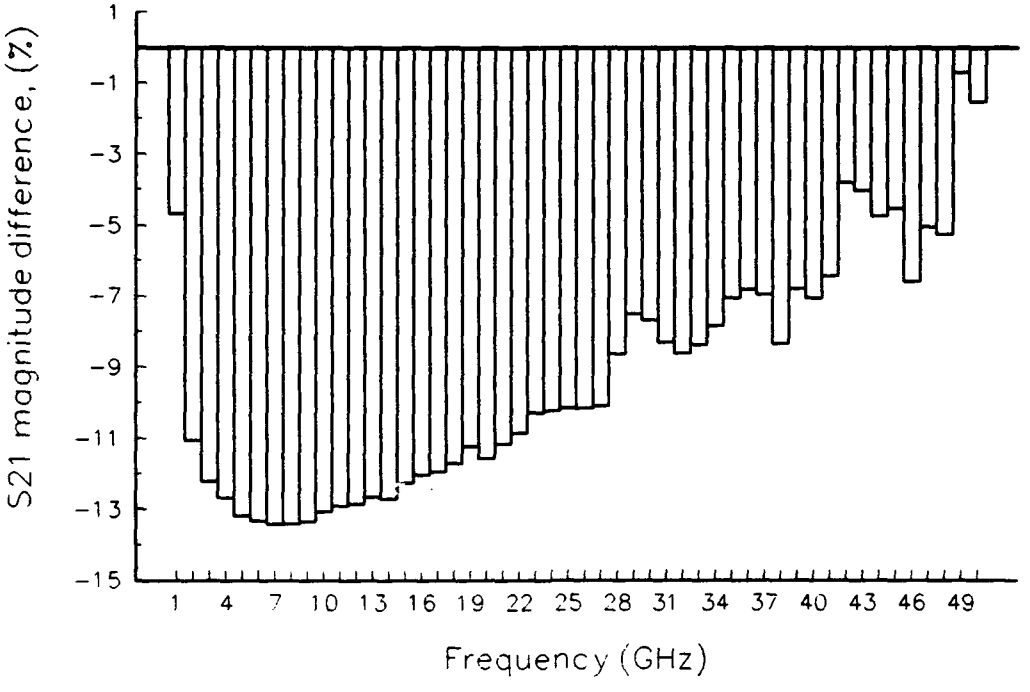

Figure 5.31 Percent difference between the modeled and measured magnitude of S_{21} for the 2u6d2f device at a 1 V, 800 μA bias.

about 17 GHz. The angle difference clearly increases linearly with frequency; a strong indication that the inductance is underestimated.

Similar to S_{11}, the magnitude of S_{22} shows excellent agreement by differing less than 3% for the entire 50 GHz range. Again, the percent difference in angle increases linearly with frequency providing further support of underestimated inductance. The model is successful in modeling S_{22} up to approximately 27 GHz.

Because the angle data for both S_{12} and S_{21} at the higher frequencies is relatively small, a plot of the percent angle difference is not a valuable metric in quantifying model performance. Clearly, the full model for both of these parameters is more accurate at the lower frequencies. Evidence supports an underestimation of the parasitic inductance as the primary cause for the limited agreement. The percent difference in the magnitudes of S_{12} and S_{21} is shown in Figs. 5.30 and 5.31. The difference in magnitude for S_{12} averages about 13% up to 28 GHz, and stays less than 18% over the entire frequency range. The difference in magnitude for S_{21} reaches a maximum of just over 13% at around 6 GHz and then decreases almost linearly for the rest of the frequency range. The difference in magnitude as well as the angle for these two gain parameters is expected to be improved by increasing the parasitics inductances. This will be confirmed in the section on sensitivity analysis.

Overall, this novel approach to a physics-based microwave HBT model produces fair agreement for all three devices. By inspection, one can see that the agreement for the 2u6d2f device is much better than for the one finger devices. As mentioned earlier, the main reason for this is expected to be the relative dominance of parasitics with respect to the intrinsic device in the one finger devices. Because the bare model data

for the 2u6d2f device is on average less than 25% from the measured data (magnitude and angle), the full model provides an adequate testbench for determining model parameter sensitivities.

5.2.3 Model parameter sensitivity analysis. The sensitivity analysis was performed by starting with the 2u6d2f model parameters as calculated by the Mathcad file. The value of each parasitic capacitor was increased and decreased by a factor of five. Similarly, since the need for increased inductances had already been hypothesized, the value of L_{ep} and L_{bp} was increased by an order of magnitude; L_{cp} was increased by two orders of magnitude to realize the expected changes. Additionally the impacts of decreasing *CJE* and *CJC* by a factor of five were investigated. Because *CJE* and *CJC* are the zero-bias depletion capacitances, a proportional change will be seen in C_π and C_μ, respectively. Recall that C_π and C_μ are the total junction capacitances (depletion and diffusion) dependent on bias as well as all the SPICE ac model parameters.

Each model parameter variation was treated as a control. The resulting HSPICE S-parameter data for each variation was compared to the original full model data to determine the effects that each parasitic had on model performance. The results are shown in Tables 5-9 through 5-15. For clarity and ease of visualization, the changes in angle ($\angle$) data are listed as either clockwise (cw) or counterclockwise (ccw) shifts around the Smith/polar charts. |M| is used as an abbreviation for magnitude. Also, in this context, low frequency refers to the 1 to 10 GHz range and high frequency refers to the 20 to 50 GHz range. The following qualitative definitions are used in Tables 5-9 through 5-15: significant for changes of greater than 25%, slight for changes of less than 20%, and minimal for changes of less than 10%.

Table 5-9

Sensitivity of C_{bcp} on S-parameters

S_{ij}	Effect on modeled S-parameters
S_{11}	- When decreased, shifted the ∠ ccw significantly at low f and decreased the $\|M\|$ at high f. - When increased, shifted the ∠ cw significantly at low f and increased the $\|M\|$ at high f.
S_{12}	- When decreased, decreased the $\|M\|$ at all f and increased the range of ∠ spread. - When increased, increased the $\|M\|$ at all f and reduced the range of ∠ spread.
S_{21}	- When decreased, increased the $\|M\|$ and shifted the ∠ ccw at all f. - When increased, decreased both the $\|M\|$ and shifted the ∠ cw significantly at all f.
S_{22}	- When decreased, shifted the ∠ ccw significantly at low f, decreased the $\|M\|$ at high f, and increased the $\|M\|$ at low f. - When increased, shifted the ∠ cw significantly at low f, increased the $\|M\|$ at high f, and significantly reduced the $\|M\|$ at low f.

Table 5-10

Sensitivity of C_{bep} on S-parameters

S_{ij}	Effect on modeled S-parameters
S_{11}	- Negligible effect.
S_{12}	- Minimal effect at low f. - Slight effect at high f.
S_{21}	- When increased, shifted the ∠ cw minimally at high f.
S_{22}	- Same as for S_{12}.

Table 5-11

Sensitivity of C_{cep} on S-parameters

S_{ij}	Effect on modeled S-parameters
S_{11}	- When increased, decreased the |M| slightly at all f.
S_{12}	- When increased, both decreased the |M| and shifted the ∠ cw significantly at high f.
S_{21}	- When increased, decreased the |M| minimally for all f, and shifted the ∠ cw at high f.
S_{22}	- When increased, increased the |M| and shifted the ∠ ccw at high f.

Table 5-12

Sensitivity of CJC on S-parameters

S_{ij}	Effect on modeled S-parameters
S_{11}	- Increased the |M| and shifted the ∠ ccw significantly at low f, and increased the |M| at high f.
S_{12}	- Decreased the |M| significantly and shifted the ∠ ccw at low f.
S_{21}	- Increased the |M| and shifted the ∠ ccw at all f.
S_{22}	- Both increased the |M| and shifted the ∠ ccw significantly at low f, and decreased the |M| at high f.

Table 5-13

Sensitivity of L_{ep} on S-parameters

S_{ij}	Effect on modeled S-parameters
S_{11}	- Minimal effect.
S_{12}	- Shifted ∠ cw at high f.
S_{21}	- Increased the |M| slightly at high f.
S_{22}	- Minimal effect.

Table 5-14

Sensitivity of L_{cp} on S-parameters

S_{ij}	Effect on modeled S-parameters
S_{11}	- Negligible effect.
S_{12}	- Decreased the |M| and shifted ∠ cw significantly at high f.
S_{21}	- Shifted the ∠ cw at high f.
S_{22}	- Increased the |M| slightly and shifted the ∠ cw significantly at high f.

Table 5-15

Sensitivity of L_{bp} on S-parameters

S_{ij}	Effect on modeled S-parameters
S_{11}	- Shifted the ∠ cw significantly at high f.
S_{12}	- Shifted the ∠ cw significantly at high f.
S_{21}	- Shifted the ∠ cw at high f.
S_{22}	- Negligible effect.

The inverse relationship that C_{bcp} has on S_{21} and S_{12} is easily conceptualized. Because S_{21} and S_{12} represent the forward and reverse transmission gains, respectively, their magnitudes are most effected by the base–collector parasitic capacitor that couples the input and output ports. Naturally, for a large gain the coupling between the input and output ports should be minimized (isolated). Increasing C_{bcp} increases the coupling between the ports which reduces gain (S_{21}) and increases feedback (S_{12}) throughout the frequency range modeled. C_{bcp} also serves to shift S_{11} and S_{22} along constant resistance circles at low frequency. A decrease in C_{bcp} increases capacitive reactance so each point on the curve is shifted counterclockwise, i.e. in the direction of increasing capacitive reactance on the Smith chart. This effect is significant only at low frequencies because the increase in reactance is inversely proportional to frequency. An increase in C_{cep} primarily decreases feedback and shifts the S_{12} curve clockwise at high frequency. By symmetry, C_{bep} will have the same effect. This change in S_{12} is one of the desired improvements identified in Fig. 5.23.

Reducing *CJE* by a factor of five had a negligible effect on the S-parameters. The reason for this is that under forward bias, C_{π} is relatively large and mostly diffusion capacitance. Therefore, any change in *CJE* will manifest only a small change in C_{π}. In fact, the script generated by HSPICE during each ac simulation (which lists the hybrid–π equivalent circuit element values), showed that reducing *CJE* by a factor of five only reduced C_{π} from 749 fF to 692 fF.

Reducing *CJC* by a factor of five had significant effect on all of the S-parameters, especially at low frequency. Under reverse bias both $C_{\mu int}$ and $C_{\mu ext}$ are dominated by their depletion components. Thus, reducing

CJC by a factor of five reduces both $C_{\mu int}$ and $C_{\mu ext}$ by a factor of five. Because all three base-collector capacitances ($C_{\mu int}$, $C_{\mu ext}$, and C_{bcp}) are to a first order approximation in parallel, the change in *CJC* effectively cuts the total base-collector capacitance in half.

The influence of L_{bp} and L_{cp} on the modeled S-parameters is exactly as envisioned in the last section. Increasing these two parameters will substantially improve the model's high frequency performance. As one might expect, L_{bp} has a negligible effect on S_{22}. By symmetry, L_{cp} has a negligible effect on S_{11}. Testbench simulation with HSPICE also shows that superposition of their independent results applies. That is, changing both L_{bp} and L_{cp} simultaneously effects the S-parameters by an amount equal to the sum of their individual effects on the S-parameters.

Based on the data observed while conducting the sensitivity analysis, increasing the parasitic inductances should provide excellent agreement through 50 GHz. Increasing the Mathcad values of L_{bp} by a factor of 20, and L_{cp} by a factor of 50 (which would result in $L_{bp} \approx 47$ pH and $L_{cp} \approx 30$ pH) is recommended. Several published HBT models have extracted values for these series inductances through various curve fitting and measurement techniques [28,31,72,73,76]. Each of these other models reports series inductances on the order of tens of picohenries.

Table 5-16 compares the 2u6d2f model parasitics with the parasitics of other published HBT models having similar equivalent circuits. Aside from one low value reported for L_{bp} [72], all of the 2u6d2f inductance values are from one to two orders of magnitude smaller than other published values. Another observation is that the 2u6d2f C_{bcp} value appears to have been overestimated.

At this point in the model derivation, the six parasitic values for the 2u6d2f device were optimized in HSPICE by fitting modeled S-parameters to measured S-parameters. The same bias (V_{CE} = 1 V and I_B = 800 μA) was used in the optimization for consistency. Table 5-17 shows the optimized parasitics. A comparison of the resulting S-parameters is shown in Figs. 5.32 - 5.35. The prediction that increasing L_{bp} and L_{cp} to 47 pH and 30 pH, respectively, would provide excellent agreement up through 50 GHz was confirmed. HSPICE optimized L_{bp} and L_{cp} at 44.35 pH and 28.68 pH, respectively. Figures 5.32 - 5.35 clearly show the very good to excellent agreement that all four S-parameters have up through 50 GHz.

To summarize, an underestimation of the parasitic base and collector series inductances was suspected as the reason for the good to poor S-parameter angle agreement at frequencies greater than 30 GHz. The sensitivity analysis assisted in predicting estimates for L_{bp} and L_{cp} that would provide excellent agreement up through 50 GHz. HSPICE optimization validated underestimation of L_{bp} and L_{cp} as the cause of the high frequency disagreement. The next step was to physically justify the optimized parasitic values. In other words, can the optimized parasitic values be substantiated using only a knowledge of the device material, geometry, and fabrication process.

The Mathcad equations for parasitic calculations were examined to see if any physical components of L_{bp} and L_{cp} were overlooked. In calculating L_{bp} and L_{cp}, only the portion of planar transmission line beneath the emitter bridge was considered. In reality, each of the devices modeled had a grounded backplane separated from the base and collector metals by 70 microns of GaAs substrate. Therefore, the grounded backplane forms a transmission line with the base and collector

Table 5-16

Comparison of 2u6d2f Parasitics With Other HBT Models

Parasitic	2u6d2f	Ref [31]	Ref [71]	Ref [74]
L_{ep} (pH)	0.4841	12	39	10
L_{bp} (pH)	2.3562	47	1	30
L_{cp} (pH)	0.6093	50	60	49
C_{bcp} (fF)	106.13	3	2	6.3
C_{bep} (fF)	7.3255	13	3	40
C_{cep} (fF)	18.488	20	13	31

Table 5-17

Optimized Parasitics for the 2u6d2f Device

Parasitic	Initial	Low	High	Optimized
L_{ep} (pH)	15	0.3	30	1.71
L_{bp} (pH)	40	8	85	44.35
L_{cp} (pH)	20	5	50	28.68
C_{bcp} (fF)	7.6	1	114	76.01
C_{bep} (fF)	6	1	30	26.42
C_{cep} (fF)	18.5	3.7	92.5	76.18

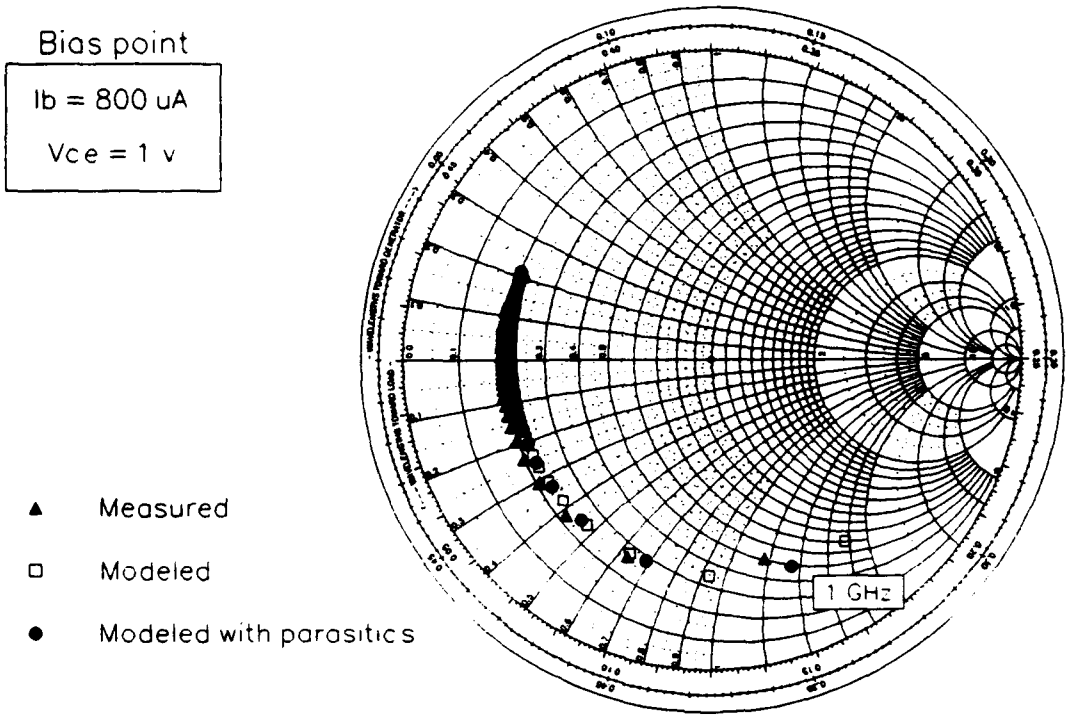

Figure 5.32 Comparison of S_{11} for the 2u6d2f device from 1 to 50 GHz with optimized parasitics.

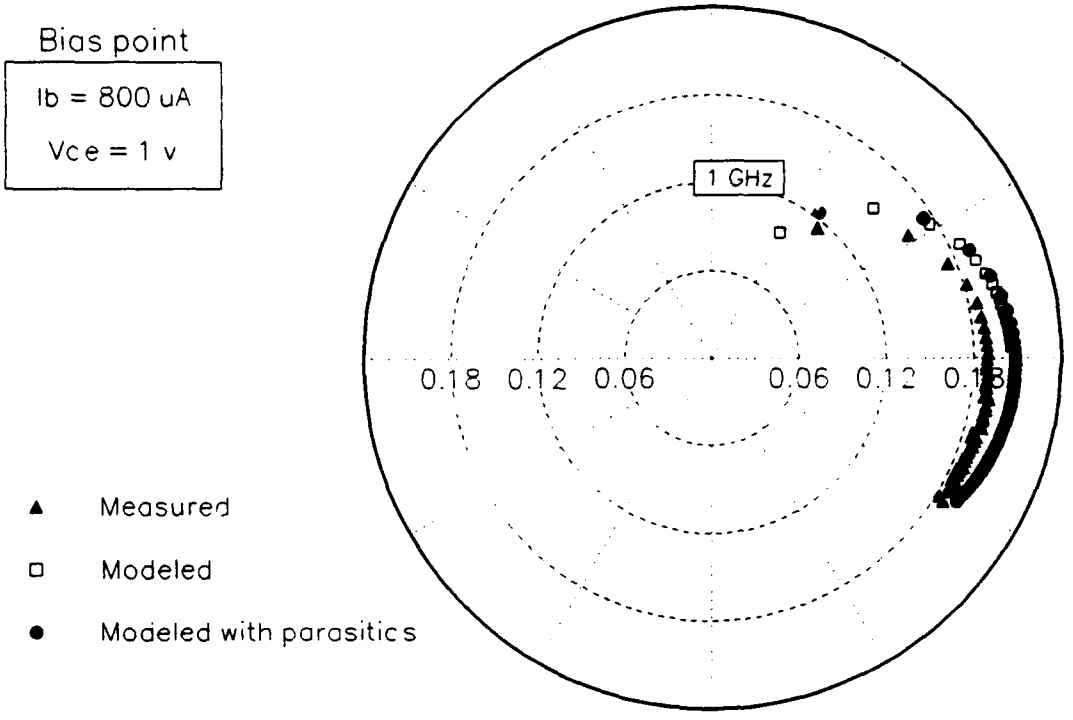

Figure 5.33 Comparison of S_{12} for the 2u6d2f device from 1 to 50 GHz with optimized parasitics.

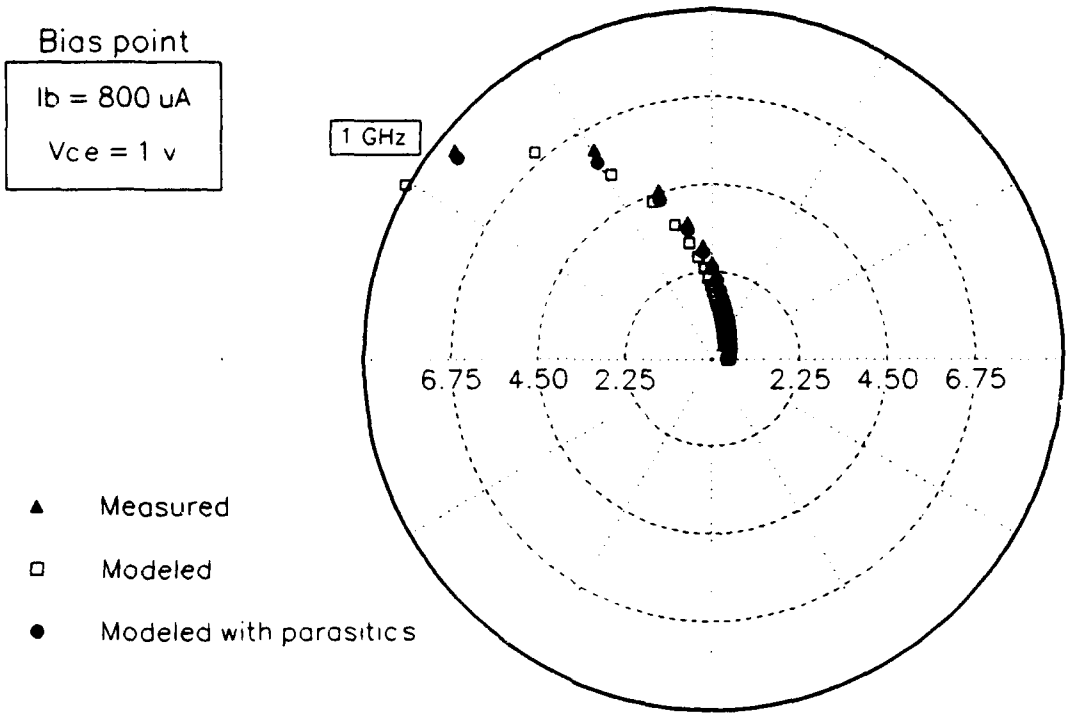

Figure 5.34 Comparison of S_{21} for the 2u6d2f device from 1 to 50 GHz with optimized parasitics.

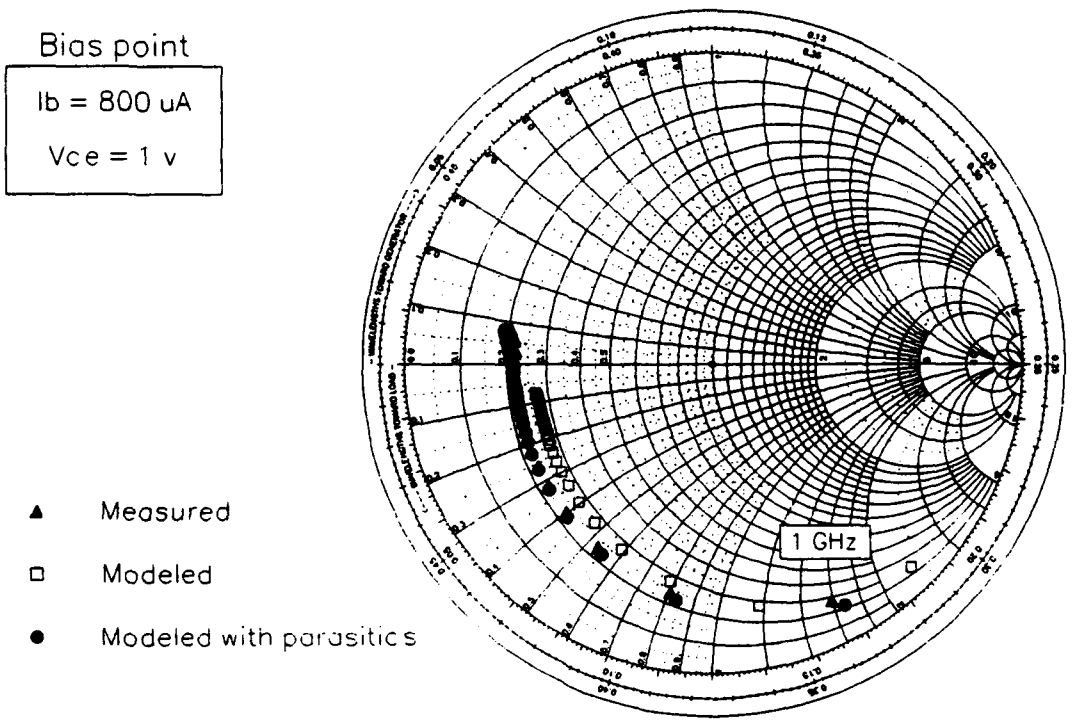

Figure 5.35 Comparison of S_{22} for the 2u6d2f device from 1 to 50 GHz with optimized parasitics.

interconnect metals between the pad and emitter bridge. The contribution of this transmission line configuration to L_{bp} and L_{cp} is much greater than the contribution of the transmission line approximation beneath the emitter bridge. The reason for this is because planar transmission line inductance is proportional to the separation between the conductors. Since the thickness of the substrate ($\approx$ 70 microns) is 25 to 70 times the separation between the conductors beneath the emitter (one to three microns), the component of L_{bp} and L_{cp} beneath the emitter bridge is almost negligible. However, the parallel combination of L_{bp} and L_{cp} beneath the emitter bridge is still a fair approximation for L_{ep}. This is assumption is substantiated by the relatively low optimized value of L_{ep}.

The calculated L_{bp} and L_{cp} due to the interconnect metals between the pad and emitter bridge was approximately a factor of three larger than the optimized L_{bp} and L_{cp}. One explanation is that the simple planar transmission line inductance equation does not accurately predict the actual inductance. This is most likely because the actual geometry is not a planar transmission line.

In Chapter 4, C_{bep} and C_{cep} were estimated using the parallel plate approximation. Due to the complex emitter geometry, one could theorize that the actual values of C_{bep} and C_{cep} would be two to three times greater than the parallel plate values. This assumption is validated by the Mathcad values for C_{bep} and C_{cep}, which are approximately two to three times smaller than the optimized values. Any contributions to C_{bep} and C_{cep} due to the grounded backplane are negligible, since parallel plate capacitance is inversely proportional to plate separation.

In summary, the attempt to physically substantiate the optimized 2u6d2f parasitic values resulted in capacitances that were two to three

times smaller than the optimized values, and inductances that were two to three times larger than the optimized values. Although larger capacitances are easy to conceptualize based on the geometry, they are too difficult to accurately calculate with a simple formula. Accurate parasitic values are best obtained using a special electromagnetic software package that can recognize random three dimensional transmission line geometries.

Table 5-18 compares the 2u6d2f SPICE bare model parameters with the parameters from other published HBT SPICE models. Obviously, since each of the HBTs characterized by the various model parameters has differences in geometry and fabrication, the listing provides only a rough comparison. The results show that the 2u6d2f model is a sound physics-based HBT model; all of the parameters are roughly the same magnitude as the other model's parameters. Any differences in the model parameters can be attributed to differences in the device material, geometry, and fabrication process. Some of the differences between the various models will now be discussed.

There are two ways to model recombination in the extended Ebers-Moll topology. The first provides more insight into the effects of recombination since four model parameters are needed to characterize. This entails calculating (or measuring) the composite recombination saturation currents *ISE* and *ISC* along with their corresponding ideality factors, *NE* and *NC*. The second method will generally give better results since it is less prone to errors; however, some of the physical insight into the various recombination mechanisms is lost. In this method, *ISE* and *ISC* are set to zero and all recombination is accounted for in an empirical value of β_F.

Table 5-18

Various HBT SPICE Model Parameters

Param.	Ref[78]	Ref[25]	Ref[26]	Ref[71]	Ref[77]	2u6d2f
BF	3.444	300	52.52		169	83.93
BR	2.1e-07	0.40	0.1987		0.1	0.6338
TF, s	1.51e-12	4.3e-12		3e-12	4e-12	9.52e-13
TR, s				3.5e-10		1.26e-10
IS, A	1.67e-26	5.00e-25	4.84e-24	9.4e-26	8.0e-24	1.11e-25
ISE, A		4.00e-17	2.46e-18	2.39e-16	3.0e-20	2.43e-19
ISC, A		1.42e-14	5.93e-14	1.8e-14		4.39e-16
RE, Ω	5.4	11.0	17.61	45	0.0	6.7896
RB, Ω	30.7	37.3	122.23	150	34	4.8379
RC, Ω	6.6	6.42	10.26	51	6	2.205
CJE, F	3.5e-14	1.25e-13		8.6e-15	1.7e-14	4.89e-14
CJC, F	9.16e-15	3.95e-14		1.9e-14		1.58e-13
VJE, V	1.72	1.45		1.45	1.7	1.7018
VJC, V	1.40	1.18		1.4	1.21	1.4107
MJE	0.5	0.51		0.5	0.5	0.5
MJC	0.5	0.5		0.33	0.5	0.5
NF	1.16	1.021	1.1331	1	1.179	1.1049
NR	1.00	1.00	1.00			1.00
NE		1.186	1.8211	2	1.6	1.7000
NC		1.950	1.9698	2		1.7595
XCJX		0.220				0.159

As discussed in earlier chapters, HBTs rarely have a region of operation in which β_F is constant. Because an HBT's recombination currents are bias dependent, any empirical β_F that accounts for recombination will also be bias dependent. Unfortunately, SPICE expects a constant *BF* and does not directly support a bias dependent *BF*. Recall from Eqs. (5.1) and (5.2) that recombination modeled via *ISE* and *ISC* is automatically bias dependent in SPICE, because the terms that include *ISE* and *ISC* are functions of $V_{B'E'}$ and $V_{B'C'}$. Therefore, if an empirical *BF* is used to account for bias dependent recombination in SPICE, one must write the SPICE HBT model file with *BF* as a function of a known bias condition, either I_B or V_{BE} (reference Fig. 5.10 and related discussion). This technique is sufficient for microwave simulations where the dc bias is generally fixed, but may be impractical for dc applications where the bias is variable.

Of the model's presented in Table 5-18, Teeter *et al.*'s model [78] is unique because their *BF* is an empirical β_F. Although not shown in Table 5-18, their *BF* is a function of V_{BE}. As expected, their model does not include values for *ISE*, *ISC*, *NE*, or *NC*.

Grossman's and Choma's model [25] is partly physical and partly empirical. Their *BF* is physically calculated due only to bulk recombination current in the neutral base. Consequently, values for *ISE*, *ISC*, *NE*, and *NC* are needed to account for the other recombination mechanisms present in the HBT. This method of modeling recombination was used to model the 2u6d2f device. The difference between the reference [25] and the 2u6d2f *BF* can be attributed to differences in base doping and thickness. All the differences in the remaining model parameters can

likewise be attributed to differences in the geometry and fabrication process.

The model of reference [71] uses physical parameters (material, geometry, and fabrication process) as well as measured data to determine the SPICE model parameters. Information on how each parameter is specifically calculated is not available. Therefore, the parameters listed provide only an example of the magnitude of each parameter that SPICE uses to model their particular HBT.

Notice that Hafizi *et al.*'s model [26] is only a dc model, since none of the charge storage, removal, and transport model parameters are included. All of their model parameters were determined via convergence of a least square fit to measured I-V data. These parameters are purely curve fit and provide no meaningful basis for a physical comparison.

Matsuno *et al.*'s model [77] includes several passive elements (diodes and resistors) external to the SPICE BJT model. Their RE is modeled by an external resistor so the model card RE is set to zero. Similar to Hafizi *et al.*'s model [26], Matsuno *et al.*'s HBT dc and ac parameters are optimized via curve fitting to measured I-V data and S-parameters, respectively. The specific optimization technique or package is not specified. Again, the model parameters listed are merely those that, given a particular equivalent circuit topology, best fit the measured data. All insight into how the device material, geometry, and fabrication process affect the model parameters (and thus, the electrical performance) is lost.

6. Conclusions and Recommendations

The objective of the research presented in this thesis was to derive a physics-based model for an HBT that would accurately predict the device's electrical behavior from dc to microwave frequencies. A model that considers a cylindrical emitter-base geometry and is directly implemented into SPICE was developed. Using semiconductor physics, the device model parameters were determined from a knowledge of the device material, geometry, and fabrication process.

A Mathcad file was written which calculates all of the necessary SPICE BJT model parameters required to accurately model an HBT. The dc model was successful at producing data that was within ± 5% of the measured data for two device geometries. dc model data for a third geometry was an average of 6.73% different from the measured data. When curve fit against measured data to determine ideality factors, the bias dependent β and offset voltage of an HBT are accurately modeled.

Parasitic inductor and capacitor elements were physically determined and added to the SPICE model. Poor to good agreement was obtained between the resulting S-parameters for two of the device geometries; good to excellent agreement was obtained for the third. Precise calculation of the base and collector parasitic inductances was verified as the limiting factor of the high frequency performance of the model. To the best of the author's knowledge, this thesis is the first to report such good agreement from a physics-based microwave HBT model.

More work needs to be accomplished to better model the devices in saturation. A known limitation is the inability of SPICE to account for the bias dependence of RC. If applications demand better agreement in

saturation, the SPICE source code could be modified to solve for RC simultaneously with the base-collector junction voltage. However, this procedure is not recommended since the ends would not justify the means.

A better analysis of the model's performance could be obtained by comparison with measurements from more than one set of data for each geometry. Because the model presented in this thesis is physics-based, only theoretical data is modeled. Collecting measured data from more than one device with the same geometry would assist in verifying the model's ability to predict actual device performance. Measured data from the other side of the wafer or even another wafer could themselves be ± 5% different. Additionally, forward and reverse Gummel plots would provide valuable insight into the device's saturation currents and ideality factors. Gummel plots are well suited to graphical extraction of all three saturation currents and the four ideality factors, because each of these SPICE model parameters can be directly related to a slope or intercept on the forward and reverse Gummel plots. Obviously, the common-emitter I-V characteristics are dependent on the model saturation currents and ideality factors; however, these parameters cannot be graphically extracted as in the Gummel plots.

The model is easily modified to account for varying degrees of graded or abrupt emitter-base heterojunctions as well as for graded base or double HBTs by revising the appropriate equations in the Mathcad file. Another improvement would be to account for HBTs fabricated from materials other than $Al_xGa_{1-x}As/GaAs$. Modeling HBTs of various materials (holding the geometry and fabrication parameters constant) could be accomplished readily by modifying the section on material constants and the empirical mobility equations in the Mathcad file.

The most significant improvement would be the development of a full electro-thermal model that considers all the effects of device self-heating and heat dissipation. Almost all of the material parameters have a temperature dependence described by equations that can be found in the literature. Additionally, HSPICE has several BJT model parameters to account for device performance as a function of temperature.

To the best of the author's knowledge, this thesis is the only physics-based HBT model that attempts to model the effects of device parasitics at microwave frequencies. All other microwave device modeling techniques first measure the S-parameters and then curve fit the measured S-parameters to a particular equivalent circuit topology. Parasitic element values are optimized to best fit the measured S-parameters.

Using the expression for parallel plate capacitance, parasitic capacitance element values were determined. Fringing was neglected with the exception of base-collector capacitance, which is mostly a fringe capacitance. To a first order approximation, the values determined should be accurate.

Using the expression for the inductance of a planar transmission line, parasitic inductance values were determined. From a strict electromagnetic perspective, this method of calculating inductance is only an approximation. The models developed in this thesis could be improved by using more exact electromagnetic equations to calculate the parasitic inductances and capacitances.

One may consider the emitter, base, and collector metallizations as three planar sections of transmission line. The geometry and dielectric constants are known. A program could be written (or an existing program modified) to calculate the characteristic impedances of the set of

transmission lines in the transistor geometry. The parasitic inductances and capacitances could then be determined from the characteristic impedances and placed in the present HSPICE HBT model. The resulting model would have more accurate parasitic element values and therefore be more accurate at microwave frequencies. The novel result would be a purely physics-based model that would perform as well as any curve fit model. The best of both worlds would be obtained in such a model: the incredible design flexibility and savings of a physics-based model with the excellent accuracy of a curve fit model.

Appendix A: Mathcad Files

HBT PHYSICAL PARAMETER CALCULATIONS

Author: James A. Fellows
Date: 20 Nov 93
Filename: H_3u1d1f.mcd
Description: This program determines all of the model parameters required to characterize a graded AlGaAs/GaAs heterojunction bipolar transistor (HBT) in SPICE. The calculated parameters will be placed directly into the SPICE BJT model card. Also calculated are the parasitic inductance and capacitance equivalent circuit element values. All values are physically determined using a knowledge of only the device material, geometry and fabrication process. Only three of the four ideality factors are empirically determined.
Inputs: This program requires the device designer to input several specific fabrication constants. These variables are included in the first section for convenience.

Fabrication Parameters:

$N_E = 5 \cdot 10^{17}$	AlGaAs emitter doping concentration (cm^-3)
$N_B = 5 \cdot 10^{19}$	GaAs base doping concentration (cm^-3)
$N_C = 2 \cdot 10^{16}$	GaAs collector doping concentration (cm^-3)
$N_{subC} = 3 \cdot 10^{18}$	Subcollector doping concentration (cm^-3)
$l_{cap} = 3 \cdot 10^{-6}$	Thickness of InGaAs emitter cap (cm)
$N_{cap} = 2 \cdot 10^{19}$	Cap doping concentration (cm^-3)
$l_{cgrad} = 2.5 \cdot 10^{-6}$	Thickness of InGaAs graded region (cm)
$N_{cgrad} = 1 \cdot 10^{19}$	Graded region doping concentration (cm^-3)
$l_{E.cont} = 1 \cdot 10^{-5}$	Thickness of GaAs emitter region (cm)
$N_{E.cont} = 5 \cdot 10^{18}$	GaAs doping concentration (cm^-3)
$l_{grade} = 5 \cdot 10^{-6}$	Thickness of AlGaAs graded region (cm)
$N_{grade} = 5 \cdot 10^{17}$	AlGaAs graded doping concentration (cm^-3)
$l_{wide} = 5 \cdot 10^{-6}$	Thickness of the AlGaAs emitter (cm)
$X_G = 1.5 \cdot 10^{-6}$	Thickness of emitter-base junction grading (cm)

$W := 7 \cdot 10^{-6}$ Thickness of the GaAs base (cm)

$l_C := 1 \cdot 10^{-4}$ Thickness of the GaAs collector (cm)

$l_{subC} := 1 \cdot 10^{-4}$ Thickness of the GaAs subcollector (cm)

$l_{ee} := 3 \cdot 10^{-4}$ Diameter of an emitter dot (cm)

$N_{dot} := 1$ Number of emitter dots/finger

$N_{fin} := 1$ Number of base-emitter fingers

$l_{cc} := 11 \cdot 10^{-4}$ The length of the collector contact (cm)

$l_{cl} := 9 \cdot 10^{-4}$ The width of the collector contact (cm)

$l_{eb} := 1 \cdot 10^{-4}$ The width of base finger contact on either side of emitter dot (cm)

$l_{bc} := 2 \cdot 10^{-4}$ The lateral distance between the base and collector contact (cm)

$\rho_{Ec} := 2 \cdot 10^{-6}$ Estimated emitter specific contact resistance (ohm.cm^2)

$\rho_{Bc} := 5 \cdot 10^{-6}$ Estimated base specific contact resistance (ohm.cm^2)

$$A_{be} := N_{dot} \cdot N_{fin} \cdot \pi \cdot \left(\frac{l_{ee}}{2} - 0.1 \cdot 10^{-4} \right)^2$$

$A_{be} = 6.1575 \cdot 10^{-8}$ Base-emitter junction area (cm^2)

$$A_{bc} := N_{dot} \cdot N_{fin} \cdot \left(l_{ee} + 2 \cdot 10^{-4} \right) \cdot \left(l_{ee} \cdot 2 \right)$$

$A_{bc} = 3 \cdot 10^{-7}$ Base-collector junction area (cm^2)

$$XCJC := \frac{A_{be}}{A_{bc}}$$ Fraction of base-collector area internal to device

$$P := N_{fin} \cdot N_{dot} \cdot \pi \cdot \left(\frac{l_{ee}}{2} - 0.1 \cdot 10^{-4} \right)^2$$ Total perimeter of emitter-base junction (cm)

$d_{eb} := 1 \cdot 10^{-4}$	Height of polyimide between the base and emitter metallizations (cm)
$t_{cp} := 0.4 \cdot 10^{-4}$	Thickness of collector pad metal (cm)
$l_{bb} := l_{ee} + 2 \cdot 10^{-4}$	Width of base finger (cm)
$t_{sub} := 70 \cdot 10^{-4}$	Thickness of GaAs substrate (cm)

General constants:

$k := 8.61738 \cdot 10^{-5}$	Boltzmann's constant (eV/K)
$q := 1.602 \cdot 10^{-19}$	Electron charge (C)
$\varepsilon_o := 8.854 \cdot 10^{-14}$	Permittivity in vacuum (F/cm)
$\mu_o := 4 \cdot \pi \cdot 10^{-9}$	Permeability in vacuum (H/cm)
$m_o := 9.1095 \cdot 10^{-31}$	Electron rest mass (Kg)
$T := 300$	Temperature (K)

Material constants:

The only user defined constant is x, the mole fraction of Al. The expressions below are taken from the following references [24, 55, 57, 59].

$x := 0.35$	Mole fraction of Al in the emitter
$E_{gE} := 1.424 + 1.247 \cdot x$	Band-gap energy of the AlGaAs emitter (eV)
$\Delta E_{gB} := 1.6 \cdot 10^{-8} \cdot N_B^{\frac{1}{3}}$	Band-gap shrinkage in the GaAs base (eV)

$E_{gB} := 1.424 - \Delta E_{gB}$ Band-gap energy of the GaAs base (eV)

$\Delta E := E_{gE} - E_{gB}$ Band-gap difference at the abrupt emitter-base heterojunction (eV)

$\varepsilon := 13.18 - 3.12 \cdot x$ Relative permittivity of the AlGaAs emitter

$\varepsilon_B := 13.18 \cdot \varepsilon_o$ Permittivity of the GaAs base (F/cm)

$\varepsilon_E := \varepsilon \cdot \varepsilon_o$ Permittivity of the AlGaAs emitter (F/cm)

$\varepsilon_p := 3.5 \cdot \varepsilon_o$ Permittivity of polyimide (F/cm)

$$n_{iB} := 1.79 \cdot 10^6 \cdot \exp\left(\frac{\Delta E_{gB}}{k \cdot T}\right)^{0.5}$$ Intrinsic carrier concentration in the GaAs base at 300K as a function of doping (cm^-3)

$$n_{iE} := n_{iB} \cdot \exp\left(\frac{\Delta E}{k \cdot T}\right)^{-0.5}$$ Intrinsic carrier concentration in the emitter at 300K (cm^-3)

$n_{iC} := 1.79 \cdot 10^6$ Intrinsic carrier concentration in the collector (cm^-3)

$v_{sat} := 1 \cdot 10^7$ Electron saturation velocity in GaAs at 300K (cm/s)

$N_t := 1 \cdot 10^{15}$ SRH recombination trap density in GaAs (cm^-3)

$N_{tI} := 1 \cdot 10^{12}$ AlGaAs/GaAs interface density of states (cm^-2)

$\sigma_n := 1 \cdot 10^{-15}$ Capture cross section of an electron (cm^2)

$m_n := 0.067 \cdot m_o$ Electron effective mass in GaAs (Kg)

$A_p := 1 \cdot 10^{-30}$ Auger recombination coefficient in GaAs (cm^6/s)

$B := 2 \cdot 10^{-10}$ Radiative recombination coefficient in GaAs (cm^3/s)

$\rho_{Au} := 2.44 \cdot 10^{-6}$ Resistivity of gold metallization (ohm.cm)

$\Delta E_c := 0.797 \cdot x$ Difference in conduction band energy at the interface (eV)

$S_o := 1 \cdot 10^6$ Intrinsic surface recombination velocity (cm/s)

$L_s := 1 \cdot 10^{-5}$ Surface diffusion length (cm)

One of the most elementary calculations is that of the built-in voltage for each junction:

$$VJE := k \cdot T \cdot \ln\left(\frac{N_E \cdot N_B}{n_{iE} \cdot n_{iB}}\right) + \Delta E_c - \frac{\Delta E}{2} \qquad VJE = 1.7018$$

$$VJC := k \cdot T \cdot \ln\left(\frac{N_B \cdot N_C}{n_{iB} \cdot n_{iC}}\right) \qquad VJC = 1.3691$$

The zero-bias depletion widths may be calculated from Ryum and Abdel-Motaleb [23:873]:

$$X_{1o} := \sqrt{\frac{2 \cdot N_B \cdot \varepsilon_E \cdot \varepsilon_B \cdot (VJE - 1.64 \cdot k \cdot T)}{q \cdot N_E \cdot (\varepsilon_E \cdot N_E + \varepsilon_B \cdot N_B)}} \qquad X_{2o} := \frac{N_E}{N_B} \cdot X_{1o}$$

$$X_{3o} := \sqrt{\frac{2 \cdot N_C \cdot \varepsilon_B \cdot (VJC - k \cdot T)}{q \cdot N_B \cdot (N_C + N_B)}} \qquad X_{4o} := \frac{N_B}{N_C} \cdot X_{3o}$$

$X_{1o} = 6.6288 \cdot 10^{-6}$ On the emitter side of the EB junction (cm)

$X_{2o} = 6.6288 \cdot 10^{-8}$ On the base side of the EB junction (cm)

$X_{3o} = 1.251 \cdot 10^{-8}$ On the base side of the CB junction (cm)

$X_{4o} = 3.1274 \cdot 10^{-5}$ On the collector side of the CB junction (cm)

The effective zero-bias base width Wb, is found by subtracting the depletion widths in the base on both the emitter and collector sides:

$$W_B := W - (X_{2o} + X_{3o}) \qquad W_B = 6.9212 \cdot 10^{-6} \quad (cm)$$

Now, calculate the depletion capacitances from Ryum and Abdel-Motaleb [23:873]:

$$CJE := A_{be} \cdot \frac{(\varepsilon_E \cdot \varepsilon_B)}{\varepsilon_E \cdot X_{2o} + \varepsilon_B \cdot X_{1o}} \qquad CJE = 9.8515 \cdot 10^{-15}$$

$$CJC := A_{bc} \cdot \frac{\varepsilon_B}{X_{3o} + X_{4o}} \qquad CJC = 1.119 \cdot 10^{-14}$$

Calculating the value of Cje with a nominal bias is helpful. Since a nominal value of Vbe is 1.5 V, we have:

$$X_{1o} := \sqrt{\frac{2 \cdot N_B \cdot \varepsilon_E \cdot \varepsilon_B \cdot (VJE - 1.64 \cdot k \cdot T - 1.5)}{q \cdot N_E \cdot (\varepsilon_E \cdot N_E + \varepsilon_B \cdot N_B)}} \qquad X_{2o} := \frac{N_E}{N_B} \cdot X_{1o}$$

$$CJE_{bias} := A_{be} \cdot \frac{(\varepsilon_E \cdot \varepsilon_B)}{\varepsilon_E \cdot X_{2o} + \varepsilon_B \cdot X_{1o}} \qquad CJE_{bias} = 3.1789 \cdot 10^{-14}$$

The minority electron mobility in the p-type base GaAs as a function of base doping can be found from the empirical relation stated by Ali and Gupta [53:202]. A similar relation for minority holes in the collector is stated by C. Selvakumar [55:773]. The diffusivities are then calculated from the Einstein relation:

$$\mu_n := \frac{7057}{1 + \left(\frac{N_B}{2.84 \cdot 10^{16}}\right)^{0.753}} + 943 \qquad \mu_n = 968.2979 \qquad D_{nB} := \mu_n \cdot k \cdot T$$

$$\mu_{pE} := \frac{360}{1 + \left(\frac{N_E}{2.5 \cdot 10^{17}}\right)^{0.417}} + 40 \qquad \mu_{pE} = 194.1658 \qquad D_{pE} := \mu_{pE} \cdot k \cdot T$$

$$\mu_{pC} := \frac{360}{1 + \left(\frac{N_C}{2.5 \cdot 10^{17}}\right)^{0.417}} + 40 \qquad \mu_{pC} = 306.902 \qquad D_{pC} := \mu_{pC} \cdot k \cdot T$$

$D_{nB} = 25.0326$ Diffusivity of minority electrons in the base (cm^2/s)

$D_{pE} = 5.0196$ Estimated diffusivity of minority holes in the emitter (cm^2/s)

$D_{pC} = 7.9341$ Diffusivity of minority holes in the collector (cm^2/s)

The base transit time has many forms [60,51], but ultimately from Hodges and Jackson [44:162]:

$$TF := \frac{W_B^2}{2.43 \cdot D_{nB}} \qquad TF := \frac{W_B^2}{2 \cdot D_{nB}} + \frac{W_B}{v_{sat}} \qquad TF := \frac{W_B^2}{2 \cdot D_{nB}}$$

$TF = 9.5681 \cdot 10^{-13}$ The forward transit time of minority electrons across the base (s)

Excess minority electron lifetime may be obtained by considering the lifetime of each recombination component. The expression for tno is taken from Lundstrom et al. [56:698]:

$$v_{th} := 100 \cdot \left(\frac{q \cdot k \cdot T}{2 \cdot \pi \cdot m_n} \right)^{0.5} \qquad v_{th} = 1.0392 \cdot 10^7$$ Average thermal velocity of an electron in GaAs (cm/s)

$$t_{SRH} := \frac{1}{\sigma_n \cdot N_t \cdot v_{th}} \qquad t_{SRH} = 9.6227 \cdot 10^{-8}$$ Shockley-Read-Hall recombination lifetime in GaAs (s)

$$t_{Aug} := \frac{1}{A_p \cdot N_B^2} \qquad t_{Aug} = 4 \cdot 10^{-10}$$ Auger recombination lifetime in p-type GaAs (s)

$$t_{rad} := \frac{1}{B \cdot N_B} \qquad t_{rad} = 1 \cdot 10^{-10}$$ Radiative recombination lifetime in p-type GaAs (s)

$$t_{no} := \left(\frac{1}{t_{SRH}} + \frac{1}{t_{Aug}} + \frac{1}{t_{rad}} \right)^{-1}$$

$t_{no} = 7.9934 \cdot 10^{-11}$ Minority electron lifetime in the base (s)

$t_{poC} := 20 \cdot 10^{-9}$ Minority hole lifetime in the collector (s)

$L_{nB} := \sqrt{D_{nB} \cdot t_{no}}$ $L_{nB} = 4.4732 \cdot 10^{-5}$ Diffusion length of electrons in the base (cm)

$L_{pC} := \sqrt{D_{pC} \cdot t_{poC}}$ $L_{pC} = 3.9835 \cdot 10^{-4}$ Diffusion length of holes in the collector (cm)

The diffusion length of minority holes in the emitter is estimated from an empirical expression found in Ryum and Abdel-Motaleb [23:876]:

$$L_{pE} := \frac{42.46 - \log(N_E)}{9.21 \cdot 10^3} \qquad L_{pE} = 0.0027$$ Diffusion length of holes in the emitter (cm)

The maximum dc Beta for an HBT is best described by Kroemer [13:15]; however, better dc agreement between modeled and measured data is obtained if beta is considered due only to recombination in the neutral base after Grossman and Choma [25:459]:

$$v_{nB} := \frac{D_{nB}}{L_{nB}} \qquad v_{pE} := \frac{D_{pE}}{L_{pE}} \qquad BF_{max} := \frac{N_E}{N_B} \cdot \frac{v_{nB}}{v_{pE}} \cdot \exp\left(\frac{\Delta E}{k \cdot T}\right)$$

$$BF := \frac{t_{no}}{TF} \qquad BF = 83.5413$$

IS can be estimated from Huang and Abdel-Motaleb [66:165]:

$$IS := \frac{q \cdot A_{be} \cdot n_{iB}^2 \cdot D_{nB}}{W_B \cdot N_B} \qquad IS = 2.2354 \cdot 10^{-26}$$

$$Ics := A_{bc} \cdot q \cdot \left(\frac{D_{nB} \cdot n_{iB}^2}{L_{nB} \cdot N_B} + \frac{D_{pC} \cdot n_{iC}^2}{L_{pC} \cdot N_C}\right) \qquad Ics = 1.702 \cdot 10^{-25}$$

Now, we can calculate the reverse beta, BR, and reverse tau, TR:

$$\text{alpha}_R := \frac{IS}{Ics} \qquad \text{alpha}_R = 0.1313 \qquad \text{Reverse common-base current gain}$$

$$BR := \frac{\text{alpha}_R}{1 - \text{alpha}_R} \qquad BR = 0.1512 \qquad \text{Reverse common-emitter current gain}$$

$$TR := \frac{t_{no}}{BR} \qquad TR = 5.287 \cdot 10^{-10} \qquad \text{Reverse base transit time (s)}$$

We can also determine the series emitter and collector resistances, RE and RC, after Ali and Gupta [53:204]. Resistivities for are calculated from the empirical mobility relations.

$$\mu_{cap} := \frac{7057}{1 + \left(\frac{N_{cap}}{2.84 \cdot 10^{16}}\right)^{0.753}} + 943 \qquad \rho_{InGaAs} := \left(q \cdot N_{cap} \cdot \mu_{cap}\right)^{-1}$$

$$\mu_{cgrad} := \frac{7057}{1 + \left(\frac{N_{cgrad}}{2.84 \cdot 10^{16}}\right)^{0.753}} + 943 \qquad \rho_{cgrad} := \left(q \cdot N_{cgrad} \cdot \mu_{cgrad}\right)^{-1}$$

$$\mu_{E.cont} := \frac{7057}{1 + \left(\frac{N_{E.cont}}{2.84 \cdot 10^{16}}\right)^{0.753}} + 943 \qquad \rho_{E.cont} := \left(q \cdot N_{E.cont} \cdot \mu_{E.cont}\right)^{-1}$$

$$\mu_{grade} := \frac{7057}{1 + \left(\frac{N_{grade}}{2.84 \cdot 10^{16}}\right)^{0.753}} + 943 \qquad \rho_{grade} := \left(q \cdot N_{grade} \cdot \mu_{grade}\right)^{-1}$$

$$\mu_E := \frac{7057}{1 + \left(\frac{N_E}{2.84 \cdot 10^{16}}\right)^{0.753}} + 943 \qquad \rho_{AlGaAs} := \left(q \cdot N_E \cdot \mu_E\right)^{-1}$$

$$\mu_C := \frac{7057}{1 + \left(\frac{N_C}{2.84 \cdot 10^{16}}\right)^{0.753}} + 943 \qquad \rho_C := \left(q \cdot N_C \cdot \mu_C\right)^{-1}$$

$$\mu_{subC} := \frac{7057}{1 + \left(\frac{N_{subC}}{2.84 \cdot 10^{16}}\right)^{0.753}} + 943 \qquad \rho_{subC} := \left(q \cdot N_{subC} \cdot \mu_{subC}\right)^{-1}$$

$$\mu_p := \frac{360}{1 + \left(\frac{N_B}{2.5 \cdot 10^{17}}\right)^{0.417}} + 40 \qquad \rho_B := \left(q \cdot N_B \cdot \mu_p\right)^{-1}$$

$\rho_{InGaAs} = 3.1423 \cdot 10^{-4}$	Estimated resistivity of the InGaAs cap layer (ohm.cm)
$\rho_{cgrad} = 6.0764 \cdot 10^{-4}$	Resistivity of the In graded region (ohm.cm)
$\rho_{E.cont} = 0.0012$	Resistivity of the continuous GaAs region (ohm.cm)
$\rho_{grade} = 0.0075$	Resistivity of the Al graded region (ohm.cm)
$\rho_{AlGaAs} = 0.0075$	Estimated resititvity of the AlGaAs emitter region (ohm.cm)
$\rho_B = 0.0017$	Resistivity of the p-type GaAs base (ohm.cm)
$\rho_C = 0.0632$	Resistivity of the n-type GaAs collector (ohm.cm)
$\rho_{subC} = 0.0018$	Resistivity of the n+ GaAs subcollector (ohm.cm)

$$\rho_{E1} := \rho_{InGaAs} \cdot l_{cap} + \left(\rho_{cgrad}\right) \cdot l_{cgrad} + \rho_{E.cont} \cdot l_{E.cont}$$

$$\rho_{E2} := \left(\rho_{grade}\right) \cdot l_{grade} + \rho_{AlGaAs} \cdot \left(l_{wide} - X_{lo}\right)$$

$\rho_E = \rho_{E1} + \rho_{E2}$ Composite emitter semiconductor resistance (ohm.cm^2)

$RE_s = \frac{\rho_E}{A_{be}}$ $RE_s = 1.1901$ Component of emitter resistance due to the semiconductor (ohm)

$RE_c = \frac{\rho_{Ec}}{A_{be}}$ $RE_c = 32.4806$ Component of emitter resistance due to the metallization (ohm)

$RE = RE_s + RE_c$ Total emitter series resistance (ohm) $RE = 33.6707$

RB for an emitter dot geometry may be calculated with the formula provided by W. Liu, Solid-State Electronics, vol. 36, p. 496, Apr. 93.

$a_1 = \frac{l_{ee}}{2} - 0.1 \cdot 10^{-4}$ $a_1 = 1.4 \cdot 10^{-4}$ Radius of emitter dot (cm)

$a_2 = \frac{l_{ee}}{2}$ $a_2 = 1.5 \cdot 10^{-4}$ Inner radius of base contact (cm)

$a_3 = \frac{l_{ee}}{2} + 1.25 \cdot 10^{-4}$ $a_3 = 2.75 \cdot 10^{-4}$ Approximate outer radius of base annulus contact (cm)

$R_{B.sh} = \frac{\rho_B}{W}$ $R_{B.sh} = 235.8873$ Base sheet resistance (ohm/sq.)

$L_t = \left(\frac{\rho_{Bc}}{R_{B.sh}}\right)^{0.5}$ $L_t = 1.4559 \cdot 10^{-4}$ Base contact transfer length (cm)

The base resistance of a junction transistor is typically the sum of three components. These components are geometry dependent and are given below [67,69]:

Spreading resistance: $R_{sp} = \frac{R_{B.sh}}{8 \cdot \pi}$ $R_{sp} = 9.3857$

Bulk resistance: $R_{bulk} = \frac{R_{B.sh}}{2 \cdot \pi} \cdot \ln\left(\frac{a_2}{a_1}\right)$ $R_{bulk} = 2.5902$

Lateral contact resistance:

$$R_{lc} = \frac{R_{B.sh} \cdot L_t}{2 \cdot \pi \cdot a_2} \cdot \frac{\left(K1\left(\frac{a_3}{L_t}\right) \cdot I0\left(\frac{a_2}{L_t}\right) + I1\left(\frac{a_3}{L_t}\right) \cdot K0\left(\frac{a_2}{L_t}\right)\right)}{\left(I1\left(\frac{a_3}{L_t}\right) \cdot K1\left(\frac{a_2}{L_t}\right) + K1\left(\frac{a_3}{L_t}\right) \cdot I1\left(\frac{a_2}{L_t}\right)\right)}$$

$R_{lc} = 31.3088$

Total base series resistance (ohm):

$$RB_T = \frac{R_{sp} + R_{bulk} + R_{lc}}{N_{dot} \cdot N_{fin}} \qquad RB_T = 43.2846$$

However, for S-parameter analysis, the base-collector capacitance is distributed across the base resistance. The base resistance is split into two elements: RB and RBext.

$$RB = \frac{R_{sp}}{N_{dot} \cdot N_{fin}} \qquad RB_{ext} = \frac{R_{bulk} + R_{lc}}{N_{dot} \cdot N_{fin}}$$

The capacitance of the base metal-semiconductor contact is in parallel with RBext. However, due to the high base doping the barrier is very thin and there is essentially no SCR. Tunneling current occurs easily; thus Cbcon can be neglected.

The collector resistance is also comprised of spreading, bulk, and lateral contact resistances. When the transistor is operated in the active region (as is the case for microwave operation), the collector layer is fully depleted and does not contribute to the series resistance. However, better agreement on the I-V characteristics is obtained when the resistance of the collector layer is considered. When the transistor is saturated, almost the entire collector region is resistive.

$$R_C = \frac{\rho_C \cdot (l_C - X_{4o})}{l_{ee}^2 \cdot N_{dot}} \qquad R_C = 48.2981 \qquad \text{Zero-bias collector series resistance (ohm)}$$

$$R_{subC.sh} = \frac{\rho_{subC}}{l_{subC}} \qquad R_{subC.sh} = 18.1238 \qquad \text{Subcollector sheet resistance (ohm/sq.)}$$

$$L_t = \left(\frac{\rho_{Ec}}{R_{subC.sh}}\right)^{0.5} \qquad L_t = 3.3219 \cdot 10^{-4} \qquad \text{Collector contact transfer length (cm)}$$

Since the collector current enters the subcollector layer through an area approximately 3x3 microns square (the emitter dot), and then follows two parallel paths, we have:

Spreading resistance: $$R_{sp} = \frac{R_{subC.sh}}{3} \qquad R_{sp} = 6.0413$$

Bulk resistance: $$R_{bulk} = \frac{l_{bc} + l_{eb}}{l_{cc} - l_{ee}} \cdot \left(R_{subC.sh}\right) \cdot \ln\left(\frac{l_{cc}}{l_{ee}}\right) \qquad R_{bulk} = 8.8305$$

Lateral contact resistance: $$R_{lc} = \frac{R_{subC.sh}}{l_{cc}} \cdot L_t \cdot \coth\left(\frac{l_{cl}}{L_t}\right) \qquad R_{lc} = 5.522$$

The total ac collector series resistance may be assumed different than the dc resistance as given by the following expressions:

$$RC_{ac} = \frac{R_{sp} + R_{bulk} + R_{lc}}{N_{fin}} \qquad RC_{ac} = 20.3938$$

$$RC_{dc} = \frac{R_{sp} + R_{bulk} + R_{lc} + R_C}{N_{fin}} \qquad RC_{dc} = 68.6919$$

The two remaining dc model parameters are ISE and ISC, the recombination diodes saturation currents. These parameters can be estimated by calculating a composite recombination saturation current that is the sum of all the individual recombination component saturation currents. ISE is the constant for the Vbe exponent and ISC is the constant for the Vbc exponent. The analytical expressions for the recombination current components are found in Ryum and Abdel-Motaleb [45], Liou [52], and Huang and Abdel-Motaleb [66].

The bulk base recombination saturation current expression comes from reference [45], with the exception that the drift-diffusion model is used to determine the base-emitter carrier concentrations.

$$ISE_{BR} = \frac{q \cdot A_{be} \cdot L_{nB} \cdot n_{iB}}{t_{no} \cdot N_B} \cdot \left(\cosh\left(\frac{W_B}{L_{nB}}\right) - 1\right) \cdot \sinh\left(\frac{W_B}{L_{nB}}\right)^{(-1)} \qquad ISE_{BR} = 4.7711 \cdot 10^{-35}$$

$$ISC_{BR} := \frac{q \cdot A_{be} \cdot L_{nB} \cdot n_{iB}}{t_{no} \cdot N_B} \cdot \left(\cosh\left(\frac{W_B}{L_{nB}}\right) - 1 \right) \cdot \sinh\left(\frac{W_B}{L_{nB}}\right)^{(-1)} \qquad ISC_{BR} = 4.7711 \cdot 10^{-35}$$

The SCR recombination saturation currents from reference [66]:

$$ISE_{SCR} := \frac{q \cdot A_{be}}{2 \cdot t_{SRH}} \cdot \left[n_{iE} \cdot (l_{wide} - X_G) + \frac{n_{iE} + n_{iC}}{2} \cdot X_G + n_{iB} \cdot X_{2o} \right] \qquad ISE_{SCR} = 7.4788 \cdot 10^{-20}$$

$$ISC_{SCR} := \frac{q \cdot A_{bc}}{2 \cdot t_{SRH}} \cdot (n_{iB} \cdot X_{3o} + n_{iC} \cdot X_{4o}) \qquad ISC_{SCR} = 1.3997 \cdot 10^{-17}$$

The surface recombination saturation current from reference [45]:

$$ISE_{SR} := q \cdot P \cdot S_o \cdot L_s \cdot n_{iB} \qquad ISE_{SR} = 5.5212 \cdot 10^{-19}$$

The sum of these individual components are the composite saturation currents ISE and ISC:

$$ISE := ISE_{BR} + ISE_{SCR} + ISE_{SR} \qquad ISE = 6.2691 \cdot 10^{-19}$$

$$ISC := ISC_{BR} + ISC_{SCR} \qquad ISC = 1.3997 \cdot 10^{-17}$$

The final dc model parameter is the forward knee current which models the degradation of beta at high currents.

$$IKF := q \cdot A_{be} \cdot N_C \cdot v_{sat} \qquad IKF = 0.002$$

Since for this device the collector metal surrounds the base finger, the parasitic base-collector capacitance, Cbcp, may be calculated as follows:

$$\kappa_s := \left[\frac{\left[\left(64 \cdot 10^{-4} + l_{bc} + l_{ee} \cdot 0.5\right) \cdot l_{bc} \right]}{\left[\left(l_{ee} \cdot 0.5 + l_{bc}\right) \cdot \left(64 \cdot 10^{-4} + l_{bc}\right) \right]} \right]^{0.5} \qquad \kappa_f := \left[\frac{\left[\left(64 \cdot 10^{-4} + l_{bc} + 48 \cdot 10^{-4}\right) \cdot l_{bc} \right]}{\left[\left(64 \cdot 10^{-4} + l_{bc}\right) \cdot \left(48 \cdot 10^{-4} + l_{bc}\right) \right]} \right]^{0.5}$$

$$\kappa_m := \left[\frac{\left(64\cdot10^{-4} + 43\cdot10^{-4} + 6\cdot10^{-4}\right)\cdot 6\cdot10^{-4}}{\left[\left(64\cdot10^{-4} + 6\cdot10^{-4}\right)\cdot\left(43\cdot10^{-4} + 6\cdot10^{-4}\right)\right]} \right]^{0.5} \qquad k_s := \left(1 - \kappa_s^2\right)^{0.5} \qquad k_f := \left(1 - \kappa_f^2\right)^{0.5}$$

$$\kappa_e := \left[\frac{\left(64\cdot10^{-4} + 35\cdot10^{-4} + 14\cdot10^{-4}\right)\cdot 14\cdot10^{-4}}{\left[\left(64\cdot10^{-4} + 14\cdot10^{-4}\right)\cdot\left(35\cdot10^{-4} + 14\cdot10^{-4}\right)\right]} \right]^{0.5} \qquad k_e := \left(1 - \kappa_e^2\right)^{0.5} \qquad k_m := \left(1 - \kappa_m^2\right)^{0.}$$

$$\kappa_t := \left[\frac{\left(52\cdot10^{-4} + 19\cdot10^{-4} + 41\cdot10^{-4}\right)\cdot 41\cdot10^{-4}}{\left[\left(52\cdot10^{-4} + 41\cdot10^{-4}\right)\cdot\left(19\cdot10^{-4} + 41\cdot10^{-4}\right)\right]} \right]^{0.5} \qquad k_t := \left(1 - \kappa_t^2\right)^{0.5}$$

The following constants and function K(k) are the solution to the required integral provided by the Naval Research Laboratory Report 8561, p. 15, 1982:

$A_o := 1.3862944$ $\qquad A_2 := 0.0725296$ $\qquad A_1 := 0.1119723$

$B_o := 0.5$ $\qquad B_1 := 0.1213478$ $\qquad B_2 := 0.0288729$

$$K(\kappa) := \left[A_o + A_1\cdot\left(1 - \kappa^2\right) + A_2\cdot\left(1 - \kappa^2\right)^2\right] + \ln\left[\frac{1}{\left(1 - \kappa^2\right)}\right]\cdot\left[B_o + B_1\cdot\left(1 - \kappa^2\right) + B_2\cdot\left(1 - \kappa^2\right)^2\right]$$

$$C_{bcp} := \left(\varepsilon_p + \varepsilon_B\right)\cdot\left[\frac{K(k_f)}{K(\kappa_f)}\cdot 2\cdot l_{eb} + \left(\frac{K(k_s)}{K(\kappa_s)} + \frac{K(k_m)}{K(\kappa_m)}\right)\cdot l_{ee} + \frac{K(k_e)}{K(\kappa_e)}\cdot 9\cdot10^{-4} + \frac{K(k_t)}{K(\kappa_t)}\cdot 2\cdot l_{bc}\right]$$

$$W_E := l_{cap} + l_{cgrad} + l_{E.cont} + l_{grade} + l_{wide}$$

$$C_{bep} := \frac{\varepsilon_p\cdot\left(A_{bc} - A_{be}\right)}{d_{eb}} + \frac{2\cdot\pi\cdot\varepsilon_p\cdot\left(t_{cp} - W_E\right)\cdot N_{dot}\cdot N_{fin}}{\ln\left(\frac{0.5\cdot l_{ee}}{0.5\cdot l_{ee} - 0.1\cdot10^{-4}}\right)} \qquad C_{cep} := C_{bep}\cdot 5$$

There is also an inductance associtated with each terminal of the transistor. The equation for estimating this inductance is given by Ladbrooke [59:99]:

$$L_{cp} := \mu_o \cdot t_{sub} \cdot \left(\frac{13}{20} + \frac{4.5}{15} + \frac{9}{11} \right) \qquad L_{bp} := \mu_o \cdot t_{sub} \cdot \left(\frac{7.5}{5} + \frac{10}{15} \right)$$

$$L_{ep} := \mu_o \cdot d_{eb} \cdot \left(\frac{l_{ee}}{l_{bb}} + \frac{l_{ee}}{2 \cdot l_{eb}} \right)$$

The resistance in series with each inductance can be calculated from Ladbrooke [59:146]:

$$R_{cp} := \frac{\rho_{Au}}{3 \cdot t_{cp}} \cdot \left(\frac{l_{cl} + 15 \cdot 10^{-4}}{l_{cc} + 4.5 \cdot 10^{-4}} \right) \qquad R_{cp} = 0.0315$$

$$R_{bp} := \frac{\rho_{Au}}{3 \cdot t_{cp}} \cdot \left(\frac{l_{ee}}{l_{bb}} + \frac{l_{ee}}{2 \cdot l_{eb}} \right) \qquad R_{bp} = 0.0427$$

The following are six parasitic equivalent circuit elements that are external to the SPICE BJT model:

$C_{bcp} = 3.3828 \cdot 10^{-15}$	The parasitic interelectrode base-collector capacitcance (F)
$C_{bep} = 1.1481 \cdot 10^{-15}$	The parasitic interelectrode base-emitter capacitance (F)
$C_{cep} = 5.7403 \cdot 10^{-15}$	The parasitic interelectrode collector-emitter capacitance (F)
$L_{cp} = 1.5554 \cdot 10^{-10}$	The parasitic collector inductance (H)
$L_{bp} = 1.9059 \cdot 10^{-10}$	The parasitic base inductance (H)
$L_{ep} = 2.6389 \cdot 10^{-12}$	The parasitic emitter inductance (H)

All of the calculated SPICE model parameters are summarized below for the 3 micron emitter, 1 dot geometry.

BF = 83.5413	Forward common-emitter current gain
BR = 0.1512	Reverse common-emitter current gain
$TF = 9.5681 \cdot 10^{-13}$	Forward base transit time (s)
$TR = 5.287 \cdot 10^{-10}$	Reverse base transit time (s)
$IS = 2.2354 \cdot 10^{-26}$	Transport saturation current (A)
$ISE = 6.2691 \cdot 10^{-19}$	Base-emitter leakage saturation current (A)
$ISC = 1.3997 \cdot 10^{-17}$	Base-collector leakage saturation current (A)
RE = 33.6707	Emitter series resistance (ohm)
RB = 9.3857	Intrinsic base series resistance (ohm)
$RB_T = 43.2846$	Total base series resistance (ohm)
$RC_{ac} = 20.3938$	Microwave collector series resistance (ohm)
$RC_{dc} = 68.6919$	DC collector series resistance (ohm)
$CJE = 9.8515 \cdot 10^{-15}$	Base-emitter zero-bias depletion capacitance (F)
$CJC = 1.119 \cdot 10^{-14}$	Base-collector zero-bias depletion capacitance (F)
VJE = 1.7018	Base-emitter built-in potential (V)
VJC = 1.3691	Base-collector built-in potential (V)
XCJC = 0.2053	Fraction of base-collector depletion capacitance internal to base
IKF = 0.002	Corner for high current BF roll-off (A)

The following is an equivalent circuit element that is external to the SPICE BJT model:

$RB_{ext} = 33.8989$	The base contact resistance (ohm)

HBT PHYSICAL PARAMETER CALCULATIONS

Author: James A. Fellows
Date: 20 Nov 93
Filename: H_3u5d1f.mcd
Description: This program determines all of the model parameters required to characterize a graded AlGaAs/GaAs heterojunction bipolar transistor (HBT) in SPICE. The calculated parameters will be placed directly into the SPICE BJT model card. Also calculated are the parasitic inductance and capacitance equivalent circuit element values. All values are physically determined using a knowledge of only the device material, geometry and fabrication process. Only three of the four ideality factors are empirically determined.
Inputs: This program requires the device designer to input several specific fabrication constants. These variables are included in the first section for convenience.

Fabrication Parameters:

$N_E = 5 \cdot 10^{17}$	AlGaAs emitter doping concentration (cm^-3)
$N_B = 5 \cdot 10^{19}$	GaAs base doping concentration (cm^-3)
$N_C = 8 \cdot 10^{15}$	GaAs collector doping concentration (cm^-3)
$N_{subC} = 3 \cdot 10^{18}$	Subcollector doping concentration (cm^-3)
$l_{cap} = 3 \cdot 10^{-6}$	Thickness of InGaAs emitter cap (cm)
$N_{cap} = 2 \cdot 10^{19}$	Cap doping concentration (cm^-3)
$l_{cgrad} = 2.5 \cdot 10^{-6}$	Thickness of InGaAs graded region (cm)
$N_{cgrad} = 1 \cdot 10^{19}$	Graded region doping concentration (cm^-3)
$l_{E.cont} = 1 \cdot 10^{-5}$	Thickness of GaAs emitter region (cm)
$N_{E.cont} = 5 \cdot 10^{18}$	GaAs doping concentration (cm^-3)
$l_{grade} = 5 \cdot 10^{-6}$	Thickness of AlGaAs graded region (cm)
$N_{grade} = 5 \cdot 10^{17}$	AlGaAs graded doping concentration (cm^-3)
$l_{wide} = 5 \cdot 10^{-6}$	Thickness of the AlGaAs emitter (cm)
$X_G = 1.5 \cdot 10^{-6}$	Thickness of emitter-base junction grading (cm)

$W := 7 \cdot 10^{-6}$ Thickness of the GaAs base (cm)

$l_C := 1 \cdot 10^{-4}$ Thickness of the GaAs collector (cm)

$l_{subC} := 1 \cdot 10^{-4}$ Thickness of the GaAs subcollector (cm)

$l_{ee} := 3 \cdot 10^{-4}$ Diameter of an emitter dot (cm)

$N_{dot} := 5$ Number of emitter dots/finger

$N_{fin} := 1$ Number of base-emitter fingers

$l_{cc} := 2 \cdot N_{dot} \cdot l_{ee}$ The length of the collector contact (cm)

$l_{cl} := 18.75 \cdot 10^{-4}$ The width of the collector contact (cm)

$l_{eb} := 1 \cdot 10^{-4}$ The width of base finger contact on either side of emitter dot (cm)

$l_{bc} := 1 \cdot 10^{-4}$ The lateral distance between the base and collector contact (cm)

$\rho_{Ec} := 2 \cdot 10^{-6}$ Estimated emitter specific contact resistance (ohm.cm^2)

$\rho_{Bc} := 5 \cdot 10^{-6}$ Estimated base specific contact resistance (ohm.cm^2)

$$A_{be} := N_{dot} \cdot N_{fin} \cdot \pi \cdot \left(\frac{l_{ee}}{2} - 0.1 \cdot 10^{-4} \right)^2$$

$A_{be} = 3.0788 \cdot 10^{-7}$ Base-emitter junction area (cm^2)

$$A_{bc} := N_{dot} \cdot N_{fin} \cdot \left(l_{ee} + 2 \cdot 10^{-4} \right) \cdot \left(l_{ee} \cdot 2 \right)$$

$A_{bc} = 1.5 \cdot 10^{-6}$ Base-collector junction area (cm^2)

$$XCJC := \frac{A_{be}}{A_{bc}}$$ Fraction of base-collector area internal to device

$$P := N_{fin} \cdot N_{dot} \cdot \pi \cdot \left(\frac{l_{ee}}{2} - 0.1 \cdot 10^{-4} \right)^2$$ Total perimeter of emitter-base junction (cm)

$d_{eb} := 1 \cdot 10^{-4}$	Height of polyimide between the base and emitter metallizations (cm)
$t_{cp} := 0.4 \cdot 10^{-4}$	Thickness of collector pad metal (cm)
$l_{bb} := l_{ee} + 2 \cdot 10^{-4}$	Width of base finger (cm)
$t_{sub} := 70 \cdot 10^{-4}$	Thickness of GaAs substrate (cm)
$l_{ec} := 3 \cdot 10^{-4}$	Thickness of polyimide between the collector pad and the emitter bridge (cm)
$A_{cp} := 9.63 \cdot 10^{-6}$	Area of thick collector pad under emitter bridge (cm^2)
$A_{cm} := 13.6925 \cdot 10^{-6}$	Area of entire collector under emitter bridge (cm^2)

General constants:

$k := 8.61738 \cdot 10^{-5}$	Boltzmann's constant (eV/K)
$q := 1.602 \cdot 10^{-19}$	Electron charge (C)
$\varepsilon_o := 8.854 \cdot 10^{-14}$	Permittivity in vacuum (F/cm)
$\mu_o := 4 \cdot \pi \cdot 10^{-9}$	Permeability in vacuum (H/cm)
$m_o := 9.1095 \cdot 10^{-31}$	Electron rest mass (Kg)
$T := 300$	Temperature (K)

Material constants:

The only user defined constant is x, the mole fraction of Al. The expressions below are taken from the following references [24, 55, 57, 59].

$x := 0.35$	Mole fraction of Al in the emitter
$E_{gE} := 1.424 + 1.247 \cdot x$	Band-gap energy of the AlGaAs emitter (eV)
$\Delta E_{gB} := 1.6 \cdot 10^{-8} \cdot N_B^{\frac{1}{3}}$	Band-gap shrinkage in the GaAs base (eV)

$E_{gB} := 1.424 - \Delta E_{gB}$ Band-gap energy of the GaAs base (eV)

$\Delta E := E_{gE} - E_{gB}$ Band-gap difference at the abrupt emitter-base heterojunction (eV)

$\varepsilon := 13.18 - 3.12 \cdot x$ Relative permittivity of the AlGaAs emitter

$\varepsilon_B := 13.18 \cdot \varepsilon_o$ Permittivity of the GaAs base (F/cm)

$\varepsilon_E := \varepsilon \cdot \varepsilon_o$ Permittivity of the AlGaAs emitter (F/cm)

$\varepsilon_p := 3.5 \cdot \varepsilon_o$ Permittivity of polyimide (F/cm)

$n_{iB} := 1.79 \cdot 10^6 \cdot \exp\left(\frac{\Delta E_{gB}}{k \cdot T}\right)^{0.5}$ Intrinsic carrier concentration in the GaAs base at 300K as a function of doping (cm^-3)

$n_{iE} := n_{iB} \cdot \exp\left(\frac{\Delta E}{k \cdot T}\right)^{-0.5}$ Intrinsic carrier concentration in the emitter at 300K (cm^-3)

$n_{iC} := 1.79 \cdot 10^{\cdot}$ Intrinsic carrier concentration in the collector (cm^-3)

$v_{sat} := 1 \cdot 10^7$ Electron saturation velocity in GaAs at 300K (cm/s)

$N_t := 1 \cdot 10^{15}$ SRH recombination trap density in GaAs (cm^-3)

$N_{tI} := 1 \cdot 10^{12}$ AlGaAs/GaAs interface density of states (cm^-2)

$\sigma_n := 1 \cdot 10^{-15}$ Capture cross section of an electron (cm^2)

$m_n := 0.067 \cdot m_o$ Electron effective mass in GaAs (Kg)

$A_p := 1 \cdot 10^{-30}$ Auger recombination coefficient in GaAs (cm^6/s)

$B := 2 \cdot 10^{-10}$ Radiative recombination coefficient in GaAs (cm^3/s)

$\rho_{Au} := 2.44 \cdot 10^{-6}$ Resistivity of gold metallization (ohm.cm)

$\Delta E_c := 0.797 \cdot x$ Difference in conduction band energy at the interface (eV)

$S_o := 1 \cdot 10^6$ Intrinsic surface recombination velocity (cm/s)

$L_s := 1 \cdot 10^{-5}$ Surface diffusion length (cm)

One of the most elementary calculations is that of the built-in voltage for each junction:

$$VJE := k \cdot T \cdot \ln\left(\frac{N_E \cdot N_B}{n_{iE} \cdot n_{iB}}\right) + \Delta E_c - \frac{\Delta E}{2} \qquad VJE = 1.7018$$

$$VJC := k \cdot T \cdot \ln\left(\frac{N_B \cdot N_C}{n_{iB} \cdot n_{iC}}\right) \qquad VJC = 1.3454$$

The zero-bias depletion widths may be calculated from Ryum and Abdel-Motaleb [23:873]:

$$X_{1o} := \sqrt{\frac{2 \cdot N_B \cdot \varepsilon_E \cdot \varepsilon_B \cdot (VJE - 1.64 \cdot k \cdot T)}{q \cdot N_E \cdot (\varepsilon_E \cdot N_E + \varepsilon_B \cdot N_B)}} \qquad X_{2o} := \frac{N_E}{N_B} \cdot X_{1o}$$

$$X_{3o} := \sqrt{\frac{2 \cdot N_C \cdot \varepsilon_B \cdot (VJC - k \cdot T)}{q \cdot N_B \cdot (N_C + N_B)}} \qquad X_{4o} := \frac{N_B}{N_C} \cdot X_{3o}$$

$X_{1o} = 6.6288 \cdot 10^{-6}$ On the emitter side of the EB junction (cm)

$X_{2o} = 6.6288 \cdot 10^{-8}$ On the base side of the EB junction (cm)

$X_{3o} = 7.8426 \cdot 10^{-9}$ On the base side of the CB junction (cm)

$X_{4o} = 4.9016 \cdot 10^{-5}$ On the collector side of the CB junction (cm)

The effective zero-bias base width Wb, is found by subtracting the depletion widths in the base on both the emitter and collector sides:

$$W_B := W - (X_{2o} + X_{3o}) \qquad W_B = 6.9259 \cdot 10^{-6} \quad (cm)$$

Now, calculate the depletion capacitances from Ryum and Abdel-Motaleb [23:873]:

$$CJE := A_{be} \cdot \frac{(\varepsilon_E \cdot \varepsilon_B)}{\varepsilon_E \cdot X_{2o} + \varepsilon_B \cdot X_{1o}} \qquad CJE = 4.9257 \cdot 10^{-14}$$

$$CJC := A_{bc} \cdot \frac{\varepsilon_B}{X_{3o} + X_{4o}} \qquad CJC = 3.5706 \cdot 10^{-14}$$

Calculating the value of Cje with a nominal bias is helpful. Since a nominal value of Vbe is 1.5 V, we have:

$$X_{1o} := \sqrt{\frac{2 \cdot N_B \cdot \varepsilon_E \cdot \varepsilon_B \cdot (VJE - 1.64 \cdot k \cdot T - 1.5)}{q \cdot N_E \cdot (\varepsilon_E \cdot N_E + \varepsilon_B \cdot N_B)}} \qquad X_{2o} := \frac{N_E}{N_B} \cdot X_{1o}$$

$$CJE_{bias} := A_{be} \cdot \frac{(\varepsilon_E \cdot \varepsilon_B)}{\varepsilon_E \cdot X_{2o} + \varepsilon_B \cdot X_{1o}} \qquad CJE_{bias} = 1.5895 \cdot 10^{-13}$$

The minority electron mobility in the p-type base GaAs as a function of base doping can be found from the empirical relation stated by Ali and Gupta [53:202]. A similar relation for minority holes in the collector is stated by C. Selvakumar [55:773]. The diffusivities are then calculated from the Einstein relation:

$$\mu_n := \frac{7057}{1 + \left(\frac{N_B}{2.84 \cdot 10^{16}}\right)^{0.753}} + 943 \qquad \mu_n = 968.2979 \qquad D_{nB} := \mu_n \cdot k \cdot T$$

$$\mu_{pE} := \frac{360}{1 + \left(\frac{N_E}{2.5 \cdot 10^{17}}\right)^{0.417}} + 40 \qquad \mu_{pE} = 194.1658 \qquad D_{pE} := \mu_{pE} \cdot k \cdot T$$

$$\mu_{pC} := \frac{360}{1 + \left(\frac{N_C}{2.5 \cdot 10^{17}}\right)^{0.417}} + 40 \qquad \mu_{pC} = 330.7825 \qquad D_{pC} := \mu_{pC} \cdot k \cdot T$$

$D_{nB} = 25.0326$ Diffusivity of minority electrons in the base (cm^2/s)

$D_{pE} = 5.0196$ Estimated diffusivity of minority holes in the emitter (cm^2/s)

$D_{pC} = 8.5514$ Diffusivity of minority holes in the collector (cm^2/s)

The base transit time has many forms [60,51], but ultimately from from Hodges and Jackson [44:162]:

$$TF := \frac{W_B^2}{2.43 \cdot D_{nB}} \qquad TF := \frac{W_B^2}{2 \cdot D_{nB}} + \frac{W_B}{v_{sat}} \qquad TF := \frac{W_B^2}{2 \cdot D_{nB}}$$

$TF = 9.5811 \cdot 10^{-13}$ The forward transit time of minority electrons across the base (s)

Excess minority electron lifetime may be obtained by considering the lifetime of each recombination component. The expression for tno is taken from Lundstrom et al. [56:698]:

$$v_{th} := 100 \cdot \left(\frac{q \cdot k \cdot T}{2 \cdot \pi \cdot m_n} \right)^{0.5} \qquad v_{th} = 1.0392 \cdot 10^7$$ Average thermal velocity of an electron in GaAs (cm/s)

$$t_{SRH} := \frac{1}{\sigma_n \cdot N_t \cdot v_{th}} \qquad t_{SRH} = 9.6227 \cdot 10^{-8}$$ Shockley-Read-Hall recombination lifetime in GaAs (s)

$$t_{Aug} := \frac{1}{A_p \cdot N_B^2} \qquad t_{Aug} = 4 \cdot 10^{-10}$$ Auger recombination lifetime in p-type GaAs (s)

$$t_{rad} := \frac{1}{B \cdot N_B} \qquad t_{rad} = 1 \cdot 10^{-10}$$ Radiative recombination lifetime in p-type GaAs (s)

$$t_{no} := \left(\frac{1}{t_{SRH}} + \frac{1}{t_{Aug}} + \frac{1}{t_{rad}} \right)^{-1}$$

$t_{no} = 7.9934 \cdot 10^{-11}$ Minority electron lifetime in the base (s)

$t_{poC} := 20 \cdot 10^{-9}$ Minority hole lifetime in the collector (s)

$L_{nB} := \sqrt{D_{nB} \cdot t_{no}}$ $L_{nB} = 4.4732 \cdot 10^{-5}$ Diffusion length of electrons in the base (cm)

$L_{pC} := \sqrt{D_{pC} \cdot t_{poC}}$ $L_{pC} = 4.1356 \cdot 10^{-4}$ Diffusion length of holes in the collector (cm)

The diffusion length of minority holes in the emitter is estimated from an empirical expression found in Ryum and Abdel-Motaleb [23:876]:

$$L_{pE} := \frac{42.46 - \log(N_E)}{9.21 \cdot 10^3} \qquad L_{pE} = 0.0027$$ Diffusion length of holes in the emitter (cm)

The maximum dc Beta for an HBT is best described by Kroemer [13:15]; however, better dc agreement between modeled and measured data is obtained if beta is considered due only to recombination in the neutral base after Grossman and Choma [25:459]:

$$v_{nB} := \frac{D_{nB}}{L_{nB}} \qquad v_{pE} := \frac{D_{pE}}{L_{pE}} \qquad BF_{max} := \frac{N_E}{N_B} \cdot \frac{v_{nB}}{v_{pE}} \cdot \exp\left(\frac{\Delta E}{k \cdot T}\right)$$

$$BF := \frac{t_{no}}{TF} \qquad BF = 83.4288$$

IS can be estimated from Huang and Abdel-Motaleb [66:165]:

$$IS := \frac{q \cdot A_{be} \cdot n_{iB}^2 \cdot D_{nB}}{W_B \cdot N_B} \qquad IS = 1.1169 \cdot 10^{-25}$$

$$Ics := A_{bc} \cdot q \cdot \left(\frac{D_{nB} \cdot n_{iB}^2}{L_{nB} \cdot N_B} + \frac{D_{pC} \cdot n_{iC}^2}{L_{pC} \cdot N_C}\right) \qquad Ics = 2.0744 \cdot 10^{-24}$$

Now, we can calculate the reverse beta, BR, and reverse tau, TR:

$$\text{alpha}_R := \frac{IS}{Ics} \qquad \text{alpha}_R = 0.0538 \qquad \text{Reverse common-base current gain}$$

$$BR := \frac{\text{alpha}_R}{1 - \text{alpha}_R} \qquad BR = 0.0569 \qquad \text{Reverse common-emitter current gain}$$

$$TR := \frac{t_{no}}{BR} \qquad TR = 1.4046 \cdot 10^{-9} \qquad \text{Reverse base transit time (s)}$$

We can also determine the series emitter and collector resistances, RE and RC, after Ali and Gupta [53:204]. Resistivities for are calculated from the empirical mobility relations.

$$\mu_{cap} := \frac{7057}{1 + \left(\frac{N_{cap}}{2.84 \cdot 10^{16}}\right)^{0.753}} + 943 \qquad \rho_{InGaAs} := \left(q \cdot N_{cap} \cdot \mu_{cap}\right)^{-1}$$

$$\mu_{cgrad} := \frac{7057}{1 + \left(\frac{N_{cgrad}}{2.84 \cdot 10^{16}}\right)^{0.753}} + 943 \qquad \rho_{cgrad} := \left(q \cdot N_{cgrad} \cdot \mu_{cgrad}\right)^{-1}$$

$$\mu_{E.cont} := \frac{7057}{1 + \left(\frac{N_{E.cont}}{2.84 \cdot 10^{16}}\right)^{0.753}} + 943 \qquad \rho_{E.cont} := \left(q \cdot N_{E.cont} \cdot \mu_{E.cont}\right)^{-1}$$

$$\mu_{grade} := \frac{7057}{1 + \left(\frac{N_{grade}}{2.84 \cdot 10^{16}}\right)^{0.753}} + 943 \qquad \rho_{grade} := \left(q \cdot N_{grade} \cdot \mu_{grade}\right)^{-1}$$

$$\mu_E := \frac{7057}{1 + \left(\frac{N_E}{2.84 \cdot 10^{16}}\right)^{0.753}} + 943 \qquad \rho_{AlGaAs} := \left(q \cdot N_E \cdot \mu_E\right)^{-1}$$

$$\mu_C := \frac{7057}{1 + \left(\frac{N_C}{2.84 \cdot 10^{16}}\right)^{0.753}} + 943 \qquad \rho_C := \left(q \cdot N_C \cdot \mu_C\right)^{-1}$$

$$\mu_{subC} := \frac{7057}{1 + \left(\frac{N_{subC}}{2.84 \cdot 10^{16}}\right)^{0.753}} + 943 \qquad \rho_{subC} := \left(q \cdot N_{subC} \cdot \mu_{subC}\right)^{-1}$$

$$\mu_p := \frac{360}{1 + \left(\frac{N_B}{2.5 \cdot 10^{17}}\right)^{0.417}} + 40 \qquad \rho_B := \left(q \cdot N_B \cdot \mu_p\right)^{-1}$$

$\rho_{InGaAs} = 3.1423 \cdot 10^{-4}$	Estimated resistivity of the InGaAs cap layer (ohm.cm)
$\rho_{cgrad} = 6.0764 \cdot 10^{-4}$	Resistivity of the In graded region (ohm.cm)
$\rho_{E.cont} = 0.0012$	Resistivity of the continuous GaAs region (ohm.cm)
$\rho_{grade} = 0.0075$	Resistivity of the Al graded region (ohm.cm)
$\rho_{AlGaAs} = 0.0075$	Estimated resititvity of the AlGaAs emitter region (ohm.cm)
$\rho_B = 0.0017$	Resistivity of the p-type GaAs base (ohm.cm)
$\rho_C = 0.1292$	Resistivity of the n-type GaAs collector (ohm.cm)
$\rho_{subC} = 0.0018$	Resistivity of the n+ GaAs subcollector (ohm.cm)

$$\rho_{E1} := \rho_{InGaAs} \cdot l_{cap} + \left(\rho_{cgrad}\right) \cdot l_{cgrad} + \rho_{E.cont} \cdot l_{E.cont}$$

$$\rho_{E2} := \left(\rho_{grade}\right) \cdot l_{grade} + \rho_{AlGaAs} \cdot \left(l_{wide} - X_{1o}\right)$$

$\rho_E = \rho_{E1} + \rho_{E2}$ Composite emitter semiconductor resistance (ohm.cm^2)

$RE_s = \frac{\rho_E}{A_{be}}$ $RE_s = 0.238$ Component of emitter resistance due to the semiconductor (ohm)

$RE_c = \frac{\rho_{Ec}}{A_{be}}$ $RE_c = 6.4961$ Component of emitter resistance due to the metallization (ohm)

$RE = RE_s + RE_c$ Total emitter series resistance (ohm) $RE = 6.7341$

RB for an emitter dot geometry may be calculated with the formula provided by W. Liu, Solid-State Electronics, vol. 36, p. 496, Apr. 93.

$a_1 = \frac{l_{ee}}{2} - 0.1 \cdot 10^{-4}$ $a_1 = 1.4 \cdot 10^{-4}$ Radius of emitter dot (cm)

$a_2 = \frac{l_{ee}}{2}$ $a_2 = 1.5 \cdot 10^{-4}$ Inner radius of base contact (cm)

$a_3 = \frac{l_{ee}}{2} + 1.25 \cdot 10^{-4}$ $a_3 = 2.75 \cdot 10^{-4}$ Approximate outer radius of base annulus contact (cm)

$R_{B.sh} = \frac{\rho_B}{W}$ $R_{B.sh} = 235.8873$ Base sheet resistance (ohm/sq.)

$L_t = \left(\frac{\rho_{Bc}}{R_{B.sh}}\right)^{0.5}$ $L_t = 1.4559 \cdot 10^{-4}$ Base contact transfer length (cm)

The base resistance of a junction transistor is typically the sum of three components. These components are geometry dependent and are given below [67,69]:

Spreading resistance: $R_{sp} = \frac{R_{B.sh}}{8 \cdot \pi}$ $R_{sp} = 9.3857$

Bulk resistance: $R_{bulk} = \frac{R_{B.sh}}{2 \cdot \pi} \cdot \ln\left(\frac{a_2}{a_1}\right)$ $R_{bulk} = 2.5902$

Lateral contact resistance:

$$R_{lc} = \frac{R_{B.sh} \cdot L_t}{2 \cdot \pi \cdot a_2} \cdot \frac{\left(K1\left(\frac{a_3}{L_t}\right) \cdot I0\left(\frac{a_2}{L_t}\right) + I1\left(\frac{a_3}{L_t}\right) \cdot K0\left(\frac{a_2}{L_t}\right)\right)}{\left(I1\left(\frac{a_3}{L_t}\right) \cdot K1\left(\frac{a_2}{L_t}\right) + K1\left(\frac{a_3}{L_t}\right) \cdot I1\left(\frac{a_2}{L_t}\right)\right)}$$

$R_{lc} = 31.3088$

Total base series resistance (ohm):

$$RB_T = \frac{R_{sp} + R_{bulk} + R_{lc}}{N_{dot} \cdot N_{fin}} \qquad RB_T = 8.6569$$

However, for S-parameter analysis, the base-collector capacitance is distributed across the base resistance. The base resistance is split into two elements: RB and RBext.

$$RB = \frac{R_{sp}}{N_{dot} \cdot N_{fin}} \qquad RB_{ext} = \frac{R_{bulk} + R_{lc}}{N_{dot} \cdot N_{fin}}$$

The capacitance of the base metal-semiconductor contact is in parallel with RBext. However, due to the high base doping the barrier is very thin and there is essentially no SCR. Tunneling current occurs easily; thus Cbcon can be neglected.

The collector resistance is also comprised of spreading, bulk, and lateral contact resistances. When the transistor is operated in the active region (as is the case for microwave operation), the collector layer is fully depleted and does not contribute to the series resistance. However, better agreement on the I-V characteristics is obtained when the resistance of the collector layer is considered. When the transistor is saturated, almost the entire collector region is resistive.

$$R_C = \frac{\rho_C \cdot (l_C - X_{4o})}{l_{ee}^2 \cdot N_{dot}} \qquad R_C = 14.6421 \qquad \text{Zero-bias collector series resistance (ohm)}$$

$$R_{subC.sh} = \frac{\rho_{subC}}{l_{subC}} \qquad R_{subC.sh} = 18.1238 \qquad \text{Subcollector sheet resistance (ohm/sq.)}$$

$$L_t = \left(\frac{\rho_{Ec}}{R_{subC.sh}}\right)^{0.5} \qquad L_t = 3.3219 \cdot 10^{-4} \qquad \text{Collector contact transfer length (cm)}$$

Since the collector current enters the subcollector layer through an area approximately 3x3 microns square (the emitter dot), and then follows two parallel paths, we have:

Spreading resistance: $$R_{sp} := \frac{R_{subC.sh}}{12 \cdot N_{dot}} \qquad R_{sp} = 0.3021$$

Bulk resistance: $$R_{bulk} := \frac{l_{bc} + l_{eb}}{l_{ee} \cdot 2 \cdot N_{dot}} \cdot \ln(2) \cdot \left(R_{subC.sh}\right) \qquad R_{bulk} = 0.8375$$

Lateral contact resistance: $$R_{lc} := \frac{R_{subC.sh}}{2 \cdot l_{cc}} \cdot L_t \cdot \coth\left(\frac{l_{cl}}{L_t}\right) \qquad R_{lc} = 1.0035$$

The total ac collector series resistance may be assumed different than the dc resistance as given by the following expressions:

$$RC_{ac} := \frac{R_{sp} + R_{bulk} + R_{lc}}{N_{fin}} \qquad RC_{ac} = 2.143$$

$$RC_{dc} := \frac{R_{sp} + R_{bulk} + R_{lc} + R_C}{N_{fin}} \qquad RC_{dc} = 16.7851$$

The two remaining dc model parameters are ISE and ISC, the recombination diodes saturation currents. These parameters can be estimated by calculating a composite recombination saturation current that is the sum of all the individual recombination component saturation currents. ISE is the constant for the Vbe exponent and ISC is the constant for the Vbc exponent. The analytical expressions for the recombination current components are found in Ryum and Abdel-Motaleb [45], Liou [52], and Huang and Abdel-Motaleb [66].

The bulk base recombination saturation current expression comes from reference [45], with the exception that the drift-diffusion model is used to determine the base-emitter carrier concentrations.

$$ISE_{BR} := \frac{q \cdot A_{be} \cdot L_{nB} \cdot n_{iB}}{t_{no} \cdot N_B} \cdot \left(\cosh\left(\frac{W_B}{L_{nB}}\right) - 1\right) \cdot \sinh\left(\frac{W_B}{L_{nB}}\right)^{(-1)} \qquad ISE_{BR} = 2.3871 \cdot 10^{-34}$$

$$ISC_{BR} := \frac{q \cdot A_{be} \cdot L_{nB} \cdot n_{iB}}{t_{no} \cdot N_B} \cdot \left(\cosh\left(\frac{W_B}{L_{nB}}\right) - 1 \right) \cdot \sinh\left(\frac{W_B}{L_{nB}}\right)^{(-1)} \qquad ISC_{BR} = 2.3871 \cdot 10^{-34}$$

The SCR recombination saturation currents from reference [66]:

$$ISE_{SCR} := \frac{q \cdot A_{be}}{2 \cdot t_{SRH}} \cdot \left[n_{iE} \cdot \left(l_{wide} - X_G \right) + \frac{n_{iE} + n_{iC}}{2} \cdot X_G + n_{iB} \cdot X_{2o} \right] \qquad ISE_{SCR} = 3.7394 \cdot 10^{-19}$$

$$ISC_{SCR} := \frac{q \cdot A_{bc}}{2 \cdot t_{SRH}} \cdot \left(n_{iB} \cdot X_{3o} + n_{iC} \cdot X_{4o} \right) \qquad ISC_{SCR} = 1.0961 \cdot 10^{-16}$$

The surface recombination saturation current from reference [45]:

$$ISE_{SR} := q \cdot P \cdot S_o \cdot L_s \cdot n_{iB} \qquad ISE_{SR} = 2.7606 \cdot 10^{-18}$$

The sum of these individual components are the composite saturation currents ISE and ISC:

$$ISE := ISE_{BR} + ISE_{SCR} + ISE_{SR} \qquad ISE = 3.1345 \cdot 10^{-18}$$

$$ISC := ISC_{BR} + ISC_{SCR} \qquad ISC = 1.0961 \cdot 10^{-16}$$

The final dc model parameter is the forward knee current which models the degradation of beta at high currents.

$$IKF := q \cdot A_{be} \cdot N_C \cdot v_{sat} \qquad IKF = 0.0039$$

Since for this device the collector metal surrounds the base finger, the parasitic base-collector capacitance, Cbcp, may be calculated as follows:

$$\kappa_s := \left[\frac{\left[\left(l_{cl} + l_{bc} + l_{ei} \right) \cdot l_{bc} \right]}{\left[\left(l_{eb} + l_{bc} \right) \cdot \left(l_{cl} + l_{bc} \right) \right]} \right]^{0.5} \qquad \kappa_l := \left[\frac{\left[\left(l_{cl} + l_{bc} + l_{bb} \right) \cdot l_{bc} \right]}{\left[\left(l_{bb} + l_{bc} \right) \cdot \left(l_{cl} + l_{bc} \right) \right]} \right]^{0.5} \qquad k_s := \left(1 - \kappa_s^2 \right)^{0.5}$$

$$\kappa_f := \left[\frac{\left[\left(l_{cc} + 45 \cdot 10^{-4} + l_{bc} + 53 \cdot 10^{-4} \right) \cdot l_{bc} \right]}{\left[\left(l_{cc} + 45 \cdot 10^{-4} + l_{bc} \right) \cdot \left(53 \cdot 10^{-4} + l_{bc} \right) \right]} \right]^{0.5} \qquad k_1 := \left(1 - \kappa_1^2 \right)^{0.5} \qquad k_f := \left(1 - \kappa_f^2 \right)^{0.5}$$

$$\kappa_e := \left[\frac{\left(l_{cc} + 40 \cdot 10^{-4} + 34 \cdot 10^{-4} + 15 \cdot 10^{-4} \right) \cdot 34 \cdot 10^{-4}}{\left[\left(l_{cc} + 50 \cdot 10^{-4} + 34 \cdot 10^{-4} \right) \cdot \left(34 \cdot 10^{-4} + 15 \cdot 10^{-4} \right) \right]} \right]^{0.5} \qquad k_e := \left(1 - \kappa_e^2 \right)^{0.5}$$

$$\kappa_t := \left[\frac{\left(l_{cc} + 60 \cdot 10^{-4} + 8.5 \cdot 10^{-4} + 35 \cdot 10^{-4} \right) \cdot 8.5 \cdot 10^{-4}}{\left[\left(l_{cc} + 60 \cdot 10^{-4} + 8.5 \cdot 10^{-4} \right) \cdot \left(8.5 \cdot 10^{-4} + 35 \cdot 10^{-4} \right) \right]} \right]^{0.5} \qquad k_t := \left(1 - \kappa_t^2 \right)^{0.5}$$

The following constants and function K(k) are the solution to the required integral provided by the Naval Research Laboratory Report 8561, p. 15, 1982:

$A_0 := 1.3862944$ $\qquad A_2 := 0.0725296$ $\qquad A_1 := 0.1119723$

$B_0 := 0.5$ $\qquad B_1 := 0.1213478$ $\qquad B_2 := 0.0288729$

$$K(\kappa) := \left[A_0 + A_1 \cdot \left(1 - \kappa^2 \right) + A_2 \cdot \left(1 - \kappa^2 \right)^2 \right] + \ln\left[\frac{1}{\left(1 - \kappa^2 \right)} \right] \cdot \left[B_0 + B_1 \cdot \left(1 - \kappa^2 \right) + B_2 \cdot \left(1 - \kappa^2 \right)^2 \right]$$

$$C_{bcp1} := 2 \cdot N_{fin} \cdot N_{dot} \cdot l_{ee} \cdot \left(\varepsilon_p + \varepsilon_B \right) \cdot \left(\frac{K(k_1)}{K(\kappa_1)} + \frac{K(k_s)}{K(\kappa_s)} + \frac{K(k_f)}{K(\kappa_f)} \cdot \frac{l_{eb}}{N_{dot} \cdot l_{ee}} \right) + \frac{N_{fin} \cdot t_{cp} \cdot \varepsilon_p}{l_{bc}} \cdot \left(2 \cdot l_{cc} + l_{bb} \right)$$

$$C_{bcp2} := \left(\varepsilon_p + \varepsilon_B \right) \cdot \left[\frac{K(k_e)}{K(\kappa_e)} \cdot 2 \cdot \left(l_{cl} - 1.5 \cdot 10^{-4} \right) + \frac{K(k_t)}{K(\kappa_t)} \cdot 1.5 \cdot 10^{-4} \cdot 2 \right] \qquad C_{bcp} := C_{bcp1} + C_{bcp2}$$

$$C_{cep} := \varepsilon_p \cdot \left(\frac{A_{cp} + A_{cm}}{l_{ec} - 0.1 \cdot 10^{-4}} \right) \qquad W_E := l_{cap} + l_{cgrad} + l_{E.cont} + l_{grade} + l_{wide}$$

$$C_{bep} := \frac{\varepsilon_p \cdot \left[A_{bc} - A_{be} + \left(N_{fin} \cdot l_{bb}^2\right)\right]}{d_{eb} - 0.1 \cdot 10^{-4}} + \frac{2 \cdot \pi \cdot \varepsilon_p \cdot \left(t_{cp} - W_E\right) \cdot N_{dot} \cdot N_{fin}}{\ln\left(\frac{0.5 \cdot l_{ee}}{0.5 \cdot l_{ee} - 0.1 \cdot 10^{-4}}\right)}$$

There is also an inductance associtated with each terminal of the transistor. The equation for estimating this inductance is given by Ladbrooke [59:99]. Only the interconnects NOT beneath the emitter bridge (and NOT part of the thick pad metal) are considered here since the inductance under the bridge is negligible in comparison.

$$L_{cp} := \mu_o \cdot t_{sub} \cdot \left(\frac{14}{45}\right) \qquad L_{bp} := \mu_o \cdot t_{sub} \cdot \left(\frac{7.5}{5} + \frac{10}{15}\right)$$

$$L_{bp1} := \frac{N_{dot}}{N_{fin}} \cdot \mu_o \cdot \left(d_{eb} - 0.1 \cdot 10^{-4}\right) \cdot \left(\frac{l_{ee}}{l_{bb}} + \frac{l_{ee}}{2 \cdot l_{eb}}\right) + \frac{\mu_o}{N_{fin}} \cdot \left(l_{ec} - 0.1 \cdot 10^{-4}\right)$$

$$L_{cp1} := \mu_o \cdot \left(l_{ec} - 0.1 \cdot 10^{-4}\right) \cdot \frac{l_{cc} + 7.8 \cdot 10^{-4}}{\left(N_{fin} + 1\right) \cdot l_{cl}} \qquad L_{ep} := \left(\frac{1}{L_{cp1}} + \frac{1}{L_{bp1}}\right)^{-1}$$

The resistance in series with each inductance can be calculated from Ladbrooke [59:146]:

$$R_{cp} := \frac{\rho_{Au}}{3 \cdot t_{cp}} \cdot \left[\frac{l_{cc} + 7.8 \cdot 10^{-4}}{\left(N_{fin} + 1\right) \cdot l_{cl}}\right] \qquad R_{cp} = 0.0205$$

$$R_{bp} := \frac{N_{dot}}{N_{fin}} \cdot \frac{\rho_{Au}}{3 \cdot t_{cp}} \cdot \left(\frac{l_{ee}}{l_{bb}} + \frac{l_{ee}}{2 \cdot l_{eb}}\right) \qquad R_{bp} = 0.2135$$

The following are six parasitic equivalent circuit elements that are external to the SPICE BJT model:

$C_{bcp} = 1.6333 \cdot 10^{-14}$ The parasitic interelectrode base-collector capacitcance (F)

$C_{bep} = 7.0116 \cdot 10^{-15}$	The parasitic interelectrode base-emitter capacitance (F)
$C_{cep} = 2.4922 \cdot 10^{-14}$	The parasitic interelectrode collector-emitter capacitance (F)
$L_{cp} = 2.7367 \cdot 10^{-11}$	The parasitic collector inductance (H)
$L_{bp} = 1.9059 \cdot 10^{-10}$	The parasitic base inductance (H)
$L_{ep} = 2.9703 \cdot 10^{-12}$	The parasitic emitter inductance (H)

All of the calculated SPICE model parameters are summarized below for the 3 micron emitter, 5 dot one finger geometry.

BF = 83.4288	Forward common-emitter current gain
BR = 0.0569	Reverse common-emitter current gain
$TF = 9.5811 \cdot 10^{-13}$	Forward base transit time (s)
$TR = 1.4046 \cdot 10^{-9}$	Reverse base transit time (s)
$IS = 1.1169 \cdot 10^{-25}$	Transport saturation current (A)
$ISE = 3.1345 \cdot 10^{-18}$	Base-emitter leakage saturation current (A)
$ISC = 1.0961 \cdot 10^{-16}$	Base-collector leakage saturation current (A)
RE = 6.7341	Emitter series resistance (ohm)
RB = 1.8771	Intrinsic base series resistance (ohm)
$RB_T = 8.6569$	Total base series resistance (ohm)
$RC_{ac} = 2.143$	Microwave collector series resistance (ohm)
$RC_{dc} = 16.7851$	DC collector series resistance (ohm)
$CJE = 4.9257 \cdot 10^{-14}$	Base-emitter zero-bias depletion capacitance (F)

CJC = $3.5706 \cdot 10^{-14}$	Base-collector zero-bias depletion capacitance (F)
VJE = 1.7018	Base-emitter built-in potential (V)
VJC = 1.3454	Base-collector built-in potential (V)
XCJC = 0.2053	Fraction of base-collector depletion capacitance internal to base
IKF = 0.0039	Corner for high current BF roll-off (A)

The following is an equivalent circuit element that is external to the SPICE BJT model:

RB_{ext} = 6.7798	The base contact resistance (ohm)

HBT PHYSICAL PARAMETER CALCULATIONS

Author: James A. Fellows
Date: 20 Nov 93
Filename: H_2u6d2f.mcd
Description: This program determines all of the model parameters required to characterize a graded AlGaAs/GaAs heterojunction bipolar transistor (HBT) in SPICE. The calculated parameters will be placed directly into the SPICE BJT model card. Also calculated are the parasitic inductance and capacitance equivalent circuit element values. All values are physically determined using a knowledge of only the device material, geometry and fabrication process. Only three of the four ideality factors are empirically determined.
Inputs: This program requires the device designer to input several specific fabrication constants. These variables are included in the first section for convenience.

Fabrication Parameters:

$N_E = 5 \cdot 10^{17}$	AlGaAs emitter doping concentration (cm^-3)
$N_B = 5 \cdot 10^{19}$	GaAs base doping concentration (cm^-3)
$N_C = 1 \cdot 10^{17}$	GaAs collector doping concentration (cm^-3)
$N_{subC} = 3 \cdot 10^{18}$	Subcollector doping concentration (cm^-3)
$l_{cap} = 3 \cdot 10^{-6}$	Thickness of InGaAs emitter cap (cm)
$N_{cap} = 2 \cdot 10^{19}$	Cap doping concentration (cm^-3)
$l_{cgrad} = 2.5 \cdot 10^{-6}$	Thickness of InGaAs graded region (cm)
$N_{cgrad} = 1 \cdot 10^{19}$	Graded region doping concentration (cm^-3)
$l_{E.cont} = 1 \cdot 10^{-5}$	Thickness of GaAs emitter region (cm)
$N_{E.cont} = 5 \cdot 10^{18}$	GaAs doping concentration (cm^-3)
$l_{grade} = 5 \cdot 10^{-6}$	Thickness of AlGaAs graded region (cm)
$N_{grade} = 5 \cdot 10^{17}$	AlGaAs graded doping concentration (cm^-3)
$l_{wide} = 5 \cdot 10^{-6}$	Thickness of the AlGaAs emitter (cm)
$X_G = 1.5 \cdot 10^{-6}$	Thickness of emitter-base junction grading (cm)

$W := 7 \cdot 10^{-6}$ Thickness of the GaAs base (cm)

$l_C := 0.35 \cdot 10^{-4}$ Thickness of the GaAs collector (cm)

$l_{subC} := 1 \cdot 10^{-4}$ Thickness of the GaAs subcollector (cm)

$l_{ee} := 2 \cdot 10^{-4}$ Diameter of an emitter dot (cm)

$N_{dot} := 6$ Number of emitter dots/finger

$N_{fin} := 2$ Number of base-emitter fingers

$l_{cc} := 2 \cdot N_{dot} \cdot l_{ee}$ The length of the collector contact (cm)

$l_{cl} := 19.55 \cdot 10^{-4}$ The width of the collector contact (cm)

$l_{eb} := 1 \cdot 10^{-4}$ The width of base finger contact on either side of emitter dot (cm)

$l_{bc} := 1 \cdot 10^{-4}$ The lateral distance between the base and collector contact (cm)

$\rho_{Ec} := 2 \cdot 10^{-6}$ Estimated emitter specific contact resistance (ohm.cm^2)

$\rho_{Bc} := 5 \cdot 10^{-6}$ Estimated base specific contact resistance (ohm.cm^2)

$$A_{be} := N_{dot} \cdot N_{fin} \cdot \pi \cdot \left(\frac{l_{ee}}{2} - 0.1 \cdot 10^{-4} \right)^2$$

$A_{be} = 3.0536 \cdot 10^{-7}$ Base-emitter junction area (cm^2)

$$A_{bc} := N_{dot} \cdot N_{fin} \cdot \left(l_{ee} + 2 \cdot 10^{-4} \right) \cdot \left(l_{ee} \cdot 2 \right)$$

$A_{bc} = 1.92 \cdot 10^{-6}$ Base-collector junction area (cm^2)

$$XCJC := \frac{A_{be}}{A_{bc}}$$ Fraction of base-collector area internal to device

$$P := N_{fin} \cdot N_{dot} \cdot \pi \cdot \left(\frac{l_{ee}}{2} - 0.1 \cdot 10^{-4} \right)^2$$ Total perimeter of emitter-base junction (cm)

$d_{eb} := 1 \cdot 10^{-4}$ Height of polyimide between the base and emitter metallizations (cm)

$t_{cp} := 0.4 \cdot 10^{-4}$ Thickness of collector pad metal (cm)

$l_{bb} := l_{ee} + 2 \cdot 10^{-4}$ Width of base finger (cm)

$t_{sub} := 70 \cdot 10^{-4}$ Thickness of GaAs substrate (cm)

$l_{ec} := 3 \cdot 10^{-4}$ Thickness of polyimide between the collector pad and the emitter bridge (cm)

$A_{cp} := 12.972 \cdot 10^{-6}$ Area of thick collector pad under emitter bridge (cm^2)

$A_{cm} := 18.555 \cdot 10^{-6}$ Area of entire collector under emitter bridge (cm^2)

General constants:

$k := 8.61738 \cdot 10^{-5}$ Boltzmann's constant (eV/K)

$q := 1.602 \cdot 10^{-19}$ Electron charge (C)

$\varepsilon_o := 8.854 \cdot 10^{-14}$ Permittivity in vacuum (F/cm)

$\mu_o := 4 \cdot \pi \cdot 10^{-9}$ Permeability in vacuum (H/cm)

$m_o := 9.1095 \cdot 10^{-31}$ Electron rest mass (Kg)

$T := 300$ Temperature (K)

Material constants:

The only user defined constant is x, the mole fraction of Al. The expressions below are taken from references [24, 55, 57, 59].

$x := 0.35$ Mole fraction of Al in the emitter

$E_{gE} := 1.424 + 1.247 \cdot x$ Band-gap energy of the AlGaAs emitter (eV)

$\Delta E_{gB} := 1.6 \cdot 10^{-8} \cdot N_B^{\frac{1}{3}}$ Band-gap shrinkage in the GaAs base (eV)

$E_{gB} := 1.424 - \Delta E_{gB}$	Band-gap energy of the GaAs base (eV)
$\Delta E := E_{gE} - E_{gB}$	Band-gap difference at the abrupt emitter-base heterojunction (eV)
$\varepsilon := 13.18 - 3.12 \cdot x$	Relative permittivity of the AlGaAs emitter
$\varepsilon_B := 13.18 \cdot \varepsilon_o$	Permittivity of the GaAs base (F/cm)
$\varepsilon_E := \varepsilon \cdot \varepsilon_o$	Permittivity of the AlGaAs emitter (F/cm)
$\varepsilon_p := 3.5 \cdot \varepsilon_o$	Permittivity of polyimide (F/cm)
$n_{iB} := 1.79 \cdot 10^6 \cdot \exp\left(\frac{\Delta E_{gB}}{k \cdot T}\right)^{0.5}$	Intrinsic carrier concentration in the GaAs base at 300K as a function of doping (cm^-3)
$n_{iE} := n_{iB} \cdot \exp\left(\frac{\Delta E}{k \cdot T}\right)^{-0.5}$	Intrinsic carrier concentration in the emitter at 300K (cm^-3)
$n_{iC} := 1.79 \cdot 10^6$	Intrinsic carrier concentration in the collector (cm^-3)
$v_{sat} := 1 \cdot 10^7$	Electron saturation velocity in GaAs at 300K (cm/s)
$N_t := 1 \cdot 10^{15}$	SRH recombination trap density in GaAs (cm^-3)
$N_{tI} := 1 \cdot 10^{12}$	AlGaAs/GaAs interface density of states (cm^-2)
$\sigma_n := 1 \cdot 10^{-15}$	Capture cross section of an electron (cm^2)
$m_n := 0.067 \cdot m_o$	Electron effective mass in GaAs (Kg)
$A_p := 1 \cdot 10^{-30}$	Auger recombination coefficient in GaAs (cm^6/s)
$B := 2 \cdot 10^{-10}$	Radiative recombination coefficient in GaAs (cm^3/s)
$\rho_{Au} := 2.44 \cdot 10^{-6}$	Resistivity of gold metallization (ohm.cm)
$\Delta E_c := 0.797 \cdot x$	Difference in conduction band energy at the interface (eV)
$S_o := 1 \cdot 10^6$	Intrinsic surface recombination velocity (cm/s)
$L_s := 1 \cdot 10^{-5}$	Surface diffusion length (cm)

One of the most elementary calculations is that of the built-in voltage for each junction:

$$VJE := k \cdot T \cdot \ln\left(\frac{N_E \cdot N_B}{n_{iE} \cdot n_{iB}}\right) + \Delta E_c - \frac{\Delta E}{2} \qquad VJE = 1.7018$$

$$VJC := k \cdot T \cdot \ln\left(\frac{N_B \cdot N_C}{n_{iB} \cdot n_{iC}}\right) \qquad VJC = 1.4107$$

The zero-bias depletion widths may be calculated from Ryum and Abdel-Motaleb [23:873]:

$$X_{1o} := \sqrt{\frac{2 \cdot N_B \cdot \varepsilon_E \cdot \varepsilon_B \cdot (VJE - 1.64 \cdot k \cdot T)}{q \cdot N_E \cdot (\varepsilon_E \cdot N_E + \varepsilon_B \cdot N_B)}} \qquad X_{2o} := \frac{N_E}{N_B} \cdot X_{1o}$$

$$X_{3o} := \sqrt{\frac{2 \cdot N_C \cdot \varepsilon_B \cdot (VJC - k \cdot T)}{q \cdot N_B \cdot (N_C + N_B)}} \qquad X_{4o} := \frac{N_B}{N_C} \cdot X_{3o}$$

$X_{1o} = 6.6288 \cdot 10^{-6}$ On the emitter side of the EB junction (cm)

$X_{2o} = 6.6288 \cdot 10^{-8}$ On the base side of the EB junction (cm)

$X_{3o} = 2.8379 \cdot 10^{-8}$ On the base side of the CB junction (cm)

$X_{4o} = 1.419 \cdot 10^{-5}$ On the collector side of the CB junction (cm)

The effective zero-bias base width Wb, is found by subtracting the depletion widths in the base on both the emitter and collector sides:

$$W_B := W - (X_{2o} + X_{3o}) \qquad W_B = 6.9053 \cdot 10^{-6} \quad (cm)$$

Now, calculate the depletion capacitances from Ryum and Abdel-Motaleb [23:873]:

$$CJE := A_{be} \cdot \frac{(\varepsilon_E \cdot \varepsilon_B)}{\varepsilon_E \cdot X_{2o} + \varepsilon_B \cdot X_{1o}} \qquad CJE = 4.8855 \cdot 10^{-14}$$

$$CJC := A_{bc} \cdot \frac{\varepsilon_B}{X_{3o} + X_{4o}} \qquad CJC = 1.5758 \cdot 10^{-13}$$

Calculating the value of Cje with a nominal bias is helpful. Since a nominal value of Vbe is 1.5 V, we have:

$$X_{1o} := \sqrt{\frac{2 \cdot N_B \cdot \varepsilon_E \cdot \varepsilon_B \cdot (VJE - 1.64 \cdot k \cdot T - 1.5)}{q \cdot N_E \cdot (\varepsilon_E \cdot N_E + \varepsilon_B \cdot N_B)}} \qquad X_{2o} := \frac{N_E}{N_B} \cdot X_{1o}$$

$$CJE_{bias} := A_{be} \cdot \frac{(\varepsilon_E \cdot \varepsilon_B)}{\varepsilon_E \cdot X_{2o} + \varepsilon_B \cdot X_{1o}} \qquad CJE_{bias} = 1.5765 \cdot 10^{-13}$$

The minority electron mobility in the p-type base GaAs as a function of base doping can be found from the empirical relation stated by Ali and Gupta [53:202]. A similar relation for minority holes in the collector is stated by C. Selvakumar [55:773]. The diffusivities are then calculated from the Einstein relation:

$$\mu_n := \frac{7057}{1 + \left(\frac{N_B}{2.84 \cdot 10^{16}}\right)^{0.753}} + 943 \qquad \mu_n = 968.2979 \qquad D_{nB} := \mu_n \cdot k \cdot T$$

$$\mu_{pE} := \frac{360}{1 + \left(\frac{N_E}{2.5 \cdot 10^{17}}\right)^{0.417}} + 40 \qquad \mu_{pE} = 194.1658 \qquad D_{pE} := \mu_{pE} \cdot k \cdot T$$

$$\mu_{pC} := \frac{360}{1 + \left(\frac{N_C}{2.5 \cdot 10^{17}}\right)^{0.417}} + 40 \qquad \mu_{pC} = 253.976 \qquad D_{pC} := \mu_{pC} \cdot k \cdot T$$

$D_{nB} = 25.0326$ Diffusivity of minority electrons in the base (cm^2/s)

$D_{pE} = 5.0196$ Estimated diffusivity of minority holes in the emitter (cm^2/s)

$D_{pC} = 6.5658$ Diffusivity of minority holes in the collector (cm^2/s)

The base transit time has many forms [60,51], but ultimately from from Hodges and Jackson [44:162]:

$$TF := \frac{W_B^2}{2.43 \cdot D_{nB}} \qquad TF := \frac{W_B^2}{2 \cdot D_{nB}} + \frac{W_B}{v_{sat}} \qquad TF := \frac{W_B^2}{2 \cdot D_{nB}}$$

$TF = 9.5243 \cdot 10^{-13}$ The forward transit time of minority electrons across the base (s)

Excess minority electron lifetime may be obtained by considering the lifetime of each recombination component. The expression for tno is taken from Lundstrom et al. [56:698]:

$$v_{th} := 100 \cdot \left(\frac{q \cdot k \cdot T}{2 \cdot \pi \cdot m_n} \right)^{0.5} \qquad v_{th} = 1.0392 \cdot 10^7$$ Average thermal velocity of an electron in GaAs (cm/s)

$$t_{SRH} := \frac{1}{\sigma_n \cdot N_t \cdot v_{th}} \qquad t_{SRH} = 9.6227 \cdot 10^{-8}$$ Shockley-Read-Hall recombination lifetime in GaAs (s)

$$t_{Aug} := \frac{1}{A_p \cdot N_B^2} \qquad t_{Aug} = 4 \cdot 10^{-10}$$ Auger recombination lifetime in p-type GaAs (s)

$$t_{rad} := \frac{1}{B \cdot N_B} \qquad t_{rad} = 1 \cdot 10^{-10}$$ Radiative recombination lifetime in p-type GaAs (s)

$$t_{no} := \left(\frac{1}{t_{SRH}} + \frac{1}{t_{Aug}} + \frac{1}{t_{rad}} \right)^{-1}$$

$t_{no} = 7.9934 \cdot 10^{-11}$ Minority electron lifetime in the base (s)

$t_{poC} := 20 \cdot 10^{-9}$ Minority hole lifetime in the collector (s)

$L_{nB} := \sqrt{D_{nB} \cdot t_{no}}$ $L_{nB} = 4.4732 \cdot 10^{-5}$ Diffusion length of electrons in the base (cm)

$L_{pC} := \sqrt{D_{pC} \cdot t_{poC}}$ $L_{pC} = 3.6238 \cdot 10^{-4}$ Diffusion length of holes in the collector (cm)

The diffusion length of minority holes in the emitter is estimated from an empirical expression found in Ryum and Abdel-Motaleb [23: 876]:

$$L_{pE} := \frac{42.46 - \log(N_E)}{9.21 \cdot 10^3} \qquad L_{pE} = 0.0027$$

Diffusion length of holes in the emitter (cm)

The maximum dc Beta for an HBT is best described by Kroemer [13:15]; however, better dc agreement between modeled and measured data is obtained if beta is considered due only to recombination in the neutral base after Grossman and Choma [25:459]:

$$v_{nB} := \frac{D_{nB}}{L_{nB}} \qquad v_{pE} := \frac{D_{pE}}{L_{pE}} \qquad BF_{max} := \frac{N_E}{N_B} \cdot \frac{v_{nB}}{v_{pE}} \cdot \exp\left(\frac{\Delta E}{k \cdot T}\right)$$

$$BF := \frac{t_{no}}{TF} \qquad BF = 83.9258$$

IS can be estimated from Huang and Abdel-Motaleb [66:165]:

$$IS := \frac{q \cdot A_{be} \cdot n_{iB}^2 \cdot D_{nB}}{W_B \cdot N_B} \qquad IS = 1.1111 \cdot 10^{-25}$$

$$Ics := A_{bc} \cdot q \cdot \left(\frac{D_{nB} \cdot n_{iB}^2}{L_{nB} \cdot N_B} + \frac{D_{pC} \cdot n_{iC}^2}{L_{pC} \cdot N_C}\right) \qquad Ics = 2.8641 \cdot 10^{-25}$$

Now, we can calculate the reverse beta, BR, and reverse tau, TR:

$$\text{alpha}_R := \frac{IS}{Ics} \qquad \text{alpha}_R = 0.3879$$ Reverse common-base current gain

$$BR := \frac{\text{alpha}_R}{1 - \text{alpha}_R} \qquad BR = 0.6338$$ Reverse common-emitter current gain

$$TR := \frac{t_{no}}{BR} \qquad TR = 1.2611 \cdot 10^{-10}$$ Reverse base transit time (s)

We can also determine the series emitter and collector resistances, RE and RC, after Ali and Gupta [53:204]. Resistivities for are calculated from the empirical mobility relations.

$$\mu_{cap} := \frac{7057}{1 + \left(\frac{N_{cap}}{2.84 \cdot 10^{16}}\right)^{0.753}} + 943 \qquad \rho_{InGaAs} := \left(q \cdot N_{cap} \cdot \mu_{cap}\right)^{-1}$$

$$\mu_{cgrad} := \frac{7057}{1 + \left(\frac{N_{cgrad}}{2.84 \cdot 10^{16}}\right)^{0.753}} + 943 \qquad \rho_{cgrad} := \left(q \cdot N_{cgrad} \cdot \mu_{cgrad}\right)^{-1}$$

$$\mu_{E.cont} := \frac{7057}{1 + \left(\frac{N_{E.cont}}{2.84 \cdot 10^{16}}\right)^{0.753}} + 943 \qquad \rho_{E.cont} := \left(q \cdot N_{E.cont} \cdot \mu_{E.cont}\right)^{-1}$$

$$\mu_{grade} := \frac{7057}{1 + \left(\frac{N_{grade}}{2.84 \cdot 10^{16}}\right)^{0.753}} + 943 \qquad \rho_{grade} := \left(q \cdot N_{grade} \cdot \mu_{grade}\right)^{-1}$$

$$\mu_E := \frac{7057}{1 + \left(\frac{N_E}{2.84 \cdot 10^{16}}\right)^{0.753}} + 943 \qquad \rho_{AlGaAs} := \left(q \cdot N_E \cdot \mu_E\right)^{-1}$$

$$\mu_C := \frac{7057}{1 + \left(\frac{N_C}{2.84 \cdot 10^{16}}\right)^{0.753}} + 943 \qquad \rho_C := \left(q \cdot N_C \cdot \mu_C\right)^{-1}$$

$$\mu_{subC} := \frac{7057}{1 + \left(\frac{N_{subC}}{2.84 \cdot 10^{16}}\right)^{0.753}} + 943 \qquad \rho_{subC} := \left(q \cdot N_{subC} \cdot \mu_{subC}\right)^{-1}$$

$$\mu_p := \frac{360}{1 + \left(\frac{N_B}{2.5 \cdot 10^{17}}\right)^{0.417}} + 40 \qquad \rho_B := \left(q \cdot N_B \cdot \mu_p\right)^{-1}$$

$\rho_{InGaAs} = 3.1423 \cdot 10^{-4}$	Estimated resistivity of the InGaAs cap layer (ohm.cm)
$\rho_{cgrad} = 6.0764 \cdot 10^{-4}$	Resistivity of the In graded region (ohm.cm)
$\rho_{E.cont} = 0.0012$	Resistivity of the continuous GaAs region (ohm.cm)
$\rho_{grade} = 0.0075$	Resistivity of the Al graded region (ohm.cm)
$\rho_{AlGaAs} = 0.0075$	Estimated resititvity of the AlGaAs emitter region (ohm.cm)
$\rho_B = 0.0017$	Resistivity of the p-type GaAs base (ohm.cm)
$\rho_C = 0.0214$	Resistivity of the n-type GaAs collector (ohm.cm)
$\rho_{subC} = 0.0018$	Resistivity of the n+ GaAs subcollector (ohm.cm)

$$\rho_{E1} := \rho_{InGaAs} \cdot l_{cap} + \left(\rho_{cgrad}\right) \cdot l_{cgrad} + \rho_{E.cont} \cdot l_{E.cont}$$

$$\rho_{E2} := \left(\rho_{grade}\right) \cdot l_{grade} + \rho_{AlGaAs} \cdot \left(l_{wide} - X_{lo}\right)$$

$\rho_E := \rho_{E1} + \rho_{E2}$ Composite emitter semiconductor resistance (ohm.cm^2)

$RE_s := \frac{\rho_E}{A_{be}}$ $RE_s = 0.24$ Component of emitter resistance due to the semiconductor (ohm)

$RE_c := \frac{\rho_{Ec}}{A_{be}}$ $RE_c = 6.5496$ Component of emitter resistance due to the metallization (ohm)

$RE := RE_s + RE_c$ Total emitter series resistance (ohm) $RE = 6.7896$

RB for an emitter dot geometry may be calculated with the formula provided by W. Liu, Solid-State Electronics, vol. 36, p. 496, Apr. 93.

$a_1 := \frac{l_{ee}}{2} - 0.1 \cdot 10^{-4}$ $a_1 = 9 \cdot 10^{-5}$ Radius of emitter dot (cm)

$a_2 := \frac{l_{ee}}{2}$ $a_2 = 1 \cdot 10^{-4}$ Inner radius of base contact (cm)

$a_3 := \frac{l_{ee}}{2} + 1.25 \cdot 10^{-4}$ $a_3 = 2.25 \cdot 10^{-4}$ Approximate outer radius of base annulus contact (cm)

$R_{B.sh} := \frac{\rho_B}{W}$ $R_{B.sh} = 235.8873$ Base sheet resistance (ohm/sq.)

$L_t := \left(\frac{\rho_{Bc}}{R_{B.sh}}\right)^{0.5}$ $L_t = 1.4559 \cdot 10^{-4}$ Base contact transfer length (cm)

The base resistance of a junction transistor is typically the sum of three components. These components are geometry dependent and are given below [67,69]:

Spreading resistance: $R_{sp} := \frac{R_{B.sh}}{8 \cdot \pi}$ $R_{sp} = 9.3857$

Bulk resistance: $R_{bulk} := \frac{R_{B.sh}}{2 \cdot \pi} \cdot \ln\left(\frac{a_2}{a_1}\right)$ $R_{bulk} = 3.9555$

Lateral contact resistance:

$$R_{lc} := \frac{R_{B.sh} \cdot L_t}{2 \cdot \pi \cdot a_2} \cdot \frac{\left(K1\left(\frac{a_3}{L_t}\right) \cdot I0\left(\frac{a_2}{L_t}\right) + I1\left(\frac{a_3}{L_t}\right) \cdot K0\left(\frac{a_2}{L_t}\right)\right)}{\left(I1\left(\frac{a_3}{L_t}\right) \cdot K1\left(\frac{a_2}{L_t}\right) + K1\left(\frac{a_3}{L_t}\right) \cdot I1\left(\frac{a_2}{L_t}\right)\right)}$$

$R_{lc} = 44.7133$

Total base series resistance (ohm):

$$RB_T := \frac{R_{sp} + R_{bulk} + R_{lc}}{N_{dot} \cdot N_{fin}} \qquad RB_T = 4.8379$$

However, for S-parameter analysis, the base-collector capacitance is distributed across the base resistance. The base resistance is split into two elements: RB and RBext.

$$RB := \frac{R_{sp}}{N_{dot} \cdot N_{fin}} \qquad RB_{ext} := \frac{R_{bulk} + R_{lc}}{N_{dot} \cdot N_{fin}}$$

The capacitance of the base metal-semiconductor contact is in parallel with RBext. However, due to the high base doping the barrier is very thin and there is essentially no SCR. Tunneling current occurs easily; thus Cbcon can be neglected.

The collector resistance is also comprised of spreading, bulk, and lateral contact resistances. When the transistor is operated in the active region (as is the case for microwave operation), the collector layer is fully depleted and does not contribute to the series resistance. However, better agreement on the I-V characteristics is obtained when the resistance of the collector layer is considered. When the transistor is saturated, almost the entire collector region is resistive.

$$R_C := \frac{\rho_C \cdot (l_C - X_{4o})}{l_{ee}^2 \cdot N_{dot}} \qquad R_C = 1.8574 \qquad \text{Zero-bias collector series resistance (ohm)}$$

$$R_{subC.sh} := \frac{\rho_{subC}}{l_{subC}} \qquad R_{subC.sh} = 18.1238 \qquad \text{Subcollector sheet resistance (ohm/sq.)}$$

$$L_t := \left(\frac{\rho_{Ec}}{R_{subC.sh}}\right)^{0.5} \qquad L_t = 3.3219 \cdot 10^{-4} \qquad \text{Collector contact transfer length (cm)}$$

Since the collector current enters the subcollector layer through an area approximately 2x2 microns square (the emitter dot), and then follows two parallel paths, we have:

Spreading resistance: $$R_{sp} := \frac{R_{subC.sh}}{12 \cdot N_{dot}} \qquad R_{sp} = 0.2517$$

Bulk resistance: $$R_{bulk} := \frac{l_{bc} + l_{eb}}{l_{ee} \cdot 2 \cdot N_{dot}} \cdot \ln(2) \cdot \left(R_{subC.sh}\right) \qquad R_{bulk} = 1.0469$$

Lateral contact resistance: $$R_{lc} := \frac{R_{subC.sh}}{2 \cdot l_{cc}} \cdot L_t \cdot \coth\left(\frac{l_{cl}}{L_t}\right) \qquad R_{lc} = 1.2543$$

The total ac collector series resistance may be assumed different than the dc resistance as given by the following expressions:

$$RC_{ac} := \frac{R_{sp} + R_{bulk} + R_{lc}}{N_{fin}} \qquad RC_{ac} = 1.2765$$

$$RC_{dc} := \frac{R_{sp} + R_{bulk} + R_{lc} + R_C}{N_{fin}} \qquad RC_{dc} = 2.2051$$

The two remaining dc model parameters are ISE and ISC, the recombination diodes saturation currents. These parameters can be estimated by calculating a composite recombination saturation current that is the sum of all the individual recombination component saturation currents. ISE is the constant for the Vbe exponent and ISC is the constant for the Vbc exponent. The analytical expressions for the recombination current components are found in Ryum and Abdel-Motaleb [45], Liou [52], and Huang and Abdel-Motaleb [66].

The bulk base recombination saturation current expression comes from reference [45], with the exception that the drift-diffusion model is used to determine the base-emitter carrier concentrations.

$$ISE_{BR} := \frac{q \cdot A_{be} \cdot L_{nB} \cdot n_{iB}}{t_{no} \cdot N_B} \cdot \left(\cosh\left(\frac{W_B}{L_{nB}}\right) - 1\right) \cdot \sinh\left(\frac{W_B}{L_{nB}}\right)^{(-1)} \qquad ISE_{BR} = 2.3607 \cdot 10^{-34}$$

$$ISC_{BR} := \frac{q \cdot A_{be} \cdot L_{nB} \cdot n_{iB}}{t_{no} \cdot N_B} \cdot \left(\cosh\left(\frac{W_B}{L_{nB}}\right) - 1 \right) \cdot \sinh\left(\frac{W_B}{L_{nB}}\right)^{(-1)} \qquad ISC_{BR} = 2.3607 \cdot 10^{-34}$$

The SCR recombination saturation currents from reference [66]:

$$ISE_{SCR} := \frac{q \cdot A_{be}}{2 \cdot t_{SRH}} \cdot \left[n_{iE} \cdot \left(l_{wide} - X_G \right) + \frac{n_{iE} + n_{iC}}{2} \cdot X_G + n_{iB} \cdot X_{2o} \right] \qquad ISE_{SCR} = 3.7089 \cdot 10^{-19}$$

$$ISC_{SCR} := \frac{q \cdot A_{bc}}{2 \cdot t_{SRH}} \cdot \left(n_{iB} \cdot X_{3o} + n_{iC} \cdot X_{4o} \right) \qquad ISC_{SCR} = 4.0848 \cdot 10^{-17}$$

The surface recombination saturation current from reference [45]:

$$ISE_{SR} := q \cdot P \cdot S_o \cdot L_s \cdot n_{iB} \qquad ISE_{SR} = 2.738 \cdot 10^{-18}$$

The sum of these individual components are the composite saturation currents ISE and ISC:

$$ISE := ISE_{BR} + ISE_{SCR} + ISE_{SR} \qquad ISE = 3.1089 \cdot 10^{-18}$$

$$ISC := ISC_{BR} + ISC_{SCR} \qquad ISC = 4.0848 \cdot 10^{-17}$$

The final dc model parameter is the forward knee current which models the degradation of beta at high currents.

$$IKF := q \cdot A_{be} \cdot N_C \cdot v_{sat} \qquad IKF = 0.0489$$

Since for this device the collector metal surrounds the base finger, the parasitic base-collector capacitance, Cbcp, may be calculated as follows:

$$\kappa_s := \left[\frac{\left[\left(l_{cl} + l_{bc} + l_{eb} \right) \cdot l_{bc} \right]}{\left[\left(l_{eb} + l_{bc} \right) \cdot \left(l_{cl} + l_{bc} \right) \right]} \right]^{0.5} \qquad \kappa_l := \left[\frac{\left[\left(l_{cl} + l_{bc} + l_{bb} \right) \cdot l_{bc} \right]}{\left[\left(l_{bb} + l_{bc} \right) \cdot \left(l_{cl} + l_{bc} \right) \right]} \right]^{0.5} \qquad k_s := \left(1 - \kappa_s^2 \right)^{0.5}$$

$$\kappa_f := \left[\frac{\left[\left(52.46 \cdot 10^{-4} + l_{bc} + l_{cc} + l_{bb} + 26 \cdot 10^{-4} \right) \cdot l_{bc} \right]}{\left[\left(l_{cc} + l_{bb} + 26 \cdot 10^{-4} + l_{bc} \right) \cdot \left(52.46 \cdot 10^{-4} + l_{bc} \right) \right]} \right]^{0.5} \qquad k_l := \left(1 - \kappa_l^2 \right)^{0.5} \qquad k_f := \left(1 - \kappa_f^2 \right)^{0.5}$$

$$\kappa_m := \left[\frac{\left(l_{cc} + 57 \cdot 10^{-4} + 23 \cdot 10^{-4} + 23.8 \cdot 10^{-4} \right) \cdot 23 \cdot 10^{-4}}{\left[\left(l_{cc} + 57 \cdot 10^{-4} + 23 \cdot 10^{-4} \right) \cdot \left(23 \cdot 10^{-4} + 23.8 \cdot 10^{-4} \right) \right]} \right]^{0.5} \qquad k_m := \left(1 - \kappa_m^2 \right)^{0.5}$$

$$\kappa_e := \left[\frac{\left(l_{cc} + 49 \cdot 10^{-4} + 38 \cdot 10^{-4} + 12 \cdot 10^{-4} \right) \cdot 38 \cdot 10^{-4}}{\left[\left(l_{cc} + 49 \cdot 10^{-4} + 38 \cdot 10^{-4} \right) \cdot \left(38 \cdot 10^{-4} + 12 \cdot 10^{-4} \right) \right]} \right]^{0.5} \qquad k_e := \left(1 - \kappa_e^2 \right)^{0.5}$$

$$\kappa_t := \left[\frac{\left(l_{cc} + 56 \cdot 10^{-4} + 8.5 \cdot 10^{-4} + 39 \cdot 10^{-4} \right) \cdot 8.5 \cdot 10^{-4}}{\left[\left(l_{cc} + 56 \cdot 10^{-4} + 8.5 \cdot 10^{-4} \right) \cdot \left(8.5 \cdot 10^{-4} + 39 \cdot 10^{-4} \right) \right]} \right]^{0.5} \qquad k_t := \left(1 - \kappa_t^2 \right)^{0.5}$$

The following constants and function K(k) are the solution to the required integral provided by the Naval Research Laboratory Report 8561, p. 15, 1982:

$A_0 := 1.3862944$ $\qquad A_2 := 0.0725296$ $\qquad A_1 := 0.1119723$

$B_0 := 0.5$ $\qquad B_1 := 0.1213478$ $\qquad B_2 := 0.0288729$

$$K(\kappa) := \left[A_0 + A_1 \cdot \left(1 - \kappa^2 \right) + A_2 \cdot \left(1 - \kappa^2 \right)^2 \right] + \ln\left[\frac{1}{\left(1 - \kappa^2 \right)} \right] \cdot \left[B_0 + B_1 \cdot \left(1 - \kappa^2 \right) + B_2 \cdot \left(1 - \kappa^2 \right)^2 \right]$$

$$C_{bcp1} := 2 \cdot N_{fin} \cdot N_{dot} \cdot l_{ee} \cdot \left(\varepsilon_p + \varepsilon_B \right) \cdot \left(\frac{K(k_l)}{K(\kappa_l)} + \frac{K(k_s)}{K(\kappa_s)} + \frac{K(k_f)}{K(\kappa_f)} \cdot \frac{l_{eb}}{N_{dot} \cdot l_{ee}} \right) + \frac{N_{fin} \cdot t_{cp} \cdot \varepsilon_p}{l_{bc}} \cdot \left(2 \cdot l_{cc} + l_{bb} \right)$$

$$C_{bcp2} := \left(\varepsilon_p + \varepsilon_B \right) \cdot \left[\frac{K(k_m)}{K(\kappa_m)} \cdot 17.8 \cdot 10^{-4} + \frac{K(k_e)}{K(\kappa_e)} \cdot 2 \cdot \left(l_{cl} - 1.5 \cdot 10^{-4} \right) + \frac{K(k_t)}{K(\kappa_t)} \cdot 1.5 \cdot 10^{-4} \cdot 4 \right]$$

$$C_{bcp} := C_{bcp1} + C_{bcp2}$$

$$C_{cep} := \varepsilon_p \cdot \left(\frac{A_{cp} + A_{cm}}{l_{ec} - 0.1 \cdot 10^{-4}} \right) \qquad W_E := l_{cap} + l_{cgrad} + l_{E.com} \cdot l_{grade} + l_{wide}$$

$$C_{bep} := \frac{\varepsilon_p \cdot \left[A_{bc} - A_{be} + \left(N_{fin} \cdot l_{bb}^2 \right) \right]}{d_{eb} - 0.1 \cdot 10^{-4}} + \frac{2 \cdot \pi \cdot \varepsilon_p \cdot \left(t_{cp} - W_E \right) \cdot N_{dot} \cdot N_{fin}}{\ln \left(\frac{0.5 \cdot l_{ee}}{0.5 \cdot l_{ee} - 0.1 \cdot 10^{-4}} \right)}$$

There is also an inductance associtated with each terminal of the transistor. The equation for estimating this inductance is given by Ladbrooke [59:99]. Only the interconnects NOT beneath the emitter bridge (and NOT part of the thick pad metal) are considered here since the inductance under the bridge is negligible in comparison.

$$L_{cp} := \mu_o \cdot t_{sub} \cdot \frac{25}{73.5} \qquad L_{bp} := \mu_o \cdot t_{sub} \cdot \left(\frac{\frac{7}{4} + \frac{10}{15}}{2} \right)$$

$$\frac{23.8}{56.28}$$

$$L_{bp1} := \frac{N_{dot}}{N_{fin}} \cdot \mu_o \cdot \left(d_{eb} - 0.1 \cdot 10^{-4} \right) \cdot \left(\frac{l_{ee}}{l_{bb}} + \frac{l_{ee}}{2 \cdot l_{eb}} \right) + \frac{\mu_o}{N_{fin}} \cdot \left(l_{ec} - 0.1 \cdot 10^{-4} \right)$$

$$L_{cp1} := \mu_o \cdot \left(l_{ec} - 0.1 \cdot 10^{-4} \right) \cdot \frac{l_{cc} + 7.8 \cdot 10^{-4}}{\left(N_{fin} + 1 \right) \cdot l_{cl}} \qquad L_{ep} := \left(\frac{1}{L_{cp1}} + \frac{1}{L_{bp1}} \right)^{-1}$$

The resistance in series with each inductance can be calculated from Ladbrooke [59:146]:

$$R_{cp} := \frac{\rho_{Au}}{3 \cdot t_{cp}} \cdot \left[\frac{l_{cc} + 7.8 \cdot 10^{-4}}{\left(N_{fin} + 1 \right) \cdot l_{cl}} \right] \qquad R_{cp} = 0.011$$

$$R_{bp} := \frac{N_{dot}}{N_{fin}} \cdot \frac{\rho_{Au}}{3 \cdot t_{cp}} \cdot \left(\frac{l_{ee}}{l_{bb}} + \frac{l_{ee}}{2 \cdot l_{eb}} \right) \qquad R_{bp} = 0.0915$$

The following are six parasitic equivalent circuit elements that are external to the SPICE BJT model:

$C_{bcp} = 2.5754 \cdot 10^{-14}$	The parasitic interelectrode base-collector capacitcance (F)
$C_{bep} = 9.877 \cdot 10^{-15}$	The parasitic interelectrode base-emitter capacitance (F)
$C_{cep} = 3.3689 \cdot 10^{-14}$	The parasitic interelectrode collector-emitter capacitance (F)
$L_{cp} = 2.992 \cdot 10^{-11}$	The parasitic collector inductance (H)
$L_{bp} = 1.0629 \cdot 10^{-10}$	The parasitic base inductance (H)
$L_{ep} = 1.5366 \cdot 10^{-12}$	The parasitic emitter inductance (H)

All of the calculated SPICE model parameters are summarized below for the 2 micron emitter, 6 dot two finger geometry.

$BF = 83.9258$	Forward common-emitter current gain
$BR = 0.6338$	Reverse common-emitter current gain
$TF = 9.5243 \cdot 10^{-13}$	Forward base transit time (s)
$TR = 1.2611 \cdot 10^{-10}$	Reverse base transit time (s)
$IS = 1.1111 \cdot 10^{-25}$	Transport saturation current (A)
$ISE = 3.1089 \cdot 10^{-18}$	Base-emitter leakage saturation current (A)
$ISC = 4.0848 \cdot 10^{-17}$	Base-collector leakage saturation current (A)
$RE = 6.7896$	Emitter series resistance (ohm)
$RB = 0.7821$	Intrinsic base series resistance (ohm)
$RB_T = 4.8379$	Total base series resistance (ohm)
$RC_{ac} = 1.2765$	Microwave collector series resistance (ohm)

$RC_{dc} = 2.2051$	DC collector series resistance (ohm)
$CJE = 4.8855 \cdot 10^{-14}$	Base-emitter zero-bias depletion capacitance (F)
$CJC = 1.5758 \cdot 10^{-13}$	Base-collector zero-bias depletion capacitance (F)
VJE = 1.7018	Base-emitter built-in potential (V)
VJC = 1.4107	Base-collector built-in potential (V)
XCJC = 0.159	Fraction of base-collector depletion capacitance internal to base
IKF = 0.0489	Corner for high current BF roll-off (A)

The following is an equivalent circuit element that is external to the SPICE BJT model:

$RB_{ext} = 4.0557$	The base contact resistance (ohm)

Appendix B: HSPICE Files

DC HSPICE Files

```
*-------------------------------------------------------------------------
* SPICE HBT I-V Characteristics
* Author:  James A. Fellows
* Date:  22 Oct 93
* Filename:  ldn_dc10.sp
* Technology:  AlGaAs/GaAs Heterojunction Bipolar
* Description: This file provides dc data for an NPN HBT (4490A,
*              single dot 3 micron emitter).
*-------------------------------------------------------------------------

*-----------------------------------------------------
* Voltage Source    (+) node     (-) node     Value
*-----------------------------------------------------
   Vce                  C            0        $ swept

*-----------------------------------------------------
* Current Source    (+) node     (-) node     Value
*-----------------------------------------------------
   Ib                   0            B        $ swept

*-----------------------------------------------------
* Circuit Elements  (+) node     (-) node     Value
*-----------------------------------------------------
   Rsrc                 B            0        1e+20

*-----------------------------------------------------
* BJT   Collector      Base      Emitter      Model
*-----------------------------------------------------
  Q1        C            B          GND       T3uldlf

.option brief post

*-------------------------------------------------------------------------
* DC Voltage/Current Sweeps: Modify step to match measured data
*-------------------------------------------------------------------------
*  Volt(1)  Start    End    Step    Crnt(1)  Start     End      Step
*-------------------------------------------------------------------------
.dc   Vce     0       4      0.05      Ib     20u      200u     20u

*-----------------------
* Data to be collected:
*-----------------------------------
*       Vce   Vbe  Ib       Ic
*-----------------------------------
.print dc v(C), v(B), i(Ib), i(Vce)

.model T3uldlf  npn
  + BF   =   28.9          BR   =   0.005        NF    =   1.116
  + NR   =   1.00000
  + RB   =   43.2846       RE   =   33.6707      RC    =   68.7
  + IS   =   1.0363e-26
```

```
  + CJE  =   9.8515e-15   MJE  =   .50          VJE  =   1.7018
  + CJC  =   1.119e-14    MJC  =   .50          VJC  =   1.3691
  + TF   =   9.5681e-13   TR   =   5.287e-10    XCJC =   0.2053
.end


*-------------------------------------------------------------------
* SPICE HBT I-V Characteristics
* Author:  James A. Fellows
* Date:  22 Oct 93
* Filename:  5dn_dc10.sp
* Technology:  AlGaAs/GaAs Heterojunction Bipolar
* Description: This file provides dc data for an NPN HBT (4491,
*              5 dot, single finger 3 micron emitter).
*-------------------------------------------------------------------

*-------------------------------------------------
* Voltage Source   (+) node    (-) node     Value
*-------------------------------------------------
   Vce                C          0        $ swept

*-------------------------------------------------
* Current Source   (+) node    (-) node     Value
*-------------------------------------------------
   Ib                 0          B        $ swept

*-------------------------------------------------
* Circuit Elements (+) node    (-) node     Value
*-------------------------------------------------
   Rsrc               B          0         1e+20

*-------------------------------------------------
* BJT   Collector    Base      Emitter      Model
*-------------------------------------------------
  Q1        C          B         GND       T3u5d1f

.option brief post

*-------------------------------------------------------------------
* DC Voltage/Current Sweeps: Modify step to match measured data
*-------------------------------------------------------------------
*  Volt(1)  Start   End   Step   Crnt(1)  Start    End     Step
*-------------------------------------------------------------------
.dc   Vce     0      4     0.05     Ib     50u     200u     50u

*-- ---------------------
* Data to be collected:
*-----------------------------
*       Vce   Vbe    Ib      Ic
*-----------------------------
.print dc v(C), v(B), i(Ib), i(Vce)
```

```
.model T3u5d1f  npn
  + BF   =   33.3          BR   =   0.0231        NF   =   1.1557
  + NR   =   1.00000
  + RB   =   8.6569        RE   =   6.7341        RC   =   16.79
  + IS   =   5.2047e-26
  + CJE  =   4.9257e-14    MJE  =   .50           VJE  =   1.7018
  + CJC  =   3.5706e-14    MJC  =   .50           VJC  =   1.3454
  + TF   =   9.5811e-13    TR   =   1.4046e-09    XCJC =   0.2053
.end


*-------------------------------------------------------------------------
* SPICE HBT I-V Characteristics
* Author:  James A. Fellows
* Date:  22 Oct 93
* Filename:  6dn_dc10.sp
* Technology:  AlGaAs/GaAs Heterojunction Bipolar
* Description: This file provides dc data for an NPN HBT (4457B,
*              6 dot, 2 finger 2 micron emitter).
*-------------------------------------------------------------------------

*-----------------------------------------------
* Voltage Source    (+) node     (-) node      Value
*-----------------------------------------------
   Vce                  C           0          $ swept

*-----------------------------------------------
* Current Source    (+) node     (-) node      Value
*-----------------------------------------------
   Ib                   0           B          $ swept

*-----------------------------------------------
* Circuit Elements  (+) node     (-) node      Value
*-----------------------------------------------
   Rsrc                 B           0          1e+20

*-----------------------------------------------
* BJT    Collector     Base      Emitter       Model
*-----------------------------------------------
  Q1        C            B          GND        T2u6d2f

.option brief post

*-------------------------------------------------------------------------
* DC Voltage/Current Sweeps: Modify step to match measured data
*-------------------------------------------------------------------------
*  Volt(1)  Start    End    Step    Crnt(1)  Start      End      Step
*-------------------------------------------------------------------------
.dc   Vce      0       3      0.05      Ib      100u     1100u    100u
```

```
*-----------------------
* Data to be collected:
*-------------------------------------
*       Vce    Vbe     Ib       Ic
*-------------------------------------
.print dc v(C), v(B), i(Ib), i(Vce)

.model T2u6d2f  npn
  + BF   =   83.926        BR   =   0.6338        NF   =   1.1049
  + NR   =   1.00000       NE   =   1.7000        NC   =   1.7595
  + RB   =   4.8379        RE   =   6.7896        RC   =   2.2
  + IS   =   1.1111e-25    ISE  =   2.432e-19     ISC  =   4.393e-16
  + CJE  =   4.8855e-14    MJE  =   .50           VJE  =   1.7018
  + CJC  =   1.5758e-13    MJC  =   .50           VJC  =   1.4107
  + TF   =   9.5243e-13    TR   =   1.2611e-10    XCJC =   0.159
.end
```

Microwave HSPICE Files

```
*-------------------------------------------------------------------------
* SPICE HBT S-Parameter Analysis
* Author:  James A. Fellows
* Date:  22 Oct 93
* Filename:  1F_21_N.sp
* Technology:  AlGaAs/GaAs Heterojunction Bipolar
* Description: This file provides S-parameter data for an NPN HBT
*              (4490A: single dot, 3 micron emitter).
*-------------------------------------------------------------------------

.net i(Vce) Ib ROUT=50 RIN=50

*-----------------------------------------------
* Voltage Source    (+) node    (-) node    Value
*-----------------------------------------------
   Vce                CC          0          2

*-----------------------------------------------------------------
* Current Source    (+) node    (-) node    AC value    DC value
*-----------------------------------------------------------------
   Ib                 0           BB         AC=1        DC=100u

*-----------------------------------------------
* Circuit Elements  (+) node    (-) node      Value
*-----------------------------------------------
   Rsrc               BB          0          1e+20
   RBext              B           Bcon       33.8989
   Cbep               Bcon        E           0.739f
   Cbcp               C           Bcon       15.0f
   Ccep               C           E           0.1f
   Lep                E           0           1.6965p
   Lbp                Bcon        BB          1.6965p
```

```
   Lcp                  C          CC         3.309p

*-------------------------------------------------------
* BJT   Collector     Base      Emitter      Model
*-------------------------------------------------------
  Q1       C           B          E        T3uld1f

.option brief post

*-------------------------------------------------------
* AC Frequency Sweeps: Modify step to match measured data
*-------------------------------------------------------
*    Scale  Points   Start   Stop
*-------------------------------------
.ac   LIN     50       1G     50G

*-------------------------------------------------------
* Data to be collected: S-Parameters (M)agnitude and (P)hase
*-------------------------------------------------------
.print ac S11(M) S11(P) S21(M) S21(P) S12(M) S12(P) S22(M) S22(P)

.model T3uld1f  npn
  + BF   =   28.9          BR   =   0.005        NF    =   1.116
  + NR   =   1.00000
  + RB   =   9.3857        RE   =   33.6707      RC    =   68.7
  + IS   =   1.0363e-26
  + CJE  =   9.8515e-15    MJE  =   .50          VJE   =   1.7018
  + CJC  =   1.119e-14     MJC  =   .50          VJC   =   1.3691
  + TF   =   9.5681e-13    TR   =   5.287e-10    XCJC  =   0.2053
.end


*-------------------------------------------------------------------------
* SPICE HBT S-Parameter Analysis
* Author:  James A. Fellows
* Date:  22 Oct 93
* Filename:  5F_23_N.sp
* Technology:  AlGaAs/GaAs Heterojunction Bipolar
* Description: This file provides S-parameter data for an NPN HBT
*              (4491A: 5 dot, single finger, 3 micron emitter).
*-------------------------------------------------------------------------

.net i(Vce) Ib ROUT=50 RIN=50

*-------------------------------------------
* Voltage Source   (+) node    (-) node    Value
*-------------------------------------------
   Vce                 CC          0          1
```

```
*-------------------------------------------------------------------
* Current Source    (+) node     (-) node     AC value       DC value
*-------------------------------------------------------------------
   Ib                   0            BB         AC=1          DC=500u

*-----------------------------------------------------
* Circuit Elements  (+) node     (-) node         Value
*-----------------------------------------------------
   Rsrc                 BB           0             1e+20
   RBext                B            Bcon         6.7798
   Cbep                 Bcon         E            3.6943f
   Cbcp                 C            Bcon        31.566f
   Ccep                 C            E           13.65f
   Lep                  E            0            1.4224p
   Lbp                  Bcon         BB           8.4823p
   Lcp                  C            CC           1.709p

*-------------------------------------------------------
* BJT   Collector      Base      Emitter      Model
*-------------------------------------------------------
  Q1        C            B           E        T3u5d1f

.option brief post

*-----------------------------------------------------------
* AC Frequency Sweeps: Modify step to match measured data
*-----------------------------------------------------------
*    Scale  Points   Start   Stop
*-----------------------------------
.ac   LIN     50       1G     50G

*-------------------------------------------------------------
* Data to be collected: S-Parameters (M)agnitude and (P)hase
*-------------------------------------------------------------
.print ac S11(M) S11(P) S21(M) S21(P) S12(M) S12(P) S22(M) S22(P)

.model T3u5d1f  npn
  + BF   =   33.3          BR   =   0.0231        NF   =   1.1557
  + NR   =   1.00000
  + RB   =   1.8771        RE   =   6.7341        RC   =   16.79
  + IS   =   5.2047e-26
  + CJE  =   4.9257e-14    MJE  =   .50           VJE  =   1.7018
  + CJC  =   3.5706e-14    MJC  =   .50           VJC  =   1.3454
  + TF   =   9.5811e-13    TR   =   1.4046e-09    XCJC =   0.2053
.end
```

```
*-------------------------------------------------------------------------
* SPICE HBT S-Parameter Analysis
* Author:  James A. Fellows
* Date:  22 Aug 93
* Filename:  6F_81_N.sp
* Technology:  AlGaAs/GaAs Heterojunction Bipolar
* Description: This file provides S-parameter data for an NPN HBT
*              (4457B: 6 dot, 2 finger, 2 micron emitter).
*-------------------------------------------------------------------------

.net i(Vce) Ib ROUT=50 RIN=50

*-----------------------------------------------------
* Voltage Source    (+) node     (-) node     Value
*-----------------------------------------------------
   Vce                  CC           0         1

*-----------------------------------------------------------------------
* Current Source    (+) node     (-) node     AC value      DC value
*-----------------------------------------------------------------------
   Ib                   0            BB        AC=1         DC=800u

*-----------------------------------------------------
* Circuit Elements  (+) node     (-) node       Value
*-----------------------------------------------------
   Rsrc                 BB           0           1e+20
   RBext                B            Bcon      4.0557
   Cbep                 Bcon         E         7.3255f
   Cbcp                 C            Bcon    106.136f
   Ccep                 C            E        18.488f
   Lep                  E            0         0.4841p
   Lbp                  Bcon         BB        2.3562p
   Lcp                  C            CC        0.6093p

*-----------------------------------------------------
* BJT   Collector     Base     Emitter     Model
*-----------------------------------------------------
  Q1        C           B          E       T2u6d2f

.option brief post

*-----------------------------------------------------
* AC Frequency Sweeps: Modify step to match measured data
*-----------------------------------------------------
*    Scale  Points   Start   Stop
*-----------------------------------
.ac   LIN     50       1G     50G

*-----------------------------------------------------
* Data to be collected: S-Parameters (M)agnitude and (P)hase
*-----------------------------------------------------
.print ac S11(M) S11(P) S21(M) S21(P) S12(M) S12(P) S22(M) S22(P)
```

```
.model T2u6d2f  npn
  + BF   =   83.926        BR   =   0.6338        NF   =   1.1049
  + NR   =   1.00000       NE   =   1.7000        NC   =   1.7595
  + RB   =   0.7821        RE   =   6.7896        RC   =   2.2
  + IS   =   1.1111e-25    ISE  =   2.432e-19     ISC  =   4.393e-16
  + CJE  =   4.8855e-14    MJE  =   .50           VJE  =   1.7018
  + CJC  =   1.5758e-13    MJC  =   .50           VJC  =   1.4107
  + TF   =   9.5243e-13    TR   =   1.2611e-10    XCJC =   0.159
.end
```

HSPICE Optimisation Files

```
* Optimization of SPICE HBT I-V Characteristics
* Author:  James A. Fellows
* Date: 2? Oct 93
* Filename:  6d_fit.sp
* Technology:  AlGaAs/GaAs Heterojunction Bipolar
* Description:    This file optimizes six SPICE BJT model parameters to
                  fit the measured data for an NPN HBT (4457B, 2 micron
                  emitter, 6 dot, 2 finger).
*-------------------------------------------------------------------------

*-------------------------------------------------
* Voltage Source    (+) node     (-) node     Value
*-------------------------------------------------
   Vce                 C            0          Vce

*-------------------------------------------------
* Current Source    (+) node     (-) node     Value
*-------------------------------------------------
   Ib                  0            B           Ib

*-------------------------------------------------
* Circuit Elements  (+) node     (-) node     Value
*-------------------------------------------------
   Rsrc                B            0          1e+20

*-------------------------------------------------
* BJT    Collector      Base      Emitter      Model
*-------------------------------------------------
  Q1         C            B         GND        T2u6d2f

.option post ingold=1

*-------------------------------------
* Physics-based HBT model parameters:
*-------------------------------------
.model T2u6d2f  npn
  + BF       =    83.926        BR   =   0.6338        NF   =   NF
  + NR       =    1.00000       NE   =   NE            NC   =   NC
  + RB       =    4.8379        RE   =   6.7896        RC   =   2.2
```

```
  + IS      =    1.1111e-25   ISE  =    ISE          ISC  =    ISC
  + CJE     =    4.8855e-14   MJE  =    .50          VJE  =    1.7018
  + CJC     =    1.5758e-13   MJC  =    .50          VJC  =    1.4107
  + TF      =    9.5243e-13   TR   =    1.2611e-10   XCJC =    0.159

*-----------------------------------------------------
* These are the empirical curve-fit model parameters:
*-----------------------------------------------------
.param NF  =  opt1(1.1, 1.0, 1.2)
     + NE  =  opt1(1.9, 1.7, 2.1)
     + NC  =  opt1(1.95, 1.75, 2.1)
     + ISE =  opt1(3.11e-18, 1e-20, 1e-16)
     + ISC =  opt1(5e-14, 1e-16, 1e-13)

*-----------------------------------------------------
* dc optimization analysis statement:
*-----------------------------------------------------
.dc data=measured optimize=opt1 results=Ib,Ic,Vce,Vbe
     + model=converge Vce LIN 31 0.0 3.0 sweep
     + Ib LIN 11 100u 1100u

.model converge opt itropt=100 grad=1e-05

.meas dc Ib errl  par(Ib) i(ib)
.meas dc Ic errl  par(Ic) i(vce)
.meas dc Vce errl par(Vce) v(c)
.meas dc Vbe errl par(Vbe) v(b)

.dc data=measured

*---------------------------------------
* Measured data to fit model parameters:
*---------------------------------------
.data measured

    Vbe      Vce       Ic        Ib

 1.07599998 0.00000000 0.00009878 0.00010000
 1.17499995 0.10000000 0.00009342 0.00010000
      :          :          :         :
 1.76400006 1.10000000 -0.04613100 0.00110000

.enddata
.end


2u6d2f dc optimization results:
-------------------------------

          residual sum of squares     =  5.95116
          norm of the gradient        =  23.6635
          marquardt scaling parameter =  0.492699
          no. of function evaluations =     234
```

```
        no. of iterations          =       66

    optimization completed

        parameters < relin=  1.0000E-03 on last iterations

**** optimized parameters opt1
                                          %norm-sen        %change

.param nf            =   1.1049       $   49.5075       -7.462e-04
.param ne            =   1.7000       $   48.3361        3.837e-04
.param nc            =   1.7595       $    0.7342       -2.402e-03
.param ise           = 2.432e-19      $    1.3952       -2.231e-02
.param isc           = 4.393e-16      $  2.698e-02       -4.936e-02
```

```
* Optimization of HBT S-Parameters by Fitting Parasitics
* Author:  James A. Fellows
* Date: 21 Oct 93
* Filename:  6dot_ac.sp
* Technology:  AlGaAs/GaAs Heterojunction Bipolar
* Description:  This file provides S-parameter data for an NPN HBT
*               (4457B: 6 dot, 2 finger, 2 micron emitter).
*-------------------------------------------------------------------

.net i(Vce) Ib ROUT=50 RIN=50

*-------------------------------------------------
* Voltage Source   (+) node    (-) node    Value
*-------------------------------------------------
   Vce                CC           0         1

*-------------------------------------------------------------------------
* Current Source   (+) node    (-) node    AC Value        DC Value
*-------------------------------------------------------------------------
   Ib                 0            BB          AC=1          DC=800u

*-------------------------------------------------
* Circuit Elements  (+) node    (-) node    Value
*-------------------------------------------------
   Rsrc               BB           0         1e+20
   Rbcon              B            Bcon      4.0557
   Cbep               Bcon         E         Cbep
   Cbcp               C            Bcon      Cbcp
   Ccep               C            E         Ccep
   Lep                E            0         Lep
   Lbp                Bcon         BB        Lbp
   Lcp                C            CC        Lcp
```

```
*-------------------------------------------------
* BJT    Collector      Base       Emitter      Model
*-------------------------------------------------
  Q1        C             B          E         T2u6d2f

.option post ingold=1


.model T2u6d2f  npn
  + BF   =   83.926        BR   =   0.6338        NF   =   1.1049
  + NR   =   1.00000       NE   =   1.7000        NC   =   1.7595
  + RB   =   4.8379        RE   =   6.7896        RC   =   2.2
  + IS   =   1.1111e-25    ISE  =   2.432e-19     ISC  =   4.393e-16
  + CJE  =   4.8855e-14    MJE  =   .50           VJE  =   1.7018
  + CJC  =   1.5758e-13    MJC  =   .50           VJC  =   1.4107
  + TF   =   9.5243e-13    TR   =   1.2611e-10    XCJC =   0.159

*-------------------------------------------------
* These are the empirical curve-fit model parameters:
*-------------------------------------------------
.param Cbep  =  optl(6f, 1f, 30f)
     + Cbcp  =  optl(7.6f, 1f, 114f)
     + Ccep  =  optl(18.5f, 3.7f, 92.5f)
     + Lep   =  optl(15p, 0.3p, 30p)
     + Lbp   =  optl(40p, 8p, 85p)
     + Lcp   =  optl(20p, 5p, 50p)

*-------------------------------------
* ac optimization analysis statement:
*-------------------------------------
.ac data=measured optimize=optl results=S11R,S11I,S12R,S12I,
     + S21R,S21I,S22R,S22I model=converge LIN 50 1 50

.model converge opt itropt=40 grad=1e-04

.meas ac S11R err1  par(S11R) S11(R)
.meas ac S11I err1  par(S11I) S11(I)
.meas ac S12R err1  par(S12R) S12(R)
.meas ac S12I err1  par(S12I) S12(I)
.meas ac S21R err1  par(S21R) S21(R)
.meas ac S21I err1  par(S21I) S21(I)
.meas ac S22R err1  par(S22R) S22(R)
.meas ac S22I err1  par(S22I) S22(I)

.ac data=measured

*---------------------------------------
* Measured data to fit model parasitics:
*---------------------------------------
.data measured
```

```
  FREQ        S11R       S11I       S21R       S21I       S12R       S12I       S22R       S22I

  1.0E9      0.172974  -0.640778  -6.634521  5.355225  0.072590  0.089401   0.388580  -0.764008
  2.0E9     -0.271027  -0.632904  -3.033936  5.400879  0.134781  0.084106  -0.135834  -0.734680
    :           :          :          :          :          :          :          :          :
 50.0E9     -0.607330   0.274536  0.412979  0.024307  0.156013  -0.094345  -0.652008  0.114655

.enddata
.end
```

HSPICE 2u6d2f ac Analysis Script

```
******  operating point information:
node   =  voltage      node   =  voltage      node   =  voltage

   b   =    1.7740      bb    =   1.7772      bcon   =   1.7772
   c   =    1.0000      cc    =   1.0000      e      =   0.
****  voltage sources
subckt
element  0:vce
 volts      1.0000
 current  -32.3848m
 power     32.3848m

***** current sources
subckt
element  0:ib
 volts     -1.7772
 current  800.0000u
 power      1.4218m

**** resistors
subckt
element  0:rsrc      0:rbcon
 r value  1.000e+20    4.0557
 v drop     1.7772    -3.2446m
 current  1.777e-20 -800.0000u
 power    3.159e-20    2.5956u

**** bipolar junction transistors
subckt
element  0:q1
model    0:t2u6d2f
 ib        800.0000u
 ic         32.3848m
 vbe         1.7740
 vce         1.0000
 vbc       773.9725m
 vs       -921.0814m
 power      33.8040m
 betad      40.4810
```

gm	711.8371m
rpi	58.3202
rx	782.1000m
ro	2.3605g
cpi	749.0504f
cmu	32.6238f
cbx	172.5862f
ccs	0.
betaac	41.5145
ft	118.7226g

Bibliography

[1] P. M. Asbeck, M. F. Chang, J. A. Higgins, N. H. Sheng, G. J. Sullivan, and K.-C. Wang, "GaAlAs/GaAs Heterojunction Bipolar Transistors: Issues and Prospects for Application," *IEEE Trans. Electron Dev.*, vol. 36, pp. 2032-2041, Oct. 1989.

[2] P. M. Asbeck, M. F. Chang, K.-C. Wang, D. L. Miller, G. J. Sullivan, N. H. Sheng, E. Sovero, and J. A. Higgins, "Heterojunction Bipolar Transistors for Microwave and Millimeter-wave Integrated Circuits," *IEEE Trans. Electron Dev.*, vol. 34, pp. 2571-2579, Dec. 1987.

[3] M. E. Kim, A. K. Oki, G. M. Gorman, D. K. Umemoto, and J. B. Camou, "GaAs Heterojunction Bipolar Transistor Device and IC Technology for High-Performance Analog and Microwave Applications," *IEEE Trans. Microwave Theory Tech.*, vol. 37, pp. 1286-1302, Sep. 1989.

[4] M. Konagi and K. Takahashi, "(GaAl)As-GaAs Heterojunction Transistors with High Injection Efficiency," *J. Appl. Phys.*, vol. 46, pp. 2120-2123, May 1975.

[5] H. Ito, T. Ishibashi, and T. Sugeta, "Fabrication and Characterization of AlGaAs/GaAs Heterojunction Bipolar Transistors," *IEEE Trans. Electron Dev.*, vol. 34, pp. 224-229, Feb. 1987.

[6] F. Ali, M. Salib, and A. Gupta, "A 1-Watt X-Ku Band HBT MMIC Amplifier with 50% Peak Power-Added Effieciency," *IEEE Microwave and Guided Wave Letters*, vol. 3, pp. 271-272, Aug. 1993.

[7] B. Bayraktaroglu, J. Barrette, L. Kehias, C. Huang, R. Fitch, R. Neidhard, and R. Scherer, "Very High-Power-Density CW Operation of GaAs/AlGaAs Microwave Heterojunction Bipolar Transistors," *IEEE Electron Device Letters*, vol. 14, pp. 493-495, Oct. 1993.

[8] M. Hafizi, R. A. Metzger, and W. E. Stanchina, "Dependence of DC Current Gain and f_{max} of AlInAs/GaInAs HBTs on Base Sheet Resistance," *IEEE Electron Device Letters*, vol. 14, pp. 323-325, Jul. 1993.

[9] F. Ren, C. R. Abernathy, S. J. Pearton, J. R. Lothian, P. W. Wisk, T. R. Fullowan, Y.-K. Chen, L. W. Yang, S. T. Fu, and R. S. Brozovich, "Self-Aligned InGaP/GaAs Heterojunction Bipolar Transistors for Microwave Power Application," *IEEE Electron Device Letters*, vol. 14, pp. 332-334, Jul. 1993.

[10] W. Matsuoka, K. Kurishima, and T. Makimoto, "High-frequency InP/InGaAs Double Heterojunction Bipolar Transistors on Si Substrate," *IEEE Electron Device Letters*, vol. 14, pp. 357-359, Jul. 1993.

[11] K. Ikossi-Anastasiou, "GaAsSb for Heterojunction Bipolar Transistors," *IEEE Trans. Electron Dev.*, vol. 40, pp. 878-884, May 1993.

[12] J. Chen, G. B. Gao, and H. H. Morkoç, "Comparative Analysis of the High-Frequency Performance of $Si/Si_{1-x}Ge_x$ Heterojunction Bipolar and Si Bipolar Transistors," *Solid-State Electronics*, vol. 35, pp. 1037-1044, Aug. 1992.

[13] W. Till and J. Luxon, *Integrated Circuits: Materials, Devices and Fabrication*, Prentice-Hall, NJ, 1982.

[14] S. M. Sze, *Physics of Semiconductor Devices*, John Wiley and Sons, NY, 1981.

[15] S. M. Sze, ed., *High-Speed Semiconductor Devices*, John Wiley and Sons, NY, 1990.

[16] T. Ikoma, ed., *Very High Speed Integrated Circuits: Heterostructure*, Semiconductors and Semimetals, Vol 30, Academic Press, CA, 1990.

[17] H. Kroemer, "Heterostructure Bipolar Transistors and Integrated Circuits," *Proceedings of the IEEE*, vol. 70, pp. 13-25, Jan. 1982.

[18] H. Kroemer, "Theory of a Wide-Gap Emitter for Transistors," *Proceedings of the IRE*, vol. 45, pp. 1353-1357, 1957.

[19] W. Shockley, U. S. Patent no. 2,569,347 assigned to W. Shockley, Jun 26, 1948.

[20] W. Dumke, J. Woodall, and V. Rideout, "GaAs-GaAlAs Heterojunction Transistor for High Frequency Operation," *Solid-State Electronics*, vol. 15, pp. 1339-1334, Dec. 1972.

[21] P. Antognetti and G. Massobrio, eds., *Semiconductor Device Modeling with SPICE*, McGraw-Hill, NY, 1988.

[22] S.J. Wang, J.Y. Lee and C.Y. Chang, "An Efficient and Reliable Approach for Semiconductor Device Parameter Extraction," *IEEE Transactions on Computer-Aided Design*, vol. 5, pp. 170-178, Jan. 1986.

[23] B. Ryum and I. Abdel-Motaleb, "A Gummel-Poon Model for Abrupt and Graded Heterojunction Bipolar Transistors (HBTs)," *Solid-State Electronics*, vol. 33, pp. 869-880, July 1990.

[24] C. Parikh and F. Lindholm, "A New Charge-Control Model for Single- and Double-Heterojunction Bipolar Transistors," *IEEE Trans. Electron Dev.*, vol. 39, pp. 1303-1311, June 1992.

[25] P. Grossman and J. Choma, "Large Signal Modeling of HBT's Including Self Heating and Transit Time Effects," *IEEE Trans. Microwave Theory and Techniques*, vol. 40, pp. 449-463, March 1992.

[26] M. Hafizi, C. Crowell, and M. Grupen, "The DC Characteristics of GaAs/AlGaAs Heterojunction Bipolar Transistors with Application to Device Modeling," *IEEE Trans. Electron Devices*, vol. 37, pp. 2121-2129, Oct. 1990.

[27] J. J. Liou and J. S. Yuan, "Physics-based Large-siganl Heterojunction Bipolar Transistor Model for Circuit Simulation," *IEE Proceedings-G*, vol. 138, pp. 97-103, Feb. 1991.

[28] D. Pehlke and D. Pavlidis, "Evaluation of the Factors Determining HBT High-frequency Performance by Direct Analysis of S-Parameter Data," *IEEE Trans. Microwave Theory and Techniques*, vol. 40, pp. 2367-2373, Dec. 1992.

[29] S. Maas and D. Tait, "Parameter Extraction Method for Heterojunction Bipolar Transistors," *IEEE Microwave and Guided Wave Letters*, vol. 2, pp. 502-504, Dec. 1992.

[30] R. Trew, U. Mishra, W. Pribble, and J. Jensen, "A Parameter Extraction Technique for Heterojunction Bipolar Transistors," *1989 IEEE MTT-S Digest*, pp. 897-900.

[31] D. Costa, W. Liu, and J. Harris, Jr., "Direct Extraction of the AlGaAs/GaAs Heterojunction Bipolar Transistor Small-Signal Equivalent Circuit," *IEEE Trans. Electron Devices*, vol. 38, pp. 2018-2024, Sep. 1991.

[32] J. J. Liou, L. L. Liou, C. I. Huang, and B. Bayraktaroglu, "A Physics-Based, Analytical Heterojunction Bipolar Transistor Model Including Thermal and High-Current Effects," *IEEE Trans. Electron Dev.*, vol. 40, pp. 1570-1577, Sep. 1993.

[33] H. Wang, C. Algani, A. Konczykowska, and W. Zuberek, "Temperature Dependence of DC Currents in HBT," *1992 IEEE MTT-S Digest*, pp. 731-734.

[34] M. Hafizi, W. E. Stanchina, R. A. Metzger, P. A. Macdonald, and F. Williams, Jr., "Temperature Dependence of DC and RF Characteristics of AlInAs/GaInAs HBT's," *IEEE Trans. Electron Dev.*, vol. 40, pp. 1583-1587, Sep. 1993.

[35] D. S. Whitefield, D. S. Wei, and J. C. Hwang, "Large Signal Characterization and Modelling of Heterojunction-Bipolar Transistors Annual Report," *Report No. AD-A253011*, June 1, 1991-May 31, 1992.

[36] C. C. McAndrew, "A Complete and Consistent Electrical/Thermal HBT Model," *IEEE 1992 Bipolar Circuits and Technology Meeting*, paper 10.1, pp. 200-203.

[37] A. Marty, T. Camps, J. Tasselli, D. Pulfrey, and J. P. Bailbe, "A Self-Consistent DC-AC Two Dimensional Electrothermal Model for GaAlAs/GaAs Microwave Power HBT's," *IEEE Trans. Electron Dev.*, vol. 40, pp. 1202-1210, July 1993.

[38] Mathcad Version 3.1, 1992. MathSoft Inc., 201 Broadway, Cambridge, MA 02139.

[39] *HSPICE User's Manual, vol. 2, Elements and Models*, HSPICE Version H92, 1992. Meta-Software, Inc., Customer Service Dept., 1300 White Oaks Rd., Campbell, CA 95008.

[40] *HSPICE User's Manual, vol. 3, Analysis and Methods*, HSPICE Version H92, 1992. Meta-Software, Inc., Customer Service Dept., 1300 White Oaks Rd., Campbell, CA 95008.

[41] *Axum Technical Graphics and Data Analysis*, Third edition, 1993. Trimetrix, Inc., 444 NE Ravenna Blvd., Suite 210, Technical Support Dept., Seattle, WA 98115.

[42] *Designer's Task Reference, vol. 2, Creating Circuits as Schematics*, HP 85150B Microwave and RF Design Systems, Release 5.0, edition 2 Dec. 1992. Hewlett-Packard Company, Santa Rosa Systems Div., 1400 Fountaingrove Pkwy., Santa Rosa, CA 95403.

[43] J. Ebers and J. Moll, "Large-Signal Behavior of Junction Transistors," *Proceedings of the IRE*, vol. 42, pp. 1761-1772, 1954.

[44] H. Gummel and H. Poon, "An Integral Charge Control Model of Bipolar Transistors," *Bell Systems Technical Journal*, vol. 49, pp. 827-852, May 1970.

[45] D. Hodges and H. Jackson, *Analysis and Design of Digital Integrated Circuits*, McGraw-Hill, NY, 1988.

[46] B. R. Ryum and I. M. Abdel-Motaleb, "Effect of Recombination Current on Current Gain of HBTs," *IEE Proceedings-G*, vol. 138, pp. 115-119, Feb. 1991.

[47] J. Yoshida, M. Kurata, K. Morizuka, and A. Hojo, "Emitter-base Bandgap Grading Effects on GaAlAs/GaAs Heterojunction Bipolar Transistor Characteristics," *IEEE Trans. Electron Dev.*, vol. 32, pp. 1714-1720, Sep. 1985.

[48] K. Yokoyama, M. Tomizawa, and A. Yoshii, "Accurate Modeling of AlGaAs/GaAs Heterostructure Bipolar Transistor by Two Dimensional Computer Simulation," *IEEE Trans. Electron Dev.*, vol. 31, pp. 1222-1229, Sep. 1984.

[49] P. Grossman and A. Oki, "A Large Signal DC Model for GaAs/$Ga_{1-x}Al_xAs$ Heterojunction Bipolar Transistors," *IEEE 1989 Bipolar Circuits and Technology Meeting*, paper 9.6, pp. 258-261.

[50] W. Shockley, "The Theory of *p-n* Junctions in Semiconductors and *p-n* Junction Transistors," *Bell Systems Technical Journal*, vol. 28, pp. 435–489, July 1949.

[51] S. M. Sze, *Semiconductor Devices, Physics and Technology*, John Wiley and Sons, NY, 1985.

[52] J. J. Liou, "Calculation of the Base Current Components and Determination of Their Relative Importance in AlGaAs/GaAs and InAlAs/InGaAs Heterojunction Bipolar Transistors," *J. Appl. Phys.*, vol. 69, pp. 3328–3334, Mar 1991.

[53] F. Ali and A. Gupta, eds., *HEMTs and HBTs: Devices, Fabrication and Circuits*, Artech House, MA, 1991.

[54] D. Pozar, *Microwave Engineering*, MA, Addison-Wesley, 1990.

[55] T. S. Laverghetta, *Practical Microwaves*, IN, Howard W. Sams & Co., 1984.

[56] C. R. Selvakumar, "A New Minority Carrier Lifetime Model for Heavily Doped GaAs and InGaAsP to Obtain Analytical Solutions," *Solid-State Electronics*, vol. 30, pp. 773–774, July 1991.

[57] M. S. Lundstrom, M. E. Klausmeier-Brown, M. R. Melloch, R. K. Ahrenkiel, and B. M. Keyes, "Device-related Material Properties of Heavily Doped Gallium Arsenide," *Solid-State Electronics*, vol. 33, pp. 693–704, June 1990.

[58] D. M. Caughey and R. E. Thomas, "Carrier Mobilities in Silicon Empirically Related to Doping and Field," *Proceedings of the IEEE*, vol. 55, pp. 2192–2193, Dec. 1967.

[59] S. Adachi, "GaAs, AlAs, and $Al_xGa_{1-x}As$: Material Parameters for Use in Research and Device Applications," *J. Appl. Phys.*, vol. 58, pp. R1–R29, Aug. 1985.

[60] P. H. Ladbrooke, *MMIC Design: GaAs FETs and HEMTs*, MA, Artech House, Inc., 1989.

[61] WL/ELR HBT Layout Design

[62] M. Lundstrom, "An Ebers-Moll Model for the Heterostructure Bipolar Transistor," *Solid-State Electronics*, vol. 29, pp. 1173–1179, 1986.

[63] H. F. Cooke, "Microwave Transistors: Theory and Design," *Proceedings of the IEEE*, vol. 59, pp. 1163–1181, Aug. 1971.

[64] D. V. Morgan and M. J. Howes, eds., *Microwave Solid-State Devices and Applications*, pp. 30–35, Peter Peregrinus Ltd. Stevenage, UK, 1980.

[65] W. Liu, D. Costa, and J. S. Harris, Jr., "Derivation of the Emitter-collector Transit Time of Heterojunction Bipolar Transistors," *Solid-State Electronics*, vol. 35, pp. 541-545, Apr. 1992.

[66] J. J. Liou, "Common-emitter current gain of $Al_xGa_{1-x}As/GaAs/GaAs$ heterojunction bipolar transistors operating at small collector current," *IEEE Trans. Electron Dev.*, vol. 36, pp. 1850-1852, Sep. 1989.

[67] C. N. Huang and I. M. Abdel-Motaleb, "Gummel-Poon model for single and double heterojunction bipolar transistors," *IEE Proceedings-G*, vol. 138, pp. 165-169, Apr. 1991.

[68] A. B. Phillips, *Transistor Engineering and Introduction to Integrated Semiconductor Circuits*, pp. 211-216, McGraw-Hill, NY, 1962.

[69] D. Ferry, ed., *Gallium Arsenide Technology Volume 2*, Howard W. Sams & Co., IN, 1990.

[70] V. Ya. Niskov and G. A. Kubetskii, "Resistance of Ohmic Contacts Between Metals and Semiconductor Films," *Soviet Physics - Semiconductors*, vol. 4, pp. 1553-1554, Mar. 1971.

[71] "GaAs/AlGaAs HBT Analog-to-Digital Converter," Rockwell, WRDC-TR-89-5041, Oct. 1989.

[72] H.-F. Chau and E. A. Beam, III, "High-Speed InP/InGaAs Heterojunction Bipolar Transistors," *IEEE Electron Device Letters*, vol. 14, pp. 388-390, Aug. 1993.

[73] B. Meskoob, S. Prasad, M. Vai, C. G. Fonstad, J. C. Vlcek, H. Sato, and C. Bulutay, "A Small-Signal Equivalent Circuit for the Collector-Up InGaAs/InAlAs/InP Heterojunction Bipolar Transistor," *IEEE Trans. Electron Dev.*, vol. 40, pp. 2629-2632, Nov. 1992.

[74] R. F. Harrington, *Introduction to Electromagnetic Engineering*, McGraw-Hill, NY, 1958.

[75] Smythe, *Static and Dynamic Electricity*, 1968.

[76] B. Meskoob, S. Prasad, M. Vai, J. C. Vlcek, H. Sato, and C. G. Fonstad, "Bias-Dependence of the Intrinsic Element Values of InGaAs/InAlAs/InP Inverted Heterojunction Bipolar Transistor," *IEEE Trans. Microwave Theory Tech.*, vol. 40, pp. 1012-1014, May 1992.

[77] C. T. Matsuno, A. K. Sharma, and A. K. Oki, "A Large-Signal HSPICE Model for the Heterojunction Bipolar Transistor," *IEEE Trans. Microwave Theory Tech.*, vol. 37, pp. 1472-1474, Sep. 1989.

[78] D. A. Teeter, J. R. East, R. K. Mains, and G. I. Haddad, "Large-Signal Numerical and Analytical HBT Models," *IEEE Trans. Electron Dev.*, vol. 40, pp. 837-845, May 1993.

Vita

James A. Fellows was born on August 13, 1965, in Concord, New Hampshire. In May 1987, he graduated with distinction from Clarkson University with a Bachelor of Science degree in Electrical Engineering and was commissioned as a Second Lieutenant in the United States Air Force. His first assignment began in January 1988 at Los Angeles AFB, California, where he was a Communications Project Engineering Manager for the Air Force Satellite Control Network (AFSCN). In April 1992, he entered the School of Engineering at the Air Force Institute of Technology (AFIT), Wright-Patterson AFB, Ohio. At AFIT his academic specialization has been in the areas of semiconductor devices and very large scale integration (VLSI) circuit design.

REPORT DOCUMENTATION PAGE

Form Approved
OMB No. 0704-0188

1. AGENCY USE ONLY (Leave blank)	2. REPORT DATE	3. REPORT TYPE AND DATES COVERED
	December 1993	Master's Thesis

4. TITLE AND SUBTITLE
A Physics-Based Heterojunction Bipolar Transistor Model For Integrated Circuit Simulation

5. FUNDING NUMBERS

6. AUTHOR(S)
James A. Fellows

7. PERFORMING ORGANIZATION NAME(S) AND ADDRESS(ES)
Air Force Institute of Technology, WPAFB OH 45433-7765

8. PERFORMING ORGANIZATION REPORT NUMBER
AFIT/GE/ENG/93D-07

9. SPONSORING / MONITORING AGENCY NAME(S) AND ADDRESS(ES)
Mr. Ken Nakano
Wright Laboratory (WL/ELRD)
Wright-Patterson AFB, OH 45433-7318

10. SPONSORING / MONITORING AGENCY REPORT NUMBER

11. SUPPLEMENTARY NOTES

12a. DISTRIBUTION / AVAILABILITY STATEMENT
Approved for public release; distribution unlimited

12b. DISTRIBUTION CODE

13. ABSTRACT *(Maximum 200 words)*

The purpose of this research effort was to derive a physics-based dc model for a Heterojunction Bipolar Transistor (HBT). The dc model was then linearized to arrive at a small-signal model that accurately predicts the device's electrical behavior at microwave frequencies. This new model offers features not found in previous analytical or physics-based HBT models such as consideration of a cylindrical emitter-base geometry and is direct implemention into SPICE (Simulation Program with Integrated Circuit Emphasis). The device model parameters were determined from a knowledge of the device material, geometry, and fabrication process. The model was then developed by using semiconductor physics to calculate modified parameters for the existing SPICE bipolar junction transistor (BJT) model.

14. SUBJECT TERMS
HBT Models, HBT, Heterojunction Bipolar Transistors, Simulation, Semiconductor Devices, SPICE

15. NUMBER OF PAGES
251

16. PRICE CODE

17. SECURITY CLASSIFICATION OF REPORT	18. SECURITY CLASSIFICATION OF THIS PAGE	19. SECURITY CLASSIFICATION OF ABSTRACT	20. LIMITATION OF ABSTRACT
UNCLASSIFIED	UNCLASSIFIED	UNCLASSIFIED	UL